UNIVERSITY OF SOUTHAMPTON

FACULTY OF ENGINEERING AND THE ENVIRONMENT

Institute of Sound and Vibration Research

The influence of various excitation mechanisms on ground vibration from trains

by

Nuthnapa Triepaischajonsak

Thesis for the degree of Doctor of Philosophy

February 2012

UNIVERSITY OF SOUTHAMPTON

ABSTRACT

FACULTY OF ENGINEERING AND THE ENVIRONMENT

INSTITUTE OF SOUND AND VIBRATION RESEARCH

Doctor of Philosophy

THE INFLUENCE OF VARIOUS EXCITATION MECHANISMS ON GROUND VIBRATION FROM TRAINS

by Nuthnapa Triepaischajonsak

Ground vibration from trains is an increasingly important environmental problem. This study investigates the various excitation mechanisms of ground vibration.

An existing semi-analytical model, TGV, which considers both the quasi-static excitation due to moving axle loads and the dynamic excitation due to vertical rail irregularities, has been validated by an extensive measurement campaign. This involved the determination of soil properties at two sites with soft clay soil. These were found to exhibit an inversion of the wave speed profile. Good agreement was found between measurements and predictions of vibration due to train pass-bys.

The relative importance of the dynamic and quasi-static excitation mechanisms has been investigated for a range of conditions including changes to track and vehicle parameters. The dynamic excitation mechanism is found to dominate the results above about 10 Hz and at all frequencies for distances beyond 10 m from the track.

In order to study other excitation mechanisms a new hybrid model has been developed. This combines a wheel/track interaction model working in the time-spatial domain and an axisymmetric layered ground model working in the wavenumber-frequency domain. In the time domain model a 'circular' track is introduced to allow longer responses to be calculated. The model is then validated by comparison with the existing TGV model. A reasonable agreement is found.

The hybrid model has then been used to investigate the relative importance of quasi-static loads, dynamic loads and some other excitation mechanisms for trains running on the ground. The sleeper-passing effect is investigated for both constant and variable sleeper spacing but it is found to give much lower responses than those due to roughness. Variable ballast stiffness is also investigated and found not to be significant. Impact forces caused by the passage of wheels over dipped welds and stepped joints are found to generate ground responses that are considerably larger than roughness excitation in the region close to these track defects. However the response decays more rapidly with distance than that due to roughness.

CONTENTS

DECLARATION OF AUTHORSHIP

I, Nuthnapa Triepaischajonsak, declare that the thesis entitled 'Investigation of ground vibration induced by trains' and work presented in the thesis are both my own, and have been generated by me as the result of my own original research. I confirm that:

- This work was done wholly or mainly while in candidature for a research degree at this University.
- No part of this thesis has previously been submitted for a degree or any other qualification at this University or any other institution.
- Where I have consulted the published work of others, this is always clearly attributed.
- Where I have quoted from the work of others, the source is always given. With the exception of such quotations, this thesis is entirely my own work.
- I have acknowledged all main sources of help.
- Where the thesis is based on work done by myself jointly with others, I have made clear exactly what was done by others and what I have contributed myself.
- Parts of this work have published as:

- N. Triepaischajonsak, D.J. Thompson and C.J.C. Jones, "The experimental validation of a semi-analytical track/ground model for vibration induced by trains," X International Conference on Recent Advances in Structural Dynamics, Southampton, UK, July 2010, No.139.
- N. Triepaischajonsak, D.J. Thompson, C.J.C. Jones and J. Ryue, "Track-based control measures for ground vibration – the influence of quasi-static loads and dynamic excitation," 10th International Workshop on Railway Noise, Nagahama, Japan, October 2010, pp.237-244.
- N. Triepaischajonsak, D.J. Thompson, C.J.C. Jones, J. Ryue and J.A. Priest, "Ground vibration from trains: experimental parameter characterization and validation of a numerical model, Proc. IMechE, Part F, Journal of Rail and Rapid Transit Vol. 225 (2011), pp 140-153.

Signed:…….

Date:…….

ACKNOWLEDGEMENTS

First of all I would like to express my appreciation to my supervisors Prof. David Thompson and Dr. Chris Jones for their guidance and encouragement during this project. Their support is greatly appreciated. I would also like to thank Dr Jungsoo Ryue, Dr Jeff Priest and the railway staff who assisted with the measurements in Chapter 3. The measurements have been partly supported by the Engineering and Physical Sciences Research Council (EPSRC) through Rail Research UK. The cooperation of the local landowners is gratefully acknowledged.

I would also like to extend my appreciation to MST and TISTR for sponsoring and giving the opportunity to study at the ISVR, particularly Mr. Surapol Wattanawong, Mr Cheumsakra Sinchaisri, Dr Wadee Wichaidit and Dr. Luxsamee Plangsangmas. In addition, I would like to thank my Thai friends for good times and kindness, especially Dr Chompoonoot Hirunyapruk who was a former student at ISVR for her advice.

Finally, I am extremely thankful to my parents Mr. Samroeng and Mrs. Wannaporn Triepaischajonsak, and my lovely brother Mr. Monthon Triepaischajonsak for their support, encouragement and true love.

LIST OF SYMBOLS

$A(r)$ amplitude at some distance r (Chapter 2)

A_0 reference amplitude (Chapter 2)

E Young's modulus (Chapter 2)

F complex amplitude of a vertical harmonic force (Chapter 4)

F_1 force (Chapter 3)

F_I external force (Chapter 4)

F_{ground} force acting on the ground (Chapter 5)

$\tilde{F}_i(f)$ discrete Fourier transform of the force $F_i(t)$ (Chapter 5)

K_b stiffness of ballast per sleeper (Chapter 5)

K_P stiffness of rail pad per sleeper (Chapter 5)

K_T static stiffness of the track (Chapter 5)

KB_{FTr} average of the maximum filtered r.m.s. signal values (Chapter 2)

L vehicle length (Chapter 5)

L width of the dipped weld (Chapter 7)

$[S_{FF}]$ matrix of power spectral density (Chapter 5)

S_{vv} power spectral density of the ground velocity (Chapter 5)

T duration of the event (Chapter 2)

T analysis length (Chapter 5)

$T_{e,j}$ exposure period of each event (Chapter 2)

T_r evaluation period (Chapter 2)

V_2 velocity amplitude (Chapter 3)

VDV Vibration Dose Values (Chapter 2)

W axle load (Chapter 5)

Y point mobility (Chapter 4)

$[Y]$ matrix of ground mobilities (Chapter 5)

Y_{12} transfer mobility (Chapter 3)

Y_{22} point mobility (Chapter 3)

Y_g ground mobility (Chapter 5)

Y^R rail mobility (Chapter 4)

Y^W wheel mobility (Chapter 4)

$a(t)$ frequency weight acceleration (Chapter 2)

c_1 longitudinal wave speed (Chapter 2)

c_2 transverse wave speed (Chapter 2)

c_2 viscous damping coefficient of the damper (Chapter 4)

c_3 viscous damping coefficient of the damper (Chapter 4)

c_b ballast damper (Chapter 5)

c_{eq} equivalent damping coefficient (Chapter 5)

c_R Rayleigh wave speed (Chapter 2)

d perpendicular distance (Chapter 5)

k_2 stiffness of the primary suspensions (Chapter 4)

k_3 stiffness of the secondary suspensions (Chapter 4)

k_b ballast stiffness (Chapter 5)

k_{eq} equivalent stiffness (Chapter 5)

m_1 mass of one wheelset (Chapter 4)

m_2 half a bogie and the upper (Chapter 4)

m_3 a quarter of the body mass (Chapter 4)

n index of refraction (Chapter 2)

r roughness amplitude (Chapter 4)

r radial distance (Chapter 5)

s_R real root (Chapter 2)

t arrival times (Chapter 3)

u x components of displacement u (Chapter 2)

u_{r_0} rail vibration at each time history (Chapter 5)

$\overline{u}_r^2$ average vibration (Chapter 5)

v y components of displacement u (Chapter 2)

v_1 the upper layer velocity (Chapter 3)

v_2 the lower layer velocity (Chapter 3)

v^R rail velocity (Chapter 4)

v^W wheel velocity (Chapter 4)

w z components of displacement u (Chapter 2)

x distance along the track (Chapter 5)

x_{cross} the crossover distance (Chapter 3)

y height of the dipped weld (Chapter 7)

y_0 overall depth (Chapter 7)

z depth of the upper layer (Chapter 3)

α factor correspond to a simple geometric spreading (Chapter 2)

α factor corresponding to the reduction in the amplitude (Chapter 7)

β parameter depends on the damping of the material (Chapter 2)

β imaginary part of a wavenumber (Chapter 5)

η loss factor representing the material damping of the soil (Chapter 2)

λ first Lamé's constant (Chapter 2)

θ angle at the bottom of the discrete track defect (Chapter 7)

μ second Lamé's constant (Chapter 2)

ν Poisson's ratio (Chapter 2)

ω circular frequency (Chapter 2)

ρ density of the soil (Chapter 2)

Superscripts

^{H} Hermitian transpose (Chapter 5)

1. Introduction

1.1 Background

Increasing demand for transportation in general and for railways in particular has had an impact on environmental problems. As the requirements for transport increase, more frequent, faster, heavier and longer trains operate which then cause more problems of noise and ground vibration along the route. Particularly the introduction of high speed trains highlights the problem of ground vibration. This may lead to an increase in complaints of disturbance and annoyance from people living and working alongside lines. Also for new lines, people often object to proposed new developments on the basis of noise and vibration. There is therefore an important need to understand the causes of noise and vibration and to derive solutions for reducing them.

When a train passes by it not only causes noise but also induces vibration in the ground which propagates away from the track. This may cause vibration or rumbling noise in the buildings nearby which is difficult to control. Noise and vibration are generated in various ways at the wheel-rail interface, but railway noise and vibration can be categorized into two main classes: vibration and noise transmitted through the ground with a frequency range of about 4 to 250 Hz and airborne noise with a frequency range of typically 100 to 5000 Hz [1].

The ground vibration at low frequency is experienced in two different ways: firstly feelable ground vibration with a frequency range of about 4 to 80 Hz and secondly ground-borne noise for which the relevant frequency range is 30 to 250 Hz [1]. Moreover people's perception of vibration depends on the frequency. For the human body the relevant frequency range is 1 to 80 Hz. Compared with airborne sound, ground vibration and ground-borne noise are less well understood and much more difficult to predict.

This thesis focuses on the ground-borne vibration or 'feelable vibration' induced by surface trains, particularly in the frequency range up to 100 Hz. This low-frequency ground-borne vibration is mainly caused by the same excitation mechanism

as airborne noise, unevenness of the rail and wheel surfaces. However, the ground-borne vibration involves a longer wavelength associated with a deflection pattern in the ground due to moving trains. The main excitation mechanisms are usually identified as the moving quasi-static load and dynamic excitation due to the wheel and track unevenness but also a number of other excitation mechanisms exist such as the variation of support stiffness [2].

The main aim of this thesis is to understand the relative importance of quasi-static loads, dynamic loads and other excitation mechanisms, by investigating the ground responses due to these parameters for different situations. A number of models have been developed to predict ground-borne noise and ground-borne vibration induced by trains. An existing semi-analytical model, TGV, which considers both the quasi-static excitation due to moving axle loads and the dynamic excitation due to vertical rail irregularities, has been used and is validated by comparison with extensive measurements in Chapter 3. Its use in studying the relative importance of quasi-static and dynamic excitations is considered in Chapter 4. However, this existing model is limited to excitation by stationary roughness profiles.

In order to consider other excitation mechanisms, a new hybrid model is developed in Chapter 5. The model works in the time domain allowing for variation of track/ground support stiffness. An axisymmetric layered ground model is then combined with the model. In order to obtain the vibration at various distances from the track the hybrid model has then been used in Chapters 6 and 7 to investigate the relative importance of quasi-static loads, dynamic loads and some other excitation mechanisms for trains running on the ground.

First, however, a literature review is presented in Chapter 2.

2. Literature review

The development of models for ground-borne noise and ground-borne vibration induced by trains has increased in recent years. Analytical, numerical and empirical approaches are all used. The main excitation mechanisms are usually identified as the moving quasi-static load and dynamic excitation due to the wheel and track unevenness but also a number of other excitation mechanisms exist such as the variation of support stiffness [2]. In this chapter a number of approaches developed to model the ground-borne noise and vibration are described. The discussion is divided into the excitation mechanisms, transmission models, mitigation measures and assessment criteria for ground-borne vibration.

2.1 Excitation mechanisms

The main sources of vibration at the line-side of a railway consist of: heavy axle-load freight traffic; high-speed passenger trains, and trains running in tunnels [3]. Long, heavy axle-load freight trains running on main line railways on the ground surface produce low frequency surface-propagating waves. Such waves propagating along the ground surface, especially in the case of soft soil, may cause the buildings near to the track to vibrate on the stiffness of their foundations. High speed passenger trains may become a significant source of vibration where they run at speeds in excess of the wave speed of vibration in the ground. Large displacements produced by high speed trains have been compared with the 'bow wave' from a ship or the 'sonic boom' from a supersonic aircraft [1,4]. The ground vibration from trains that run in tunnels is mainly perceived as structure-borne noise. The frequency content of this vibration is higher, and may cause the bending vibration in the floors and walls of a building which produces a rumbling noise in its rooms [3].

The dynamic component due to rail irregularities is the main excitation mechanism used by most authors to predict ground-borne noise and vibration [3]. For example the model Igitur, developed by Jones [5], and the Pipe-in-Pipe (PiP) model, developed by Hunt and Hussein [6], both use rail roughness as the excitation to predict surface ground vibration and vibration from train in the tunnel respectively.

A harmonic load, at sufficiently high frequency can directly excite propagating waves in the ground at any load speed. However a propagating wave can be excited by a quasi-static load only if the load speed is greater than that of a propagating wave in the ground [7].

The prediction of ground vibration due to moving trains was presented by Krylov [8] using a Green's function formalism based on the quasi-static load. It was found that vibration spectra depend strongly on the train speed when this speed exceeds a critical value which corresponds to the speed of propagating waves in the track.

Also in [9] Krylov showed that a very large increase in ground vibration level can be found as the speed of a high-speed train approaches or exceeds the Rayleigh wave speed in the ground. However, the amplitude of ground vibration generated by trains is reduced as the speed of the train approaches the minimal phase velocity of track bending waves [9]. Krylov's model takes only quasi-static excitation into account for the prediction of ground vibration. The moving quasi-static load causes local deflection of the track under each wheel and, in rare cases, can lead to a 'bow wave' effect in the ground [10]. In practice, the issue of trains exceeding the wave speed in the ground has long been a consideration of track engineers [3]. For a soft ground, where there is a danger of trains exceeding the 'critical speed of the track and ground, speed restrictions would be imposed.

Sheng et al [11] showed that for the vibration generated by a train at speeds below the wave speed of the ground the dynamic component is more important than the quasi-static component. The quasi-static loads are not sufficient to represent the ground vibration in practice for many measurement conditions especially at high excitation frequencies [12].

The case of a moving load on a layered ground is considered in [13] using an analytical model (described further in Section 2.2). A localised quasi-static response pattern is found when a constant load moves at a speed below any of the wave speeds in the ground. On the other hand, propagating waves occur in the ground when the load speeds exceed the Rayleigh wave speed of the upper layer. In [13] a ground was

considered consisting of a weathered surface layer over a stiffer half-space. The maximum amplitude was found when the speed of the constant load reaches the Rayleigh wave speed of the underlying half-space. In the latter case, two angles of Mach cone were found, one associated with the upper layer and one with the half-space. The propagating wave in the half-space travels further than the one in the upper layer. A rise in vertical displacement occurs as the speed of the constant load exceeds the Rayleigh wave speed of the layer material where the load speed line intersects the dispersion curve for the first P-SV mode [13].

Moreover, comparing the responses at a distance 10 m away from the track, a greater attenuation of the response was found at low load speeds compared with the higher speeds that excite propagating modes. The vibration contains more complicated frequency content at distances further away from the track than at the point under the track [13].

Jones et al present results from this model for quasi-static and dynamic loads in [14]. Considering a moving quasi-static load acting on the track, propagating waves are expected when the speed of the load exceeds the speeds of propagating waves in the track/ground structure. For a soft soil the S-wave speed can be 120 m/s or less. However in [14] it was found that for harmonic loads as the train speed reaches and exceeds the phase velocities of the first P-SV wave, no large amplitudes of propagating vibration occur due to the vibration energy transferring to a higher order mode.

The magnitudes of the ground vibrations due to quasi-static moving load and dynamic loads are both significant parameters in different frequency bands [13]. However, even if the load speed exceeds the ground wave speeds, the dynamic loads are still found to be significant compared with a constant moving load at the frequencies above the onset of the first wave of the upper layer (typically 10-40 Hz) [13].

In [2] Lombaert and Degrande predicted the vibration due to the quasi-static and dynamic excitation, using a numerical model similar to Sheng's. InterCity and high speed trains running at a subcritical train speed were analysed at a site along the

Belgian high-speed line L2 Brussels-Köln. The soil was represented as a softer layer overlying a stiffer half-space. The coupled analytical – boundary element model method was used for the coupled track-soil system for excitation due to multiple moving loads. It was found that the quasi-static load dominates the track response, whereas the dynamic load dominates the response propagating away from the track. The response due to the quasi-static load increases as the load speed gets higher. Due to the spectrum shape of the random track unevenness, the free-field vibrations are influenced by train speed when applying the dynamic excitation. The average free-field response is therefore expected to increase as the speed of the train increases.

Apart from those two main excitation mechanisms, various other mechanisms have also been proposed. Hunt [15] classified such mechanisms according to the effectiveness of added resilience: trackbed roughness, 'bent rail', variation of rail-support stiffness, variation of rail bending stiffness and variation of sleeper spacing. These five sources of excitation were described mathematically using a simplified analytical approach. The first three of these mechanisms [15] are shown in Figure 2.1.

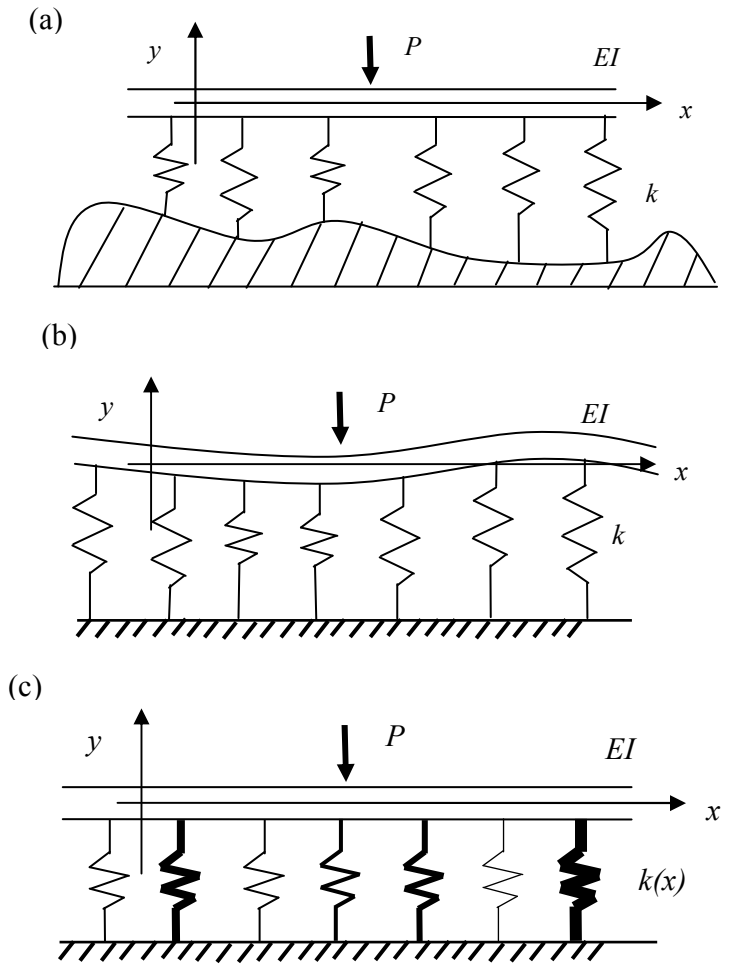

Figure 2.1. Beam on a Winkler foundation with (a) an uneven trackbed (b) an initially-bent rail and (c) variable spring stiffness [15].

2.2 Vibration transmission

In order to investigate the propagation of ground vibration, many different modelling techniques have been developed [3,7]. These can be categorized into empirical methods which are based on measurements, numerical methods such as the finite element or boundary element method, and analytical methods which are usually expressed in terms of wavenumbers in the ground [3,7]. Analytical models are usually more efficient than numerical models but they are limited in scope to simple geometry and homogeneous material.

2.2.1 Fundamentals of wave propagation in solids

Vibration can propagate in infinite solid elastic materials by two fundamental mechanisms: shear or dilatation. Two fundamental wave speeds are related to the

material properties of the soil. In an elastic medium the equations of wave motion can be derived from the equilibrium of a small element [16].

The ground can be represented as an elastodynamic material, described by Navier's equations, [17]

$$(\lambda+\mu)\frac{\partial\Delta}{\partial x}+\mu\nabla^2 u=\rho\frac{\partial^2 u}{\partial t^2} \tag{2.1}$$

$$(\lambda+\mu)\frac{\partial\Delta}{\partial y}+\mu\nabla^2 v=\rho\frac{\partial^2 v}{\partial t^2} \tag{2.2}$$

$$(\lambda+\mu)\frac{\partial\Delta}{\partial z}+\mu\nabla^2 w=\rho\frac{\partial^2 w}{\partial t^2} \tag{2.3}$$

where u, v, w are the x, y, z components of displacement u,
$\Delta=\partial u/\partial x+\partial v/\partial y+\partial w/\partial z$ is the dilatation and λ and μ are Lamé's constants for the material, λ is the first Lamé constant,

$$\lambda=\frac{\nu E}{(1+\nu)(1-2\nu)} \tag{2.4}$$

and μ is the second Lamé constant, or shear modulus

$$\mu=\frac{E}{2(1+\nu)} \tag{2.5}$$

where E is Young's modulus, and v is Poisson's ratio. Damping can be included into Lamé's constants as follows [13]

$$\lambda=\frac{\nu E\left(1+i\eta\,\mathrm{sgn}(\omega)\right)}{(1+\nu)(1-2\nu)},\quad \mu=\frac{E\left(1+i\eta\,\mathrm{sgn}(\omega)\right)}{2(1+\nu)}, \tag{2.6}$$

where ω is the circular frequency and η is the loss factor representing the material damping of the soil. The sgn function is introduced to prevent problems at negative frequencies when considering moving loads [13].

The first fundamental wave speed is the longitudinal wave speed (the P-wave speed) and the second, the transverse wave speed (the S-wave speed). These two mechanisms of vibration can appear independently in a homogeneous full-space with no free surface [3,17,18]. The longitudinal wave speed is given by

$$c_1=\sqrt{\frac{\lambda+2\mu}{\rho}} \tag{2.7}$$

while the transverse wave speed (the S-wave speed), is given by

$$c_2 = \sqrt{\frac{\mu}{\rho}} \tag{2.8}$$

In these expressions the ground properties are described in terms of the density of the soil ρ and the Lamé constants. The longitudinal wave speed is always greater than the transverse wave speed.

Vibration may also propagate parallel to the surface of the ground via a number of wave types, called Rayleigh waves and Love waves. Rayleigh waves are also called P-SV waves since they involve coupled components of compressive deformation (P) and vertically polarised shear deformation (SV). Love waves are also known as SH-waves, horizontally polarised shear waves. The Rayleigh wave speed of a half-space is given by [19],

$$c_R = \frac{\omega}{s_R} \tag{2.9}$$

where s_R is the real root of

$$-4s^2\sqrt{s^2-n^2}\sqrt{s^2-1}+\left(1-2s^2\right)^2 = 0 \tag{2.10}$$

and n is the index of refraction

$$n = \frac{c_2}{c_1} \tag{2.11}$$

The Rayleigh wave speed can also be approximated using the formula below [20]

$$c_R = \frac{0.87+1.12\nu}{1+\nu}c_2 \tag{2.12}$$

The results of using these two formulae for calculating the Rayleigh wave speed are compared in Figure 2.2 in terms of the ratio of the Rayleigh wave speed to the shear wave speed corresponding to various values of Poisson's ratio. The maximum difference is only 0.46%, while for values of Poisson's ratio between 0.15 and 0.35 it is less than 0.08%.

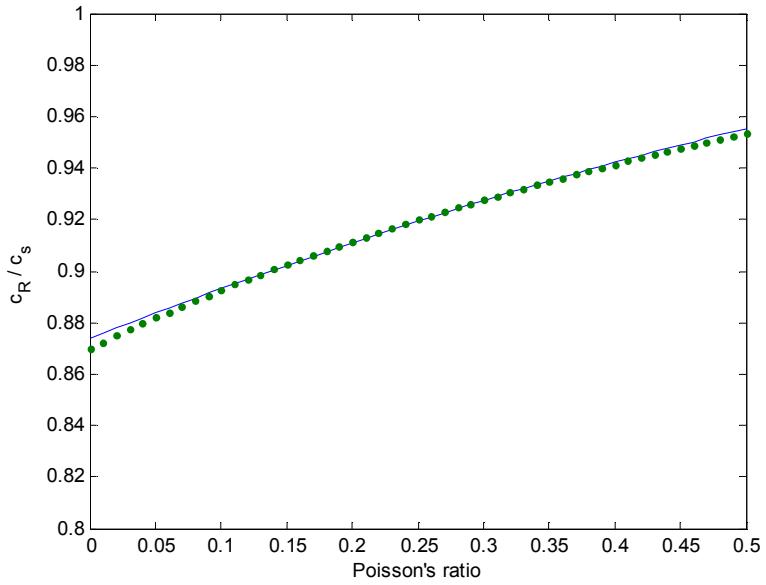

Figure 2.2. The ratio of the Rayleigh wave speed to the shear wave speed against various values of Poisson's ratio obtained using equation (2.9) (___) and (2.12) (…).

The Rayleigh wave is the slowest wave in a homogeneous half-space and usually carries the greatest part of the wave energy. It has a speed between approximately 87% and 95% of the shear wave speed [3], as shown in Figure 2.2.

To investigate the vibration propagation at further distances, decay with distance laws can be established. These will differ for a point source and for a line of sources representing a train. In the far field, the decay of vibration depends theoretically on the geometric spreading of the waves and the material damping. This can be expressed as [3]

$$\frac{A(r)}{A_0} = \underbrace{r^{-\alpha}}_{\text{Geometric dispersion}} \times \underbrace{e^{-r\beta}}_{\text{damping losses}} \qquad (2.13)$$

where $A(r)$ is the amplitude at some distance r, and A_0 is a reference amplitude. For a simple geometric spreading from a point source, α can be assumed to be ½ corresponding to a cylindrical wave tied to the surface, for instance a Rayleigh wave, while it can be assumed to be 1 for a spherical wave [3,16]. The parameter β depends

on the damping of the material. Geometric spreading will dominate at short distances from the source while damping losses will become dominant at further distances.

Nelson [21] found that saturation of soil introduces excess attenuation in the vibration response of the soil. The study used seismic reflectivity methods combined with multi-degree of freedom vehicle models to predict the ground vibration from trains. In [22] it is stated that higher material damping in the soil is related to the effect of saturated soil. This was found from measured results obtained at a site next to the HST line in Lincent (Belgium).

2.2.2 Empirical methods

Ground-borne vibration associated with transportation is difficult to predict accurately. Therefore predictions are often made using a large amount of empirical data [23]. Many papers have estimated the ground-borne noise and vibration using empirical data [24,25].

In the US, the Federal Transit Administration (FTA) guidance manual [26] recommends the use of an empirical method to predict ground-borne vibration associated with a transportation project. The procedure is based on site tests of vibration propagation. The prediction method was developed to allow the use of data from an existing site to predict the vibration response at a new site. Transfer mobilities are determined at the existing site. These are then used to normalize ground-borne vibration from trains to represent it as a 'force density'. The force density can be combined with the transfer mobilities measured at a new site to predict the vibration level at the new site.

This procedure was presented by Nelson and Saurenman [24] to predict the ground-borne noise and vibration based on experimental results at residential and commercial buildings near at-grade and subway tracks. In [24] impact-testing procedures and the 1/3 octave band force densities have been used to characterize vibration propagation in soils and to represent specific vehicle and track systems respectively. The main steps of the prediction procedure are: selection of a trackbed force density to represent the trains, determination of a line source response from measured mobilities, calculation of building response and calculation of noise.

In [27,28] Verbraken et al used numerical methods to investigate the validity and robustness of this empirical approach. Verbraken et al [27] derived expressions for the force density and the line source transfer mobility using a coupled finite element-boundary element method [29,30] discussed further below. The tunnel structure and the soil are modelled with the finite and boundary element method respectively. The only excitation mechanism considered was random track unevenness.

The vibration velocity level and line transfer mobility were investigated for three different soil characteristics [28]. It was found that the soil characteristic has an influence when the prediction of vibration velocity is made at a position adjacent to the track. For positions further away from the track, the soil characteristic has less influence on the estimated vibration velocity [28].

In another empirical approach Greer [31] presented a method for the calculation of re-radiated noise in the receiving building due to trains in tunnels. This procedure is based on a large number of measurements (over 1200 measured results) at 15 sites during the operation of the London Underground Central Line.

This empirical method to predict ground-borne noise and perceptible vibration is described further in [32]. Hood et al [32] developed procedures for assessment criteria and calculation for ground-borne noise and perceptible vibration from trains in tunnels. Two calculation procedures are provided separately for the prediction of noise and vibration. The source terms were derived from measurements due to the passage of TGV on surface tracks. Corrections have to be made for the case of a different train type and its speed, the geometry of the tunnels and a location within the buildings. The propagation model for vibration was derived from a statistical analysis of the results of measurements carried out in the UK and France. The assessment methodology was successfully applied to the Channel Tunnel Rail Link in the UK.

Madshus et al [25] also developed a semi-empirical model for the prediction of vibration due to passage of high speed trains on soft ground in Norway. It is based on a large number of vibration measurements. This method can also be used to predict re-radiated train noise levels.

2.2.3 Analytical models

2.2.3.1 Ground model

A ground can be modelled most simply as a homogeneous half-space or an infinite whole space. For instance the model Igitur, developed by Jones [5], and the Pipe-in-Pipe (PiP) model, developed by Hunt and Hussein [6], use ground models representing a homogeneous half-space and an infinite whole space respectively. In practice, grounds usually have a layer of softer weathered material at the surface and one or more stiffer layers underneath. At sufficient depth the lowest layer is often represented as a homogeneous half-space. In the frequency range of interest for railway ground vibration the layered structure of the ground has effects on the propagation of surface vibration [3]. To model these layered grounds, the method presented by Kausel and Roesset [33] can be used. This is based on stiffness matrices which are expressed in terms of wavenumbers in the ground [34].

The calculation of the wave fields of layered soils is based on well-known ideas: the integration in the frequency-wavenumber domain for a homogeneous half-space, first used by Lamb [35] and the transfer matrix method given by Haskell [36] and Thomson [37]. Kausel and Roesset [33] used this transfer matrix method to derive layer stiffness matrices which is a more convenient approach for a treatment of multiple loadings. Many other papers used these methods to discuss surface wave modes, to fit measured dispersion curves [38,39] and to solve soil-structure interaction problems.

The theoretical method commonly used to calculate the wave fields of layered soils is based on the layer stiffness matrices method working in the frequency-wavenumber domain and the description of layered soils by matrix methods [33]. More details are given in Appendix A. In general, differential equations can be solved analytically by applying Fourier transformations from the time to the frequency domain and from the space to the wavenumber domain [40]. The solution is then obtained by an inverse transformation technique. Grundmann et al. presented the use of a wavelet transformation as an additional transformation for the inverse transformation [40].

An analytical model of a layered ground was used by Sheng et al in [34]. The ground model consisted of a shallow layer of weathered material (2 m deep) above a deep layer of stiffer material modelled as an infinite half-space. The damping parameter was estimated from comparison between the model and measurements [7]. The vibration at various distances from the track was obtained by a reverse Fourier Transform of the wavenumber results. The presence of a shallow weathered layer of material overlying a stiffer half-space caused the response to rise in the frequency range 10-40 Hz. This feature is typical of many grounds but is a function of the layer material parameters and depth [7]. This indicates the necessity of including the layered structure of the ground in the model.

The description of the ground properties at a site in terms of its layered structure and material properties needs to be known in order to predict the correct behaviour of vibration. In [7] a mathematical model representing the track-ground system was used to investigate the waves propagating at the surface of the ground. A soft weathered soil of 2 m depth overlying a stiffer half-space was again used as the ground model in this paper. Using this model without any track, it was found that by 40 Hz the lower velocity mode (first mode) of the P-SV waves involved mainly deformation of the softer layer material whereas the second mode involved greater deformation in the underlying half-space [7].

A stationary harmonic load acting on a track/ground structure has been investigated by Sheng et al in [34] using the same theoretical model as in [13,14]. This can be used to study vibration induced dynamically due to the irregular vertical profile of the track at low speed train. This analytical method allows a large number of points for the response. Two different ground models with layers of 2 or 7 m overlying a stiff half-space were investigated. For the 7 m depth of layer, P-SV waves are expected to occur at a frequency of 40 Hz propagating in the layer. The attenuation rate of vibration away from the loading point for the 2 m layer ground is higher than those for the 7 m layer [34].

Auersch also determined wave propagation in layered soil using numerical integration in the wavenumber domain and the matrix method for layered soils [41].

The wave amplitudes at different distances and frequencies appear to be a characteristic of a soil profile.

Auersch calculated wave fields for three different soils, a soft layer on a stiff half-space, a stiff layer on a soft half-space, and a soil with continuously varying material properties [41]. The different soils can be characterized by their shear wave velocity; other parameters, density or Poisson's ratio, have less effect. The material damping has a strong influence on the amplitude at high frequencies. The results in the case of a soft layer on stiffer half-space are explained by discussing the Rayleigh wave of the softer soil. It was found that the soil material of this layer has an influence on the response at the surface only when the depth of the soil is more than half a wavelength of the Rayleigh wave [41].

2.2.3.2 Track and layered ground model and comparisons with measurements

The analytical ground model has been extended by Sheng et al in [34,13] to include the track coupled with a layered ground in order to predict the vibration level difference between different situations. In [13] the track is represented as an infinite, layered beam, resting on one or more elastic layers overlying a three-dimensional half-space of ground material. Into this model has later been included the vertical dynamics of vehicles running at constant speed, providing the incorporation of vehicles, track and ground [42]. Therefore the model in [42] can be presented in terms comparable to the measurements.

In [7,14] this analytical model of a layered ground was used to calculate the response to a quasi-static or dynamic single moving load. Results were expressed as a function of propagating wavenumber along and perpendicular to the track at speeds both below and above the wave speed in a coupled ground-track system. A layered, infinite beam model represented the track and was coupled to the ground. The coupling consisted of a pressure on the ground surface with a constant amplitude across a finite width of track. A similar track system but coupled with a homogeneous half-space is contained in the model Igitur [5].

In [11] Sheng et al compared predictions and measurements for three sites. For each situation the vehicle was modelled as a multi-body system in which only vertical

dynamics were considered. Both primary and secondary suspensions of the vehicle were included [11].

The first of these sites, at Ledsgård in Sweden, had very soft ground so that at 200 km/h the train speed exceeded the wave speed in the ground and the quasi-static loads were found to dominate the response. At this site [43] the Swedish National Rail Administration (Banverket) had encountered very large vibrations when high speed trains operated. At lower speeds dynamic excitation due to roughness dominated. It was found in [11] that the predicted response gave a good agreement with the measured one in the case of a train speed both below and above the speed of waves in the ground/embankment.

In [44] Karlstrom and Bostrom also used an analytical approach to simulate ground vibrations at the site with soft soil at Ledsgård in Sweden. Euler-Bernoulli beams were used to represent the rails, supported by an anisotropic Kirchhoff plate representing the sleepers, overlying a layered ground model. The simulated results give a good agreement with the measurements at 70 km/h while at 200 km/h they disagree a little due to simplification in the model. However this can be improved by increasing the thickness of the second layer, the organic clay layer at this site, from 3.0 to 3.5 m. This shows that the thicknesses of the first few layers of the soft ground are quite critical at higher train speeds.

Results are given in [11] for two other sites with stiffer soil where the propagating waves are excited by the dynamic generation mechanism. The second site was at via Tedalda in Italy where high vibration was found especially in the frequency range from 8 to 16 Hz due to the cut-on of the propagating wave in the upper layer at 11 Hz. Here the quasi-static excitation was found to be negligible (the train speed was 70-80 km/h).

The third site considered in [11] was at Burton Joyce in Nottinghamshire, UK where measurements of two-axle freight wagons had been taken [45]. The ground was modelled as a single layer overlying a homogeneous half-space. The response amplitudes for frequencies above 10 Hz were affected by the choice of track parameters whereas for the case of excitation by quasi-static loads, this would have

less effect on the vibration response. Again dynamic excitation dominated the response.

Degrande [46] provided experimental data of free field vibrations at various speeds of a Thalys high-speed train for the validation of numerical prediction models. The speed of the train varied between 223 and 314 km/h.

2.2.3.3 Models for ground-borne noise

Ground vibration produced by trains running in tunnels is usually associated with the frequency range between about 15 Hz and 200 Hz [47]. This vibration gives rise to structure-borne or ground-borne noise. Several mathematical models have been developed using either two-dimensional or three-dimensional analysis. A two-dimensional model provides more rapid calculations. However, it is not able to treat the effect of waves propagating in the direction of the track. Therefore a three-dimensional model is required for the wave propagation in the direction of both ground and tunnel. However, three-dimensional models require larger computing resources [3].

An analytical three-dimensional model was developed by Forrest and Hunt [48] for an underground railway tunnel of circular cross-section. The tunnel was represented as an infinitely long, thin cylindrical shell surrounded by soil of infinite radial extent. Fourier decomposition was used to solve the coupled problem in the frequency domain. A track model was added to the model in [49] to assess the effectiveness of floating-slab track.

Hunt and Hussein [6] developed this approach further as the Pipe-in-Pipe (PiP) model which is a simple three-dimensional analytical model. The model consists of a floating slab track coupled to a circular tunnel immersed in an infinite homogeneous ground. The results are calculated in terms of the Power Spectral Density (PSD) of the vertical displacement at a selected point in the soil. It is also used to determine the relative effects (Insertion Loss) of changing parameters relating to the vehicle, track or ground.

In [50] Hussein and Hunt presented a model of the floating-slab track with continuous slabs under oscillating moving loads. An Euler-Bernoulli beam was used to represent two rails and the slab. The Fourier transform method was applied for the calculation of the track displacement. The basic concepts of vibration of infinite systems and coupling of systems in the wavenumber-frequency domain are demonstrated in [50].

The dynamic effect of slab discontinuity on trains running in the tunnels has also been investigated. Hussein and Hunt [51] used a new method based on a Fourier series representation to couple a moving train to a track with a discontinuous slab.

Hussein and Hunt [52] also used PiP in conjunction with a multi-layered half-space model, which is based on the solution of Navier's equations in the frequency-wavenumber domain. This method is used for calculating vibration from underground railways buried in a multi-layered half-space. The tunnel's near-field displacements are controlled by the dynamics of the tunnel and the layer that contains the tunnel. The displacements at the tunnel-soil interface can be calculated using the PiP model whereas the far-field displacement is calculated using the direct stiffness method based on Green's functions for a multi-layered half-space.

In [47] the use of several discrete wavenumber methods to model ground vibration from underground trains has been investigated. These methods were divided in [47] into three categories: the discrete wavenumber fictitious forces method, the discrete wavenumber finite element method and the discrete wavenumber boundary element method. These methods are based on the moving Green's functions for a layered half-space. An infinite length cylinder was added to these to represent a tunnel, modelled by boundary integral equations. For a stationary or moving harmonic load acting within a circular lined or unlined tunnel, the wave propagation on the ground surface is greatly affected by the presence of the tunnel in the tunnel direction. Above the tunnel, the vibration on the ground surface is reduced for the lined tunnel whereas its vibration is greater than the unlined tunnel at distances further away from the tunnel at high frequencies [47].

Kuo and Hunt [53] also developed a coupled model using the theory of joining subsystems. A two-dimensional, infinitely-long, portal-frame building model was connected to an existing model of a pile group embedded near an underground railway. This was used to evaluate the dynamic response of foundation designs for a given set of ground and loading conditions.

Soil subsidence around sectors of the tunnel wall may affect vibration level due to trains running in the tunnel. Jones and Hunt [54] developed a 3D, semi-analytical model to quantify the effect of voids of various shapes and sizes on near-field and far-field surface vibrations. Later this method has been used to quantify the level of uncertainty in ground vibration predictions associated with neglecting such voids [55]. By uncoupling the appropriate nodes at the interface used to represent force transfer between the systems, this represented the void. An uncertainty of $\pm$5 dB was found to be associated with assuming a perfect bond at the tunnel-soil interface in an area with known voidage.

2.2.4 Numerical models

An analytical model such as those mentioned above is limited in scope to simple geometry and homogeneous material [7]. For analysis of arbitrary geometry of structures, numerical models using finite or boundary elements are required [47]. Dynamic train/track interaction due to various excitation mechanisms can be included using such numerical models. The ground and built structures can often be assumed to be homogeneous in the track direction. In such a situation a sequence of 2D models can be used, each of which corresponds to a particular wavenumber in the track direction [56].

For periodic structures, an alternative method is possible. In this a solution for the structural response and the radiated wave field is based on a model for a unit cell of the periodic structure and periodic structure theory is used to determine the three dimensional response [57, 22].

A fully three dimensional multi-body-finite element-boundary element model has been developed by Galvin et al [4]. The quasi-static and the dynamic excitation mechanisms due to a train passage can be considered using this model.

An alternative approach to investigate ground vibrations has been developed by Katou et al [58]. The mechanism of ground vibrations induced by a high-speed train has been investigated using a 3-D viscoelastic finite difference method (FDM). The rail length was set to 120 m and the grid spacing was chosen as 0.25 m to give stable FDM simulations without numerical dispersion. The model used about 32 million grid points in the numerical simulations. Instead of using a complicated source model with the parameters of rail, sleeper, ballast and soil, however, Katou et al. proposed a direct approach to observe the dynamic force using strain gauges on the wheels. Force time histories were measured using load measuring wheels. Using these time series from an observed set of wheels, a realistic source function was developed. They then employed Krylov's theory [9] to determine the force acting on the ground below the track. This was used as an external force in the 3-D numerical simulations. The 3-D numerical model was designed to represent a field test site including an embankment. In spite of the simplifying assumption, using Krylov's theory, and only applying a dynamic moving load, the results from the simulated ground vibration give a good agreement with the observed ones at the test site in the specific cases considered. Generally the authors claim this model can be used to simulate the response of ground vibration adequately. Nevertheless the model requires a very large FDM grid and specific measurement using the strain gauges on the wheels to determine the forcing.

However, the time consumed for the calculation of three-dimensional dynamic soil-structure interaction is large as it is required to account for waves propagating towards infinity [22].

In [59] Jones et al developed numerical models using a coupled 2D boundary element/finite element method for vibration propagation to predict the effect of structural alterations to cuttings, embankments and tunnels. This two-dimensional model can represent an inhomogeneous ground structure of arbitrary geometry. The wave propagation is incorporated by the use of Green's functions which represent the character of waves propagating to infinity. The finite element method was used to model structures, for instance the solid concrete tunnel invert, and the boundary element method was used for modelling infinite media. A comparison between a lined and an unlined tunnel using this model was investigated in [59]. It was found that the

response at the crown of the lined tunnel was greater than that of the unlined case at an example frequency of 100 Hz. Coupled finite and boundary elements methods have also been used to analyse a cut-and-cover tunnel with a double track railway in [59].

In [60] Andersen and Jones compared two- and three-dimensional models for a railway tunnel by applying a coupled finite element and boundary element approach. The results from both models give a similar trend in the wave pattern. A two-dimensional model appears to be useful to see whether reductions in the vibration can be achieved when the structure is changed, especially for tunnels buried deeply in the ground. As the analysis using a two-dimensional model takes much less time than for a three-dimensional model, parameter studies can be run more easily. However, a full three-dimensional model is required for absolute vibration predictions [60].

In [61] a comparison is given between two- and three- dimensional models for this cut-and-cover tunnel with masonry abutment walls and a concrete roof. The model was based on the combined finite element (FE) and boundary element (BE) methods. The results showed that the wave pattern in the two- and three-dimensional models had similar trends, but the response in the two-dimensional model was larger than that of three-dimensional models. This was attributed to the use of a strip load over a confined area in the three-dimensional models. It was concluded, however, that the two-dimensional model had adequate accuracy to indicate relative effects such as reductions in vibration [61].

As an alternative to the three dimensional approach for longitudinally invariant structures, a computationally efficient two-and-a half dimensional (2.5D) approach can be applied. In this approach a 2D discretisation is used with a series of assumed wavenumber in the third dimension. The advantage of 2.5D approach is a reduction of the size of the boundary element and finite element mesh [22].

To minimise the time consumed for the prediction using 3D, many papers have used the 2.5D approach [34,59,62]. Sheng et al [56] developed a model based on the wavenumber finite and boundary element methods (the 2.5D FE/BE model) to predict ground vibration from trains both in tunnels and on the ground surface. The model is shown to be accurate by comparison with results from measurement. It is

shown that 2.5D FE/BE model can be used with much shorter computing times than a three-dimensional (3D) FE/BE model [56].

Wavenumber finite- and boundary-element methods have been used by Sheng et al [62] for modelling of track/ground vibration induced by trains. The calculation in the model was done in terms of the wavenumber in the *x*-direction and FE/BE discretization in the *yz*-plane. A 'boundary truncation element' was developed which greatly improves accuracy compared with an ordinary boundary element [62].

In [56] Sheng et al presented results using the coupled wavenumber finite and boundary element method [62]. This was used in [56] to compare the prediction of surface vibration from this model with measurement data from the ETR500 train at Via Tedalda in Italy. The ground and built structures were modelled as homogeneous in the track direction, including the shaped cross-section. The ground was modelled as one layer of 10 m depth overlying a homogeneous half-space. The track included an embankment. A good agreement between prediction and measurement was shown from about 6.3 to 80 Hz. Moreover, the model was also used for another two cases: the reduction of vibration due to a wave impeding block and vibration from trains running in tunnels.

Using this model to compare two tunnel designs, it has been found that tunnel design has significant effect on the ground vibration level. A large single bore tunnel carrying two tracks was found to produce higher response levels than two single-track tunnels at the ground surface [62] for the same track depth below the ground surface.

Jean et al [63] also developed a model using a full boundary element method (BEM) approach for ground and structure. It combined a BEM and wave analysis by using a 2.5D Green's function for given wave number along the infinite direction. Again the 2.5D approach was shown to give faster calculated times than a full 3D implementation.

In [64] Lombaert et al used a numerical model to predict track/ground vibration, accounting for the dynamic interaction between the train, the track and the ground. This model has been validated with the experiments at a site in Lincent, along

the line L2 of the new Belgian high speed track between Brussels and Köln. The track-soil interaction was determined in the frequency-wavenumber domain taking advantage of the assumption of constant track geometry along the longitudinal direction. In order to determine the dynamic soil characteristics, the spectral analysis of surface waves (SASW) method [38,39] has been used (see section 2.3). The SASW method is used to determine the dynamic shear modulus of shallow soil layers. This is based on the dispersive characteristics of propagating wave on the surface. The response in the free field involves an in situ experiment. Several experiments have been carried out to validate this model separately i.e. track receptance test, track-free field transfer function, the sleeper response and the free field vibrations etc. The results from comparison between the experimental and the numerical results of the free field vibrations show reasonable agreement. However, some discrepancy remains that cannot be explained. It might be that only a single layer overlying a stiffer half-space is not sufficient to represent the ground. The model is used to assess the vibration isolation efficiency of a floating slab track [65].

Lombaert et al [66] used a 2.5D coupled FE-BE model including the embankment [67] to compare predictions to measured ground vibrations at a site along the LGV Atlantique and at a site along the line Paris-Bordeaux. The experimental free field vibrations have been compared with the predictions for three different train speeds. A good agreement was found, although a ratio of 3 or 5 of vibration level was found comparing these results. It seems that an overestimation of the dynamic axle loads caused the difference.

A periodic coupled finite element-boundary element model developed by Degrande et al [29] is also used to study the dynamic interaction between a tunnel and a layered soil. Rather than use a 2.5D approach this is based on periodic structure theory. In this method a finite length in the axial direction is modelled using conventional finite elements. The waves in the infinite structure are found using periodic structure theory. Later Gupta et al [68] presented the validation of this model by comparing with the experiments performed at a site on the Bakerloo line of London Underground. This showed the applicability of the model to make realistic predictions of the vibrations from trains in the tunnel as reasonably good agreement was found. Gupta et al [69] also used the same model to predict the free field response

due to a Thalys high speed train in the Groene Hart tunnel in the Netherlands. The study considered the effect of soft layered ground on vibration levels. A large contribution of the quasi-static forces can be found at high train speed.

Gupta et al [70] used the coupled periodic finite element-boundary element model and the PiP model to study the vibration from underground railways to identify the important parameters. It was found that a larger tunnel gives a smaller response above the tunnel as waves propagate downwards more. The response close to the tunnel was found to be affected by the tunnel geometry.

The importance of the traction distribution at the track/ground interface was discussed by Galvin et al [71]. It was found that a relatively good approximation of the traction distribution at the interface between the embankment and the soil by using the continuum model of the ballast and the embankment leads to good agreement with the measured free field response at low frequencies where the quasi-static contribution dominates.

2.3 Determining soil properties

The analytical methods described in Section 2.2.3.1 can be used with measured data to determine soil properties.

Nazarian and Desai [38,39], developed the spectral analysis of surface waves method (SASW) that is used for determining shear wave velocity profiles of soil sites and stiffness profiles of pavement systems. The SASW method consists of field testing, determination of the dispersion curve (a plot of phase velocity and wavelength or frequency) and finally determination of stiffness profile. A weighted least-squares best-fit solution is used to estimate the phase of cross-power spectra at each frequency with coherence as a weighing function. Two n^{th}-degree polynomials are used to fit the cross-power spectrum. Knowing the distance between the receivers and the phase at each frequency, phase velocity and wavelength associated with that frequency are determined.

To find the actual phase of the dispersion curve for each frequency, the number of 360° cycles preceding each frequency is counted and then added to the

fraction of the remaining cycle. An automated procedure for construction of the dispersion curve from cross-power spectra and coherence functions was developed in [38]. The number of idealized data points is limited to 50 due to an excessively long computation time. However, the number of data points can be up to several hundred for manual inversion. For determination of a representative dispersion curve, the predicted data is determined using simultaneous curve fitting for both real and imaginary components. The polynomial coefficients are then determined. This gives the predicted phase velocity. Using the least absolute value best-fit criterion, the dispersion curve is constructed from these raw data, phase velocity and wavelength associated with the frequency. A case study is presented in [38]. It is found that dispersion curves can be used to determine the shear wave velocity profile with a variation of 10-15%.

Yuan and Nazarian [39] improved the SASW testing by using an automated technique based upon the general inverse theory. This involves construction of the results from experiment shown in terms of dispersion curves and determines the stiffness of the ground by inversion of those curves. Two cases studies compared the experimental results with the results from the inversion process. It gives a good agreement down to a depth of about 20 m comparing results from the SASW and cross-hole seismic tests. It can be concluded that the inversion process is a useful alternative method to seismic site investigation in term of cost-effectiveness and time.

Another method to identify the dynamic soil characteristics is presented in [22]. Using an impulse hammer or a vibration generator to generate ground vibrations, the measurements can be obtained as a function of time and distance. The shear and dilatational wave velocities can then be estimated by inspecting the response at the ground surface as a function of time and distance from the source.

Forchap and Schmid [72] also determined the shear wave velocity profile of the soil by analysing the Rayleigh wave dispersion obtained from experimental results. Through data inversion the shear wave profile can be identified. A method which identifies and separates the modes of Rayleigh waves for stationary harmonic excitations was introduced, based on the wavenumber analysis. This method is faster

than the phase difference method. However, only a single mode of propagation can be determined.

2.4 Mitigation methods

2.4.1 Introduction

Ground-borne noise and vibration can be mitigated at source, in the propagation part or at the receiver; mitigation at source is generally the most effective means [73]. However, there are few applicable mitigation measures for vibration from trains at low frequency [3]. Moreover the reduction of vibration depends on its excitation mechanisms. At the frequencies where the dynamic component dominates the vibration, the vibration can be reduced by the track alignment, for instance tamping the track. However, this has no effect on vibration near the source due to the quasi-static load [3]. Strong ground surface vibration occurs when a ground is soft, so at low frequencies stiffened soil can be used as a means of reducing the feelable vibration [3]. For ground-borne vibration, reducing unsprung mass and improving the stiffness of the foundation by soil treatment or piling, are techniques listed in [1].

Track design for ground-borne noise attenuation is based on reducing the coupled vehicle-track resonance by introducing resilient elements. However, it is not possible to use vibration isolating track forms to control low frequency vibration due to the increase in vibration associated with the resonance frequency itself [1].

In [73] for existing rail systems it is suggested to: minimize the rail roughness at wavelengths associated with ground-borne vibration or ground-borne noise by mean of rail grinding, joint removal by welding rail joints, re-adjustment of built-up switch and crossing components, wheel truing and grinding, and rail alignment. For track design in a new line [73] recommends that mitigation of ground-borne vibration or ground-borne noise is achieved by increasing the vertical dynamic resilience of the track and ultimately by the provision of increased mass above any resilience provided.

2.4.2 Measures in the propagation path

In [22] possible mitigation measures in the transmission path are discussed using: trenches, buried wall barriers, subgrade stiffening, wave impeding blocks and wave reflectors. Above a certain frequency, a trench or buried wall can be considered

as a barrier to ground vibration. Karlstrom and Bostrom [74] use a full 3D analytical approach to study open trenches as wave barriers. It is found that trenches can achieve the attenuation of low-frequency vibration. However, trenches can only be used as barriers for the surface vibration. Andersen and Nielsen [75] also found that open trenches are more efficient than infilled trenches or soil stiffening even at low frequencies.

The installation of trenches in the ground has been found to affect the vibration isolation effectiveness at low frequencies. In [76,77] Garcia-Bennett has investigated the effectiveness of trenches using a two-dimensional numerical model. For a homogeneous non-layered ground, the response was reduced by 5 and 13 dB for a 2 and 10 m deep trench respectively. The effectiveness of trenches is observed to be greater in a layered ground. Moreover, the greatest benefit is achieved for locations of trench close to the load, whereas at distances further away less effectiveness is achieved. The reduction of vibration using practical trenches can be found for frequencies greater than 6 Hz.

Jones et al. [78] also investigated the reduction of surface-propagating vibration from trains by using a frequency-domain, two-dimensional vibration propagation model. In [78] the attention was paid to the performance of two trenches, constructed using sheet piles, and a wall of stiffened soil compared with a theoretical trench without retaining walls. It was found that a 6 m deep trench is effective in reducing vibration in the frequency range 8 to 16 Hz. It was also found in this study that stiffening the soil under the track has effectiveness in reducing vibration in the same frequency range. However, stiffening of the soil next to the track to form a buried wall barrier seemed not to be effective.

To reduce ground vibration, a stiffer plate may also be inserted into the soil at some depth. Several researchers have investigated this concept which is called a wave impeding block (WIB) [56,79]. In [79] Peplow et al investigated theoretically the reduction of vibration at low frequencies using wave impeding blocks (WIBs). The reduction of vibration on the ground surface in the far-field was determined due to a harmonic load acting over a strip. A 2D boundary element method was used for this model. The principle of a WIB is to introduce an artificial stiffened layer (inclusion)

under the load. In this case the inclusion was placed under the load at the bottom of the upper ground layer on the top of the underlying half-space. The model predicted the frequency response of a layered ground away from a finite-width strip load. The effects of introducing various configurations of WIBs at two example sites were predicted by correcting the response of real ground sites with the insertion losses of the WIBs. The results show that for practicable dimensions of WIB it is possible to achieve reductions of vibration at low frequencies associated with surface running, heavy axle-load trains. However, the design of a WIB should also take possible increases of vibration amplitude at some higher frequencies into account. This might occur if the excitation amplitude is significant at these frequencies; the level of perceived vibration may therefore be higher in some situations.

In [56] Sheng et al developed a model using the wavenumber finite and boundary element method to investigate the reduction of vibration using WIBs. The WIB was expected to mitigate the vibration at frequencies lower than the cut-on frequency of the upper layer, although this is only the case when the plate is rigid and extends to infinity. The results showed that the WIB provided more than 10 dB reduction of vibration for all frequencies at 5 m from the track centre-line. At 10 and 20 m the same level of reduction was achieved above 10 Hz.

Lane et al [80] used an integrated rigid body – FEM model to investigate the reduction of vibration using lime cement columns directly underneath the track and as a straight barrier at a distance from the centre of the track. It was found that the centred column method gave a better result than the other for reduction of vibration close to the track. However, for the free field response the effects of these approaches seemed similar.

A similar trend of isolating the vibration using pile rows embedded in a poroelastic half-space is presented by Lu et al [81]. It was found that stiffer pile rows tend to give a better result for isolation of vibration than a soft one. The higher the speed of moving loads, the shorter the length of the piles would need to be.

2.4.3 Isolating track forms

Mitigation of vibration leading to ground-borne noise at higher frequencies can be achieved by isolating the vibration of the rail from the track-ground system. Floating slab track can achieve this isolation very effectively as the highest possible mass is added above the track spring to form a system with a very low resonance frequency [3]. However floating slab is a very expensive construction including the need for specific design.

Phillips and Nelson [82] also used Finite Element Analysis (FEA) to investigate the use of rails fastened directly to discrete slabs replacing the ballast and sleeper track. FEA was used to predict the dynamic interaction of track and vehicle for the vibration isolation system. It was found that the stiffness transferred between slabs through the rails affects significantly the overall stiffness of the isolation system.

An alternative to floating slab track is soft rail fasteners. An example of soft rail fasteners is the Pandrol Vanguard system. This consists of a very soft support to the rails provided by elastomer elements holding the rail web. A trial of the Pandrol Vanguard rail fastening baseplates for vibration control is presented in [83]. The measurements were taken in China. They indicated that a significant reduction in vibration level at the track and at the ground surface was achieved when the Pandrol Vanguard fasteners were installed.

The reduction of vibration has also been achieved by means of introducing resilient layers at other locations within the track in order to isolate the track from the ground. In [84] Triepaischajonsak has investigated the effect of sleeper soffit pads on both rolling noise and ground-borne noise. To do this, TWINS [85,86,87] has been used for prediction of rolling noise and Igitur [5] for ground-borne noise respectively. TWINS is a tool for predicting the noise radiation from wheels and track developed by Thompson [85]. Three stiffnesses of sleeper soffit pad were investigated. As the soffit pad becomes softer the ground-borne noise is reduced but the rolling noise is increased. The results for the soft soffit pad, based on the manufacturer's data for the stiffness, indicated that the rolling noise will increase by up to 2 dB(A), which is similar to results found in Switzerland [88], whereas the ground-borne noise can be

reduced by typically up to 20 dB(A). Thus, although the rolling noise is increased, the effect is much smaller than the benefit in terms of ground-borne noise.

2.4.4 Transmission into buildings and building isolation

An effective method of reducing vibration levels especially at high frequencies is to isolate the source from the ground system. In practical terms isolation at the base of the building can sometimes be appropriate. Many papers have investigated a reduction of vibration by use of inserting isolation material [89,90]. Predictions have shown that a low isolation frequency improves the insertion performance of the bearings.

In [91] it was found that a simple model of a rigid mass on a spring is inadequate to assess the base isolation of buildings. Therefore, Newland & Hunt [91] developed models that represented flexible columns and floors by using a dynamic stiffness approach as well as using the finite element method to assess isolation from ground vibration transmitted through the buildings.

A model was developed by Hunt in [92] to predict the vibration transmission from railways into buildings. A vehicle/track model is applied with a building model of infinite length. The reduction of vibration levels in buildings was used to compare the use of rail pads, under-sleeper pads, ballast mats, floating-slab track or base isolation.

Pyl et al [93,94] developed a method of coupling a validated source model with the receiver model to predict free-field traffic-induced vibrations in buildings. A finite element method was applied to the structure. By using the Green's functions of a homogeneous or a layered half-space, a boundary element method has been used for the dynamic soil structure. The results of in situ experiments were used for the validation of the numerical prediction model. The predicted structural response during the passage of a truck was then compared with those from experiments. A good agreement was found.

2.5 Assessment criteria for ground-borne vibration

Human response to vibration can be determined in many environments in terms of the acceptability of vibration. The vibration will be felt and become annoying and in rare cases it may damage a building or disturb sensitive equipment. The guidance for assessment of vibration is given in the approaches of the British and German standards in the form of Vibration Dose Values and KB values [3]. In ISO 2631-1 (and in BS 6472) a 'Vibration Dose Value' (VDV), for a single event, is defined as

$$VDV = \left[\int_0^T a^4(t)\, dt \right]^{0.25} \tag{2.14}$$

where $a(t)$ is the frequency weighted acceleration as a function of time and T is the duration of the event. The total VDV for a number of events is then calculated as

$$VDV_T = \left[VDV_1^4 + VDV_2^4 + VDV_3^4 + \ldots \right]^{0.25} \tag{2.15}$$

The calculated total VDV can be compared with broad criteria for acceptability that are reproduced in Table 2.1.

Table 2.1 Ratings for residential buildings in VDV from BS 6472 [3].

Period	Low probability of adverse comment ($m/s^{1.75}$)	Adverse comment possible ($m/s^{1.75}$)	Adverse comment probable ($m/s^{1.75}$)
16 hour day	0.2-0.4	0.4-0.8	0.8-1.6
8 hour night	0.13	0.26	0.51

For KB values [3], use of a running root-mean square vibration velocity measurement (based on a 0.125 second time constant) is applied for a calculation as

$$KB_{FT_r} = \sqrt{\frac{1}{T_r} \sum_j T_{e,j} KB_{FTm,j}^2} \tag{2.16}$$

where KB_{FTr} is the average of the maximum filtered r.m.s. signal values during each 30 second interval of the whole event, T_r is the evaluation period (day- or night-time) and $T_{e,j}$ is the exposure period of each event, j.

Another typical assessment criterion used to assess potential impact due to ground-borne vibration from rail transit is stated in the US Department of

Transportation guidance [95] and shown in Table 2.2. ANSI standard S3.29-1983(4) states a vibration level of 100 VdB to be equivalent to the threshold of perception for the most sensitive humans [95]. Ground-borne noise levels are also listed.

Table 2.2 Typical assessment criteria for ground-borne vibration from [95] – US Department of Transportation

Land use	Ground-borne vibration impact levels (VdB re 10^{-9} m/s)		Ground-borne noise impact levels, L_{Amax} (dB re $2x10^{-5}$ Pa)	
	Frequent events[1]	Infrequent events[2]	Frequent events[1]	Infrequent events[2]
Residences and buildings where people normally sleep	100	108	35	43
Institutional land uses with primarily daytime use	103	111	40	48

Note: 1. "Frequent events" is defined as more than 70 vibration events per day.
2. "Infrequent events" is defined as between 30 and 70 vibration events of the same source per day.

A survey of the environmental noise and vibration from London Underground trains was presented by Edwards [96]. It was found that approximately 56000 dwellings in London are estimated to experience re-radiated internal noise levels in excess of the 40 dBA, L_{Amaxf} criterion. Ground borne noise levels of above 60 dB(A) were predicted for a very small number of properties [96].

Guidelines relating to rail systems generating ground-borne noise and ground-borne vibration are also issued in International Standard ISO 14837 [73]. This provides a general introduction and guidance of the requirements for planning purposes where a new or extended railway is proposed.

To evaluate the risk of vibration-induced damage on building structures, the frequency range relevant is 1 to 500 Hz. The source, propagation and receiver system are defined in [73]. Prediction models for ground-borne vibration and/or ground-borne noise may be parametric or empirical, or a combination of these. The models can be used to predict and make adjustment for the reduction of the response.

2.6 Scope and objectives

This thesis considers the ground-borne vibration or 'feelable vibration' induced by surface trains, particularly in the frequency range up to 100 Hz. Although many papers [3,7,97,11,2,69] have found the relative importance of quasi-static and dynamic components, the aim of this thesis is to understand more of the relative importance of quasi-static loads and dynamic loads as well as other excitation mechanisms: variation of sleeper spacing, variation of ballast stiffness and surface irregularity of the railhead, dipped welds and rail joints. The investigations of the ground response due to these parameters are focussed on different situations: at the distances near to and further away from the track, for different track support stiffness, different vehicle parameters, and different ground parameters.

This chapter has given an introduction to a background of vibration propagating in the ground induced by trains. A number of models have been reviewed which can predict ground vibration or relative level for a change in parameters. Mitigation measures for the vibration are also described briefly.

In the Appendices a brief introduction is given to some of the existing models used in this thesis. In Appendix B, an introduction is provided to the Train-induced Ground Vibration (TGV) model developed by Sheng [12]. An axisymmetric layered ground model [33] (called in this thesis 'kandr') is described in Appendix A.

Measurements have been carried out at two sites adjacent to railway lines in Southern England to validate the TGV model. As described in Chapter 3 two experiments were carried out at each site. To determine the ground properties, various methods have been used. Then results from the experiment involving the measurement of ground vibration due to various passing trains are compared to the prediction using the TGV model.

The TGV model is used in Chapter 4 in an extensive parameter study to investigate the relative importance of quasi-static loads and dynamic loads in different situations. The effects of changes in various track/train parameters are estimated for locations close to the track and further away in terms of an insertion gain in order to see the effect of the quasi-static and dynamic loads on the ground vibration.

A new hybrid model is then developed in Chapter 5 in order to investigate other excitation mechanisms. It is a combination of a time-domain wheel/track interaction model and an axisymmetric layered ground model. The TGV model and a simple frequency domain model are then used to validate the hybrid model.

In Chapter 6, a study is carried out using the hybrid model to investigate various excitation mechanisms, including parametric excitation due to sleeper-passing effects and excitation due to variations in ballast or ground stiffness beneath each sleeper. The effects of changes in various track/train parameters are estimated for locations close to the track and further away in order to see the effect of the sleeper passing frequency with and without roughness applied as an excitation.

Chapter 7 applies the hybrid model to investigate the effects of discrete track defects such as dipped welds and rail joints on the ground vibration for two ground conditions at locations close to the track and further away.

Conclusions and recommendations for future work are summarized in Chapter 8.

2.7 Contributions of this thesis

The main contributions of this thesis can be summarized as follows:

This work concentrates on the relative importance of the quasi-static load and dynamic load. Although many papers have found that the dynamic contribution dominates the free-field response [12,2,69], in this thesis it is shown particularly that an assessment of the insertion gain due to a change in track stiffness should not be based on measurements too close to the track – for the parameters considered the distance should be at least 10 m to give representative results of the effect on the far field response.

The TGV model used in this study was previously validated using measured data available from the measurements at three sites in Sweden, Italy and England [12]. However, some of the parameters used in the model were estimated, especially the rail roughness. Measurements of ground vibration carried out at two sites adjacent to

railway lines in Southern England are used to validate the model in a more complete way.

A new hybrid model is developed in this work. The model is the combination of a time and spatial domain track/wheel interaction model and the frequency-wavenumber domain layered ground model. The hybrid model is validated using the TGV model along with a third independent model.

The effects of parametric excitation due to sleeper-passing effects and excitation due to variations in ballast stiffness, sleeper spacing and ground stiffness beneath each sleeper on the ground response have been investigated using the hybrid model. The sleeper passing frequency for both constant and variable sleeper spacing and variation of ballast stiffness have a fairly small effect on the ground vibration as the dynamic load dominates the response. These effects are about 30 dB below those due to dynamic component.

The effect of discrete defects such as dipped welds and rail joints has also been investigated using the hybrid model. The rail joint is found to be more important than the parametric excitations described above.

Finally the decay with distance of vibration due to passing trains has been investigated and found to differ from the conventionally assumed power law.

3. Validation measurements

The ground vibration is dependent on a number of track/ground parameters especially the ground properties. Although, the TGV model has previously been validated using results from the measurements at three sites, some of the parameters used in the model were estimated or obtained from third parties. In the present chapter new measurements are presented which allow a more complete validation.

3.1 Measurement of ground vibration

3.1.1 Introduction

In order to validate models of ground vibration and to investigate the relevance of alternative excitation mechanisms, measurements of ground vibration are required. The measurements of ground vibration described here have been carried out at two sites adjacent to railway lines in Southern England during September 2008. These sites were chosen due to their locations next to the railway line and the fact that access was allowed by the farm owners. Most importantly they had ground conditions with relatively soft soil.

The two sites were located at Steventon, on the Didcot to Swindon line and Grazeley Green on the Basingstoke to Reading line, as shown in Figures 3.1 and 3.2 respectively.[1] The soil in both cases consisted of deep layers of clay, which at the time of the measurements was saturated.

[1] The measurements were carried out with Dr Jones and Dr Ryue as part of RRUK project work.

Figure 3.1. Location of Steventon test site (a) satellite and (b) earth view.

Figure 3.2. Location of Grazeley Green test site (a) satellite and (b) earth view.

Two experiments were carried out at each site. The first experiment used hammer excitation to determine the soil properties. Accelerometers were used to measure the vibration at positions every 1 m away from the forcing point, up to 42 m, as shown in Figure 3.3. There were two lines of measurement, which were approximately 36 m apart, for each site. The measurements were made every 1 m along both lines for the Steventon site. However for Grazeley Green they were made every 1 m on line 1 and every 2 m on line 2 as shown in Table 3.1. The accelerometers were mounted on square plates of aluminium with dimensions 0.15 x 0.15 m. Plaster of Paris was used to attach the plates to the ground. These square plates have a mass of 0.3 kg (or 0.7 kg for plates with a mounting block on the top). The force impulse was applied to a small circular footing of diameter 0.4 m. This was also made of aluminium and has mass 4.1 kg. The accelerometers were covered by upturned plastic buckets in an attempt to reduce disturbance by wind or rain.

The following equipment was used: piezoelectric ICP accelerometers PCB type 353B03 with frequency range of up to 7 kHz and mass of 10.5 g; a signal conditioner ICP type 480E09; a PROSIG analyser with 8 channels; a large hammer with mass 6.76 kg. An accelerometer was attached to the back of the hammer head and used to obtain the applied force indirectly. This was calibrated by exciting a known mass (a piece of rail of mass 25.9 kg) in the laboratory and measuring its response. From the results it was found that the active mass of this hammer was 6.38 kg.

For the hammer excitation measurements, the force and ground response due to each impact were recorded at a sample rate of 2 kHz for 0.5 seconds. Transfer functions were calculated using an average of 10 impacts. Single time histories were also recorded. These measurements are used with various techniques to determine the ground properties. The results can be used to identify the number of layers in the ground, the thicknesses of the layers and the wavespeeds in each layer as described in Sections 3.2 to 3.5.

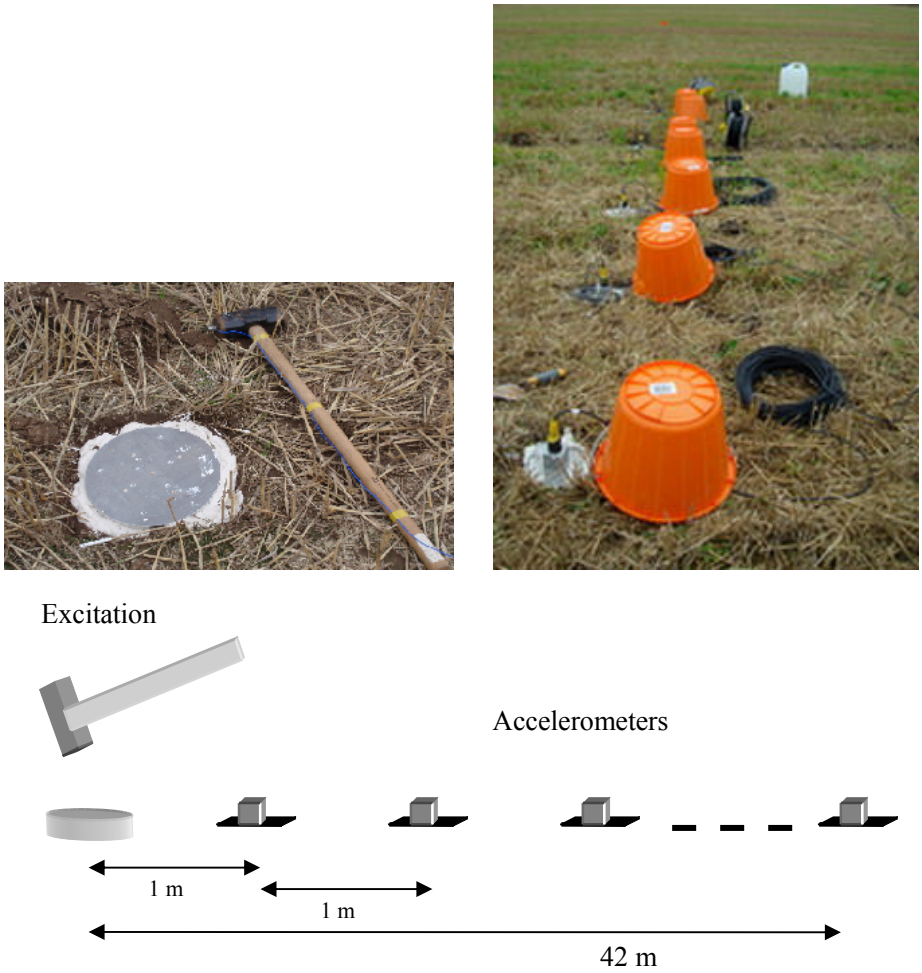

Figure 3.3. The position of accelerometers at every 1 m away from the applied force.

The second experiment at each site involved measuring vibration due to various passing trains. In these experiments the vibration was measured at different distances away from the track, from the middle of the track up to 80 m away at Steventon and up to 70 m away at Grazeley Green. The results from various types of trains will be used with the track/ground models (after the properties of the soil have been identified from the first experiment) to validate the TGV model. These results will be calculated to help identify the source of vibrations, for instance the relative importance of quasi-static loads or dynamic loads. This second experiment is described in more detail in Section 3.6.

Table 3.1. The positions of each measurement at Steventon and Grazeley Green sties.

		Channel number of analyser / Position away from the excitation point							
		1	2	3	4	5	6	7	8
Steventon site (line 1 up to 42m) (line 2 up to 32m)	1st measurement	Hammer	1m	2m	3m	4m	5m	6m	7m
	2nd measurement		8m	9m	10m	11m	12m	13m	14m
	3rd measurement		15m	16m	17m	18m	19m	20m	21m
	4th measurement		22m	23m	24m	25m	26m	27m	28m
	5th measurement		29m	30m	31m	32m	33m	34m	35m
	6th measurement		36m	37m	38m	39m	40m	41m	42m
Grazeley Green site (line 1)	1st measurement	Hammer	1m	2m	3m	4m	5m	6m	7m
	2nd measurement		8m	9m	10m	11m	12m	13m	14m
	3rd measurement		15m	16m	17m	18m	19m	20m	21m
	4th measurement		22m	23m	24m	25m	26m	27m	28m
	5th measurement		29m	30m	31m	32m	33m	34m	35m
Grazeley Green site (line 2)	1st measurement	Hammer	2m	4m	6m	8m	10m	12m	14m
	2nd measurement		16m	18m	20m	22m	24m	26m	28m
	3rd measurement		30m	32m	34m	36m	38m	40m	42m

3.1.2 Borehole information

Some information on the soil properties was obtained from historical borehole survey data collected by the British Geological Survey (BGS). A number of borehole surveys were inspected from the area around each site. These show that various kinds of soil are present down to a depth of about 200 m. The results show that the soil is formed of clay even down to a depth of 90 m. Although different colours and textures of clay are identified, the stiffness of the soil is not easily identified from this information. The results are summarised in Figures 3.4 and 3.5 for the sites in the vicinity of Steventon and Grazeley Green respectively.

SU49SE2	Depth(m)		SU49SE80	Depth(m)		SU49SE187	Depth(m)		SU49SE193	Depth(m)		SU49SE194	Depth(m)	
Clay	17.7	17.7	Clayey, Silty	0.4	0.4	Firm to stiff silty Clay	0.9	0.9	Top soil	0.2	0.2	Top soil	0.2	0.2
Rock	0.2	17.8	Very clayey sandy gravel	2.0	2.4	Soft very silty Clay	1	1.9	Clay	0.9	1.1	Clay	0.1	0.3
Sand	0.3	18.1	Clay soft dark bluish grey	0.4	2.8	Firm very silty Clay	1.1	3	Sand	0.9	2	Clay	0.5	0.8
Rock	0.1	18.2				Very stiff, very close to fissured	12.5	15.5	Clay stiff	0.1	2.1	Sand	0.5	1.3
Sand	0.5	18.7										Clay	0.1	1.4
Rock	1.8	20.4												
Clay	4.3	24.7												
Boulders & clay	34.7	59.4												
Rock	1.5	61.0												
Clay	4.6	65.5												
Rock	0.3	65.8												
Clay	0.3	66.1												
Boulders	1.2	67.4												
Rock	1.2	68.6												
Boulders & Rock	4.0	72.5												
Clay&stones	1.1	73.6												
Rock	4.4	78.0												
Clay&stones	2.7	80.8												
Clay	4.9	85.6												
Sandy clay	3.0	88.6												
distance to the test site	150 m		distance to the test site	500 m		distance to the test site	350 m		distance to the test site	300 m		distance to the test site	550 m	

Figure 3.4. The borehole survey records measured in the vicinity of Steventon.

SU66NE37	Depth(m)		SU66N28	Depth(m)		SU66N25	Depth(m)	
Soil	0.3	0.3	Top soil	0.6	0.6	Soil	0.4	0.4
Grey clay	1.1	1.4				Clay, soft&gravelly clay	1.1	1.5
Fine Gravel	0.2	1.5	Mottled clay	1.2	1.8	Clay,firm,mottled grey	1.7	3.2
Red clay	1.2	2.7				Clay,firm,grey	0.3	3.5
Blue clay	6.4	9.1	Blue clay	14.0	15.8			
Clay&Shell Deposit	4.0	13.1						
Fine Sand	0.9	14.0						
Brown clay	4.0	18.0	Mottled clay	6.1	21.9			
Grey sand	0.5	18.4						
Sandy clay	5.0	23.5						
Grey sand	1.2	24.7	Dark grey sand	6.4	28.3			
Sandy clay	1.2	25.9						
Brown sand	1.5	27.4						
Sand with odd Fossils	1.5	29.0						
Grey sand	3.0	32.0	Mottled clay	4.0	32.3			
Sand&Gravel	2.1	34.1	Light gray sand	4.9	37.2			
Chalk&Flints	40.2	74.4	Chalk	45.1	82.3			
Flint Bed	1.8	76.2						
Chalk&Flints	29.3	105.5						
Hard Chalk&Flints	37.2	142.6						
Very Hard Chalk&Flints	0.6	143.3						
Hard Chalk&Flints	9.1	152.4						
Chalk&Flints	3.0	155.4						
Chalk&Flints	3.7	159.1						
Chalk	37.5	196.6						
Very Hard Chalk	8.2	204.8						
distance to the test site	450 m		distance to the test site	350 m		distance to the test site	400 m	

Figure 3.5. The borehole survey records measured in the vicinity of Grazeley Green.

3.1.3 Methods for determining ground parameters

Although the automated spectral analysis of surface waves (SASW) method (as described in Chapter 2) could be used to determine the dynamic soil characteristics, some other methods are considered in order to gain more insight into the results. The following methods have been used for determining ground parameters.

1. Seismic survey method

2. Axisymmetric layered ground model – transfer mobilities
3. Axisymmetric layered ground model using dispersion diagram

From these various methods the properties of the ground are refined by adding additional layers to the representation of the ground. Finally the ground model is used in Section 3.6 in a comparison with measurements of passing trains.

3.2 Parameters for the ground using seismic survey method

To determine the ground properties, initially a seismic surveying method is used, based on Snell's law [98]. This is based on inspecting time-histories to identify travel times. On the basis of previous experience, [3,7], the number of layers in the ground was assumed initially to be two, which are an upper layer of weathered material and a stiffer half-space, in order to construct a simple model. This method was also used in [99].

Figure 3.6 shows a typical graph of arrival times t at various distances x from the source. Direct arrivals occur due to waves in the surface layer with speed v_1, while refracted arrivals occur due to waves in a lower layer with a higher speed as shown in Figure 3.7. In these, a delay is introduced by the layer depth. The depth of the upper layer z can be approximated using [98],

$$z = \frac{t_i v_1 v_2}{2(v_2^2 - v_1^2)^{1/2}} \tag{3.1}$$

where t_i is the intercept time shown in Figure 3.6, v_1 is the upper layer velocity and v_2 is the lower layer velocity. This depth of the upper ground layer is also given by the following formula [98],

$$x_{cross} = 2z\left[\frac{v_2 + v_1}{v_2 - v_1}\right]^{1/2} \tag{3.2}$$

where x_{cross} is the crossover distance as shown in Figure 3.6.

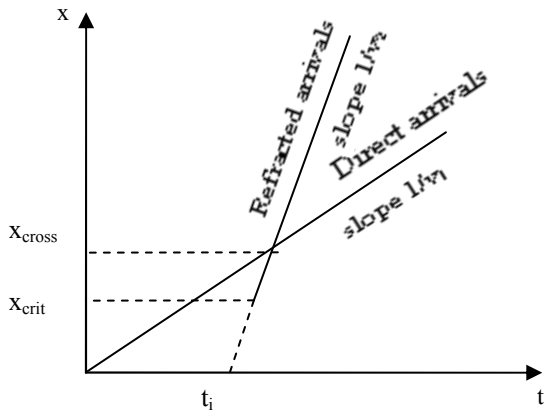

Figure 3.6. Travel-time curves for the direct wave and the refracted wave from a single horizontal refractor [98].

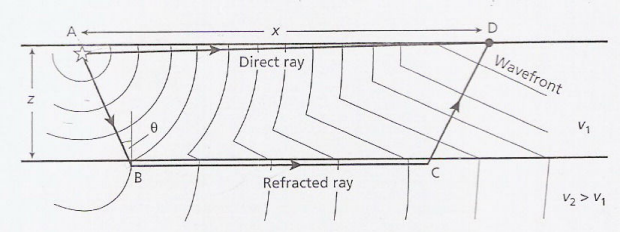

Figure 3.7. Successive positions of the expanding wavefronts for direct and refracted waves through a two-layer model. Only the wavefront of the first arrival phase is shown. Individual ray paths from source A to detector D are drawn as solid lines [98].

Figure 3.8 shows the acceleration time-histories for each measurement distance from Steventon. The results are average from 10 for each distance. By arranging the traces in this way, wave speeds can be identified as diagonal lines of activity. Similar results are shown in Figure 3.9 for Grazeley Green. The amplitude of the propagating waves drops off as the distance increases. To obtain similar amplitudes for each distance, the responses are normalized by the maximum value at each distance. The P-wave speeds can be approximated from the slope of the initial response in Figures 3.8 and 3.9 as shown in Figure 3.6. The P-waves are generally the fastest waves in the graph and can be identified as 1700 and 1400 m/s respectively. However the wave speed of 340 m/s may not be due to a ground-borne wave; it may be an acoustic wave as this has the same speed as air-borne sound. The two wave speeds v_1 and v_2, the P-wave speeds for the upper and lower layer derived from these graphs, are listed in Table 3.2. The S-wave speed, v_s, for the upper layer can also be

approximated from the slope of the line nearest to the *x*-axis. By using the above formulae the two estimates of the depth of the upper layer, z , were then calculated.

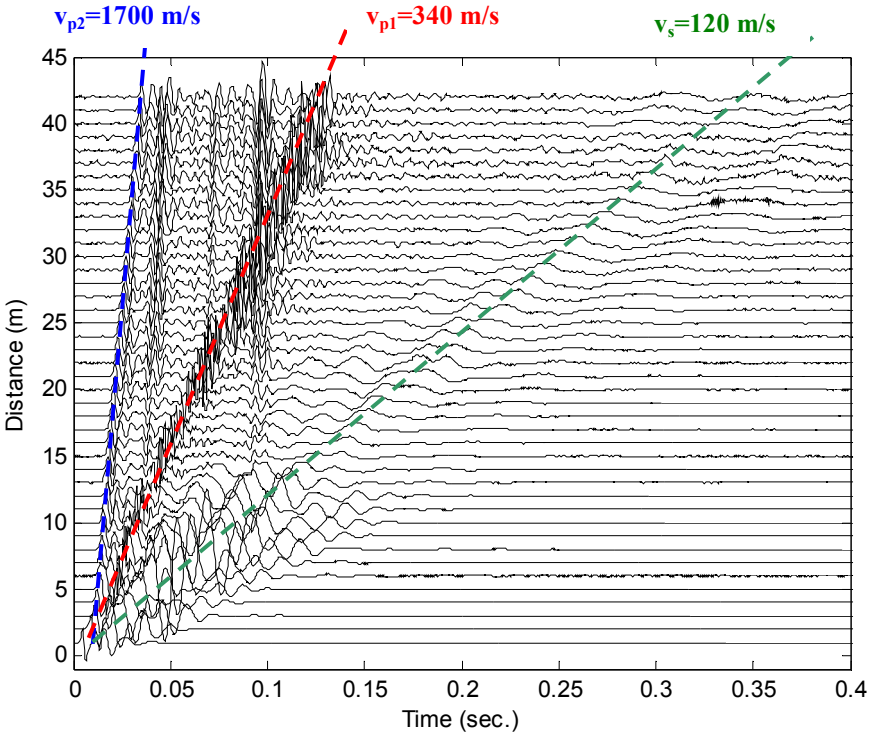

Figure 3.8. Acceleration time-histories on the surface of the ground at various distances for Steventon.

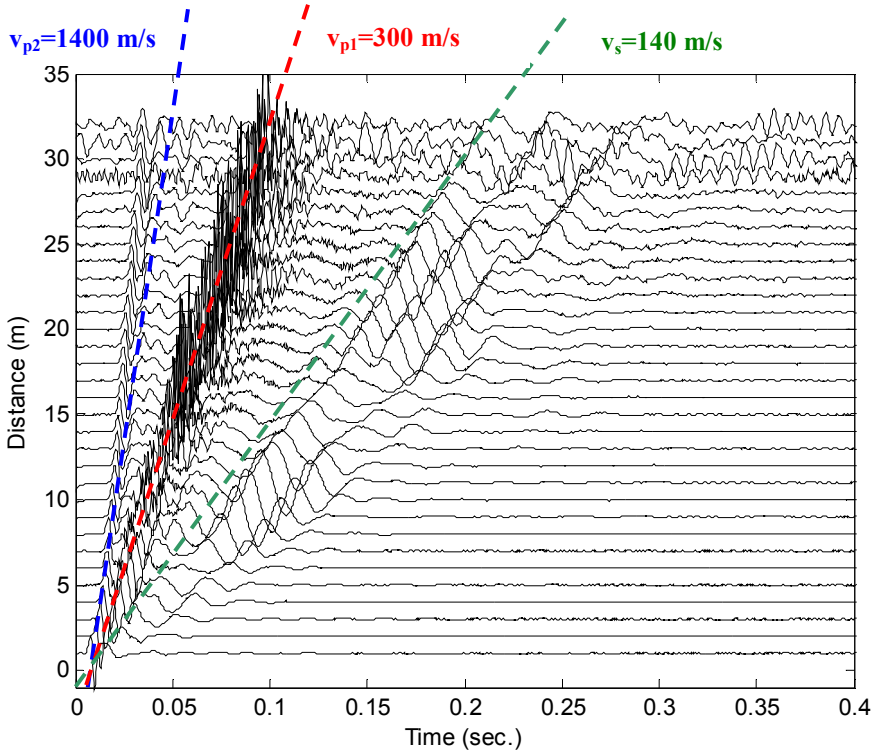

Figure 3.9. Acceleration time-histories on the surface of the ground at various distances for Grazeley Green.

As noted, the P-wave speeds of the upper layer v_{p1} may be subject to considerable uncertainty due to possible contamination by acoustic waves. As a result, the layer depths calculated using the above formula, are not reliable. Moreover by using the seismic surveying method the S-wave speeds for the lower layer, v_{s2}, could not be estimated. As the S-wave speeds and layer depths have a strong influence on the predicted vibration, a different technique will be considered.

Table 3.2. The ground properties approximated from the measured data using seismic survey methods, equations (3.1) and (3.2).

Ground properties	Steventon site	Grazeley Green site
P-wave speed, v_{p1} for upper layer	340 m/s	300 m/s
P-wave speed, v_{p2} for lower layer	1700 m/s	1400 m/s
S-wave speed, v_s for upper layer	120 m/s	140 m/s
The depth of the upper layer, z using equation (3.1)	1.39 m	1.53 m
The depth of the upper layer, z using equation (3.2)	1.30 m	1.60 m

3.3 Axisymmetric layered ground model

3.3.1 Model

An axisymmetric layered ground model based on stiffness matrices, presented by Kausel and Roesset [33], has been used to determine the frequency response of the ground to point loads. This model has previously been implemented in a Matlab program kandr. The point and transfer mobilities are calculated based on formulae presented by Kausel and Roesset [33] as shown in Appendix A.

The appropriate model at this stage would have two layers, a weathered layer of surface material and a stiffer half-space. The results from the measurements, presented as transfer mobilities on the surface of the ground at various distances, have next been used to determine the ground properties by fitting the results of this model to them.

Initially the parameters from Table 3.2 were used in the kandr model for comparison with the measurement. The S-wave speeds in the lower layer were chosen arbitrarily to be 240 m/s for both sites. The results are shown in Figure 3.10 for Steventon and in Figure 3.11 for Grazeley Green for four distances. In each case there are two sets of measured results, from the two measurement lines, which are both shown.

For the Steventon site it can be seen that the measured vibration rises sharply to a peak at about 60 Hz at 2m away from the forcing point. This is likely to correspond to the cut-on frequency of the upper layer. Similarly at Grazeley Green, the cut-on frequency of the upper layer is at about 40 Hz.

From these figures it is clear that the agreement with the model is poor. Consequently in the following sections the parameters have been modified in an attempt to get a better fit.

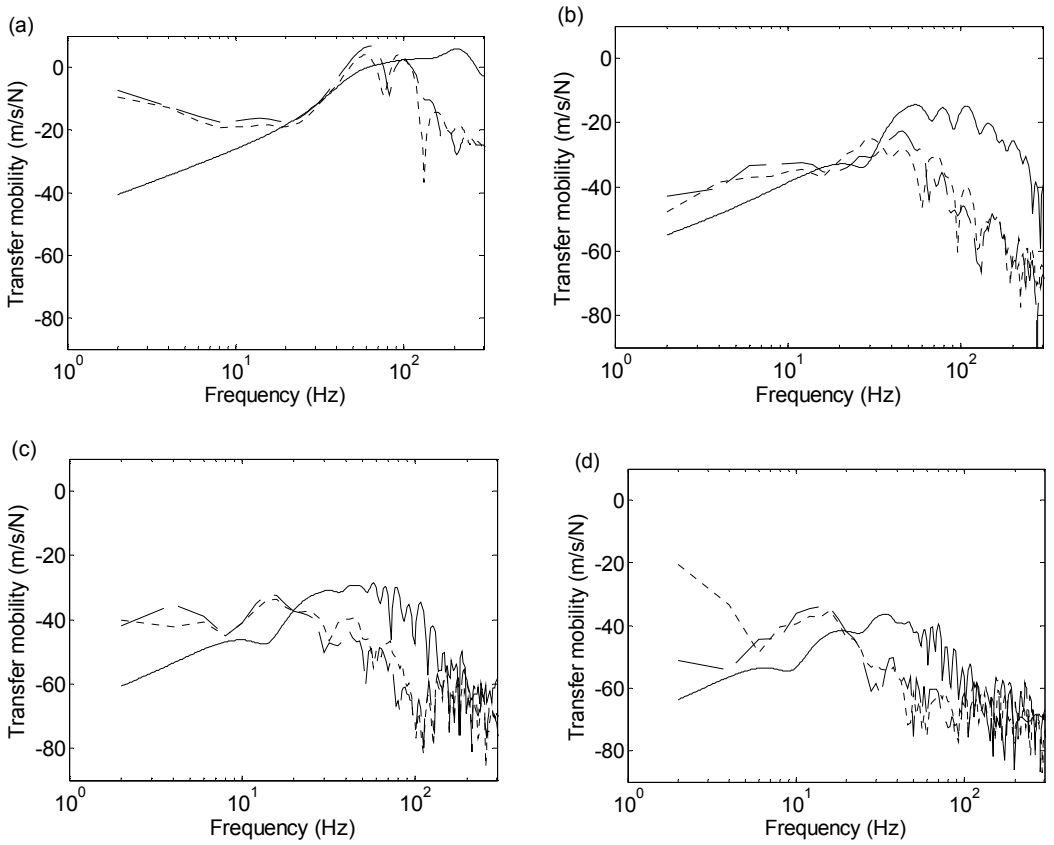

Figure 3.10. Comparison of transfer mobilities for Steventon on the surface of the ground obtained using the kandr model with initial parameters from Table 3.2 and the measurements. —, predicted; ––, measured at line 1; ·····, measured at line 2: (a) 2, (b) 10, (c) 20 and (d) 30 m away from applied force.

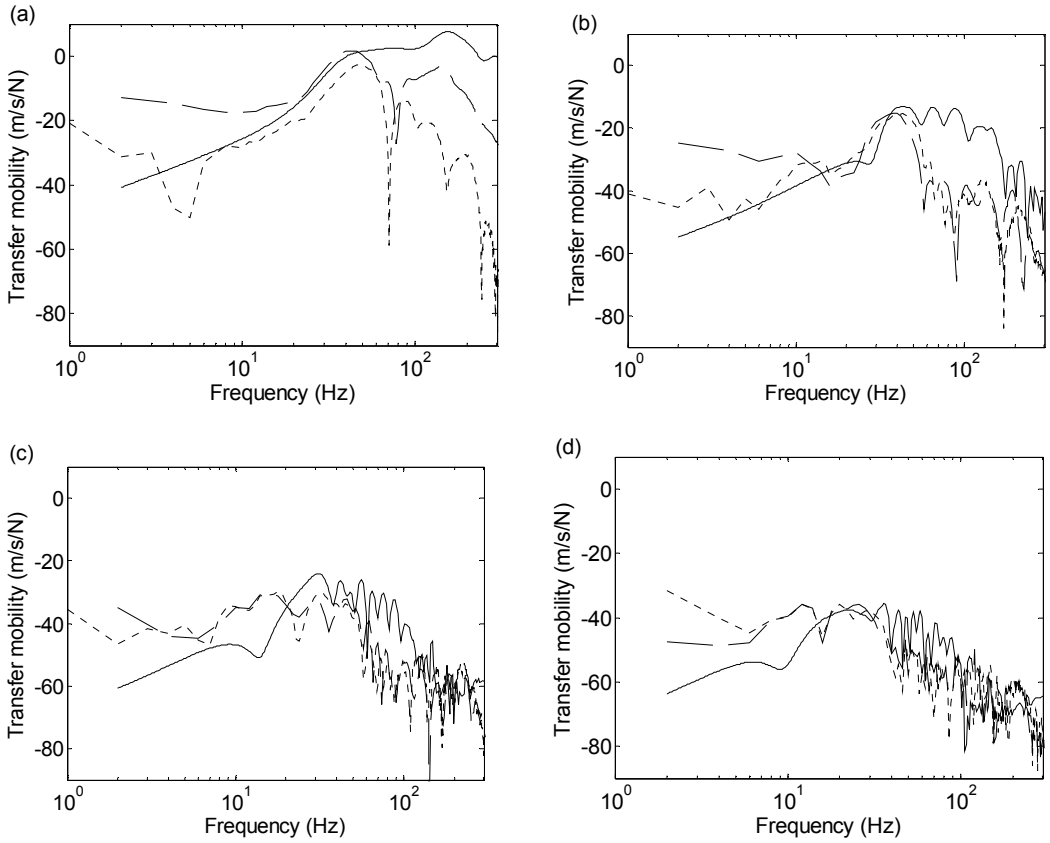

Figure 3.11. Comparison of transfer mobilities for Grazeley Green on the surface of the ground obtained using the kandr model with initial parameters from Table 3.2 and the measurements. —, predicted; ––, measured at line 1; ·····, measured at line 2: (a) 2, (b) 10, (c) 20 and (d) 30 m away from applied force.

3.3.2 Added mass at excitation point

As well as changes in the wave speeds and layer depth, one aspect considered was the addition of a mass at the force point to represent the person applying the hammer excitation. The mass of this person is taken to be approximately 70 kg, although it may be expected that the apparent mass will be less than this at higher frequencies [100].

The addition of a mass follows the principle of Figure 3.12. For harmonic motion at frequency ω the transfer mobility between a force of amplitude F_1 at position 1 and the velocity amplitude V_2 at position 2 is given by [101]

$$\hat{Y}_{12} = \frac{V_2}{F_1} = \frac{Y_{12}Y_{33}}{Y_{22} + Y_{33}} \tag{3.3}$$

where Y_{12} is the transfer mobility for the response point 2 from the force at point 1 (without the mass), Y_{22} is the point mobility of the ground, while Y_{33} represents the point mobility of the added mass.

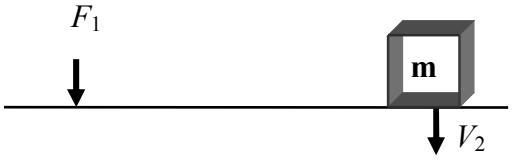

Figure 3.12. Coupling together complex arbitrary systems in series connection.

By reciprocity the mobility $\hat{Y}_{12}$ is equal to the mobility $\hat{Y}_{21}$ where the mass is applied at the forcing point.

In order to see the effect of the mass on the vibration response, the results from the model with different masses were compared with the measurement, as shown in Figure 3.13. The vibration responses were also converted from narrow band spectra to 1/3 octave bands for ease of interpretation. The value of the mass was set to 0, 7, 20, and 70 kg in the model and the vibration responses are compared with the measurements at 1 m away from the applied force for the Steventon site. (Other parameters in the model are as listed in Table 3.3 and discussed in the next section) These various masses have an effect especially at the peak at 60 Hz and above 100 Hz due to the mass bouncing on the ground. The higher the mass, the lower the response level becomes at high frequencies. The results show that the best fit for the model at the Steventon site is found for an added mass of 20 kg.

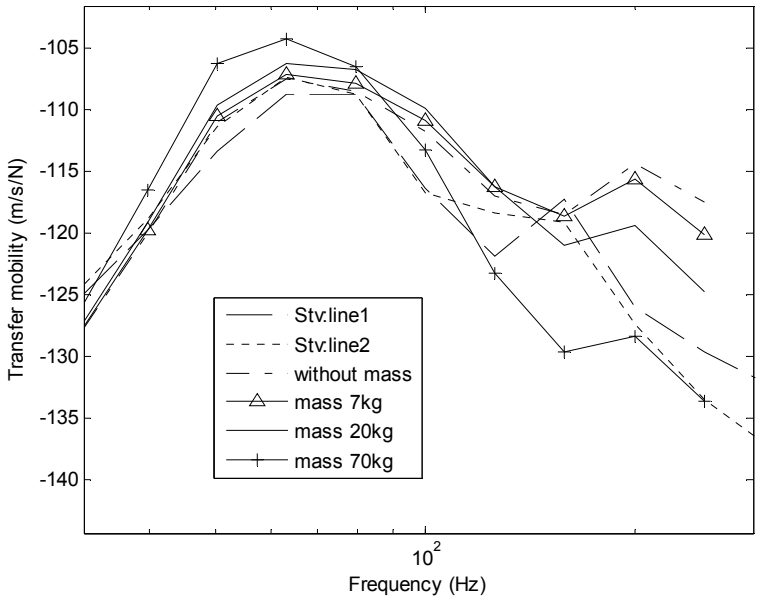

Figure 3.13. The effect of various extra masses on the vibration response at 1m away from the applied force for Steventon site.

3.3.3 Adjustments to ground parameters

The parameters for the ground have been changed as the results in Figures 3.10 and 3.11 gave a poor agreement. The S-wave speed and the depth of the upper layer are found to have a strong effect on the amplitude at the cut-on frequency and on the stiffness-like slope at low frequencies. On the other hand the P-wave speeds have much less effect on the vibration response as will be discussed further in Section 3.5.3. The density of the soil also has less effect and is unlikely to vary greatly. According to this, the S-wave speeds have been changed to 110 and 400 m/s for the upper and lower layers at Steventon and to 130 and 200 m/s for Grazeley Green. The depths of the upper layer have been estimated as 1.0 and 1.4 m for Steventon and Grazeley Green respectively, as shown in Table 3.3.

The damping loss factor for the layer materials has more effect on the response at distances further away from the source. As shown in Table 3.3 the damping loss factor has been identified as being frequency dependent, and is chosen to increase linearly from 0.1 at 0 Hz to 0.2 or 0.3 at 300 Hz. This is discussed further in Section 3.3.4 below.

The results are shown in Figures 3.14 and 3.15 for the Steventon and Grazeley Green sites respectively, using the parameters listed in Table 3.3. As in the previous section 1/3 octave band spectra are used for improved clarity. The predictions from the kandr model and the measurements for frequencies above 10 Hz are shown in one-third octave bands. The measurements have been extended below 10 Hz by plotting points every 2 Hz up to 10 Hz. However the results below 10 Hz are probably subject to large measurement uncertainty as the corresponding acceleration level is small. Agreement with the model is poor at these low frequencies. The results show the response has a broad peak at about 40-80 Hz for Steventon and at 30-40 Hz for Grazeley Green. These are probably the cut-on frequencies of the upper layer for these sites. The dashed lines (blue) represent the vibration response from the model without the extra mass of 20 kg. The solid lines (red) represent the adapted model with the added 20 kg. Adding this extra mass causes the level of vibration from the model to become closer to the measurement. Also at Grazeley Green the model has been modified using the same mass, although the agreement would be better using a larger mass.

Table 3.2. The parameters used in the kandr model for Steventon and Grazeley Green sites obtained by fitting mobilities.

Parameters		Steventon site	Grazeley Green site
upper layer	P-wave speed	500 m/s	500 m/s
	S-wave speed	110 m/s	130 m/s
	density of layer material	2000 kg m^{-3}	2000 kg m^{-3}
	Loss factor for layer material	[0.1 at 0 Hz] [0.3 at 300 Hz]	[0.1 at 0 Hz] [0.3 at 300 Hz]
	Layer depth	1.0 m	1.4 m
Half space	P-wave speed	1700 m/s	1400 m/s
	S-wave speed	400 m/s	200 m/s
	density of layer material	2000 kg m^{-3}	2000 kg m^{-3}
	Loss factor for layer material	[0.1 at 0 Hz] [0.3 at 300 Hz]	[0.1 at 0 Hz] [0.3 at 300 Hz]
	Layer depth	inf.	inf.

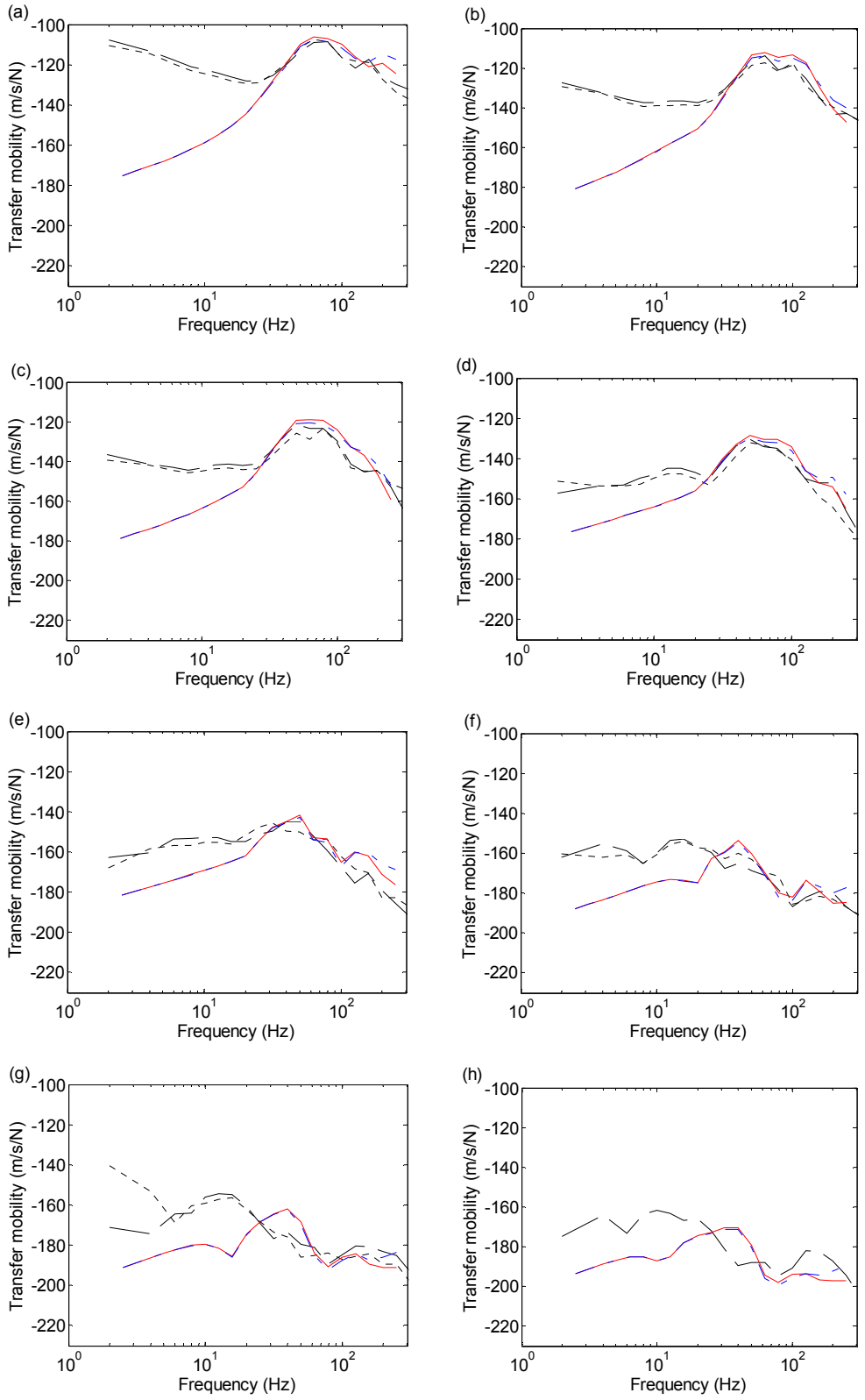

Figure 3.14. Vibration response for Steventon site comparing between the measurement. — –, measured at line 1; ·····, measured at line 2, and kandr model. — with; – · – without the extra mass of 20 kg: (a) 1, (b) 2, (c) 3, (d) 5, (e) 10, (f) 20, (g) 30 and (h) 42 m away from the applied force.

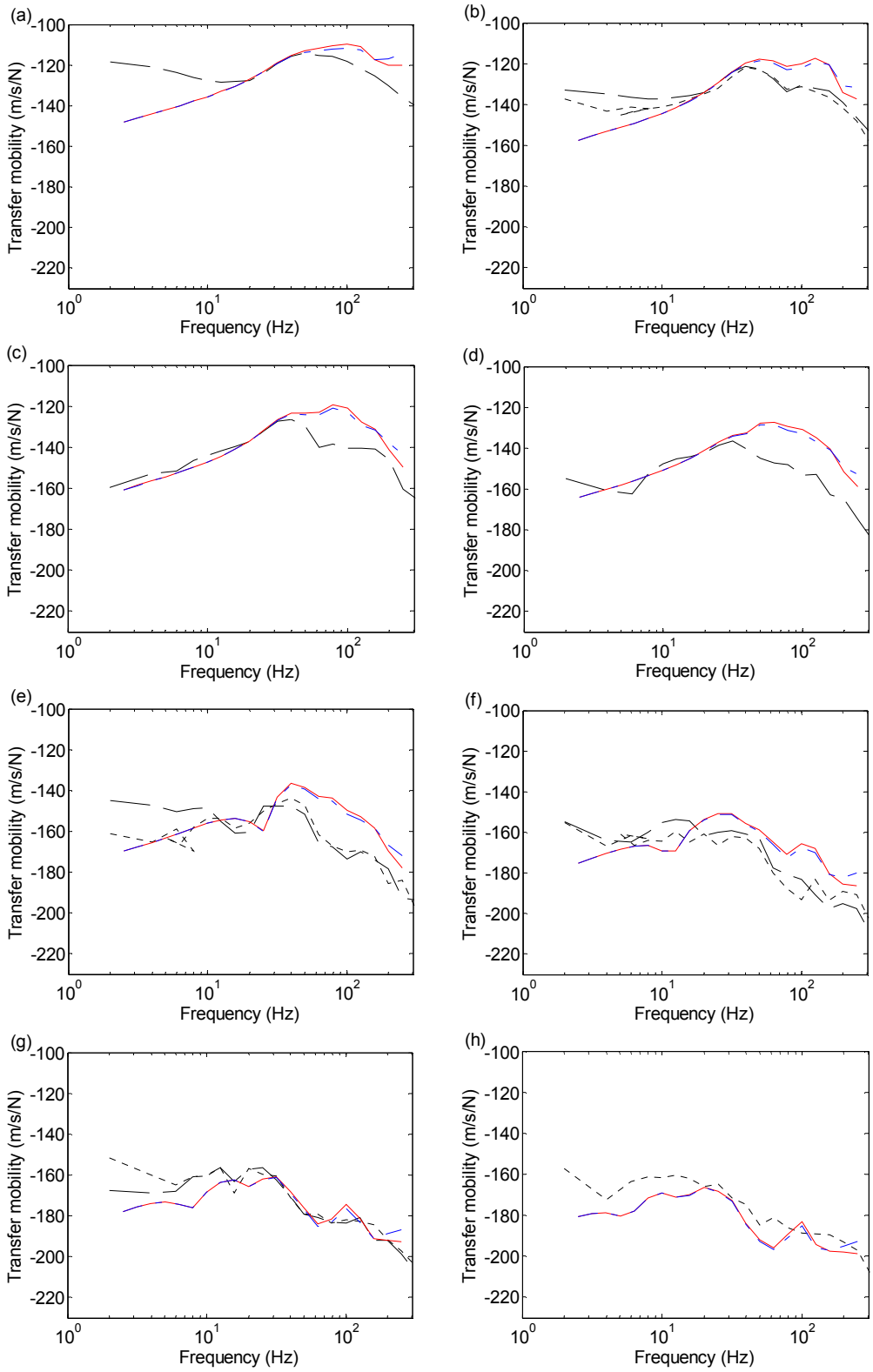

Figure 3.15. Vibration response for Grazeley Green site comparing between the measurement. — –, measured at line 1; ·····, measured at line 2, and kandr model. — with; – · – without the extra mass of 20 kg: (a) 1, (b) 2, (c) 3, (d) 5, (e) 10, (f) 20, (g) 30 and (h) 42 m away from the applied force.

3.3.4 Damping

The loss factors for the soil material were chosen to give a suitable decay with distance at low and high frequency. In order to investigate this decay of propagating vibration, the damping loss factor was set to constant values of 0.05, 0.1, 0.2 and 0.4 over the whole frequency range. Results from the kandr model are calculated every 0.5 m up to 32 m whereas the measurements are acquired every 1 m. The results of these calculations for 20, 40, 80 and 160 Hz at both sites are shown in Figures 3.16 and 3.17. From the results at 20 Hz, a damping loss factor of 0.1 gives good agreement, at 40 Hz it is between 0.1 and 0.2 while at 80 Hz a loss factor of 0.2 gives good agreement. At 160 Hz the damping appears to be 0.4. This confirms the choice of a frequency-dependent damping loss factor, although the value used of 0.1 increasing to 0.3 at 300 Hz is slightly smaller than implied by some of these results.

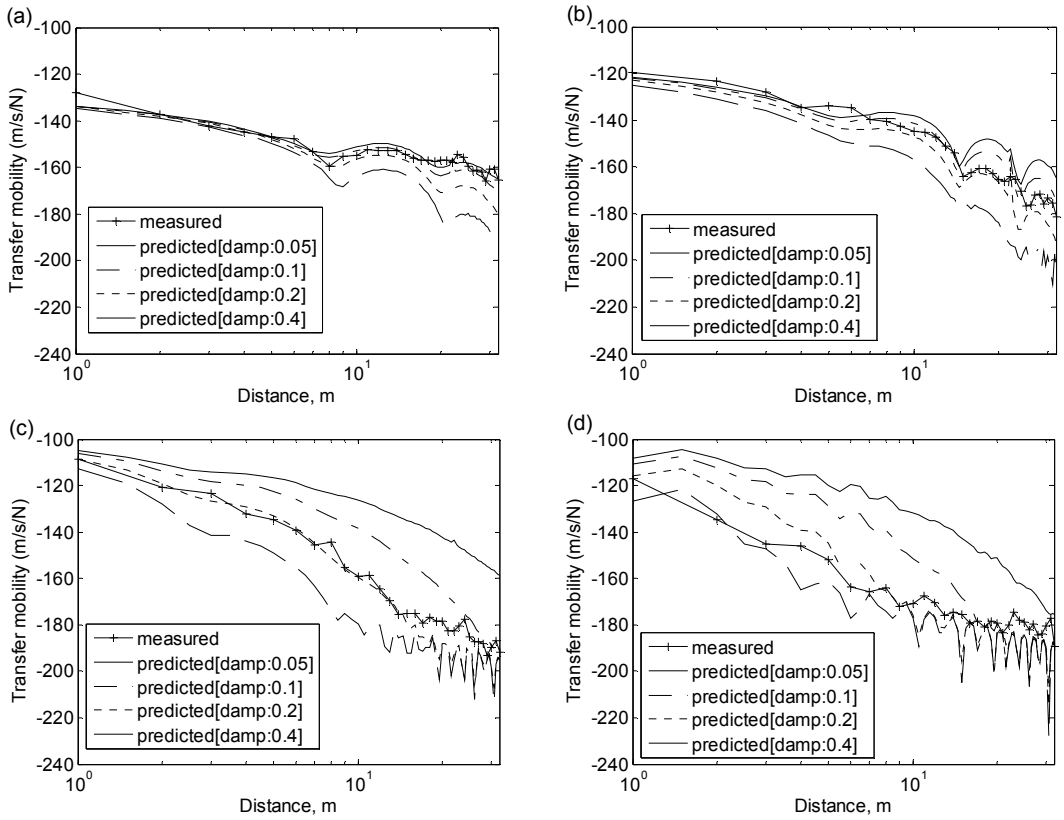

Figure 3.16. Propagation of vibration away from hammer excitation, comparing the measurement and kandr model with various constant damping loss factors ranging from 0.05 to 0.4; for (a) 20, (b) 40, (c) 80 and (d) 160 Hz at Steventon site.

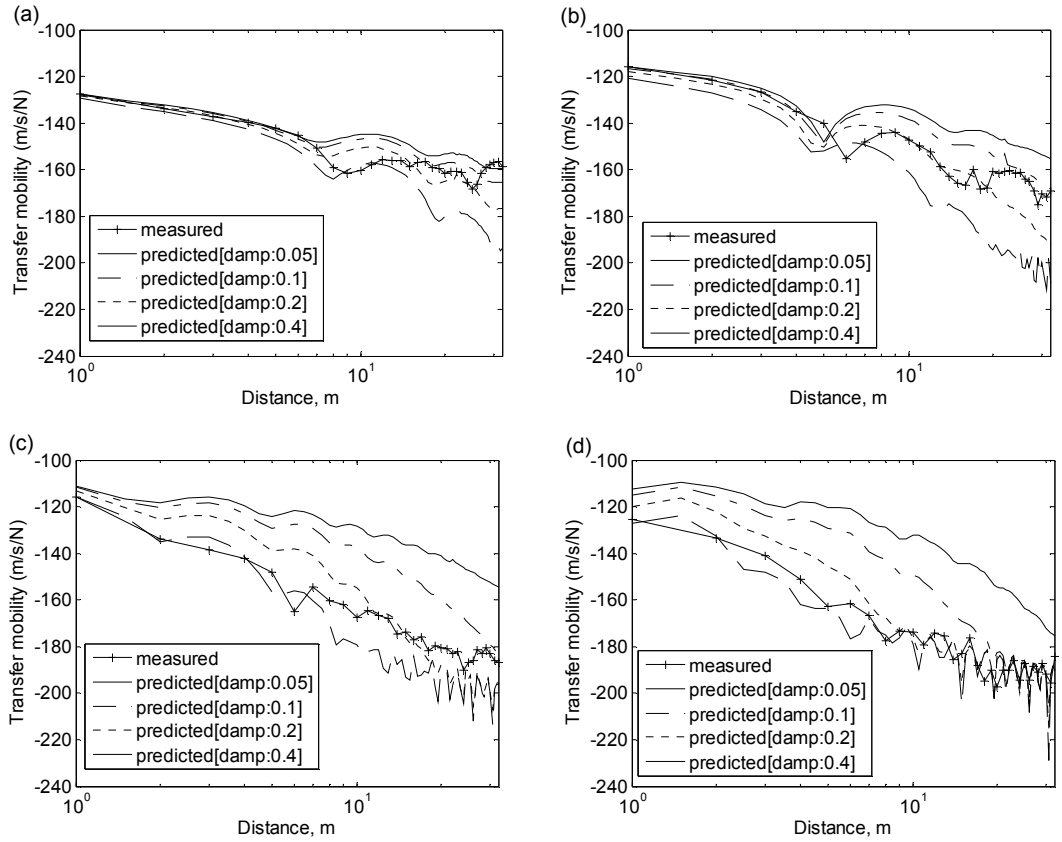

Figure 3.17. Propagation of vibration away from hammer excitation, comparing the measurement and kandr model with various constant damping loss factors ranging from 0.05 to 0.4; for 20, 40, 80 and 160 Hz at Grazeley Green site.

Although the loss factors for the soil material found from measurements are higher than those often found in literature, this is believed to be due to the fact that at both sites the soil consists of soft clay, which at the time of the measurement was saturated.

3.4 Alternative approach using dispersion diagram

3.4.1 Initial parameters

An alternative approach to analysing the measured data, which can be used for comparison with the kandr model, is to plot a dispersion diagram for the ground structure[2]. At each frequency the vibration responses at distances every 1 m up to 32 m have been converted to the wavenumber domain by using a Hankel transform [102]. (A Hankel transform is used rather than a Fourier transform as the waves are circular). Results are shown in Figures 3.18 and 3.19 from the measurements on lines

[2] The assistance of Dr J Ryue in constructing this dispersion diagram is gratefully acknowledged.

1 and 2 at Steventon, and on line 1 at Grazeley Green. The responses are normalized by the maximum at each frequency. The results are plotted as colour maps on a frequency-wavenumber axis. Regions of high response (dark red) indicate the strong presence of waves on the surface of the ground. In other words, the bright pattern represents which waves are most strongly excited. The blue regions represent small amplitudes of vibration.

A similar method has been used on data predicted using kandr. Here the responses are predicted every 0.5 m up to 32 m. Initially the parameters from Table 3.3 were used in the kandr model. In these models the layered structure of the ground is represented as a shallow layer of weathered material lying on a stiffer half-space for both sites. The results are shown in Figure 3.20 for Steventon and in Figure 3.21 for Grazeley Green.

Below 10 Hz in the measured dispersion curves, the results are unreliable for both sites, as seen previously in the transfer mobilities. Moreover, the measured results are affected by aliasing for wavenumbers greater than about 3 rad/m (the smallest wavelength that can be detected is 2 m). For the predictions from the kandr model, this problem only affects results for wavenumbers above 6 rad/m as the predictions have a spatial resolution of 0.5 m.

In the measured results from Steventon the main wave is seen at about 120 m/s below 30 Hz and above 50 Hz but there is a gap between 30 and 50 Hz where the dominant wave speed instead occurs at about 200 m/s. On the other hand, the main wave at about 120 m/s has no gap for the Grazeley Green data. Besides this the wave at about 200 m/s is not so strongly present as at Steventon. These features are not found in the dispersion curves obtained from the predicted data, suggesting that further refinement of the ground parameters is required. The wave at about 1700 m/s (P-wave speed), seen in Figures 3.8 and 3.9, is not found in these dispersion plots. This is due to the normalisation used in Figures 3.8 and 3.9. If the dispersion plot is derived instead from this normalised data the wave is found close to the frequency axis in the dispersion plot.

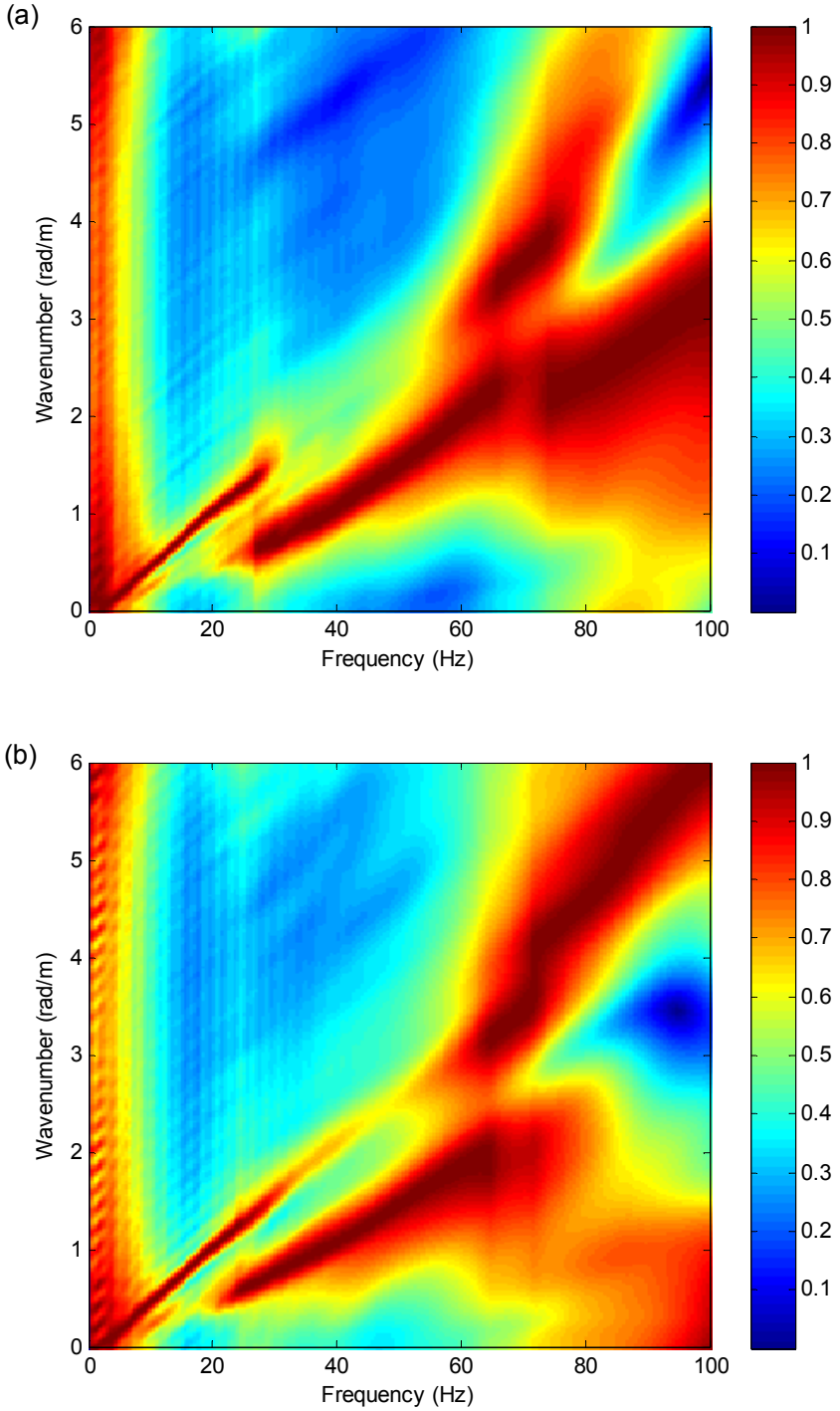

Figure 3.18. Dispersion curves of the ground from the measurements at Steventon site on (a) line 1 and (b) line 2, red indicates stronger presence of waves on the surface of the ground.

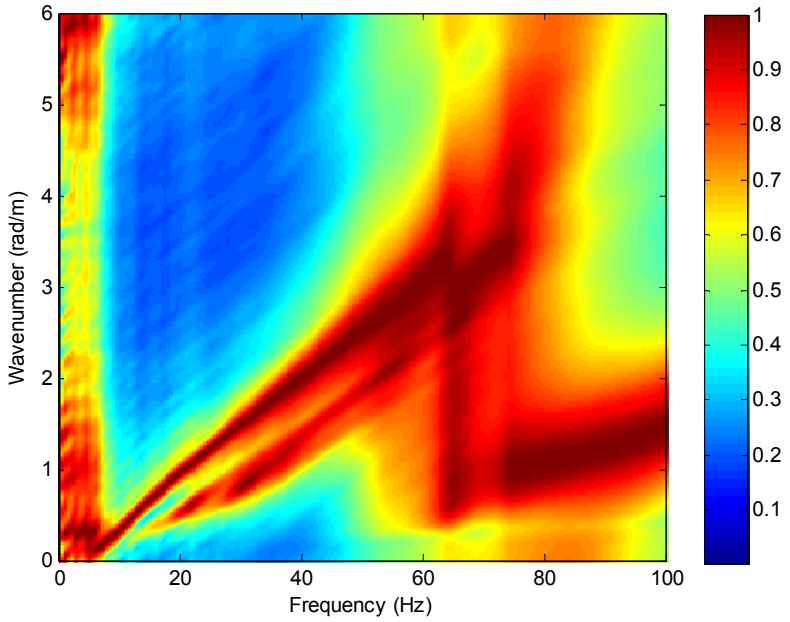

Figure 3.19. Dispersion curves of the ground from the measurements at Grazeley Green site on line 1, red indicates stronger presence of waves on the surface of the ground.

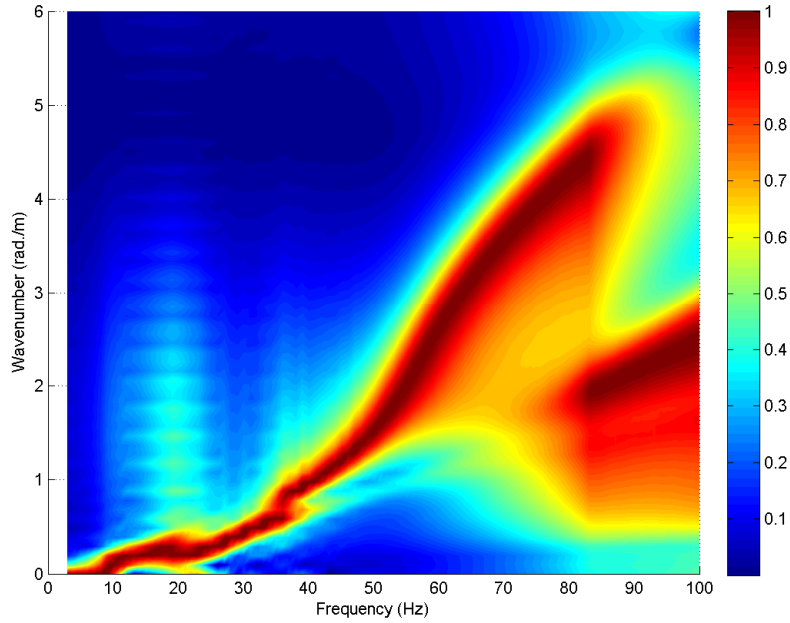

Figure 3.20. Dispersion curves of the ground obtained from results of the kandr model for the Steventon site with parameters from Table 3.3, red indicates stronger presence of waves on the surface of the ground.

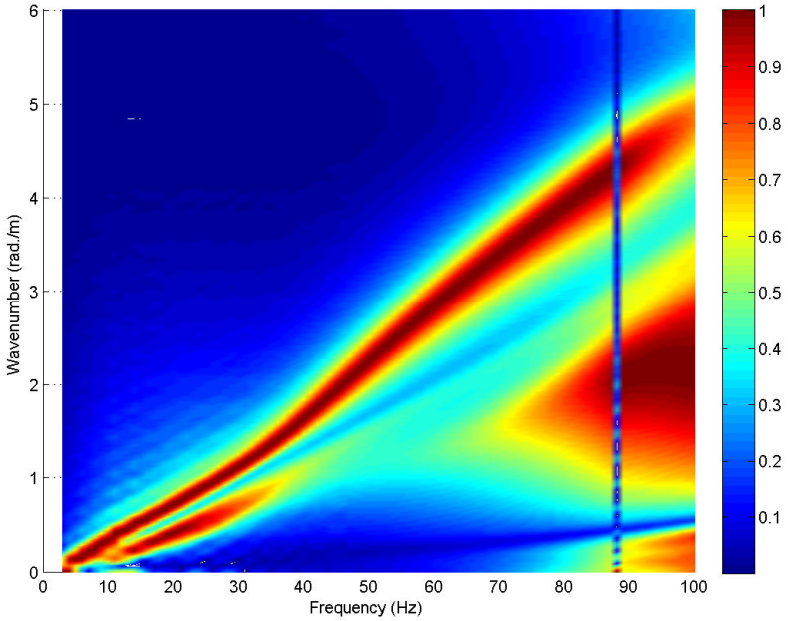

Figure 3.21. Dispersion curves of the ground obtained from the results of the kandr model for the Grazeley Green site with parameters from Table 3.3, red indicates stronger presence of waves on the surface of the ground[3].

3.4.2 Improved parameters

From the above figures it is clear that the agreement is poor between measurements and predictions despite the relatively good agreement found for the transfer mobilities. Consequently the parameters have been modified in an attempt to get a better fit. A number of alternative models have been considered. In the end it was found that three layers was the minimum number required to achieve a good fit to the dispersion behaviour, particularly the gap in the slowest wave found at Steventon. The ground in the model has therefore been divided into two layers above a deep layer (half-space) of soft material. The middle layer is stiffer than the upper layer and the underlying half-space as this feature is found to lead to the gap in the slowest wave. The layer depths are found to affect the lower and upper frequencies of this gap.

The parameters used are listed in Table 3.4. As the P-wave speed has less effect on the vibration response, it is set to 1700 m/s for each layer. The S-wave speeds and the layer depths of the ground strongly affect the slope of the broad peak

[3] The vertical line at about 90 Hz is due to numerical artifact.

at about 50 to 70 Hz in the dispersion plots and the cut-on frequency in the transfer mobilities. The resulting dispersion plots are shown in Figures 3.22 and 3.23 for the two sites while Figures 3.24 and 3.25 show the transfer mobilities.

Table 3.4. The parameters used in the final kandr model for both Steventon and Grazeley Green sites.

Parameters		Steventon site	Grazeley Green site
upper layer	P-wave speed	1700 m/s	1700 m/s
	S-wave speed	120 m/s	130 m/s
	density of layer material	2000 kg m^{-3}	2000 kg m^{-3}
	Loss factor for layer material	[0.1 at 0 Hz] [0.3 at 300 Hz]	[0.1 at 0 Hz] [0.3 at 300 Hz]
	Layer depth	0.7 m	1.4 m
middle layer	P-wave speed	1700 m/s	1700 m/s
	S-wave speed	200 m/s	200 m/s
	density of layer material	2000 kg m^{-3}	2000 kg m^{-3}
	Loss factor for layer material	[0.1 at 0 Hz] [0.3 at 300 Hz]	[0.1 at 0 Hz] [0.3 at 300 Hz]
	Layer depth	2.0 m	0.7 m
Half space	P-wave speed	1700 m/s	1700 m/s
	S-wave speed	120 m/s	120 m/s
	density of layer material	2000 kg m^{-3}	2000 kg m^{-3}
	Loss factor for layer material	[0.1 at 0 Hz] [0.3 at 300 Hz]	[0.1 at 0 Hz] [0.3 at 300 Hz]
	Layer depth	inf.	inf.

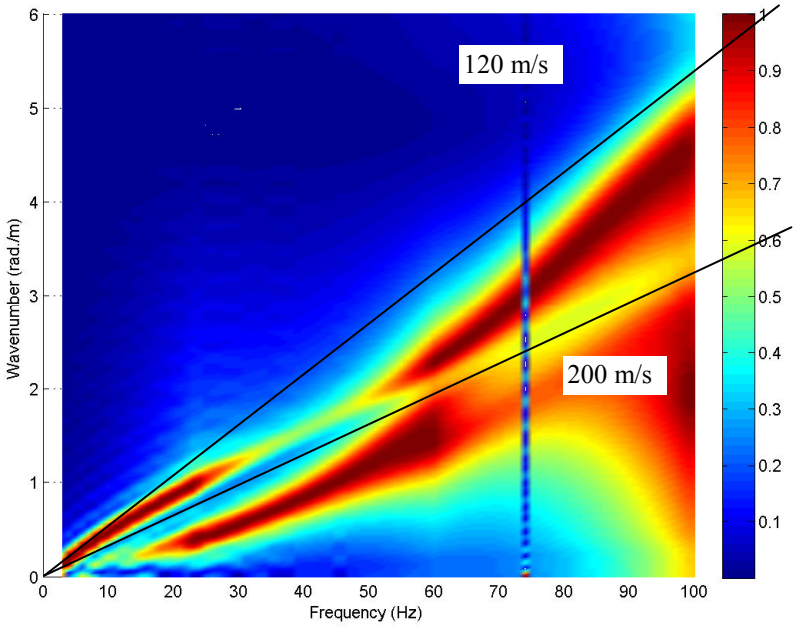

Figure 3.22. Dispersion curves of the propagating wave number from kandr model for the Steventon site, using parameters from Table 3.4, red indicates stronger presence of waves on the surface of the ground.

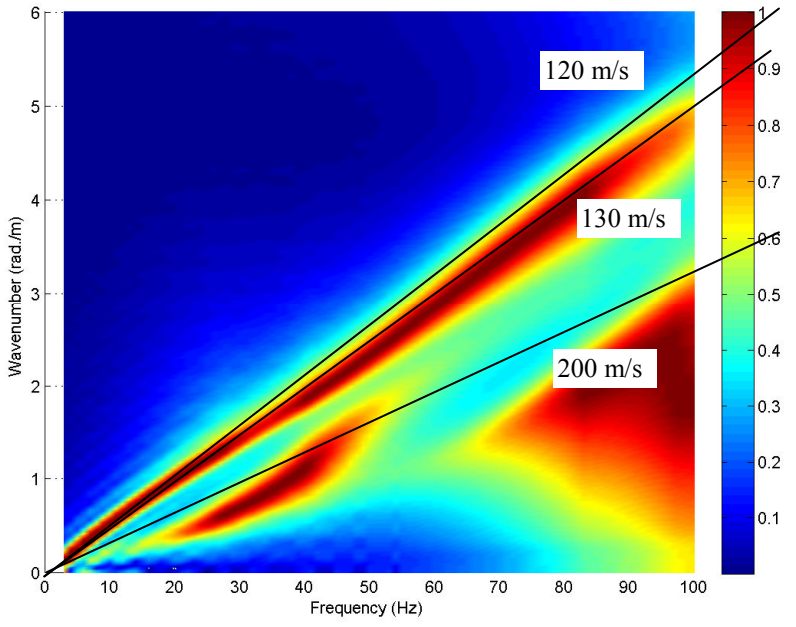

Figure 3.23. Dispersion curves of the propagating wave number from kandr model for the Grazeley Green site, using parameters from Table 3.4, red indicates stronger presence of waves on the surface of the ground.

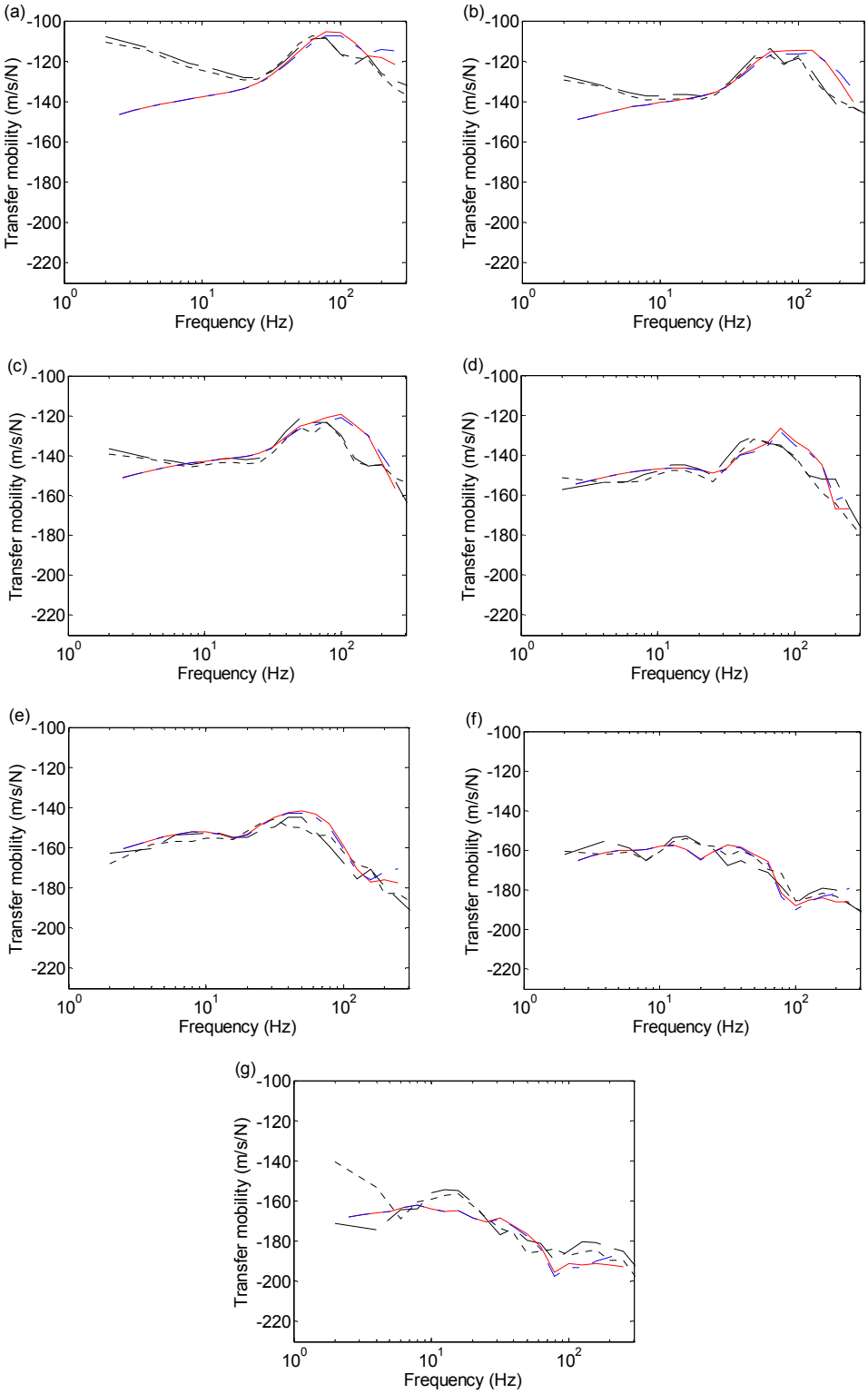

Figure 3.24. Comparison of transfer mobilities for Steventon on the surface of the ground obtained using the kandr model with parameters from Table 3.4. — with; – · – without the extra mass of 20 kg and the measurements. — –, measured at line 1; ·····, measured at line 2: (a) 1, (b) 2, (c) 3, (d) 5, (e) 10, (f) 20 and (g) 30 m away from the applied force.

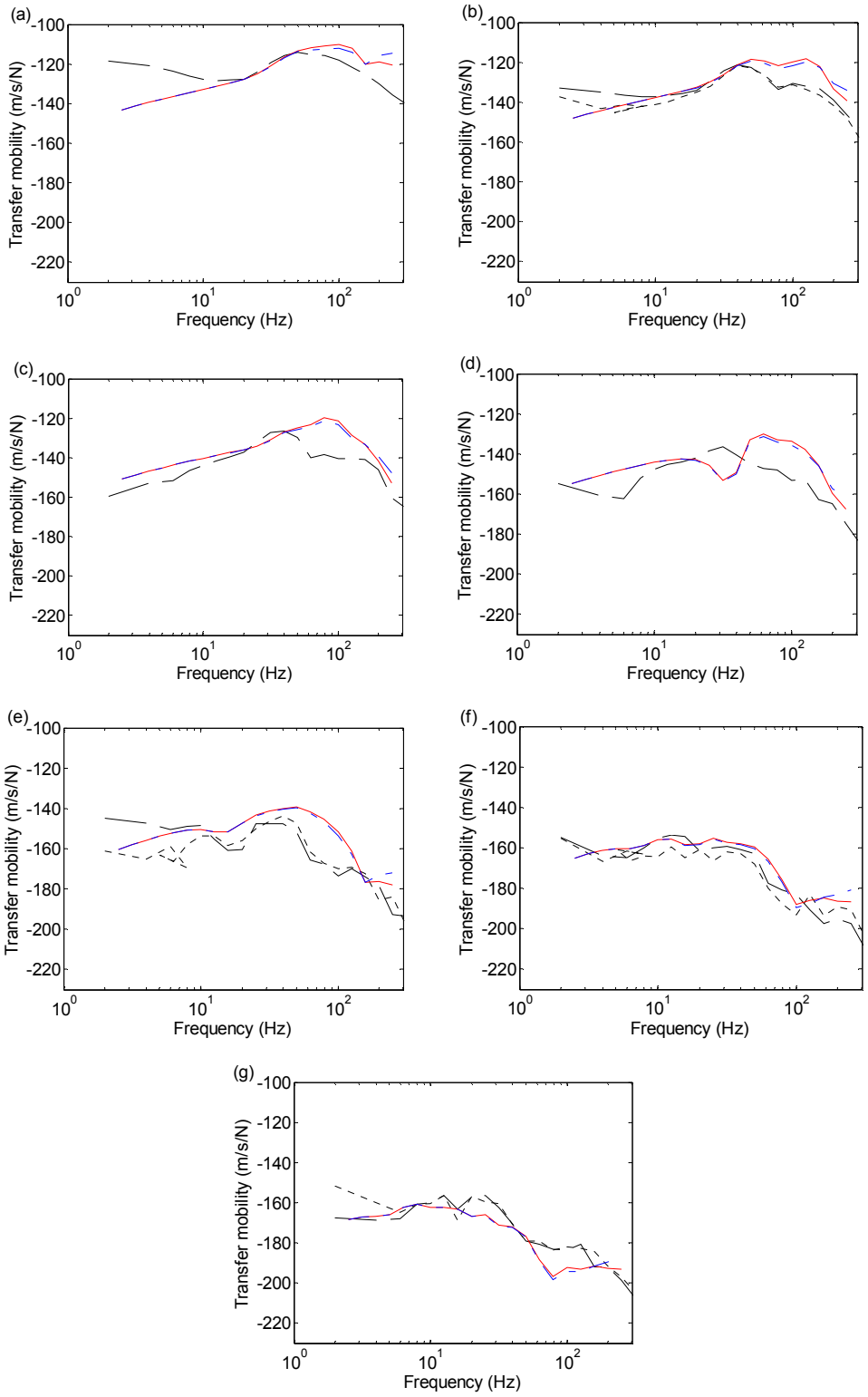

Figure 3.25. Comparison of transfer mobilities for Grazeley Green on the surface of the ground obtained using the kandr model with parameters from Table 3.4. — with; – · – without the extra mass of 20 kg and the measurements. — –, measured at line 1; ·····, measured at line 2: (a) 1, (b) 2, (c) 3, (d) 5, (e) 10, (f) 20 and (g) 30 m away from the applied force.

The results presented in the dispersion curves and transfer mobilities show a good agreement with the measurements especially for Steventon. For Grazeley Green further improvement could be found by using yet more layers but this is not considered to be justified. As the extra mass has been added to the model, as in Section 3.3.2, it affects the vibration response over the broad peak 50-60 Hz and above 100 Hz. This effect is consistent for all distances.

The damping loss factor has been identified as frequency dependent, as before. This gives reasonable decays with distance as found in Figures 3.24 and 3.25. The decay of propagating vibration with distance at frequencies of 20, 40, 80 and 160 Hz is plotted for both sites in Figures 3.26 and 3.27.

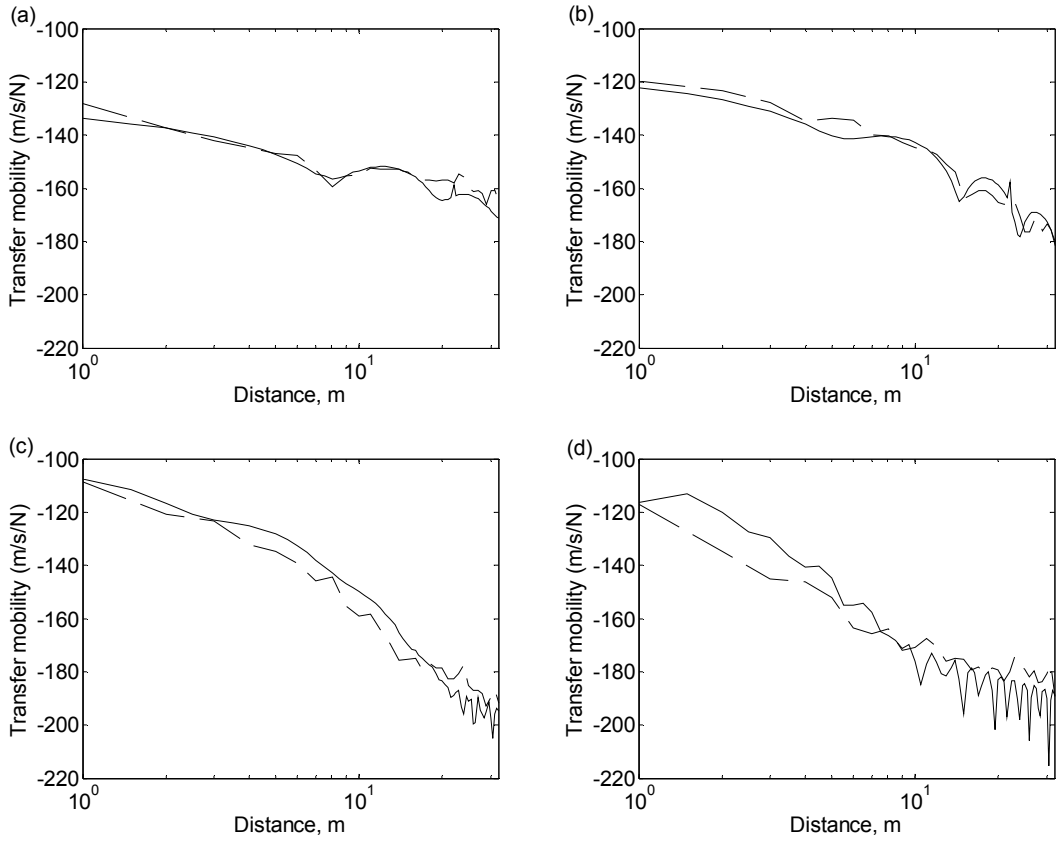

Figure 3.26. Propagation of vibration away from the track comparing between; – – the measurement and; —, the prediction using kandr model, for (a) 20, (b) 40, (c) 80 and (d) 160 Hz at Steventon site.

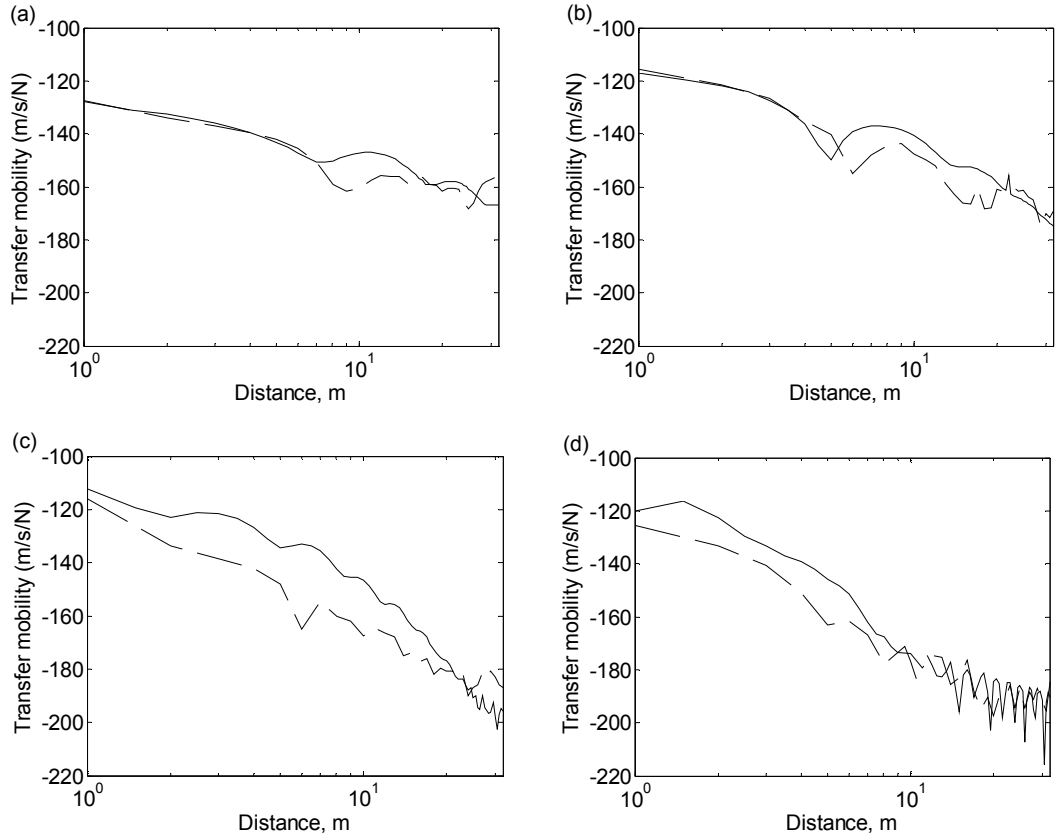

Figure 3.27. Propagation of vibration away from the track comparing between; – – the measurement and**; —,** the prediction using kandr model, for (a) 20, (b) 40, (c) 80 and (d) 160 Hz at Grazeley Green site.

3.5 Parameter variations

Having established a model giving a good fit to both mobility and dispersion data, the sensitivity of the predictions to various parameters in the kandr model has been investigated based on the Steventon site.

3.5.1 S-wave speeds

The factors which most strongly affect the vibration response are the S-wave speeds and the layer depths. In order to see the effect of different S-wave speeds on the vibration response, transfer mobilities from the kandr model are shown in Figure 3.28 as the wave speed in each layer is varied separately while the other parameters remain the same. As the S-wave speed of the upper layer is increased the vibration responses decrease over most of the frequency range. The S-wave speeds in the upper layer mainly affect the vibration response above 20 Hz. They affect particularly the upward slope of the mobility and the peak at the cut-on frequency. Increasing the S-

wave speed of the middle layer reduces the response in much of the frequency region but increases it at the peak around 80-100 Hz. The S-wave speeds in the half-space have negligible effect on the response above 15 Hz.

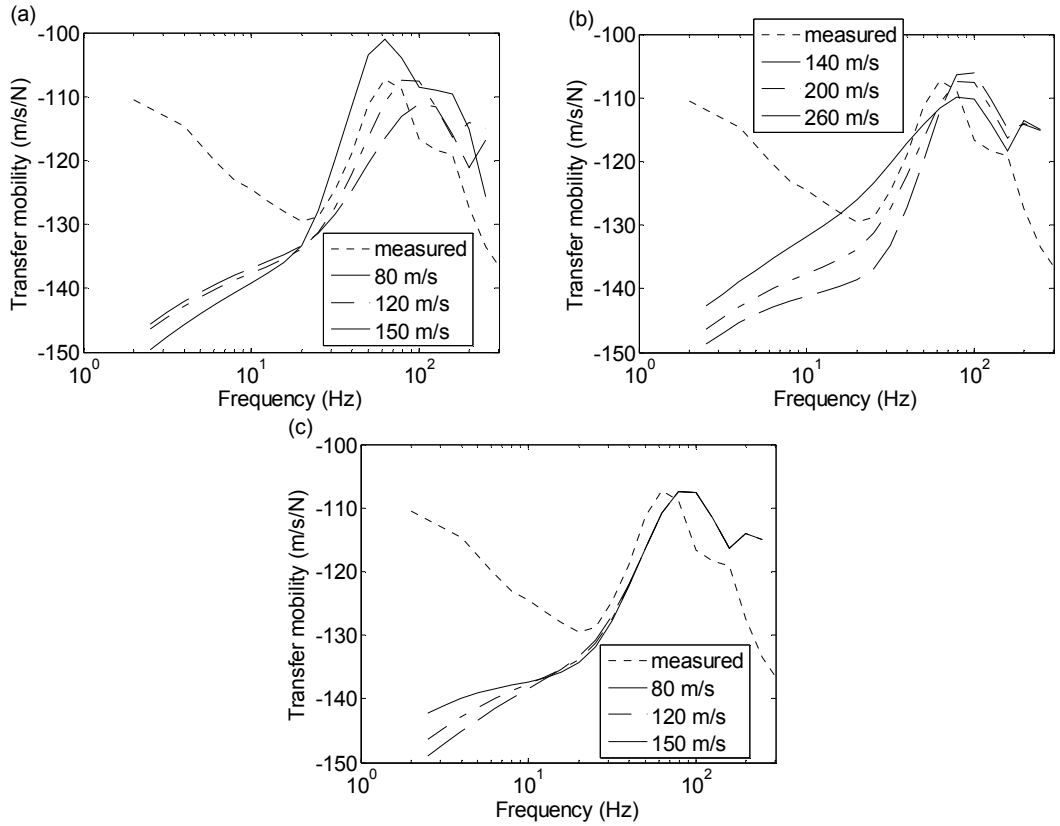

Figure 3.28. Effect of three different S-wave speeds on the vibration response presented as transfer mobilities, (a) in the upper layer, (b) the middle layer and (c) half-space of the ground model.

The results of varying the S-wave speeds on the dispersion diagrams are plotted in Figures 3.29 to 3.34. These can be compared with the results in Figure 3.22 for the best fit model.

Firstly the effects of changing the S-wave speed of the upper layer from 120 to 80 and 150 m/s are shown in Figures 3.29 and 3.30 respectively. The various wave speeds of the material are shown for reference. Changing the wave speed of the upper layer mainly affects the results above about 30 Hz, where the dominant wave tends towards the S-wave speed of this upper layer. For a wave speed of 80 m/s, the high frequency dominant wave appears as a continuation of the higher speed wave between 10 and 40 Hz (above 70 Hz these results are subject to aliasing). For a wave speed of

150 m/s it forms a continuation of the lower speed wave extending from low frequencies.

The peak in the mobility in Figure 3.28 corresponds to the region above 40 Hz with the largest response amplitude in the dispersion plots; this occurs close to the S-wave speed of the upper layer.

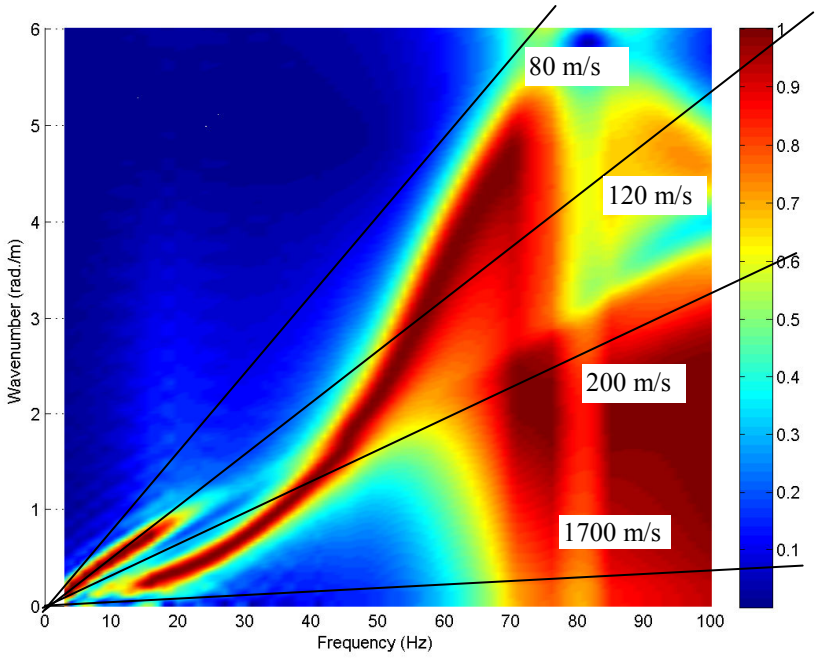

Figure 3.29. Effect of changing the S-wave speed on the upper layer presented as dispersion curve for 80 m/s, red indicates stronger presence of waves on the surface of the ground.

Secondly the effects of changing the S-wave speed of the middle layer from 200 to 140 or 260 m/s are shown in Figures 3.31 and 3.32 respectively. When the S-wave speed of the middle layer is reduced to 140 m/s, there is little difference between the wave speeds in the three layers. Consequently the dominant wave has an unbroken trend following the wave speed of the upper layer. The second wave, present from about 20 Hz, has a lower amplitude. When the middle layer has a higher wave speed of 260 m/s this second wave is dominant between 30 and 60 Hz and has a higher wave speed, greater than 260 m/s. From the dispersion plots and the mobilities, the middle layer wave speed affects the response mainly between 10 and 60 Hz.

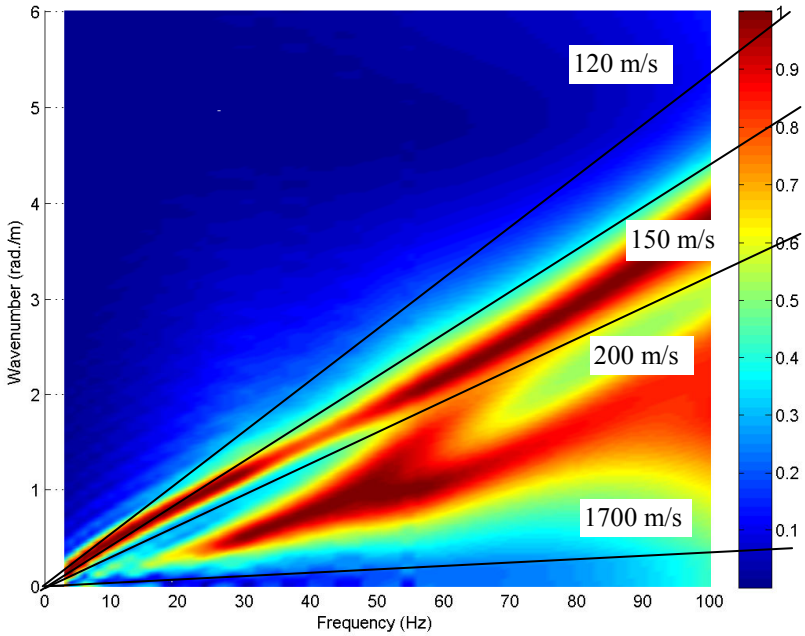

Figure 3.30. Effect of changing the S-wave speed on the upper layer presented as dispersion curve for 150 m/s, red indicates stronger presence of waves on the surface of the ground.

Thirdly the effects of changing the S-wave speed of the half-space from 120 to 80 or 150 m/s are shown in Figures 3.33 and 3.34 respectively. Changing the properties of the half-space only has an effect below 10 Hz, as also seen in the mobilities.

In Figures 3.29 to 3.34 it can be seen that no waves exist below the line corresponding to the P-wave speed (1700 m/s).

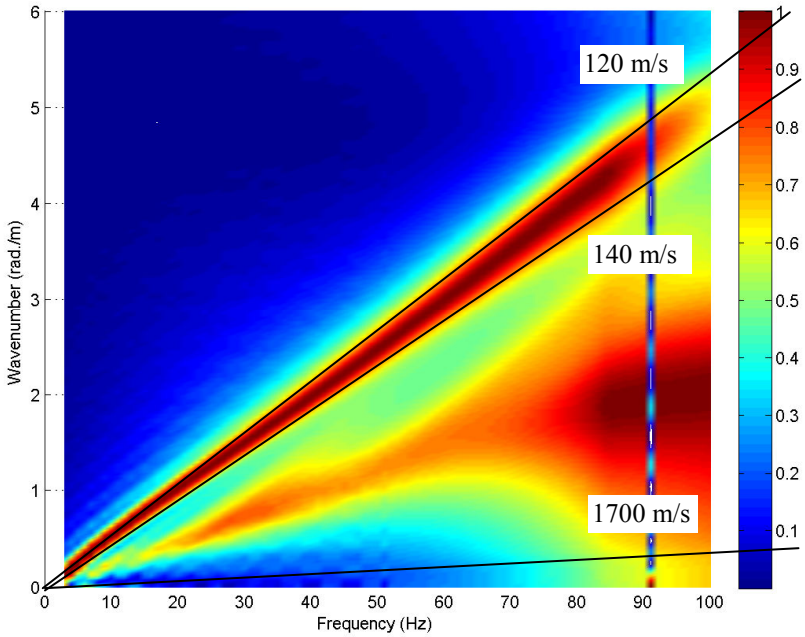

Figure 3.31. Effect of changing the S-wave speed on the middle layer presented as dispersion curve for 140 m/s, red indicates stronger presence of waves on the surface of the ground.

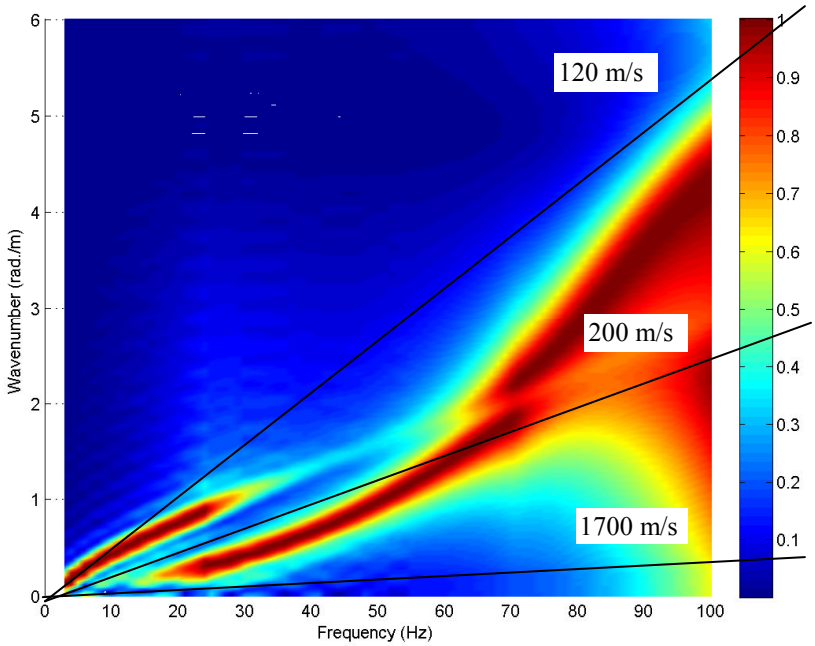

Figure 3.32. Effect of changing the S-wave speed on the middle layer presented as dispersion curve for 260 m/s, red indicates stronger presence of waves on the surface of the ground.

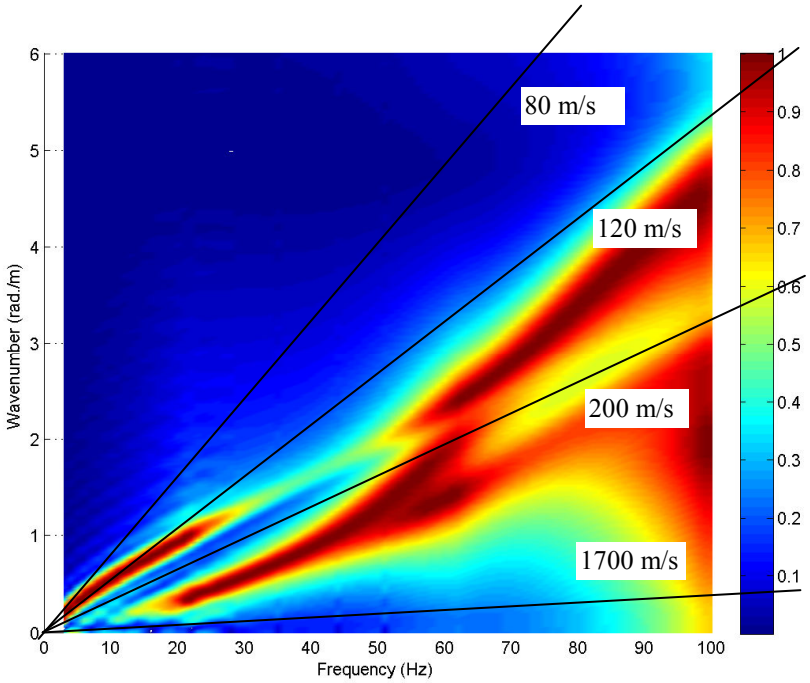

Figure 3.33. Effect of changing the S-wave speed on the half-space presented as dispersion curve for 80 m/s, red indicates stronger presence of waves on the surface of the ground.

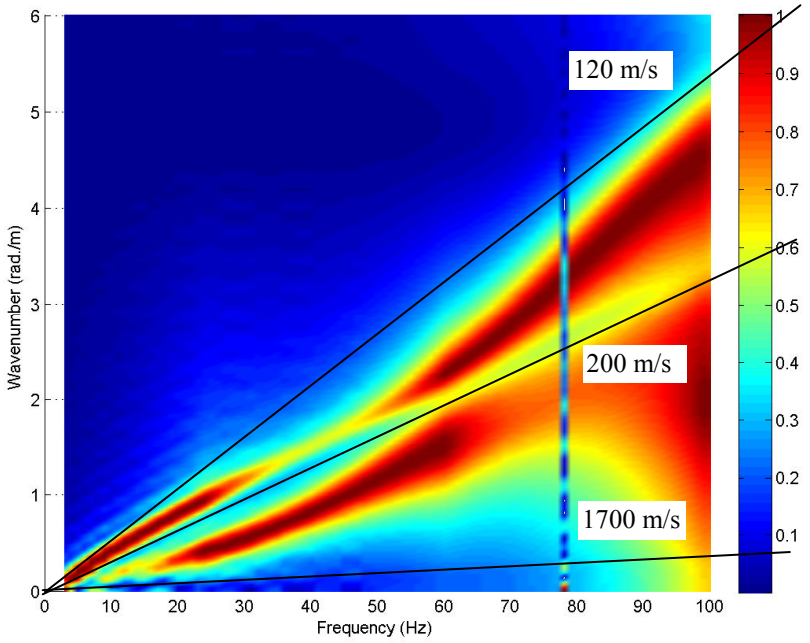

Figure 3.34. Effect of changing the S-wave speed on the half-space presented as dispersion curve for 150 m/s, red indicates stronger presence of waves on the surface of the ground.

3.5.2 Layer depth

Another important factor that strongly affects the vibration response is the depth of each layer. Three different layer depths have been investigated for each layer separately. The transfer mobilities on the ground surface for various layer depths are shown in Figure 3.35. These results show that the depth of the upper layer has the greatest effect. Although it has been changed only between 0.5 and 1.0 m, this gives a large difference in the response above 20 Hz. On the other hand, the depth of the middle layer gives differences only below 30 Hz. Above this frequency the vibration is localised in the upper and middle layers and the bottom of the middle layer has no effect. Replacing the underlying half-space by a layer of 7 m depth has negligible effect above 10 Hz.

The effect of changing the layer depths has also been investigated in terms of the dispersion curves, as shown in Figures 3.36 to 3.39. Firstly the effects of changing the depth of the upper layer from 0.7 to 0.5 or 1.0 m are shown in Figures 3.36 and 3.37 respectively. This mainly affects the cut-on frequency of the main wave. In the left figure the cut-on frequency is shifted from 55 to 75 Hz compared with Figure 3.22 whereas in the right figure it is reduced to 40 Hz. Hence with the shallow layer, the wave with speed greater than 200 m/s dominates over a wider frequency region while for a 1 m layer its influence is limited to about 50 Hz. Thus although a layer of 1 m appears to give better agreement in terms of mobilities, the layer of 0.7 m is preferred from the dispersion curves.

Secondly the effects of changing the depth of the middle layer from 2.0 to 1.0 or 3.0 m are shown in Figures 3.38 and 3.39 respectively. This has most effect on the frequency at which the slowest wave is no longer dominant – this is about 40 Hz for the shallow layer and 20 Hz for the thicker layer.

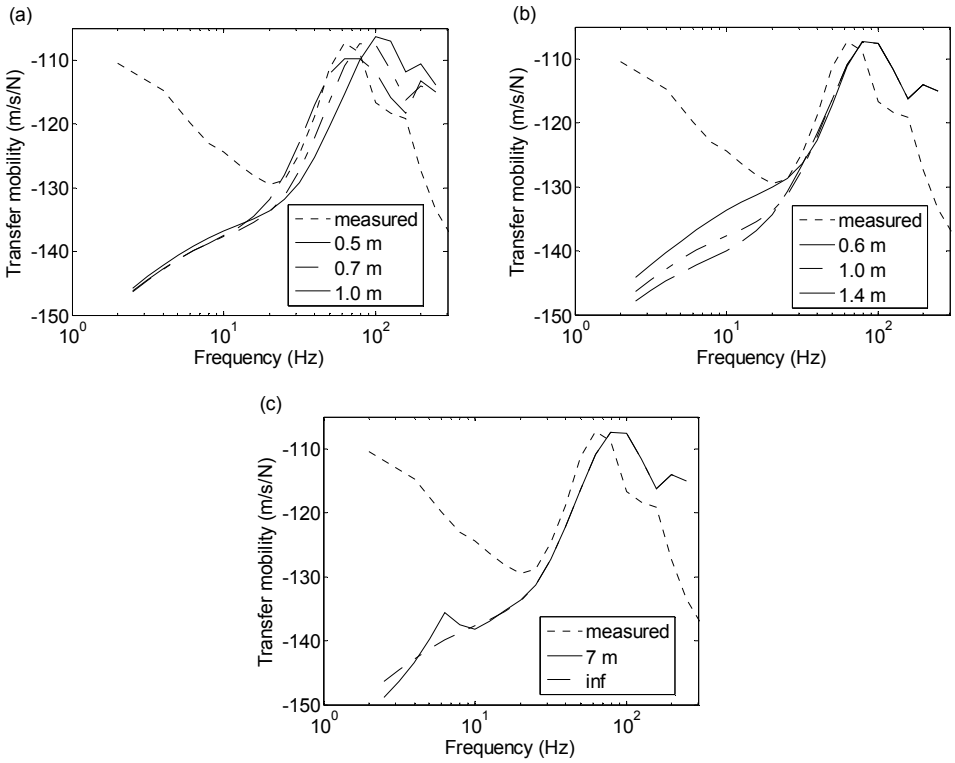

Figure 3.35. Effect of various layer depths on the vibration response presented as transfer mobilities, (a) in the upper layer, (b) the middle layer and (c) half-space of the ground model.

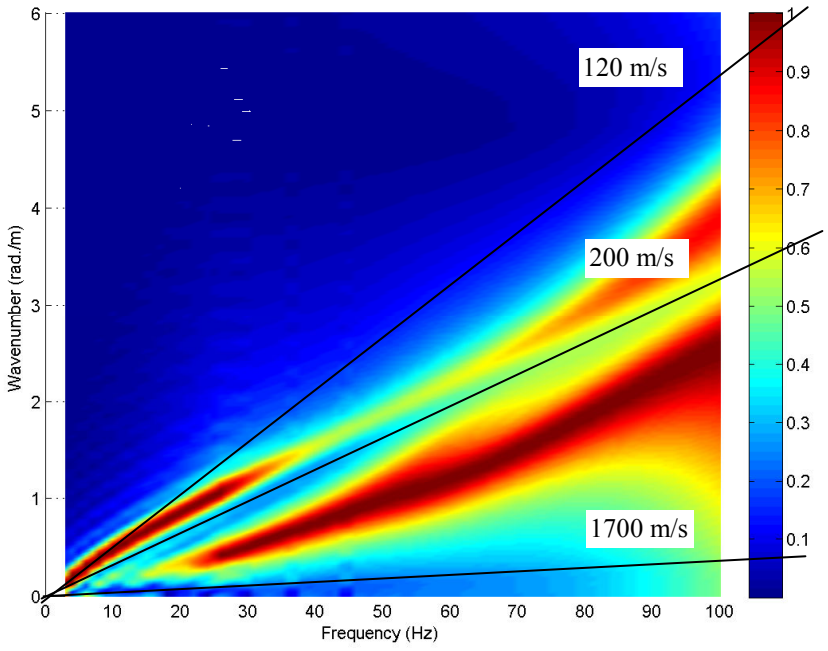

Figure 3.36. Effect of changing the layer depth on the upper layer presented as dispersion curve for 0.5 m, red indicates stronger presence of waves on the surface of the ground.

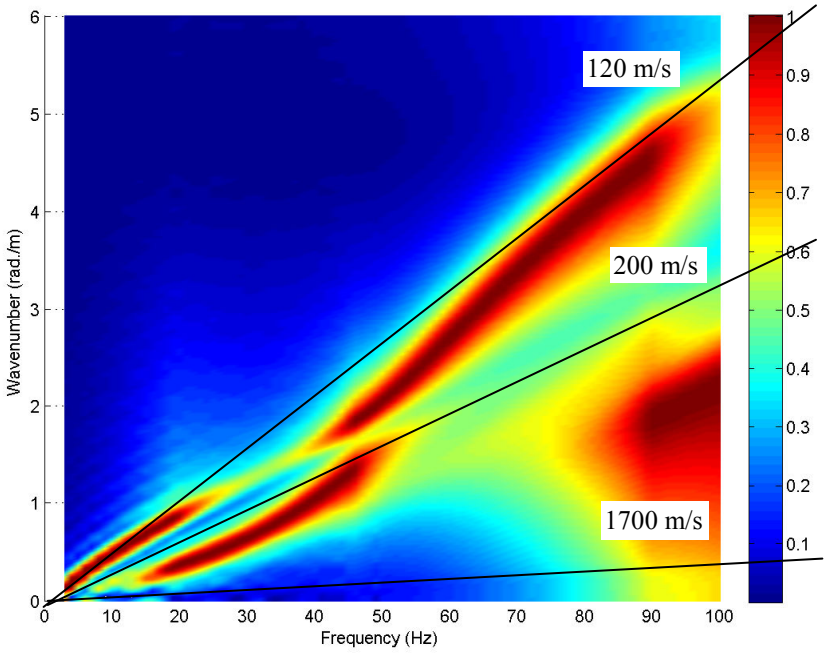

Figure 3.37. Effect of changing the layer depth on the upper layer presented as dispersion curve for 1.0 m, red indicates stronger presence of waves on the surface of the ground.

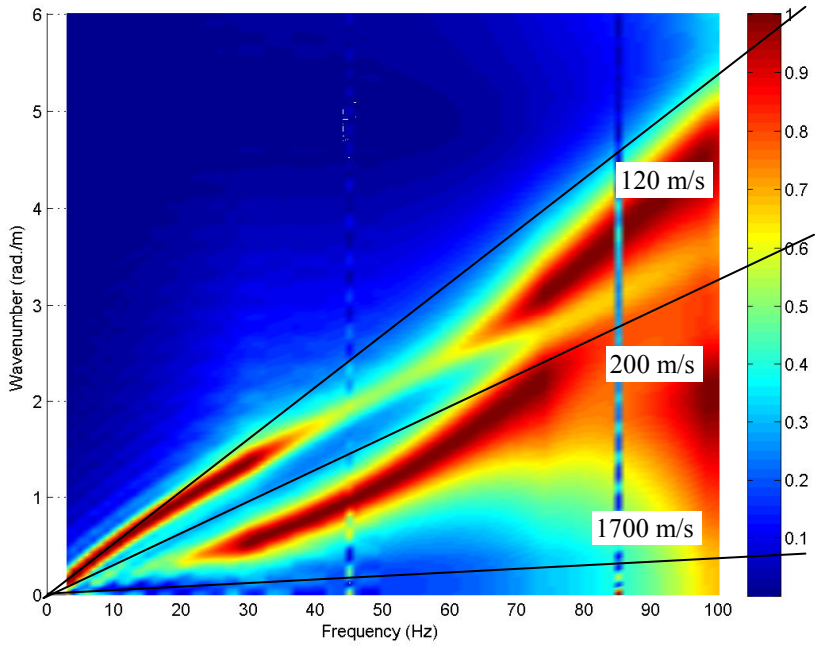

Figure 3.38. Effect of changing the layer depth on the middle layer presented as dispersion curve for 1.0 m, red indicates stronger presence of waves on the surface of the ground.

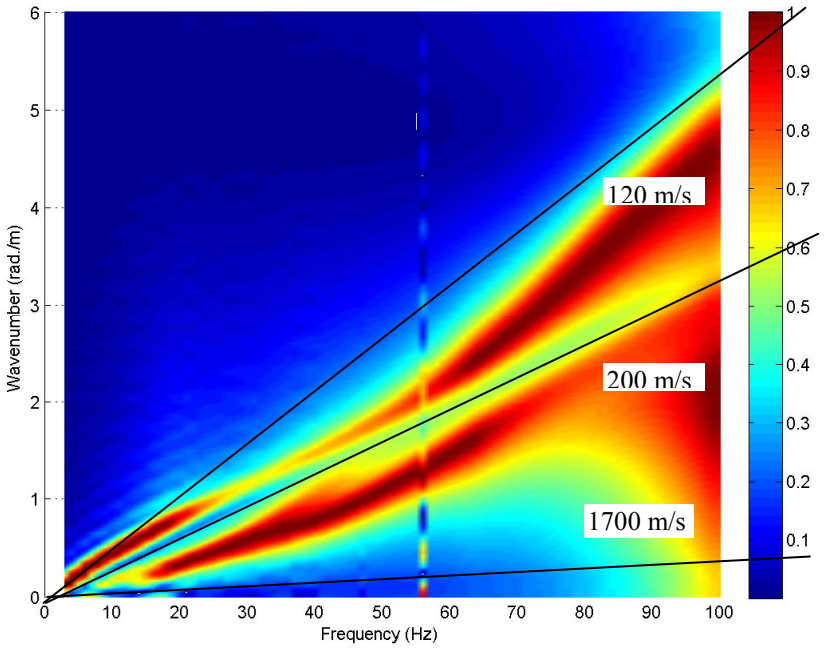

Figure 3.39. Effect of changing the layer depth on the middle layer presented as dispersion curve for 3.0 m, red indicates stronger presence of waves on the surface of the ground.

3.5.3 P-wave speeds

Figure 3.40 shows results for P-wave speeds set either to 1000 or 1700 m/s for each layer of the ground. This clearly has a negligible effect on the mobility at all distances.

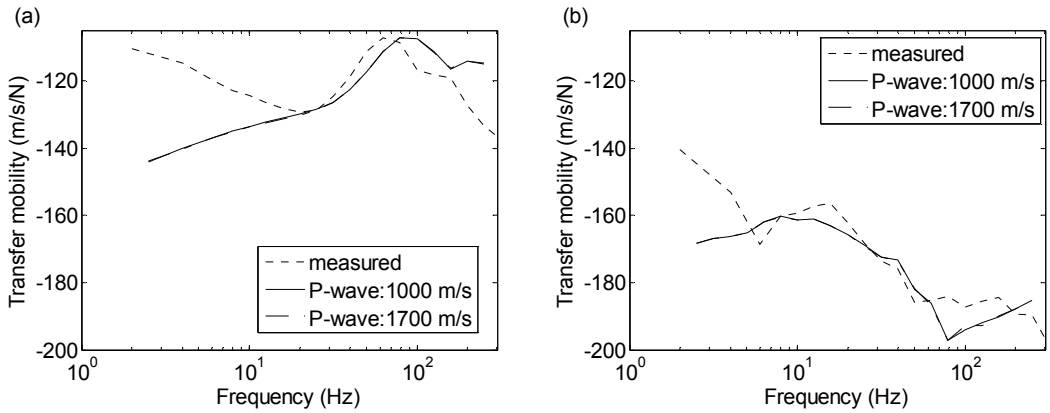

Figure 3.40 Comparison of different P-wave speed 1000 and 1700 m/s represented as transfer mobilities at (a) 1 and (b) 30 m away from the applied force.

3.6 Train measurements

Immediately following the measurements due to hammer excitation, the second experiment was carried out involving the measurement of ground vibration due to various passing trains at the two sites. In these experiments the vibration was measured at different distances away from the track, from the middle of the track out to 80 m at Steventon and to 74 m at Grazeley Green, as shown in Figure 3.41. Accelerometers were used to measure the vibration response at 8 positions simultaneously, using an analyser with 8 channels, as shown in Table 3.5. All the equipment used was the same as in the first measurement.

In order to calculate the speed of the trains, a digital video camera was used to record the time taken for the train to pass over the site. Three types of trains were measured on the Didcot to Swindon line at Steventon and two types of trains on the Basingstoke to Reading line at Grazeley Green. These are indicated, with the corresponding lengths, in Table 3.6. The speeds of the trains were calculated from their length and the time taken to pass the site and are shown in Table 3.6. In the present work, only passenger trains are considered as the lengths and composition of the freight trains were more difficult to determine.

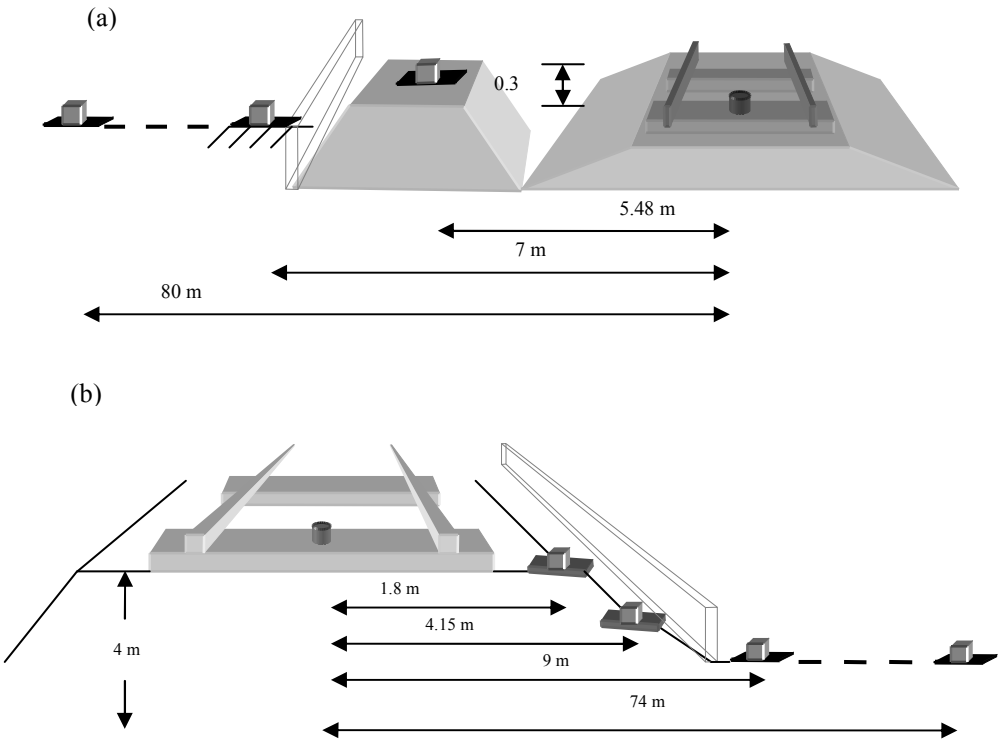

Figure 3.41. The position of accelerometers at (a) Steventon and (b) Grazeley Green for train pass-by measurements.

Table 3.5. The positions of each train measurement at Steventon and Grazeley Green sites.

Channel	Position			
	Steventon		Grazeley Green	
	Day 1	Day 2	Day 1	Day 2
1	7.5 m	0 m (middle of the sleeper)	9 m	0 m (middle of the sleeper)
2	10 m	5.48 m (top of the embankment)	12 m	1.8 m (top of the embankment)
3	15 m	7 m (fence)	15 m	4.15 m (middle of the embankment)
4	20 m	12 m	19 m	9 m
5	30 m	20 m	24 m	15 m
6	50 m	30 m	34 m	24 m
7	80 m	50 m	44 m	44 m
8	20 m (Line 2)	80 m	74 m	74 m

Table 3.6. The lengths, times taken and speeds for each type of trains passing by Steventon and Grazeley Green sites.

Location / Type of the train		Length (m) / car		Time taken (s)	Speed (km/hr)	Total number of trains
		Power cars	Coaches car			
Steventon	HST	17.79	22.86	6.16 - 3.95	127.7 – 199.1	47
	Class 66	(freight train)				9
Grazeley Green	Class 165	22.91	-	1.48 – 1.36	111.4 – 121.3	16
	Class 220/221	23.85	22.82	2.96 - 2.82	113.5 – 119.1	7
	Class 66	(freight train)				5

For each train measurement time-histories were recorded. The times taken were chosen properly to ensure all useful data were kept. Figure 3.42 (a) shows examples of acceleration time-histories for an HST on day 2 at Steventon. Similar results are shown in Figure 3.42 (b) for a train of class 220 on day 2 at Grazeley Green.

The acceleration time-histories were acquired at a sample rate of 1 kHz for 32.7 seconds. The data were converted to power spectra using a Fourier transform. A single FFT was used with no averaging. Then the vibration responses were converted from narrow band spectra to 1/3 octave bands for ease of interpretation. In accordance

with the International Standard EN ISO 3095:2005, the data were normalised by the pass-by time, T_P [103] to give transit exposure levels (TEL). The same sets of data corresponding to Figure 3.42 (a) and (b) are plotted as velocity response levels in Figures 3.43 and 3.44 for the two sites. The results show both the responses and the background vibration signals at each point. The first figures show only the response on the sleeper with its background vibration signals.

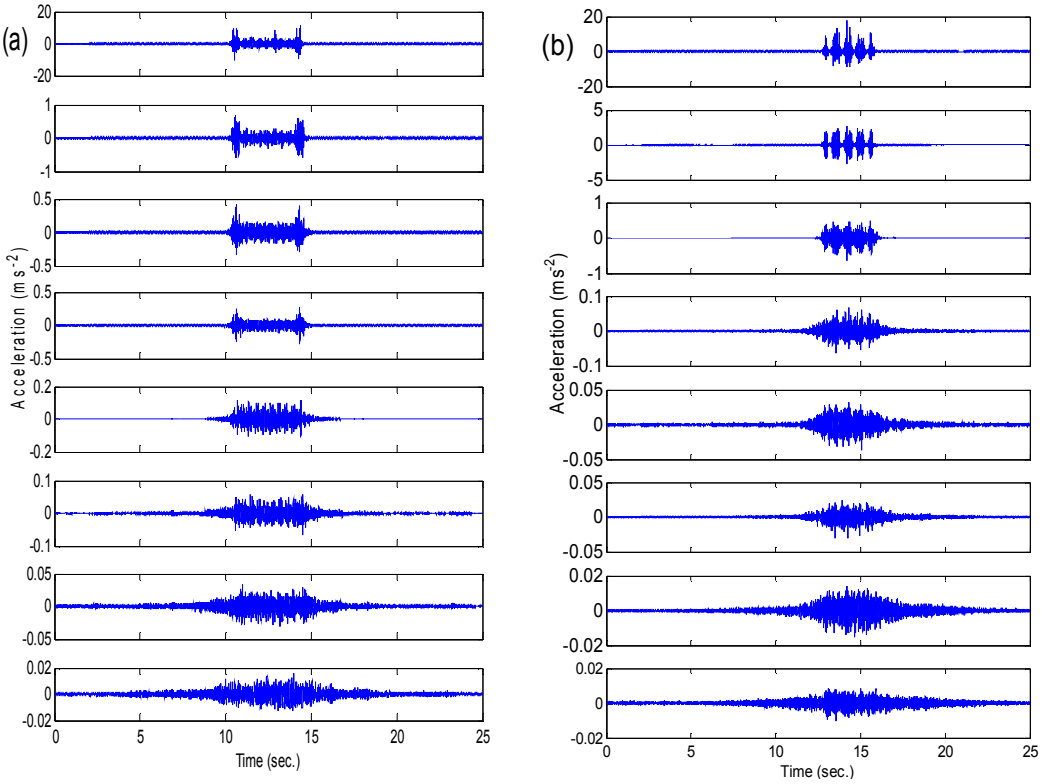

Figure 3.42. Acceleration time-histories in 8 channels for (a) an HST on day 2 at Steventon and (b) the train class 220 on day 2 at Grazeley Green.

Apart from the closest distances, the measured data can be seen to be affected by background noise below 3 Hz for Steventon and below 6 Hz for Grazeley Green. However at frequencies above 100 Hz the background might affect the response at 15 m and further away. At 44 and 74 m for Grazeley Green and 80 m for Steventon, the data are affected by background noise above 30 Hz. For the main frequency range considered in this thesis of up to 100 Hz, the results used to investigate the effect of changes in parameters would not be affected by background noise.

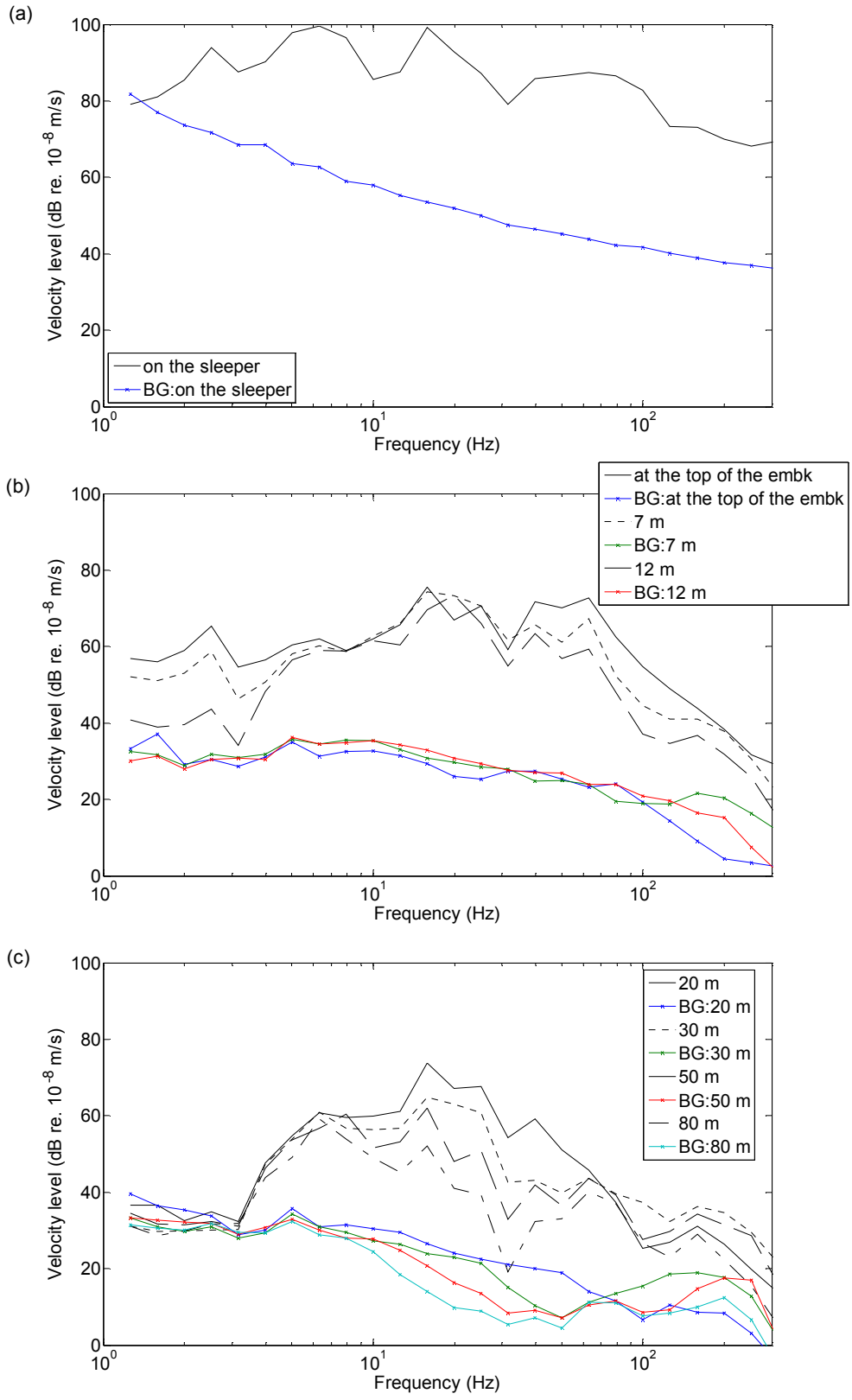

Figure 3.43. Velocity level of the response from train passing by at various positions, corresponding with Figure 3.42 for Steventon at various positions perpendicular to the track (BG = background level).

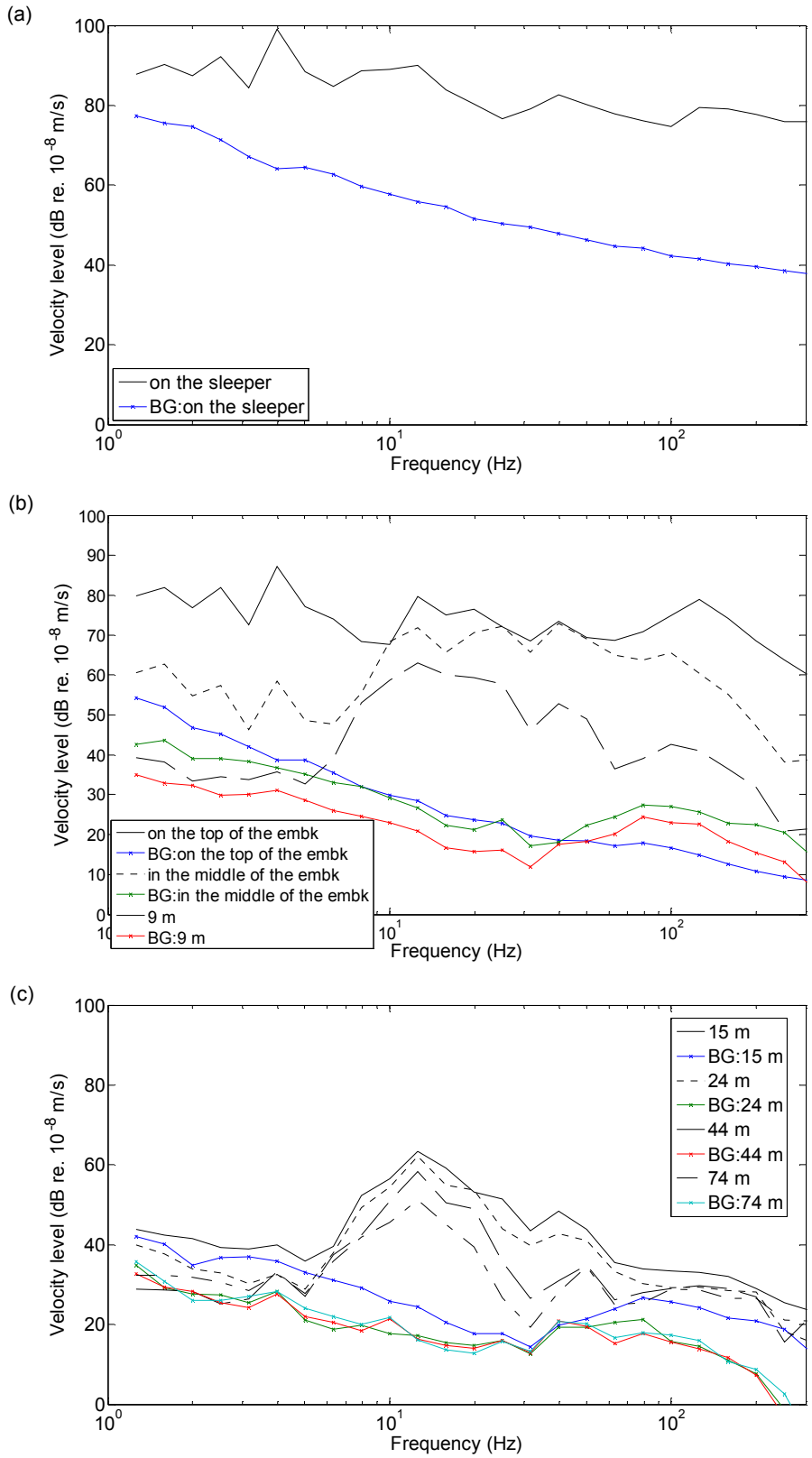

Figure 3.44. Velocity level of the response from train passing by at various positions, corresponding with Figure 3.42 for Grazeley Green at various positions perpendicular to the track (BG = background level).

3.6.1 TGV model

To predict the ground vibrations induced from surface trains, a semi-analytical model, Train-induced Ground Vibration (TGV) developed by Sheng [12], has been used. This is described further in Appendix B. The vehicles can be described as multiple rigid body systems. The track is represented as an infinite, layered beam resting on one or more elastic layers overlying a three-dimensional half-space of ground material. This model uses the quasi-static loads and the vertical irregular profile of the rails as the sources of excitation. The output is given in the form of displacement power spectra of the track and the ground. Sheng implemented this TGV model as a FORTRAN program and Jones has recently modified this program including the summation of the results from TGV by using a MATLAB program named 'passby_post.m' [104]. This program calculates the summations of the vertical displacement power spectrum generated by the quasi-static loads and the track irregularity [104].

3.6.2 Train and track parameters

Details of power cars and trailer coaches for an HST and diesel multiple units, DMU, are listed in Table 3.7 [12]. These parameters are used in the model TGV [34] with the soil properties from Table 3.4 in order to predict the ground vibrations induced from trains at both sites. The parameters of the track systems used in the model are typical values as shown in Table 3.8. This was necessary as it was not possible to gain access onto the track. A low embankment of height 0.75 m is included in the model for Steventon; for Grazeley Green a higher embankment is present and this is assigned a height of 3.5 m.

The roughness was obtained from measurements at both sites, as shown in Figures 3.45 and 3.46. These comprise rail head roughness obtained using the CAT system [105] at short wavelengths (< 3 m) and track recording coach measurements at long wavelengths (> 3 m). The latter are "loaded" profiles of the track. Note that the wheel of the track recording coach will follow the loaded profile for frequencies up to about 60 Hz, see equation (D.10). Compared with other measurements of rail roughness in the literature, these rails are relatively smooth.

Table 3.7. Parameters for vehicles, [12].

Parameters / Types of Vehicle	Steventon		Grazeley Green
	Power car (HST)	Mk3 Passenger Coach (UK) (4 axles)	DMU Class 220
Body mass (kg)	45000	21400	37200
Body pitch inertia (kg-m^2)	7.95 $x10^5$	8.3$x10^5$	12$x10^5$ *
Bogie sprung mass (kg)	8100	2707	1900
Bogie pitch inertia (kg-m^2)	8800	1970	1000 *
Secondary vertical stiffness per bogie (N/m)	2.12 $x10^6$	0.81$x10^6$	0.81$x10^6$ *
Secondary vertical damping per bogie (Ns/m)	80000	74000	74000 *
Secondary damper stiffness per bogie (N/m)	-	-	-
Primary vertical stiffness per axle (N/m)	3.7 $x10^6$	0.359 $x10^6$	0.359 $x10^6$ *
Primary vertical damping per axle (Ns/m)	60000	8400	8400 *
Primary damper stiffness per axle (N/m)	3.5 $x10^6$	14 $x10^6$	14 $x10^6$ *
Bogie centres (m)	10.3	16	16.2
Bogie wheelbase (m)	2.6	2.6	2.25
Wheelset mass (kg)	2175	1375	1350
Wheel diameter (m)	-	0.914	0.78
Vehicle length (m)	17.792	23	23.85 (front and rear), 22.82
Total mass (kg)	70000	32300	46400

Note: symbol * indicates an estimated parameter.

Table 3.8. Parameters for a ballasted railway track (two rails).

Parameters		Unit	
		Steventon	Grazeley Green
Rails	Mass per unit track length	120 kg/m	
	Bending stiffness	1.26×10^7 Nm^2	
	Loss factor	0.01	
Rail pads	Rail pad stiffness per unit track length	3.5×10^8 N/m^2	
	Loss factor	0.15	
Sleeper	Mass per unit length	490 kg/m	
Ballast	Ballast stiffness	3.15×10^8 N/m^2	
	Loss factor	0.2	
	Mass per unit length	1200 kg/m	
Contact width	Half-width of load on the ground	2.0 m	
Embankment	Density	1800 kg/m^3	
	Young's modulus	2×10^7 N/m^2	
	Loss factor	0.05	
	Half width at the top	1.35 m	5 m
	Height	0.75 m	3.5 m

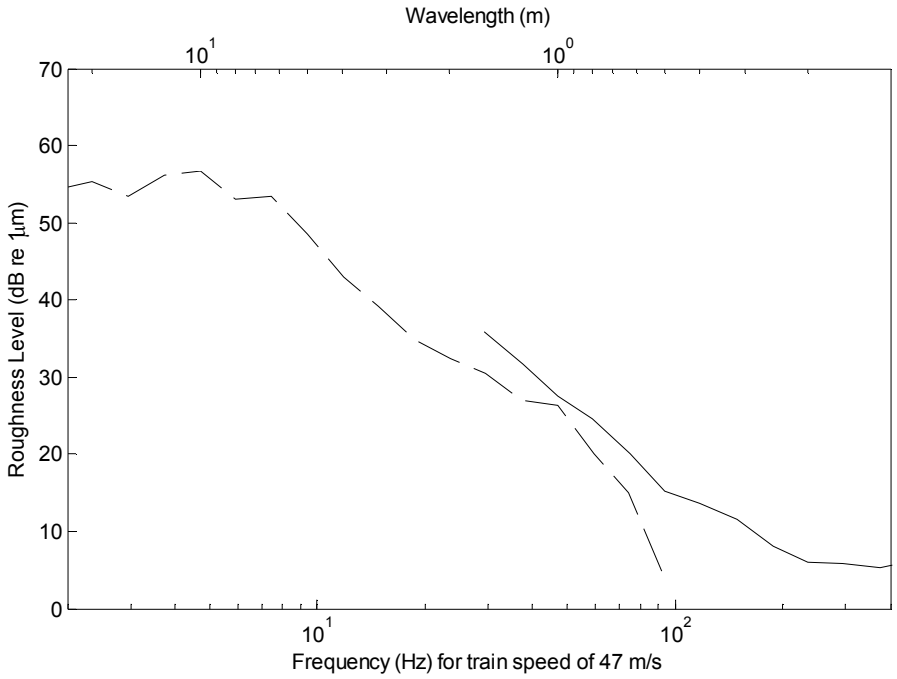

Figure 3.45. The roughness obtained from the measurements at Steventon site.

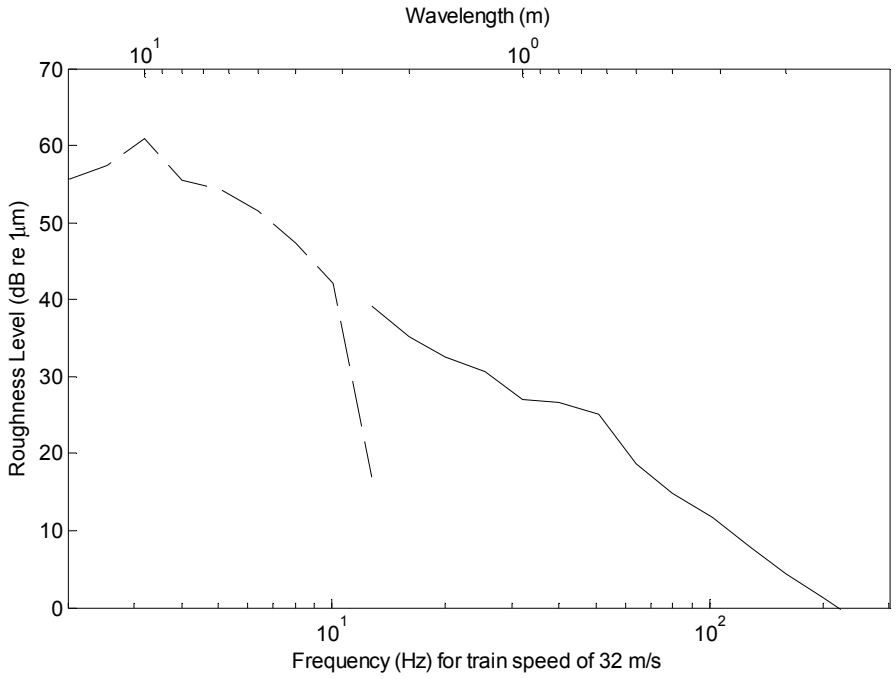

Figure 3.46. The roughness obtained from the measurements at Grazeley Green site.

3.6.3 Results

Initially the parameters of the ground from Table 3.4 were used in the TGV model for comparison with the measurements at both sites. The results from the train measurements at various distances away from the source shown in Figures 3.43 and 3.44, are compared with the predictions using this model as shown in Figures 3.47 and 3.48 for Steventon and Grazeley Green respectively[4]. The predicted results can only be obtained up to 100 Hz due to numerical problems. The predicted results are converted from narrow band to one-third octave band. The highest frequency band predicted using TGV is then 80 Hz.

The velocity level of the responses from the train measurements at Steventon and the model are compared only at the positions 0, 7, 12, 20, 30 m. At further distances the background noise affects the response as described above. The measured

[4] In Figures 3.47 to 3.50 the predicted results have been increased by 3 dB. Later in Chapter 5 it was found that the results from TGV have to be increased by 3 dB to achieve the agreement. This was believed to be an error in the program passby-post.m.

data at 0 m is on the sleeper whereas the predicted data is at the ground below. The same procedure is also used for Grazeley Green at the positions 0, 9, 15 and 24 m.

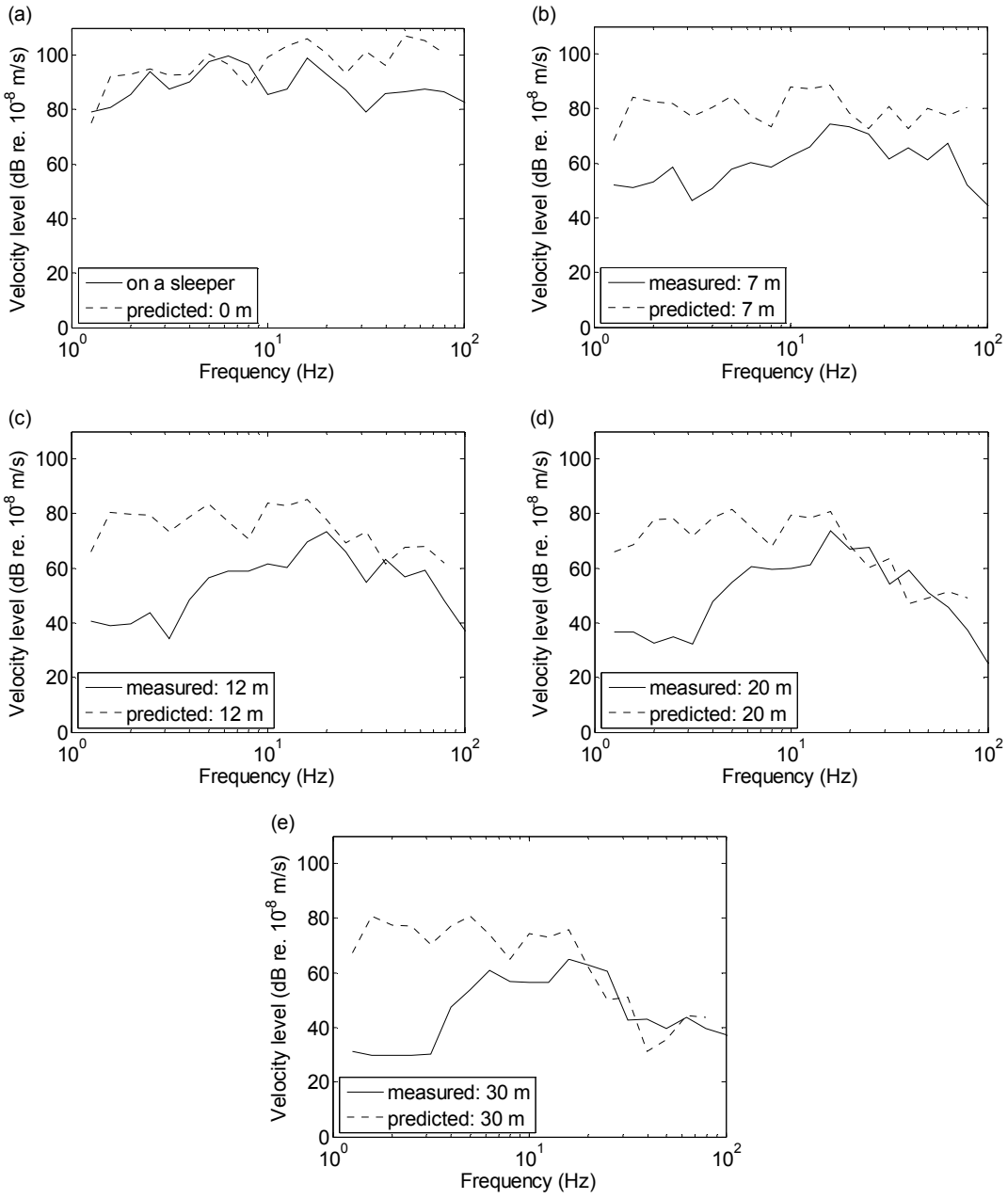

Figure 3.47. Comparison of the velocity level of the responses on the ground surface between the measurements and the results from TGV model, at distances (a) 0, (b) 7, (c) 12, (d) 20 and (e) 30 m away from the source for the Steventon.

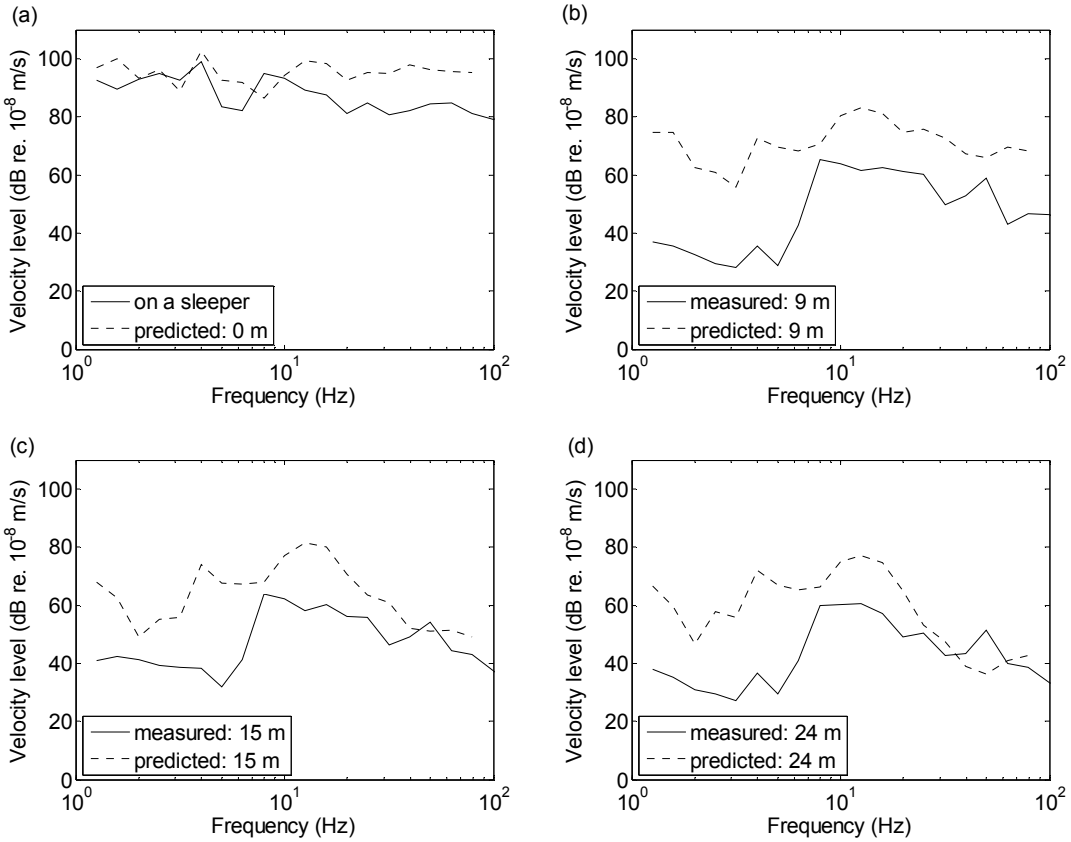

Figure 3.48. Comparison of the velocity level of the responses on the ground surface between the measurements and the results from TGV model, at distances (a) 0, (b) 9, (c) 15 and (d) 24 m away from the source for the Grazeley Green.

From the results, it can be seen that the amplitude level of the response from the TGV model is higher than those from the measurements at all positions especially in low frequency range below 10 Hz. It is clear that the agreement with the model is poor in this low frequency region. At these low frequencies the hammer measurements gave unreliable results so the model developed in Section 3.4 is only reliable above 10 Hz. Consequently the parameters have been modified in an attempt to get a better fit at low frequencies. The upper two layers are retained but the lower layer is modified as this controls the low frequency behaviour.

3.6.4 Modified model

The parameters for the ground have been changed since the results in Figures 3.47 and 3.48 gave a poor agreement at low frequencies. The depth of the lower layer affects the response at low frequency. The depth of third layer of the soft material has been changed to 3.0 m below which a stiffer half-space is introduced. The parameters

of the modified model are shown in Table 3.9. The other parameters remain the same. The responses at various distances on the ground surface are shown in Figures 3.49 and 3.50 for Steventon and Grazeley Green respectively. Besides, comparison of transfer mobilities on the surface of the ground obtained using the kandr model and the measurements, shows that these remain in good agreement as well as the response represented in wavenumber domain as shown in Figures 3.51 to 3.54.

Table 3.9. Parameters of the ground properties after modification.

Parameters		Steventon site	Grazeley Green
first layer	P-wave speed	1700 m/s	1700 m/s
	S-wave speed	120 m/s	130 m/s
	density of layer material	2000 kg m^{-3}	2000 kg m^{-3}
	Layer depth	0.7 m	1.4 m
second layer	P-wave speed	1700 m/s	1700 m/s
	S-wave speed	200 m/s	200 m/s
	density of layer material	2000 kg m^{-3}	2000 kg m^{-3}
	Layer depth	2.0 m	0.7 m
third layer	P-wave speed	1700 m/s	1700 m/s
	S-wave speed	120 m/s	120 m/s
	density of layer material	2000 kg m^{-3}	2000 kg m^{-3}
	Layer depth	3.0 m	3.5 m
half-space	P-wave speed	1700 m/s	1700 m/s
	S-wave speed	400 m/s	700 m/s
	density of layer material	2000 kg m^{-3}	2000 kg m^{-3}
	Layer depth	infinite	infinite

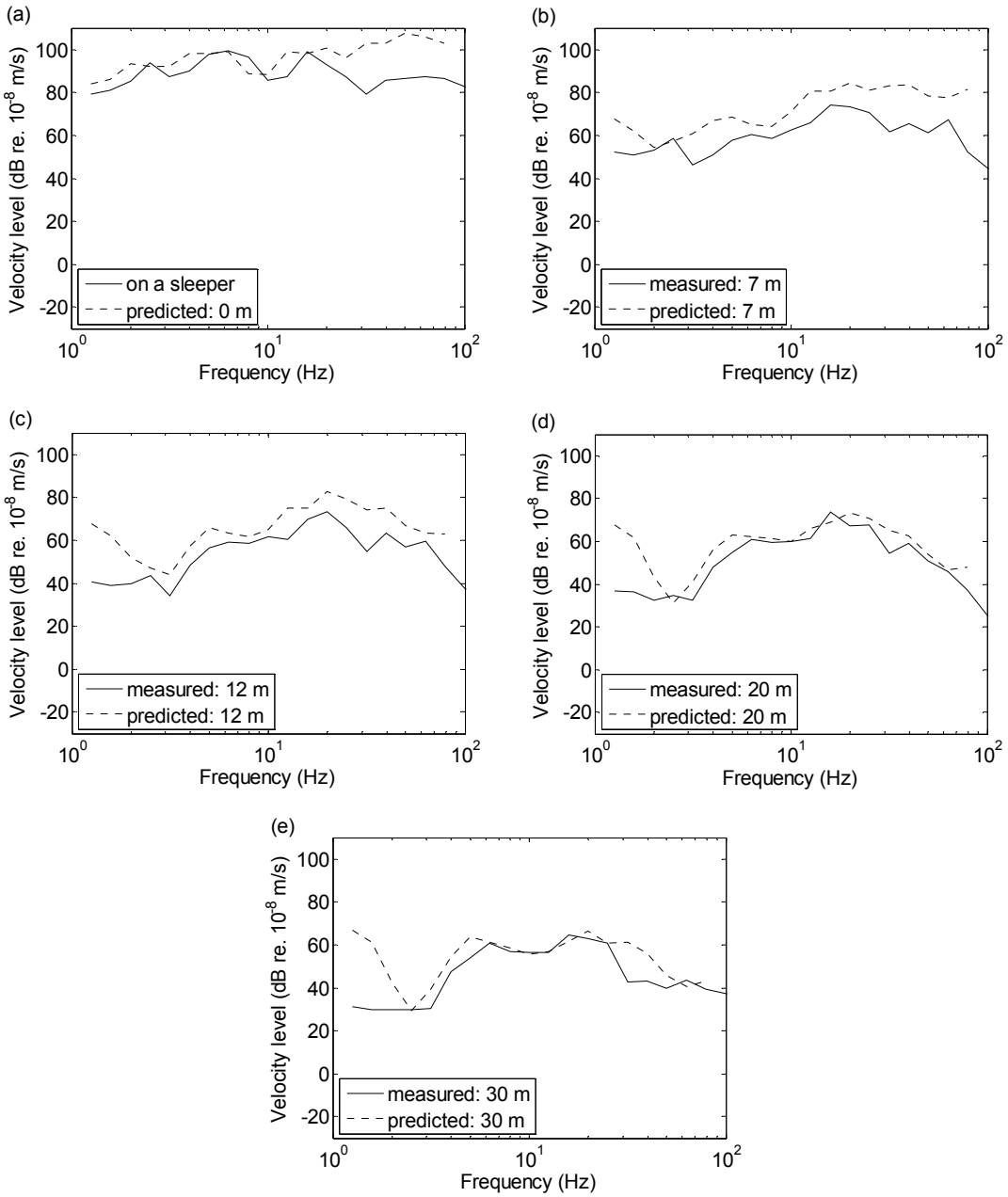

Figure 3.49. Comparison of the velocity level of the responses on the ground surface between the measurements and the results from TGV model (after modification), at distances (a) 0, (b) 7, (c) 12, (d) 20 and (e) 30 m away from the source for the Steventon.

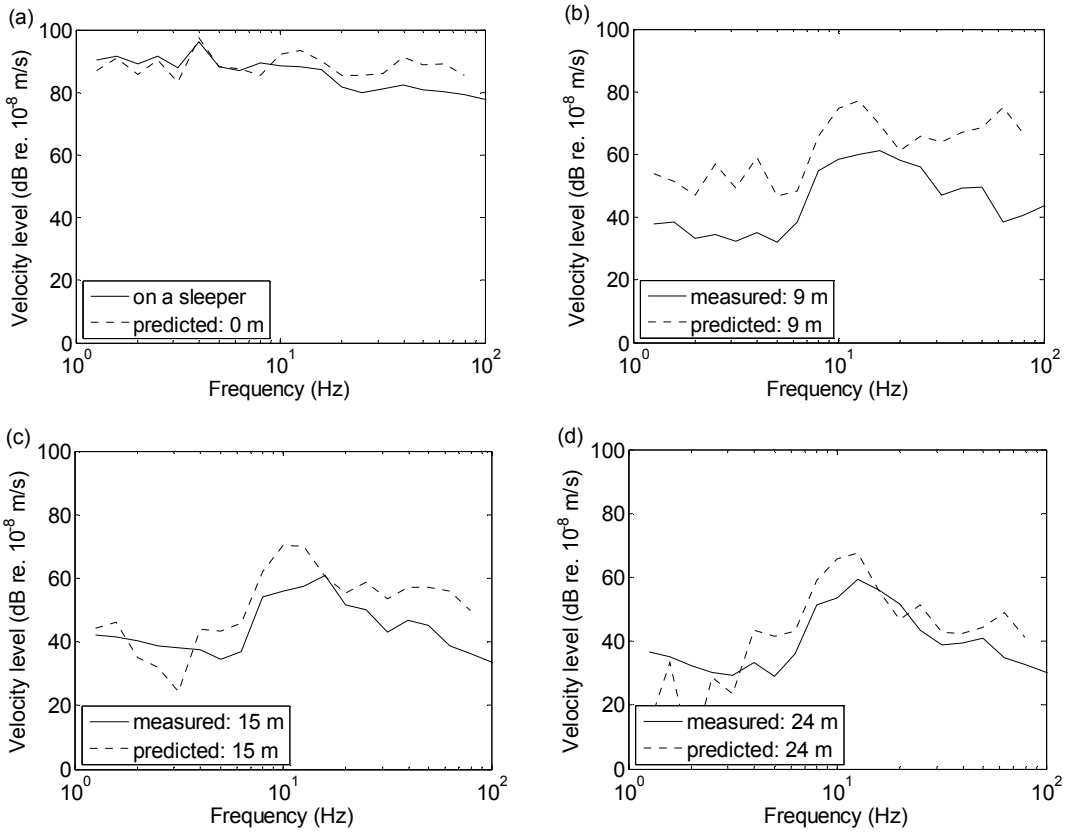

Figure 3.50. Comparison of the velocity level of the responses on the ground surface between the measurements and the results from TGV model (after modification), at distances (a) 0, (b) 9, (c) 15 and (d) 24 m away from the source for the Grazeley Green.

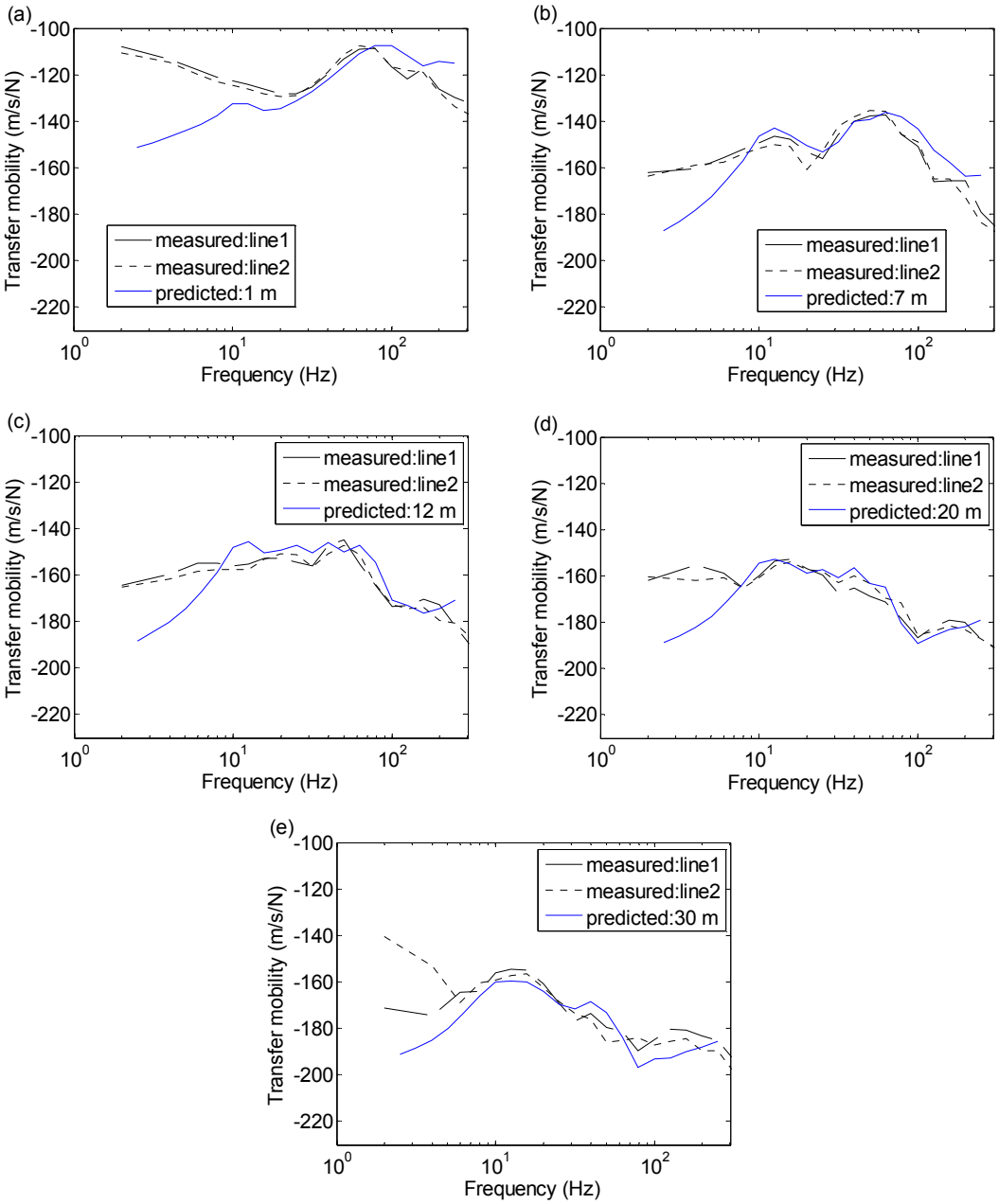

Figure 3.51. Comparison of transfer mobilities on the surface of the ground obtained using the kandr model with parameters of the ground properties from Table 3.9 and the measurements, at (a) 1, (b) 7, (c) 12, (d) 20 and (e) 30 m away from applied force for Steventon.

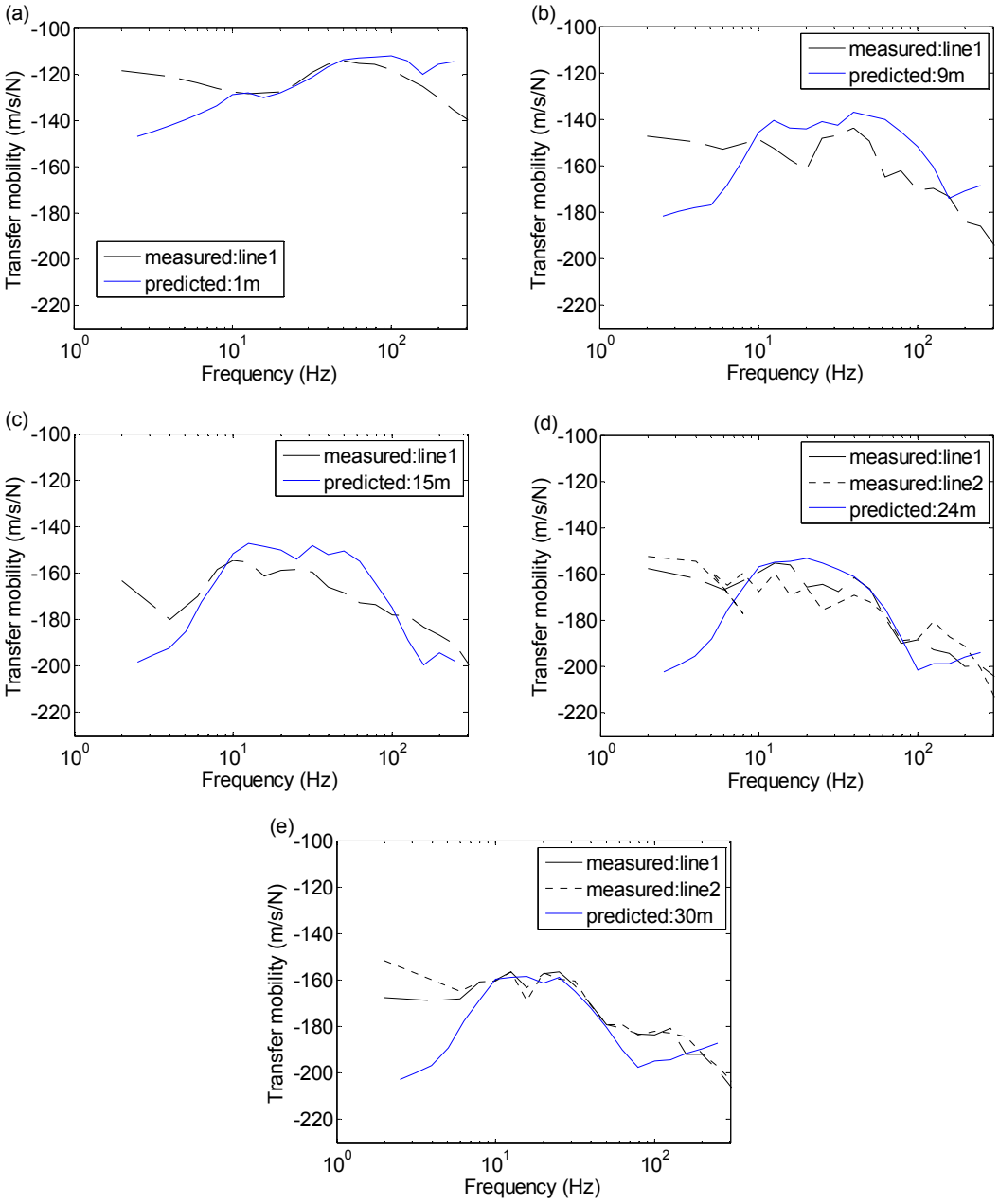

Figure 3.52. Comparison of transfer mobilities on the surface of the ground obtained using the kandr model with parameters of the ground properties from Table 3.9 and the measurements, at (a) 1, (b) 9, (c) 15, (d) 24 and (e) 30m away from applied force for Grazeley Green.

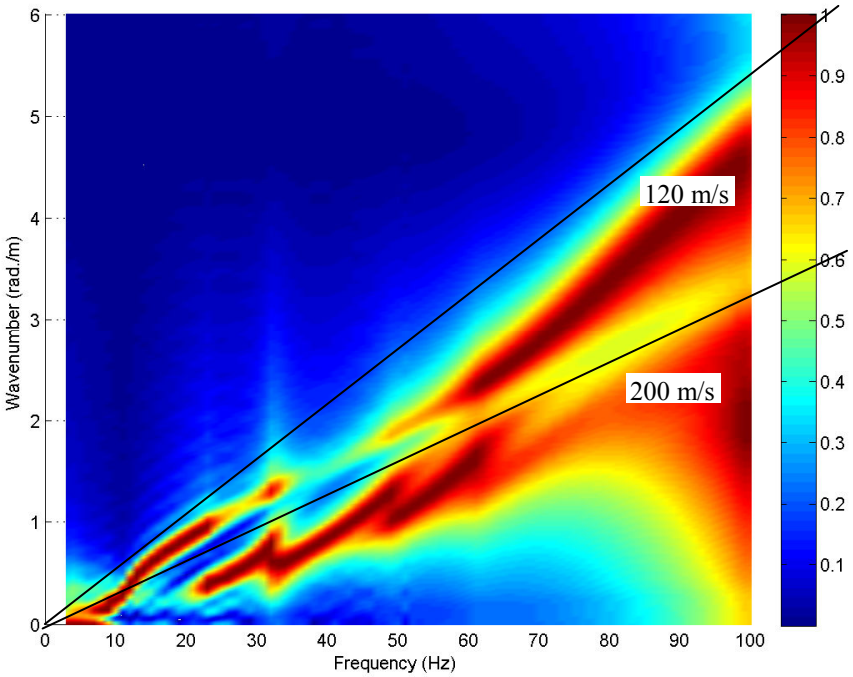

Figure 3.53. Dispersion curves of the propagating wave number from kandr model for the Steventon, using parameters of the ground properties from Table 3.9.

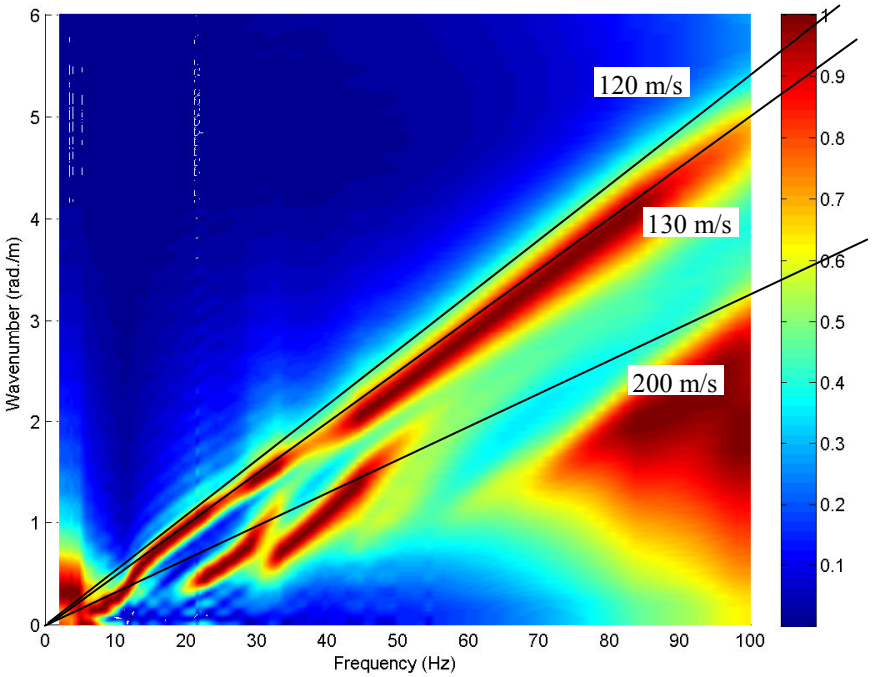

Figure 3.54. Dispersion curves of the propagating wave number from kandr model for the Grazeley Green, using parameters of the ground properties from Table 3.9.

3.7 Conclusions

Measurements using hammer excitation have been performed at two sites with clay soil in order to determine ground parameters for use in the model. The ground at both sites can be modelled using three layers overlying a stiffer half-space of material. It is found that the second layer is stiffer than the first and third layers at both sites. This feature causes the response to have a gap in the dispersion diagram for the slowest wave. The upper layer influences the response above about 30 Hz. The third layer and the half-space have an effect on the response at low frequencies. The depth of the third layer is important for the response below 10 Hz. This could not be seen in the hammer measurements but could be observed in the train measurements.

Good agreement is found between predictions using the TGV model and measurements of vibration from passing trains. Therefore this model can be used to investigate the relative importance of quasi-static load and dynamic load for different situations in the next chapter.

4. Investigation of track/train parameters

4.1 Introduction

After a good agreement was found for the validation of the TGV model in Chapter 3, it is now used for an investigation of the effect of changes in track/train parameters. The purpose of this chapter is to study the effects of different parameters on the ground vibration for a wide range of conditions at locations close to the track and further away. The relative importance of the moving quasi-static loads and the dynamic loads due to track and wheel roughness is also investigated. Whereas the dynamic loads induce propagating waves on the surface of the ground at distances up to as much as 100 m from the track, the moving quasi-static loads produce large displacements under the track which, for train speeds lower than the wave speeds in the ground, do not propagate into the far field. Nevertheless, this could still be considered as an important factor in the vibration for sensitive properties close to the track. The effects of changes in various track/train parameters are estimated for locations close to the track and further away in terms of an insertion gain in order to see the effect of the quasi-static and dynamic loads on the ground vibration.

The TGV model used in this chapter is described in Appendix B and has been validated against measurements at Steventon and Grazeley Green in Chapter 3. Train motion is included in the model, allowing the prediction of vibration due to both dynamic and quasi-static loads. The vertical dynamic behaviour of the train is modelled using a multi-body system with both primary and secondary suspensions. The support system underneath the track is also included, as well as a representation of an embankment. For simplicity, the ground model throughout this chapter consists of a single weathered layer overlying a stiffer half-space. For the vehicle the initial parameters represent a generic electric multiple unit (EMU).

4.2 Simplified train and track models

The dynamic excitation can be understood in terms of the mobilities of the vehicle and track [3]. Before considering results from the TGV model, simpler models are used to determine the vehicle and track mobilities. To understand the effect of changing track/ground parameters, the system representing the vehicle is considered

as a simplified three degree of freedom model, as shown in Figure 4.1. The lowest mass m_1 represents the mass of one wheelset, the middle mass m_2 represents half a bogie and the upper mass m_3 represents a quarter of the body mass. The external force (due to interaction with the track) acts on mass m_1. Stiffnesses k_2 and k_3 represent primary and secondary suspensions respectively with associated damping coefficients c_2 and c_3. This model therefore gives an approximation to the mobility at a single wheelset. Pitching motion is ignored, which when included would make the mobilities different at the four wheelsets.

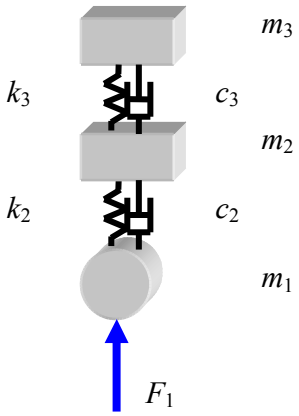

Figure 4.1. A simplified train model for calculating the point mobility.

For harmonic motion at frequency ω, the equation of motion can be written in matrix form as

$$\left(-\omega^2\mathbf{m}+i\omega\mathbf{c}+\mathbf{k}\right)\mathbf{x}=\mathbf{F} \tag{4.1}$$

where the mass, damping and stiffness matrices are given by

$$\mathbf{m}=\begin{bmatrix} m_1 & 0 & 0 \\ 0 & m_2 & 0 \\ 0 & 0 & m_3 \end{bmatrix} \tag{4.2}$$

$$\mathbf{c}=\begin{bmatrix} c_2 & -c_2 & 0 \\ -c_2 & c_2+c_3 & -c_3 \\ 0 & -c_3 & c_3 \end{bmatrix} \tag{4.3}$$

$$\mathbf{k}=\begin{bmatrix} k_2 & -k_2 & 0 \\ -k_2 & k_2+k_3 & -k_3 \\ 0 & -k_3 & k_3 \end{bmatrix} \tag{4.4}$$

and the displacement and force vectors are given by

$$\mathbf{x} = \begin{Bmatrix} x_1 \\ x_2 \\ x_3 \end{Bmatrix} \tag{4.5}$$

$$\mathbf{F} = \begin{Bmatrix} F_1 \\ 0 \\ 0 \end{Bmatrix} \tag{4.6}$$

The equation can be inverted to give

$$\mathbf{x} = \left(-\omega^2 \mathbf{m} + i\omega \mathbf{c} + \mathbf{k}\right)^{-1} \mathbf{F} \tag{4.7}$$

The point mobility can be expressed as

$$Y = \frac{i\omega x_1}{F_1} \tag{4.8}$$

The mobility of the vehicle calculated using this model with the vehicle parameters listed in Table 4.1 is shown in Figure 4.2(a). (Some of these parameters are not used here but are included later in the vehicle model in TGV). The mobility can be seen to be mass-controlled at low and high frequency with two well-damped resonances occurring at about 1.6 and 7.5 Hz. The peak at around 1.6 Hz corresponds to a resonance of the bogie mass and secondary suspension:

$$f_1 = \frac{1}{2\pi}\sqrt{k_3\left(\left(\frac{1}{m_3}\right)+\left(\frac{1}{m_1+m_2}\right)\right)} = 1.57 \text{ Hz} \tag{4.9}$$

The second resonance at about 7.5 Hz corresponds to the unsprung mass and primary suspension:

$$f_2 = \frac{1}{2\pi}\sqrt{k_2\left(\left(\frac{1}{m_1}\right)+\left(\frac{1}{m_2}\right)\right)} = 7.14 \text{ Hz} \tag{4.10}$$

Two anti-resonances can be identified with the first anti-resonance $f_{A1} = \frac{1}{2\pi}\sqrt{\frac{k_3}{m_3}} = 0.89$ Hz and the second anti-resonance $f_{A2} = \frac{1}{2\pi}\sqrt{k_2\left(\frac{1}{m_2}\right)} =$ 4.15 Hz. The mass-controlled line below the first resonance frequency corresponds to the total mass whereas above the second resonance frequency the unsprung mass dominates the response.

Table 4.1. Properties used to represent the vehicles. (*: used in simple mobility model)

Parameters / Types of Vehicle	Electric multiple unit (EMU)
Body mass (kg) *	30000
Body pitch inertia (kg-m^2)	$1.19x10^6$
Bogie sprung mass (kg) *	4700
Bogie pitch inertia (kg-m^2)	4000
Secondary vertical stiffness per bogie (N/m) *	$0.47x10^6$
Secondary vertical damping per bogie (Ns/m) *	$33.6\ x10^3$
Secondary damper stiffness per bogie (N/m)	-
Primary vertical stiffness per axle (N/m) *	$1.6\ x10^6$
Primary vertical damping per axle (Ns/m) *	$20\ x10^3$
Primary damper stiffness per axle (N/m)	$18\ x10^6$
Bogie centres (m)	16
Bogie wheelbase (m)	2.6
Wheelset mass (kg) *	1200
Vehicle length (m)	23
Total mass (kg)	44200
Axle load (kN)	108.3
Contact stiffness (MN/m)	2420
Speed of trains (m/s)	25

As noted the vehicle mobility is predominantly mass-controlled with two strongly damped resonances, whereas the track is stiffness-controlled below 100 Hz. The mobilities are also shown in Figure 4.2 along with their phase. The dotted line for the vehicle mobility represents a case in which the primary and secondary damping have been made 10 times smaller compared with the reference case. This shows the two resonances and anti-resonances more clearly.

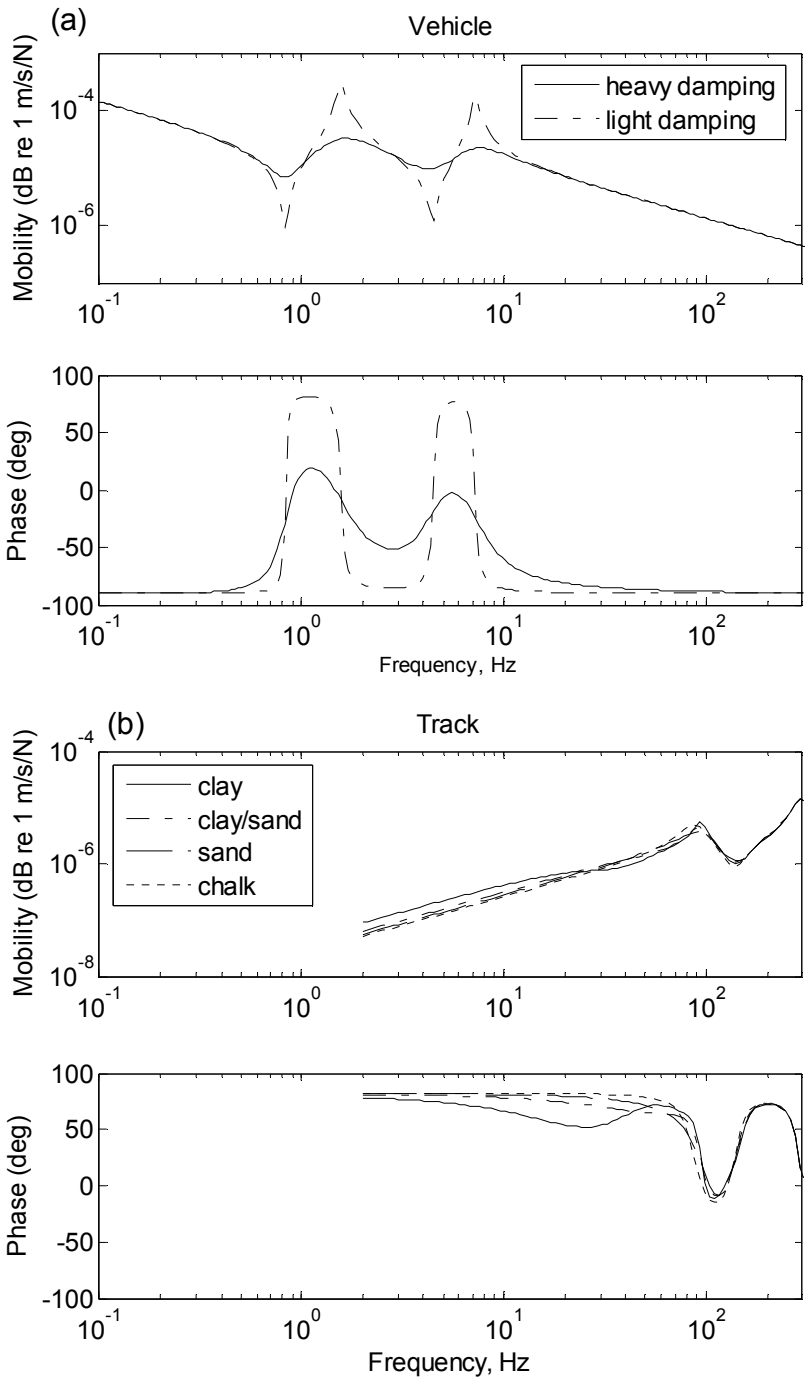

Figure 4.2. Mobilities of (a) vehicle for normal and reduced damping and (b) track system for various types of ground.

In order to estimate the mobility of the rail for various different ground properties, an analytical vehicle, track and ground model, called Igitur developed by Jones [5], is applied. The track in the Igitur model is represented as an infinite, layered beam resting on a three-dimensional half-space of ground material. The contact between the ground and track is by a vertical pressure over the width of the

track. This provides a summation of the contribution of vibration from all points along and across the width of the track to the response at the receiver location [5].

The track properties used to predict the track mobility are shown in Table 4.2. The parameters used for the ground are shown in Table 4.3. The mobilities of the track for various ground properties are shown in Figure 4.2(b). These are plotted for the reference track situation with the various ground types underneath. The mobility of the track can be seen to be stiffness-controlled below 100 Hz. The mobilities of the wheel and track systems therefore have opposite phase.

The material properties of the soil are related to the fundamental wave speeds as mentioned in Chapter 2. The density of the upper layer material is set throughout to 2000 kg m^{-3} as a typical value. According to typical properties of some soils and rocks [20] and a variety of commonly encountered ground types [19,16], the P- and S-wave speeds are chosen as shown in Table 4.3. It was found in Chapter 3 that the P-wave speed has less effect on the ground response than the S-wave speed. On the other hand the S-wave speed strongly affects the vibration response of the surface ground. The S-wave speeds are chosen as 120, 220, 350 and 1100 m/s to represent 'clay', 'clay/sand', 'sand' and 'chalk' respectively. These values for 'clay' and 'sand' represent soft and stiffer soils. 'Clay/sand' represents a medium stiffness soil while 'chalk' represents something much stiffer and more like rock.

Table 4.2. Parameters used to represent track in Igitur.

Parameters		Value
Rail	bending stiffness, N/m^2	1.26×10^7
	loss factor	0.01
	mass per unit length, kg/m	120
Rail pad	stiffness per unit track length, N/m^2	3.5×10^8
	loss factor	0.15
Sleeper	mass per unit length, kg/m	490
Ballast	stiffness, N/m^2	3.15×10^8
	loss factor	0.2
	mass per unit length, kg/m	1200

Table 4.3. The parameters used in Igitur for various types of ground.

Parameters of ground	Type			
	Clay	Clay/Sand	Sand	Chalk
P-wave speed	1700 m/s	1700 m/s	1700 m/s	2000 m/s
S-wave speed	120 m/s	220 m/s	350 m/s	1100 m/s
density of material	2000 kg m^{-3}	2000 kg m^{-3}	2000 kg m^{-3}	2000 kg m^{-3}

Figure 4.3 shows that the mass-controlled vehicle mobility and the stiffness-controlled track mobility curves intersect at about 65 Hz, for clay soil, corresponding to a 'resonance' of the coupled vehicle-track system. Also their phase is opposite (see Figure 4.2). For a given roughness input a maximum in the excitation force as well as in the velocity of both systems can be expected at this frequency. This can be explained by the relationship between the wheel/rail interaction and excitation by roughness presented in Thompson [3].

The rail is excited by a vertical harmonic force $Fe^{i\omega t}$ of circular frequency ω and complex amplitude F. Then the velocity amplitude v^R, with moving direction positive downwards, is given by

$$v^R = Y^R F \tag{4.11}$$

where Y^R is the rail mobility. An equal reaction force acts upwards on the wheel so the downwards wheel velocity v^W is given by

$$v^W = -Y^W F \tag{4.12}$$

where Y^W is the wheel mobility. The roughness amplitude r at circular frequency ω, and the various velocities are related by

$$v^R = i\omega r + v^W \tag{4.13}$$

where $i\omega r$ is the roughness velocity amplitude. The frequency $\omega = 2\pi f$ is determined from $f = \frac{v}{\lambda}$, where v is the train speed and λ is the wavelength of irregularity of the wheel or rail surface. Therefore, the relationship between the wheel/rail interaction force and excitation by roughness is given by

$$F = \frac{i\omega r}{Y^R + Y^W} \tag{4.14}$$

If the wheel is mass-controlled $Y^w \simeq \frac{1}{i\omega M_w}$, while the stiffness-controlled track mobilities is given by $Y^R \simeq \frac{i\omega}{K_T}$.

When the mobilities of the wheel mass and the stiffness of the track are equal and opposite, a resonance of the coupled wheel/track system can be found

$$\omega = \sqrt{\frac{K_T}{M_w}} \tag{4.15}$$

where K_T and M_w are track stiffness and wheel unsprung mass.

The peak at 90-100 Hz in the track mobility is a resonance of the track mass on the support stiffness. Some variation in track mobility can be seen at low frequencies due to the different ground types. However the track mobility is not greatly affected by the ground properties, especially above about 100 Hz.

Results from these simplified mobility models will be used in the rest of the chapter to help interpret results of ground vibration predictions.

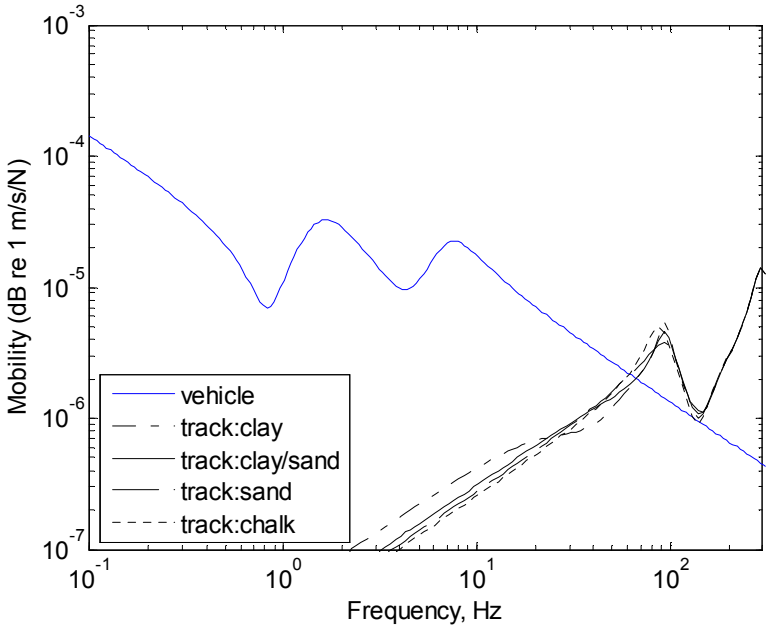

Figure 4.3. Point mobilities of vehicle and track on the various types of ground.

4.3 Reference calculations

The purpose of this section is to investigate the effect of a variety of track/ground parameters on the surface ground vibration. The sensitivity of the model to these parameters is investigated. The relative importance of the moving quasi-static loads and dynamic loads due to track roughness in the generation of vibration is also investigated in order to see their effects separately.

For this study the TGV model has been used to predict the ground vibration induced from surface trains. To consider a range of ground stiffnesses four typical soil types are considered. Each consists of an upper layer over a stiffer half space. The assumed properties are listed in Table 4.4. In each case the upper layer properties correspond to those used in the previous section. The ground properties for clay have been chosen as the reference case. The maximum frequency band of interest is limited to 80 Hz due to limitations of the numerical integration techniques used in TGV.

The parameters used to represent the vehicles are typical values applying to a five-coach electric multiple unit train (a notional EMU) based loosely on a class 322, as listed in Table 4.1. Unless otherwise stated the train speed is 25 m/s. For simplicity the train has only a single value of unsprung mass throughout and the bogie mass corresponds to an unpowered bogie. The assumed roughness spectrum used in the predictions is obtained from the Steventon site in Chapter 3. The ground vibration is normalised by the time taken for the passage of the "train".

Table 4.4. The parameters used in TGV for various types of ground.

Parameters of ground	Type				
	Clay	Clay/Sand	Sand	Chalk	Half-space
P-wave speed	1700 m/s	1700 m/s	1700 m/s	2000 m/s	2100 m/s
S-wave speed	120 m/s	220 m/s	350 m/s	1100 m/s	1200 m/s
density of layer material	2000 kg m^{-3}	2000 kg m^{-3}	2000 kg m^{-3}	2000 kg m^{-3}	2000 kg m^{-3}
Layer depth	3.0 m	3.0 m	3.0 m	3.0 m	infinite

A number of track design variants are considered as listed in Table 4.5. These include changing the rail pad stiffness, adding a ballast mat or sleeper soffit pad, the effects of an embankment and various soil conditions. The effects of changing these

parameters will be investigated in terms of an insertion gain at different distances from the track.

The "original" track parameters shown in Table 4.5 are the same as those used for Steventon in Chapter 3 but without an embankment. These typical values are defined as the reference situation. The parameters used for the rail, rail pad, sleeper, ballast mat and sleeper soffit pad are obtained from Thompson [3]. For the ballast in particular a loss factor of 0.2 is used as found in recent measurements of the dynamic stiffness of ballast by Herron [106]. The factors $d\beta$ and $d\gamma$ used in the TGV model to transform into the wavenumber domain are 0.05 in the x and y direction.

Table 4.5. Parameters used to represent different track variants (values are for two rails).

Parameters			Original	Variants	
Rail	bending stiffness, N/m^2		1.26×10^7	-	
	loss factor		0.01	-	
	mass per unit length, kg/m		120	-	
Rail pad	stiffness per unit track length, N/m^2	very soft baseplates	-	3.5×10^7	
		typical soft baseplates	-	1×10^8	
		soft rail pad	3.5×10^8	-	
		moderate stiffness rail pad	-	1×10^9	
	loss factor		0.15	-	
Sleeper	mass per unit length, kg/m	concrete	490	-	
		wooden	-	100	
Ballast	stiffness, N/m^2		3.15×10^8	-	
	loss factor		0.2	-	
	mass per unit length, kg/m		1200	-	
Ballast mat	stiffness, N/m^2	softer	-	40×10^6	
		stiffer	-	100×10^6	
	loss factor		-	0.2	
Sleeper soffit pad	stiffness, N/m^2	softer	-	40×10^6	
		stiffer		247.5×10^6	
	loss factor		-	0.05	
Embankment	Young's modulus, N/m^2		-	$2x10^7$	
	density, kg/m^3		-	1800	
	height, m		-	0.75	4.0
	width at top, m		-	2.7	2.7
	width at base, m		4	4	11

4.3.1 Results for reference situation

For the reference situation the results shown in Figure 4.4 present the predicted vibration on the soft clay soil at 0 m (directly under the track) and at 10 m from the track. It can be seen that the response beneath the track is dominated by the quasi-static loads up to 12.5 Hz whereas at 10 m away the dynamic loads are dominant above about 3 Hz. Similar conclusions are found by Lombaert [2] and Gupta et al [69]. The peaks in the response at low frequency are related to the axle spacing (see Section 4.5.6 below).

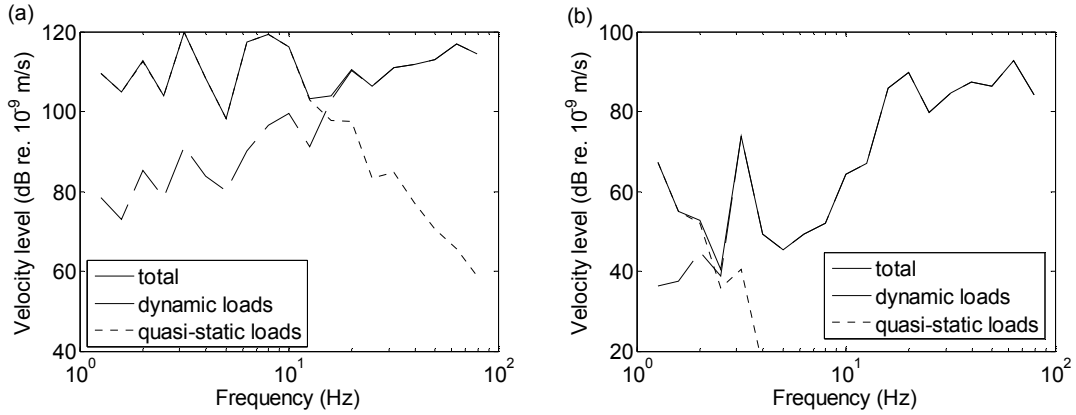

Figure 4.4. Ground vibration for reference case on soft clay (a) at 0 m and (b) 10 m from the track; comparing total, quasi-static and dynamic loads.

In order to see the effect of different ground properties on the vibration response, Figure 4.5 shows the overall responses at 0 m and 10 m for the different ground parameters. The responses at 0 m are significantly affected by the ground stiffness whereas the response at 10 m is affected to a lesser extent. As the ground becomes softer the ground responses are greater by about 35 dB from chalk to clay just underneath the track. Similar conclusions are found by Galvin et al [4] and Verbraken et al [28]. At 10 m from the track a peak at 20 Hz found for clay soil shifts towards higher frequency as the ground becomes stiffer. This corresponds to the cut-on frequency of the ground layer as shown in Figure 4.6. The stiffer the ground, the higher this cut-on frequency would be as seen in Figure 4.5 (b). The vibration level changes in this frequency region as a result of this shift in cut-on frequency.

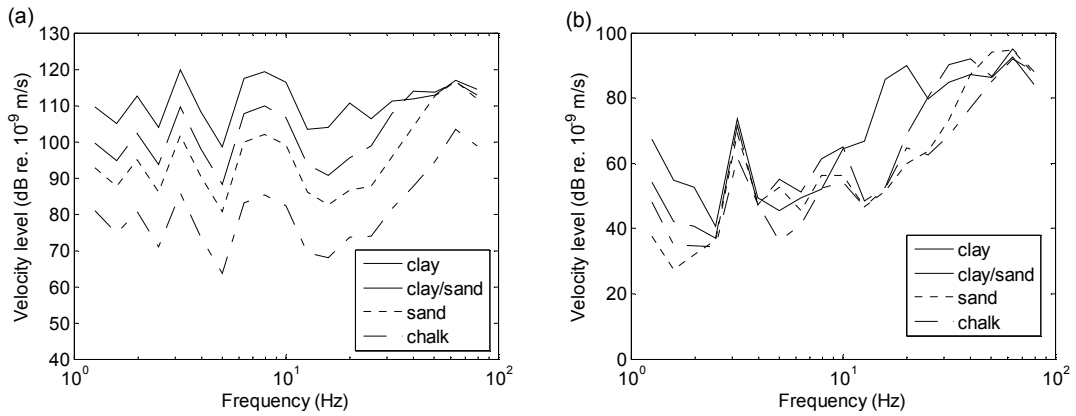

Figure 4.5. Ground vibration for reference case on different soils (a) at 0 m and (b) 10 m from the track.

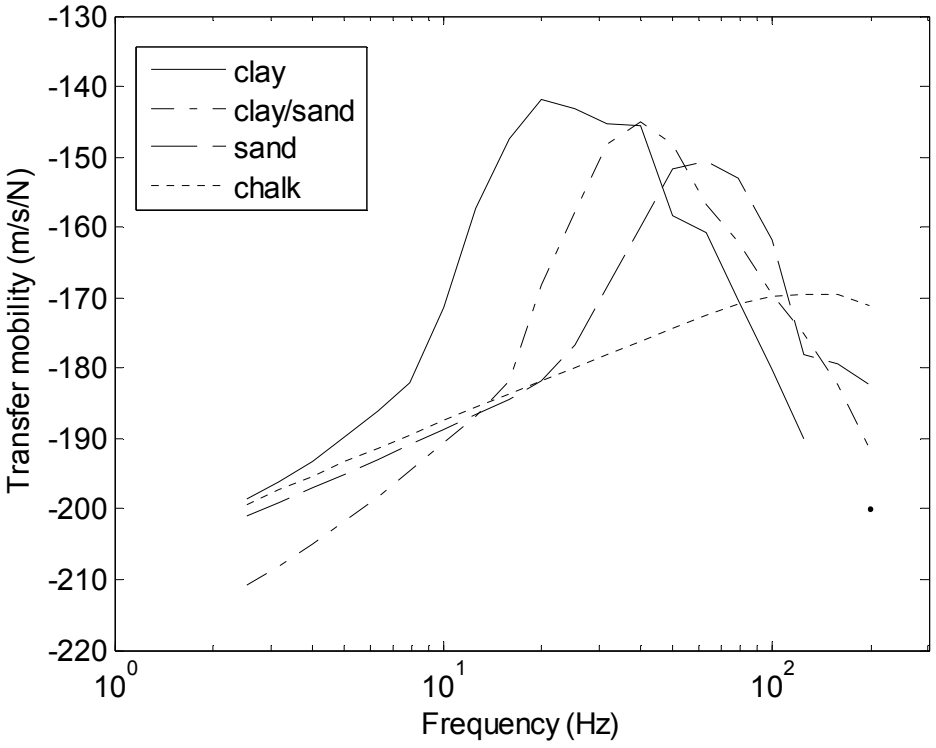

Figure 4.6. Transfer mobilities on the surface of the ground obtained using the kandr model with parameters of the ground properties from Table 4.3 at 10 m away from applied force.

4.4 Investigation of track parameters

In order to see the extreme effects, the stiffness of the rail pad is set ten times softer to represent a soft rail pad. Two other values of rail pad stiffness are also considered. A sleeper soffit pad is set to represent a stiff soffit pad of 247.5×10^6 N/m^2

and a soft soffit pad of 22.5×10^6 N/m^2. A ballast mat and an embankment are also inserted into the system. Finally wooden sleepers are investigated as an alternative to the concrete ones.

4.4.1 The effect of rail pad stiffness

In this section different rail pad stiffness are considered. The rail pad stiffnesses are chosen as 3.5×10^7, 1×10^8, 3.5×10^8 and 1×10^9 N/m^2 to represent 'very soft baseplates', 'typical soft baseplates', 'soft rail pad' and 'moderate stiffness rail pad' respectively. These values are for both rails and expressed per unit length of track; they correspond to 1.05×10^7, 3×10^7, 1.05×10^8 and 3×10^8 N/m per pad respectively. The rail pad stiffness for the soft rail pad has been chosen as the reference case in the previous section.

Introducing a softer spring in the track support lowers the coupled vehicle/track resonance frequency (see Equation (4.15) and reduces the ground response at higher frequencies. Figure 4.7 illustrates this by showing the difference between the results for very soft baseplates ($3.5\text{x}10^7$ N/m^2) and the reference case ($3.5\text{x}10^8$ N/m^2).

Results are shown in terms of the difference in level at various distances for total, dynamic component and quasi-static component. The insertion gain is deifined as

$$IG = 20\log_{10}\left(\frac{\text{modified velocity}}{\text{reference velocity}}\right) \tag{4.16}$$

Although the stiffness of the rail pad has been reduced by a factor of 10, the overall track stiffness is only reduced by a factor of 2.4 at low frequencies, as shown in Figure 4.8. Consequently the coupled resonance frequency is lowered from 65 Hz to about 40 Hz. The insertion gain for the dynamic component shows the classic trend of an increase in vibration at the new resonance frequency (40 Hz), followed by a maximum reduction at the old resonance (65 Hz) before tending to a constant reduction at high frequency. The latter is not visible in these results due to the restricted frequency range of the predictions.

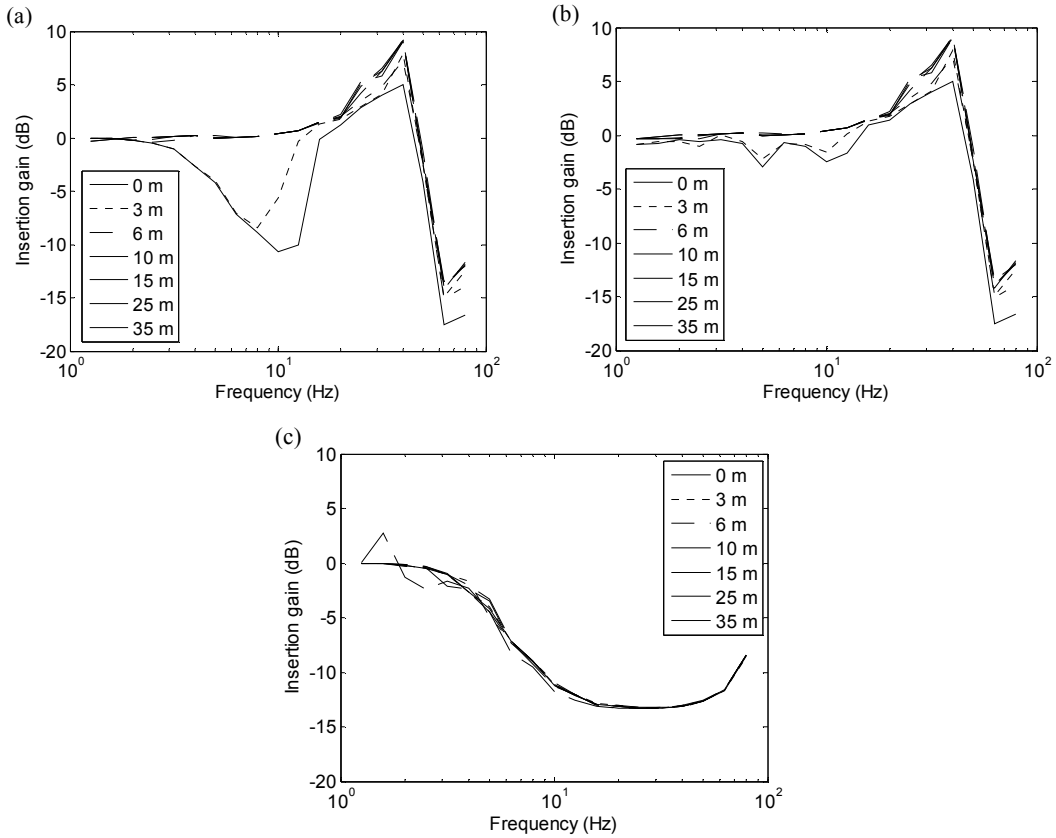

Figure 4.7. Insertion gain due to changing the stiffness of rail pad, comparison of very soft baseplates case ($3.5x10^7$ N/m^2) to reference case ($3.5x10^8$ N/m^2), for (a) total, (b) dynamic loads and (c) quasi-static loads, at various distances away from the track.

On the other hand the quasi-static component is reduced at all distances above 3 Hz. The softer track support leads to a smoothening of the quasi-static deflection under each bogie so that the higher frequency content of the deflection pattern is reduced. The insertion gain for the quasi-static load is virtually identical at all distances.

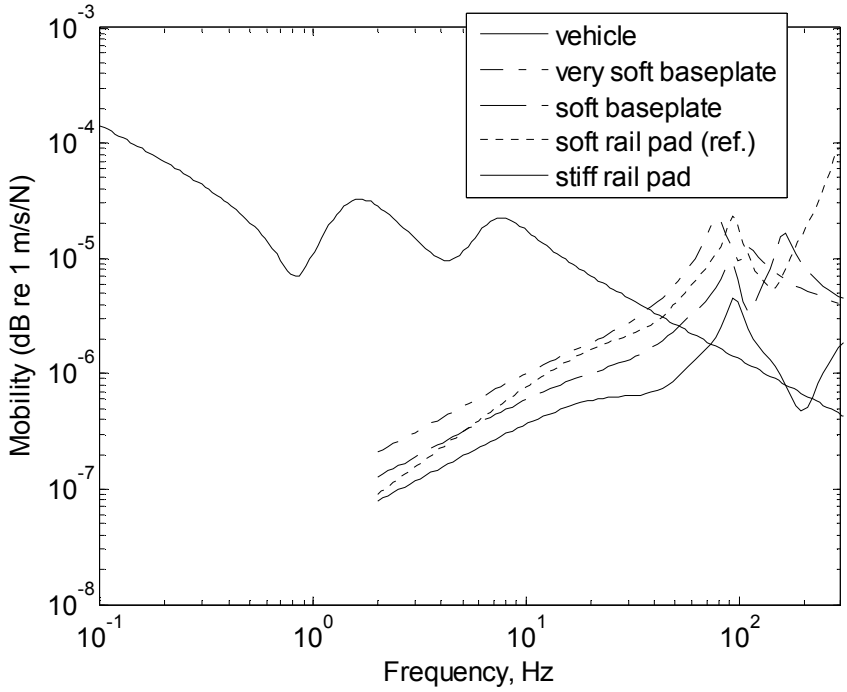

Figure 4.8. Point mobilities of vehicle and track for various rail pad stiffness.

The insertion gain for the overall response follows that of the dynamic excitation for locations far from the track, but at 0 m it follows the quasi-static curve up to about 10 Hz, above which it tends towards the curve for dynamic excitation. This can be understood from the contributions of the two mechanisms shown in Figure 4.4. It is clear from these results that an assessment of the insertion gain due to a change in rail pad stiffness should not be based on measurements too close to the track – in this case the distance should be at least 10 m to give representative results of the effect on the far field response.

The variations of ground properties have virtually no effect on the dynamic and quasi-static components of the insertion gain due to changing pad stiffness, as shown in Figure 4.9. Although the peaks in the insertion gain shift up in frequency slightly with increasing ground stiffness at distances near the track (up to about 10 m), it can be seen that both dynamic and quasi-static components are only slightly affected by the ground stiffness. For a softer ground the peak in the insertion gain is lower. More significantly, however, the relative importance of the quasi-static component reduces with increasing ground stiffness, so that on the stiff ground the insertion gain follows that for the dynamic load more closely even at 3 m.

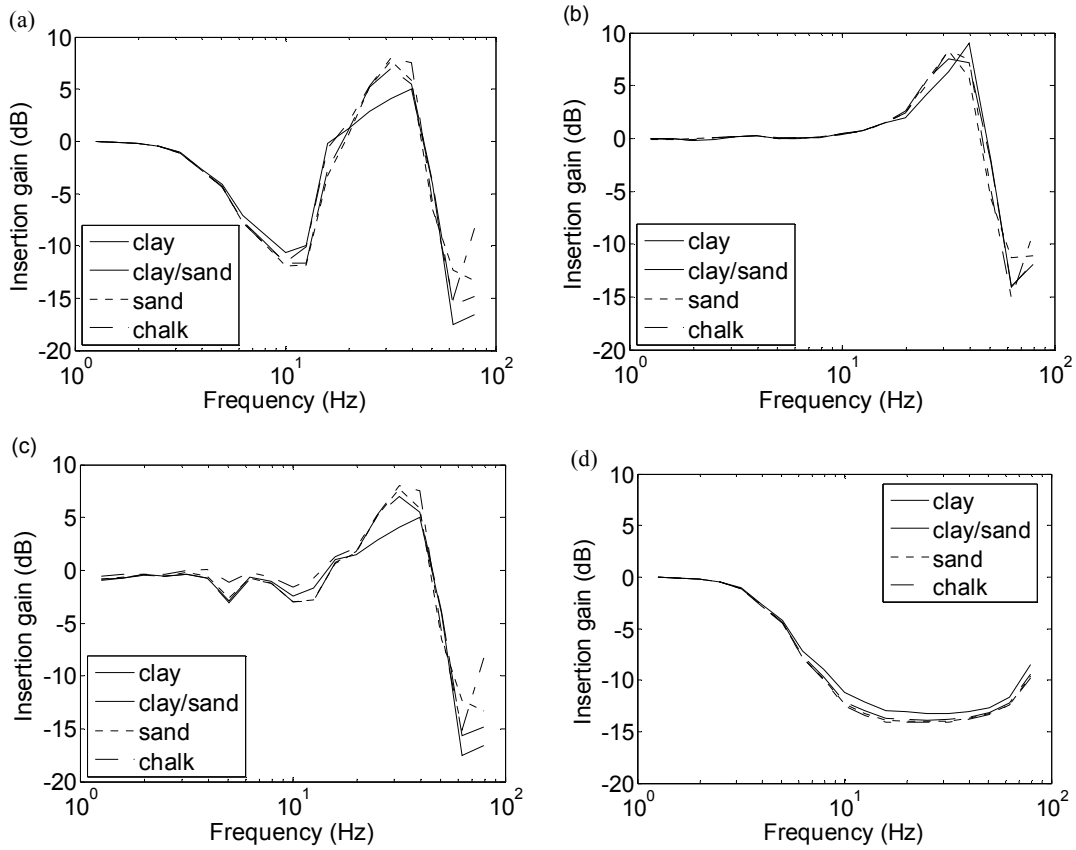

Figure 4.9. Insertion gain of the ground vibration due to change in rail pad stiffness on different soil types: (a) all four sites total at 0 m; (b) all four sites total at 10 m; (c) all four sites dynamic at 0 m and (d) all four sites quasi-static at 0 m.

Introducing a typical soft baseplate with a more moderate change in stiffness ($1x10^8$ N/m^2) in the track support gives similar but reduced trends of insertion gains to the case for very soft baseplate ($3.5x10^7$ N/m^2) as shown in Figure 4.10. The peak in the insertion gain occurs at 50 Hz and is smaller than for the very soft baseplate

On the other hand introducing a rail pad with a greater stiffness (of $1x10^9$ N/m^2) increases the ground response above 65 Hz as shown in Figure 4.11. It can be seen that the effects of insertion gain for the case of the stiffer rail pad look similar to the case of the soft one but in the opposite sense.

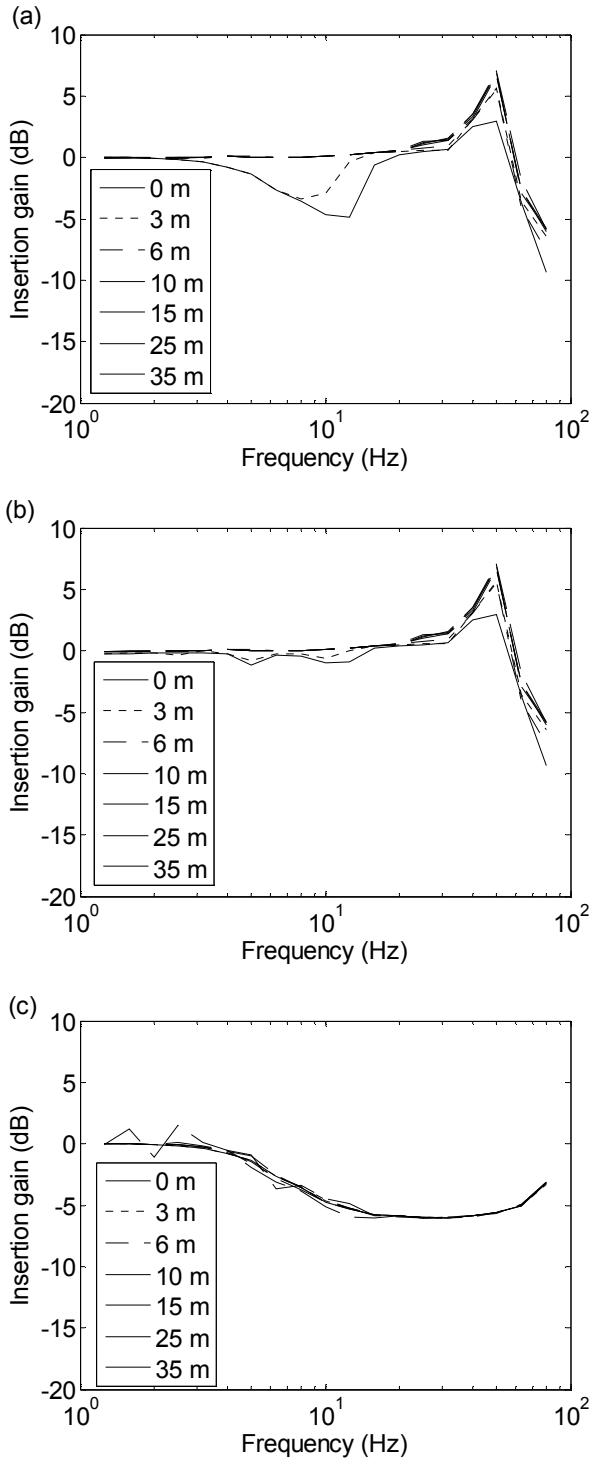

Figure 4.10. Insertion gain due to changing the stiffness of rail pad, comparing soft base plate case ($1x10^8$ N/m^2) to reference case ($3.5x10^8$ N/m^2), for (a) total, (b) dynamic loads and (c) quasi-static loads at distances away from the track.

Figure 4.12 shows the insertion gains due to a change in rail pad stiffness for the soft ground site at a train speed of 50 m/s. At 0 m the overall response follows the quasi-static curve up to 16 Hz (compared with 12.5 Hz for 25 m/s).

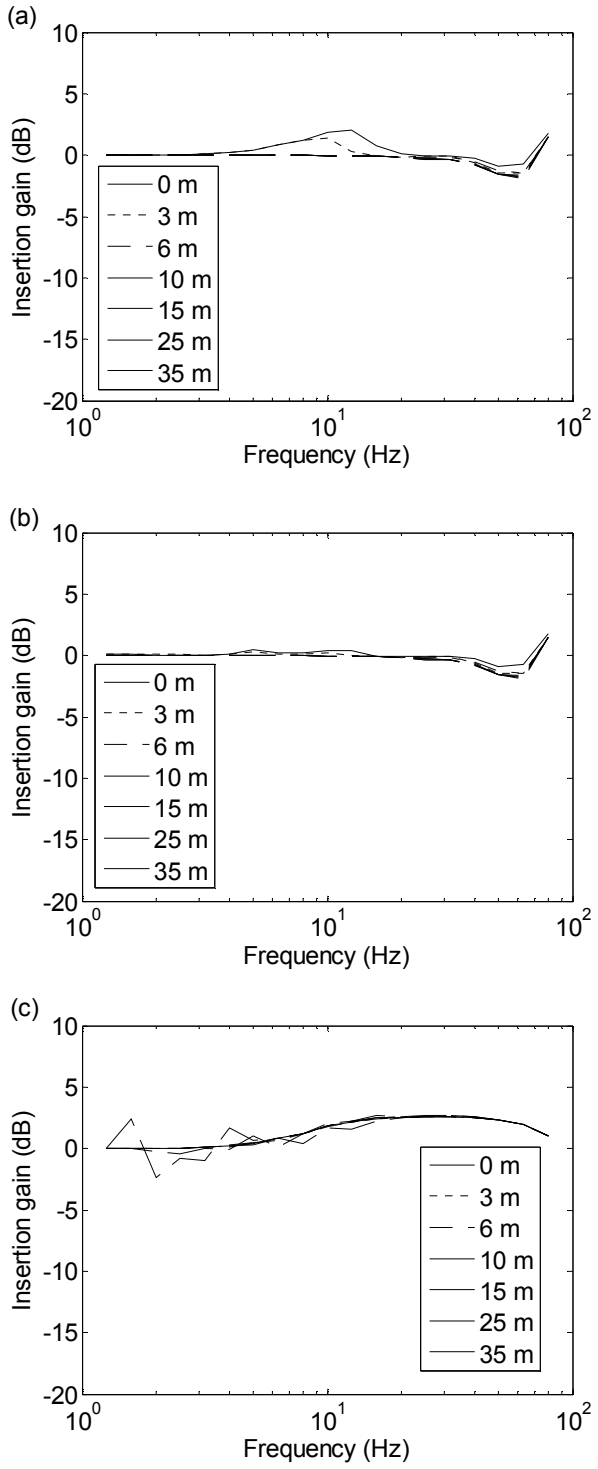

Figure 4.11. Insertion gain due to changing the stiffness of rail pad, comparing stiffer rail pad case ($1x10^9$ N/m^2) to reference case ($3.5x10^8$ N/m^2), for (a) total, (b) dynamic loads and (c) quasi-static loads at distances away from the track.

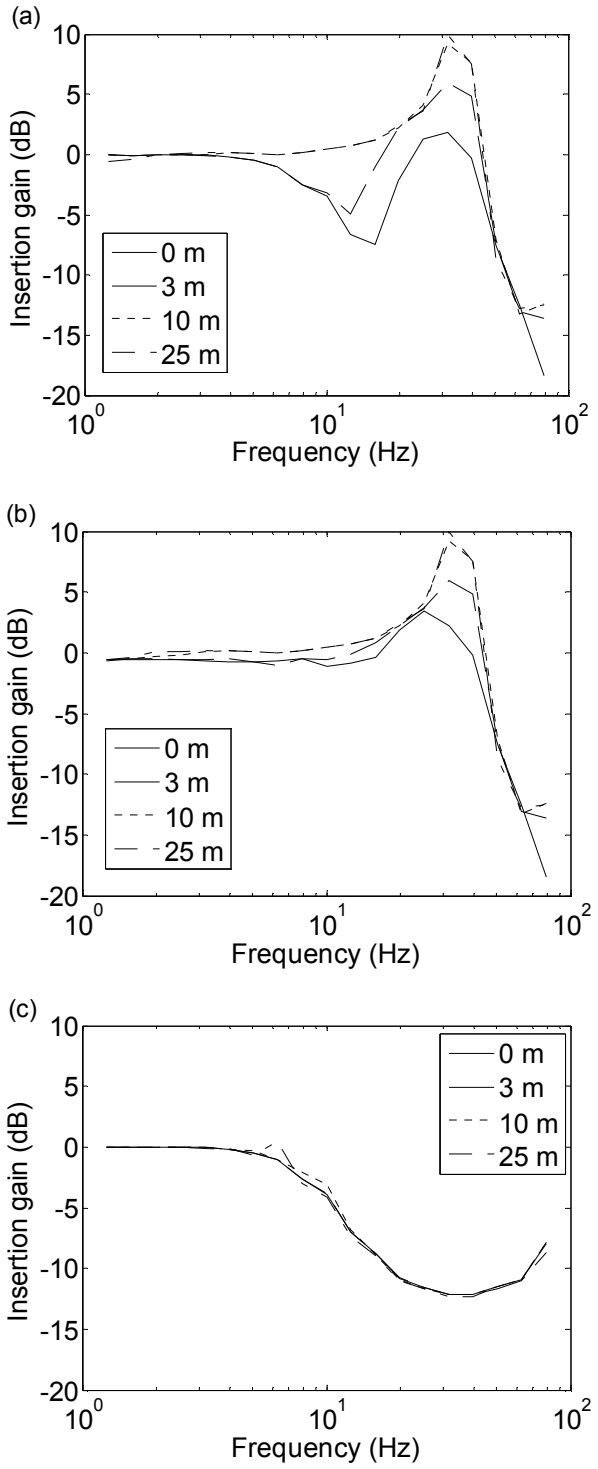

Figure 4.12 Insertion gain of the ground vibration due to change in rail pad stiffness for soft clay soil at 50 m/s; (a) total, (b) dynamic component and (c) quasi-static component.

Figure 4.13 shows the insertion gains due to a change in rail pad stiffness on clay soil at the distance of 0 m comparing the two different train speeds. The quasi-static excitation dominates the response over a greater frequency range as the speed of

the train increases. The insertion gain corresponding to the quasi-static component shifts towards higher frequencies as the speed increases whereas that for the dynamic component is independent of train speed. Thus the overall results are slightly different for the two speeds. Similar conclusions were found by Lombaert [2], and Gupta et al [69].

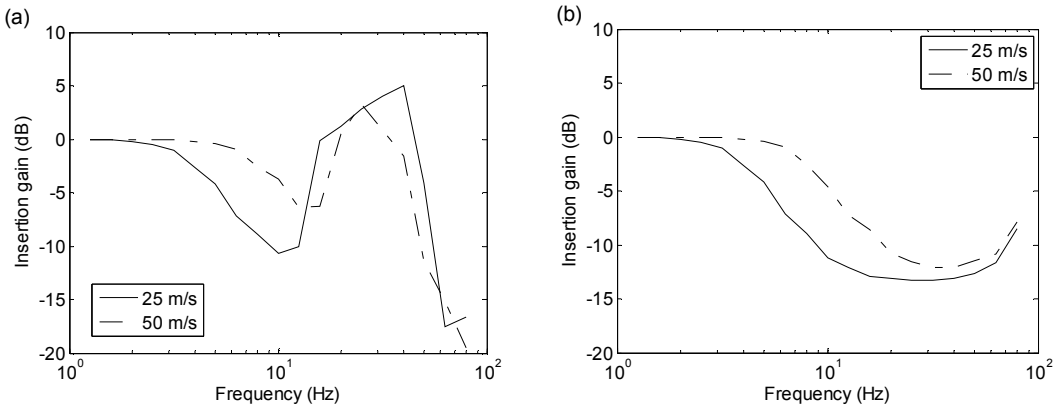

Figure 4.13. Insertion gain due to change in rail pad stiffness on clay soil underneath the track (0 m) at the train speed of 25 and 50 m/s (a) for total and (b) quasi-static component.

Summarizing, introducing a soft rail pad increases the ground vibration at the new resonance frequency. Although the vibration is reduced at higher frequencies, above about 50 Hz, it may not be of benefit to the reduction of ground-borne vibration for which frequencies below this are usually more important. The effect of changes in support stiffness on the ground response due to the quasi-static load differs from dynamic one. As the results have shown, a considerable insertion gain is found corresponding to the quasi-static component over almost the entire frequency range.

4.4.2 The effect of ballast mat and sleeper soffit pad

The results obtained when a ballast mat or a sleeper soffit pad are introduced, show similar trends to those for a soft rail pad. Figure 4.14 shows the insertion gains for two stiffness of ballast mat and two stiffness of sleeper soffit pad. The stiff soffit pad gives little benefit. The softer soffit pad gives very similar results to the soft ballast mat.

It is clear from these various results that, like softer rail pads, ballast mats and soffit pads lead to significant increases in ground vibration in the region 20-40 Hz at 10 m and beyond due to the lowered vehicle/track resonance. Reductions in vibration only occur above about 50 Hz. However, a measurement close to the track would suggest that the benefits extend to lower frequencies.

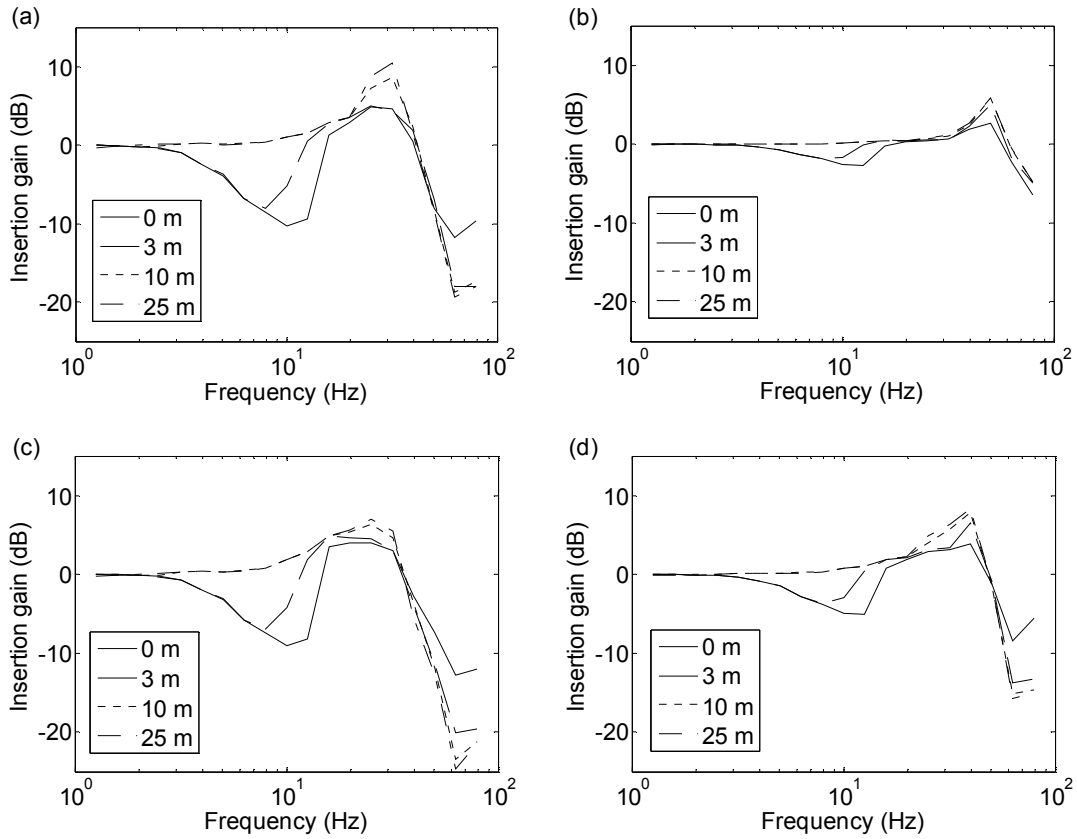

Figure 4.14. Insertion gain for the total response of the ground vibration with the case of inserting; (a) softer soffit pad, (b) stiffer soffit pad, (c) softer ballast mat and (d) stiffer ballast mat.

4.4.3 The effect of an embankment

Tracks are often constructed on an embankment, the height and stiffness of which can vary considerably. Figure 4.15 shows the effects of introducing an embankment into the model. Two different heights of embankment are considered, as listed in Table 4.5. The embankment is modelled in TGV only as a layer of damped springs with consistent mass. Inserting the embankment gives a similar trend in terms of the insertion gain as for the reduced rail pad stiffness, as shown in Figure 4.16. However, for the larger embankment the width of the connection with the ground is also increased. This leads to a reduction in level at 0 m (as the load is spread over a

wider area) and an increase at 10 m (as this position is now closer to the base of the embankment).

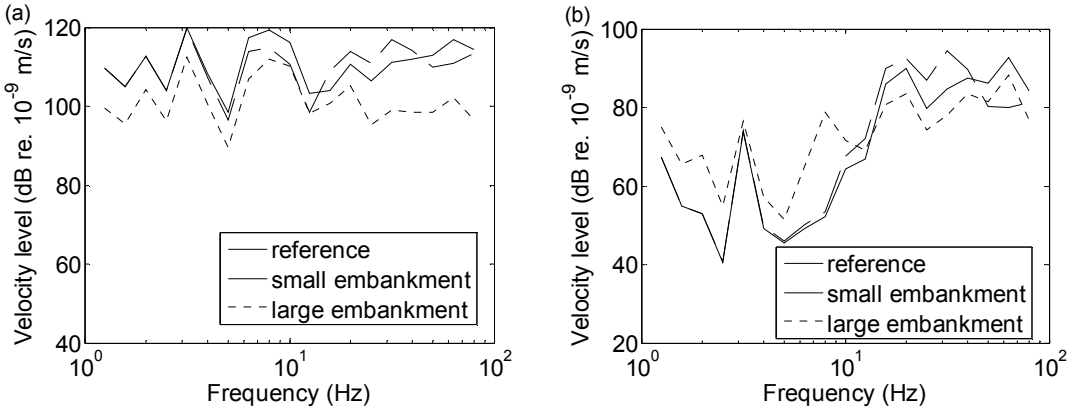

Figure 4.15. Ground vibration for the case of none, small and large embankment on soft clay (a) at 0 m and (b) 10 m from the track.

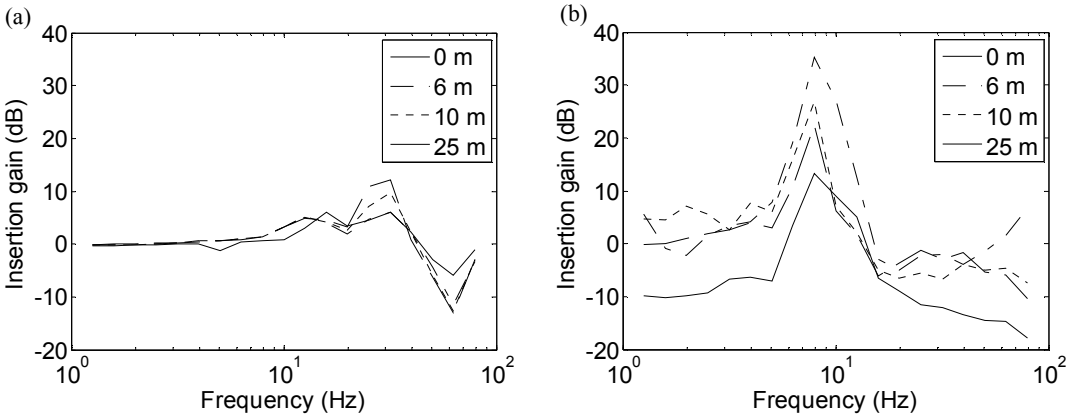

Figure 4.16. Insertion gain of the ground vibration with the case of inserting; (a) small embankment and (b) large embankment for the dynamic response.

4.4.4 The effect of roughness

In the calculations so far the roughness corresponds to that obtained at the Steventon site (see Figure 3.45). In some situations the roughness amplitude may be less. Particularly this may be the case for a slab track, where the track geometry may potentially be smoother than for a ballasted track. Consequently a low amplitude of roughness as shown in Figure 4.17 has been applied to the system in order to see the effect on the vibration response. The amplitude for wavelengths shorter than 1 m is left unchanged but for wavelengths greater than 2.5 m the roughness has been reduced by 10 dB.

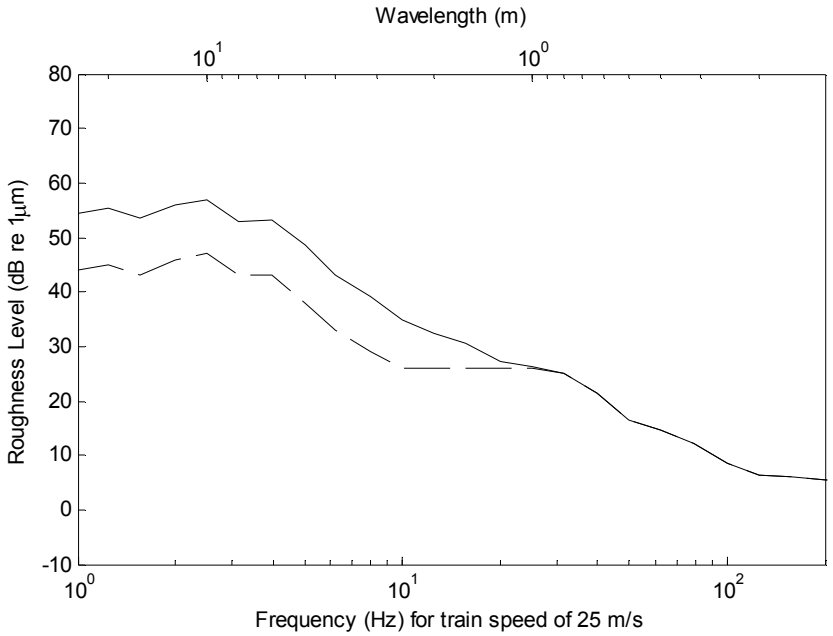

Figure 4.17. The roughness obtained. -, from the measurements at Steventon site and --, modified roughness.

Figure 4.18 shows the insertion gains due to the change in the roughness. The quasi-static component is unchanged whereas the dynamic component is reduced below 20 Hz due to the assumed roughness. The overall insertion gain corresponds to the quasi-static component up to 10 Hz at 3 m and only up to 3 Hz at 10 m. At the distances further away the quasi-static component is less important and the insertion gain follows the dynamic one.

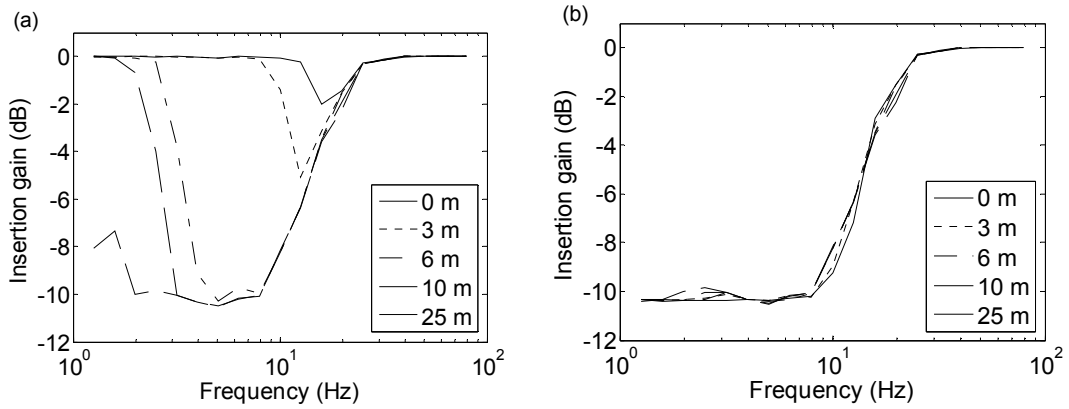

Figure 4.18. Insertion gain of the ground vibration with the case of low amplitude of the roughness; at different distances for the applied force (a) total and (b) dynamic load only.

4.4.5 The effect of sleeper mass

Concrete sleepers are commonly used in the construction of new railway tracks. However wooden sleepers are also still widely used. Wooden sleepers have a much lower mass than concrete ones. The track mobilities are first estimated using Igitur for the soft clay soil. Having a lighter sleeper affects the track response around and above the resonance of the track mass on the support stiffness, which shifts from 90 Hz to 110 Hz as seen in Figure 4.19.

In Figure 4.20 results are shown from TGV for the effect of changing the sleeper on different ground stiffness. The insertion gains are all less than about 1 dB. However the dip at about 50 Hz is larger for stiffer grounds. This corresponds to a small difference in point mobilities of a track with concrete and wooden sleepers as shown in Figure 4.19.

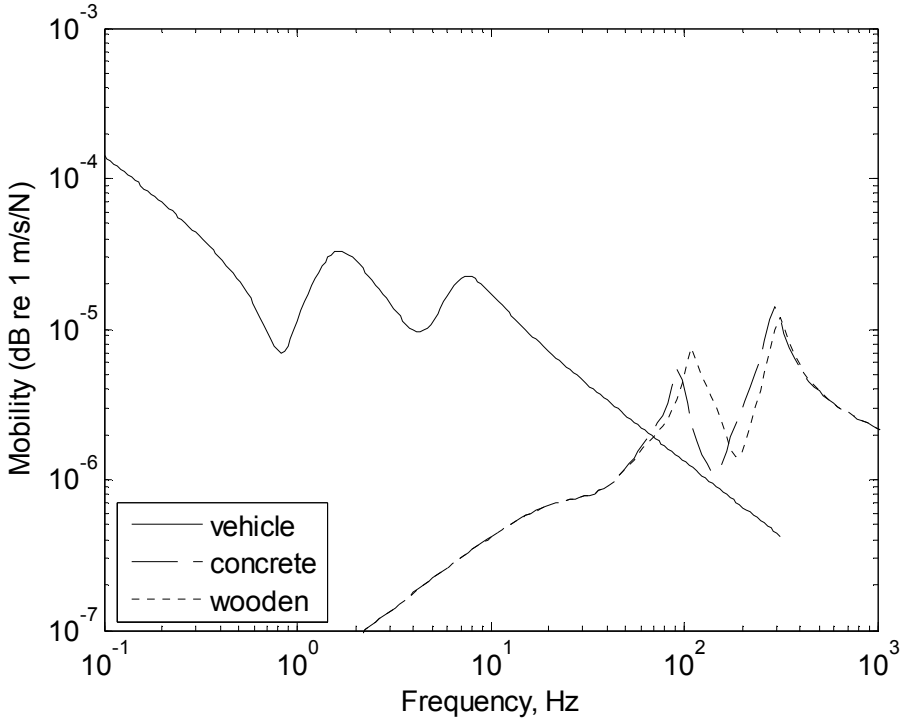

Figure 4.19. Point mobilities of vehicle and track for concrete sleeper (reference situation) and wooden sleeper on soft clay soil.

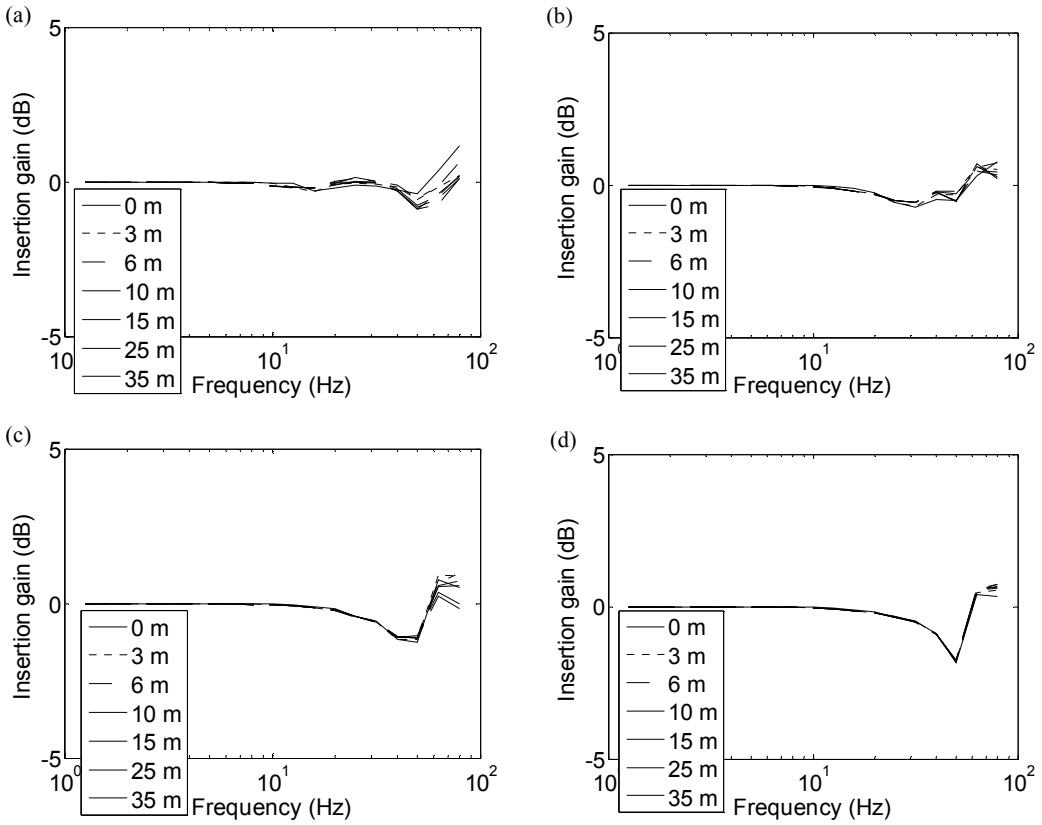

Figure 4.20. Insertion gain of the ground vibration due to change in mass of sleeper (a) for total on clay, (b) clay/sand, (c) sand and (d) chalk at distances away from the track.

4.5 Investigation of vehicle parameters

Many papers have investigated the effect of changes in track parameters, [42,107]. However the vehicle system also has an important effect and should be considered [108]. The purpose of this section is to investigate the effect of changes to the vehicle on the surface ground vibration response. The relative importance of the moving quasi-static loads and dynamic loads has again also been investigated. The track parameters used are the same as those used for the reference case in the previous section.

A number of vehicle design variants are considered as listed in Table 4.6. These include changing the mass components, suspension systems, axle spacing and the vehicle speed.

Table 4.6. Properties used to represent the reference and modified vehicles.

Parameters of Vehicle	Reference	Modified parameters					
		1.Axle load	2.Unsprung mass	3.Primary suspension stiffness	4.Speed	5.Axle spacing	6.Bogie mass
Body mass (kg)	30000	60000					
Body pitch inertia (kg-m^2)	$1.19x10^6$						
Bogie sprung mass (kg)	4700						9400
Bogie pitch inertia (kg-m^2)	4000						
Secondary vertical stiffness per bogie (N/m)	$0.47x10^6$						
Secondary vertical damping per bogie (Ns/m)	$33.6 x10^3$						
Secondary damper stiffness per bogie (N/m)	-						
Primary vertical stiffness per axle (N/m)	$1.6 x10^6$			$6.4 x10^6$			
Primary vertical damping per axle (Ns/m)	$20 x10^3$			$40 x10^3$			
Primary damper stiffness per axle (N/m)	$18 x10^6$			$36 x10^3$			
Bogie centres (m)	16					11.5	
Bogie wheelbase (m)	2.6					5.75	
Wheelset mass (kg)	1200		2400				
Vehicle length (m)	23						
Total mass (kg)	44200	74200					
Axle load (kN)	108.3	181.8					
Speed of trains (m/s)	25				10 12.5 16 20 31.5 40 50		

4.5.1 The effect of axle load

The effect of axle load has been investigated by doubling the body mass. This increases the axle load from 108 kN to 182 kN. The results are shown in terms of an insertion gain at various distances between 0 and 25 m away from the track in Figure 4.21. The body mass affects the quasi-static component by a constant factor at all frequencies. This is 4.5 dB, corresponding to 20 log of the ratio of the axle loads. Conversely the dynamic excitation is only affected at low frequencies, mainly below 5 Hz, due to the change in body mass. It can be seen that the overall insertion gain is

dominated by the quasi-static excitation at 0 m. The effect is limited to lower and lower frequencies as the distance increases.

The dynamic response can also be analysed in terms of the mobilities of the vehicle and track, which are shown in Figure 4.22. As the body mass increases the mobility is reduced at very low frequency and increased between the first anti-resonance and the first resonance frequency. The mobility is virtually unchanged above about 2 Hz.

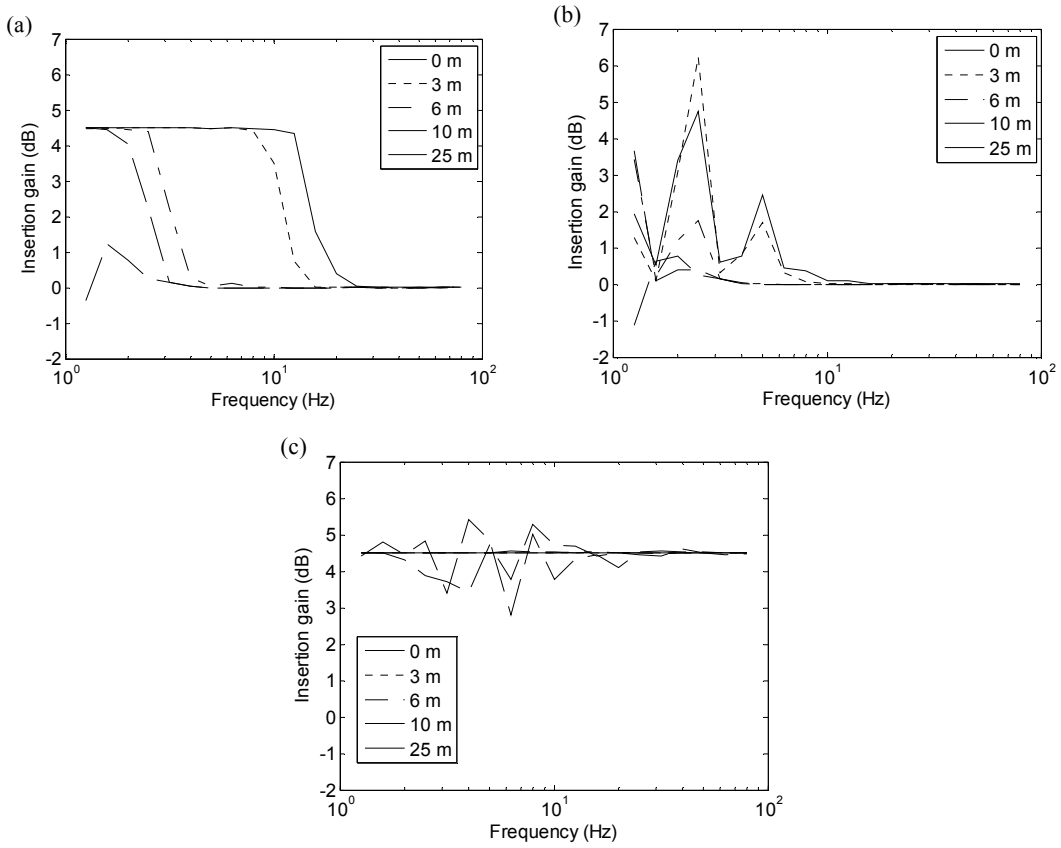

Figure 4.21. Insertion gain of the ground vibration due to change in axle load on clay (a) for total, (b) dynamic component and (c) quasi-static component at distances away from the track.

The effects of axle load are also considered for the different ground stiffnesses. Figure 4.23 shows the influence of the different ground properties on these insertion gains due to increased axle load. The insertion gains for the total vibration due to changing body mass are virtually unaffected by the ground stiffness.

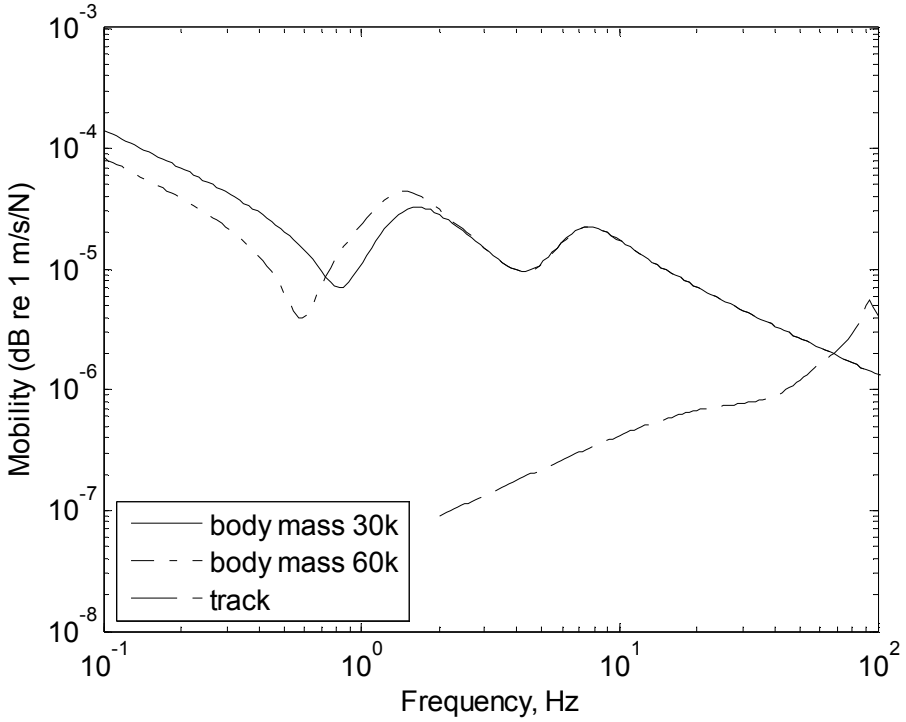

Figure 4.22. Point mobilities of vehicle and track for reference situation and increased body mass.

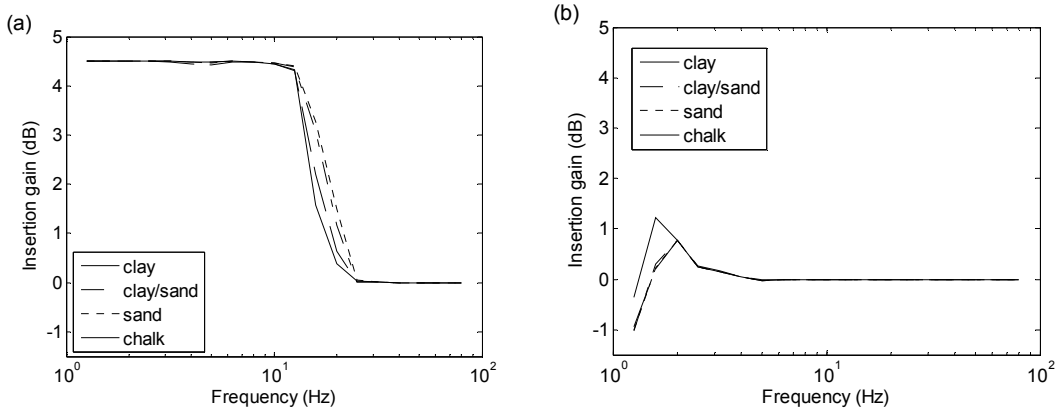

Figure 4.23. Insertion gain of the total ground vibration due to change in axle load on various ground stiffnesses (a) at 0 m and (b) 25 m.

4.5.2 The effect of unsprung mass

The effect of the vehicle unsprung mass has also been investigated. The wheelset mass is set to twice the reference value, corresponding to a typical powered axle. This causes the vehicle resonances to shift to lower frequencies and the mass-controlled vehicle mobility is reduced above about 6 Hz as shown in Figure 4.24. The intersection between the mass-controlled vehicle mobility and the stiffness-controlled

track mobility occurs at a lower frequency (50 Hz instead of 65 Hz) as shown in Figure 4.24.

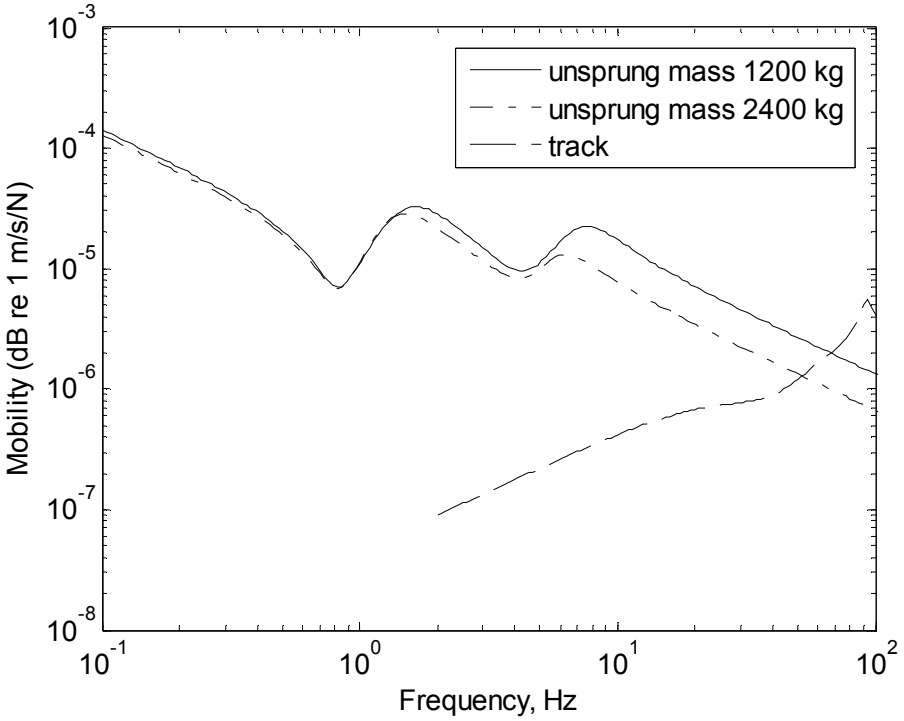

Figure 4.24. Point mobilities of vehicle and track for light unsprung mass (reference situation) and heavy unsprung mass.

The results are shown in terms of an insertion gain in Figure 4.25. It is found that the dynamic component is affected by the unsprung mass above about 6 Hz. At most frequencies doubling the wheelset mass leads to a 7 dB insertion gain. However at the new coupled resonance frequency of 50 Hz the insertion gain reaches a peak of almost 12 dB, followed by a minimum at the old coupled resonance frequency. However, the quasi-static component is unaffected at all frequencies.

Figure 4.26 shows the influence of the different ground properties on these insertion gains due to unsprung mass. It can be seen that the insertion gains for the dynamic component are slightly affected by the ground stiffness above 20 Hz due to the influence of the ground on the track mobility and hence on the location of the coupled resonance (see Figure 4.3).

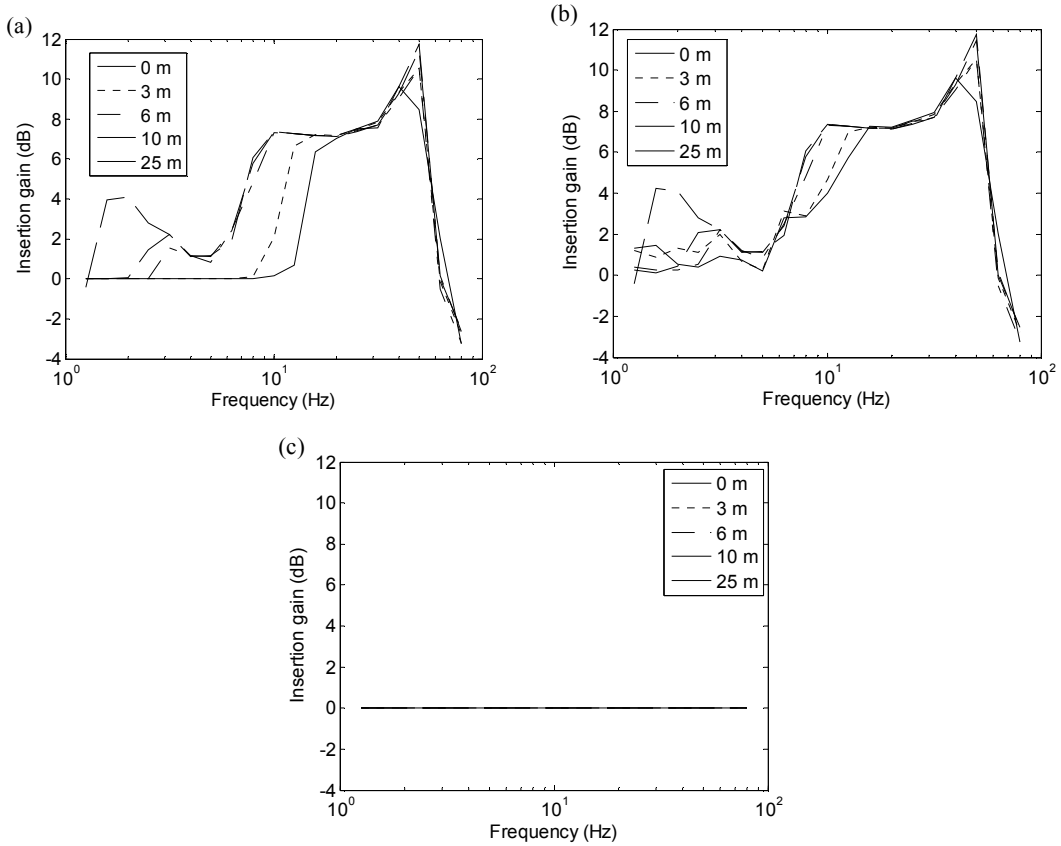

Figure 4.25. Insertion gain of the ground vibration due to change in unsprung mass on clay at distances away from the track (a) for total, (b) dynamic component and (c) quasi-static component.

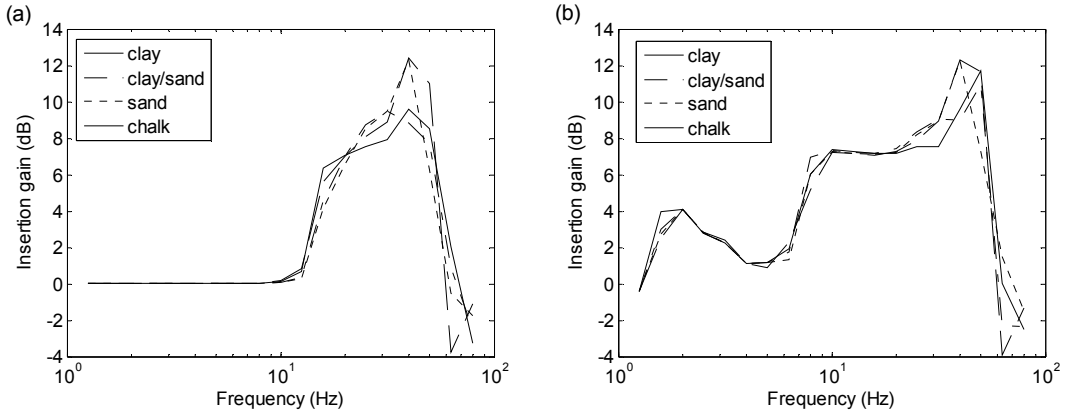

Figure 4.26. Insertion gain of the total ground vibration due to change in unsprung mass on various ground stiffnesses (a) at 0 m and (b) 25 m.

4.5.3 The effect of primary suspension stiffness

The effects of the primary suspension stiffness are investigated in this section. Note, from Table 4.6, that the primary damper and parallel spring stiffness are also

modified. The primary damper is modified in such a way as to maintain the same damping ratio at the second resonance frequency, which shifts from 8 Hz to 16 Hz (see Figure 4.27).

The results are shown in terms of an insertion gain in Figure 4.28 for different ground stiffnesses. The primary suspension stiffness affects only the dynamic component. For the quasi-static component, it again has no effect as found when changing the unsprung mass. At 25 m from the track the peak in the insertion gain at about 8 Hz is caused by shifts in the resonance and anti-resonance frequencies in the vehicle mobility, as seen in Figure 4.27. This can also be seen in Figure 4.29, which shows the vibration spectra at 25 m away from the track. The ground vibration has a sharp peak at about 8 Hz for the modified suspension for all of the ground properties considered.

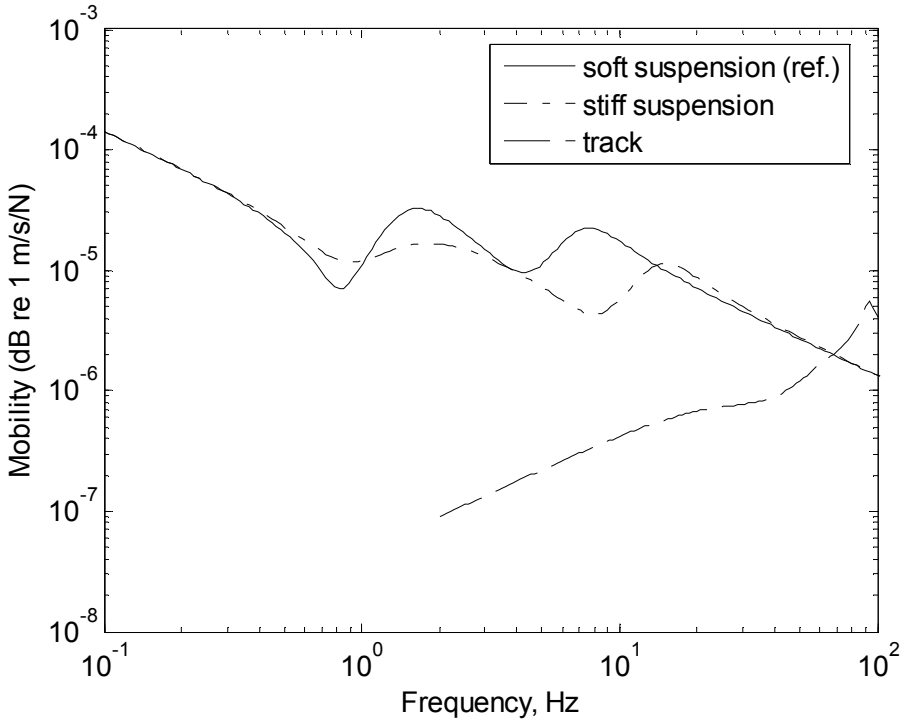

Figure 4.27. Point mobilities of vehicle and track for soft primary suspension stiffness (reference situation) and stiff primary suspension stiffness.

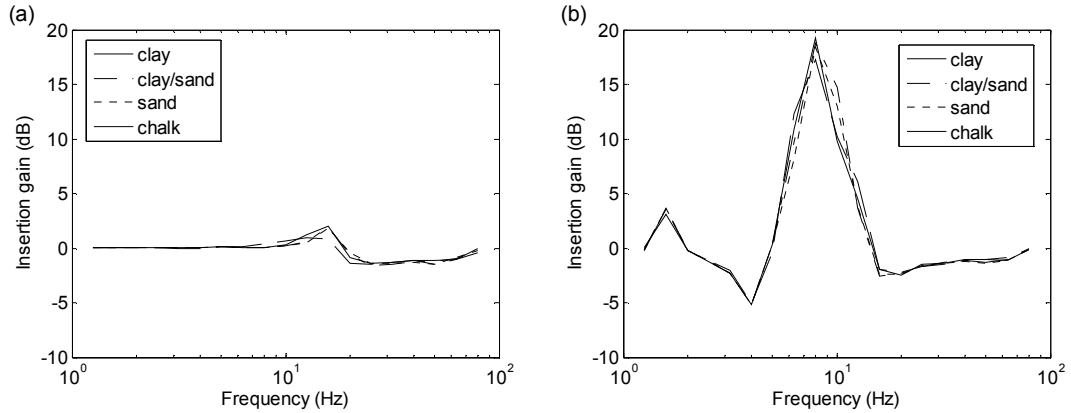

Figure 4.28. Insertion gain of the ground vibration due to change in primary suspension stiffness for various ground stiffnesses (a) at 0 m and (b) 25 m.

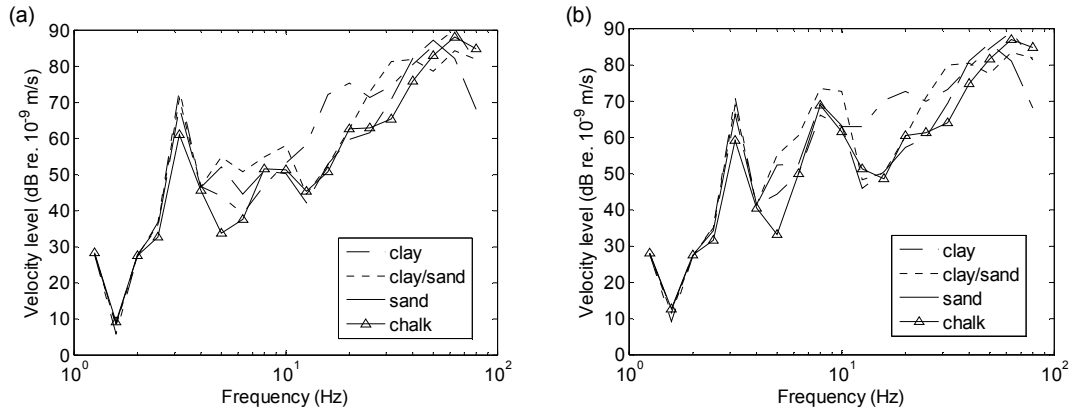

Figure 4.29. Ground vibration at 25 m away from the track for various ground properties (a) for reference case and (b) for modified primary suspension stiffness.

4.5.4 The effect of bogie mass

The effects of changing bogie mass are investigated next. The bogie mass has been doubled from its original value. Increasing the bogie mass shifts both suspension resonances and affects the vehicle mobility between 1 and 10 Hz, as shown in Figure 4.30. The insertion gain due to changing the bogie mass is shown in Figure 4.31. The large increase at 3 Hz and reduction at 5 Hz at 25 m correspond to changes in the mobility. At 0 m the low frequency part is dominated by the quasi-static component which is unaffected by the bogie mass. The influence of soil stiffness is seen to be small.

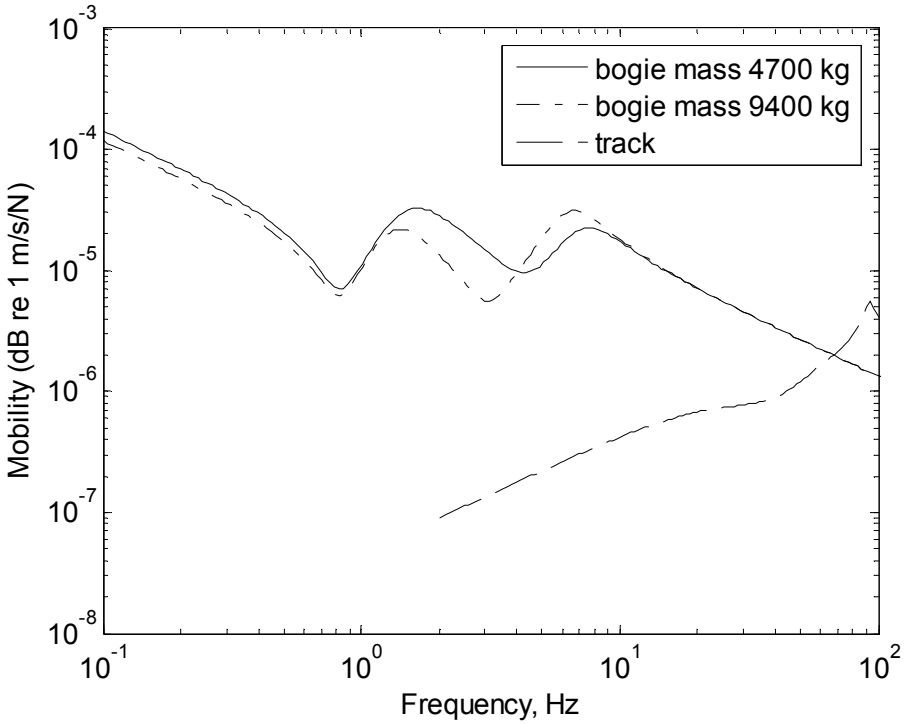

Figure 4.30. Point mobilities of vehicle and track for light bogie mass (reference situation) and heavy bogie mass.

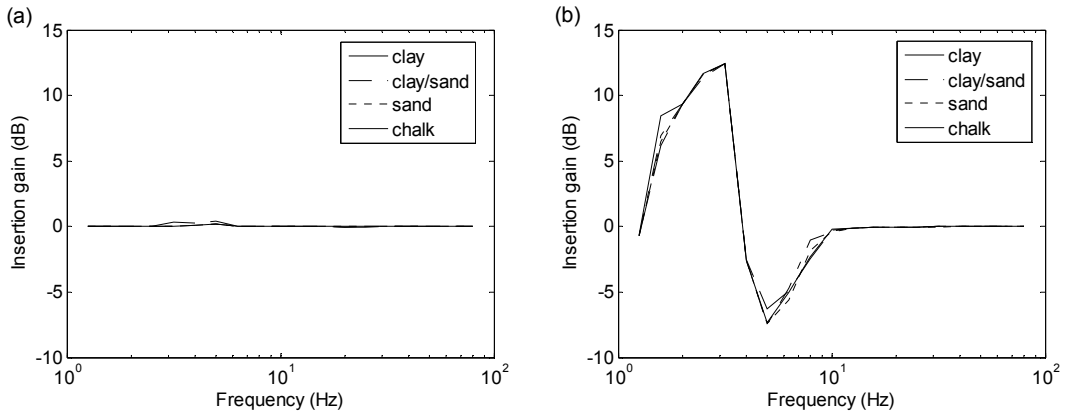

Figure 4.31. Insertion gain of the ground vibration due to change in bogie mass on various ground stiffnesses (a) at 0 m and (b) 25 m.

4.5.5 The effect of train speed

The responses at the distances close to and further away from the track are predicted on clay soil for a number of speeds of the train. Comparisons between the responses at various speeds, from 10 to 50 m/s, are shown in Figure 4.32. The results show a consistent increase in the amplitude at high frequencies. At 0 m the results show clear peaks in the response which correspond to the first few harmonics of the

vehicle length. For example, a strong peak is seen at 3.15 Hz at 25 m/s (see also Figure 4.4) increasing to 6.3 Hz at 50 m/s. This corresponds to a wavelength of 8 m, approximately 1/3 of the vehicle length. Another broad peak occurs at just over twice these frequencies which may be related to the bogie wheelbase of 2.6 m and distance between outer wheels of adjacent vehicles of 4.4 m. At 25 m from the track the results also show peaks in the response at certain speeds. The peak at about 4 Hz for various speeds is caused by the combination of the harmonics of the vehicle length and an anti-resonance in wheel mobility (see Figure 4.3).

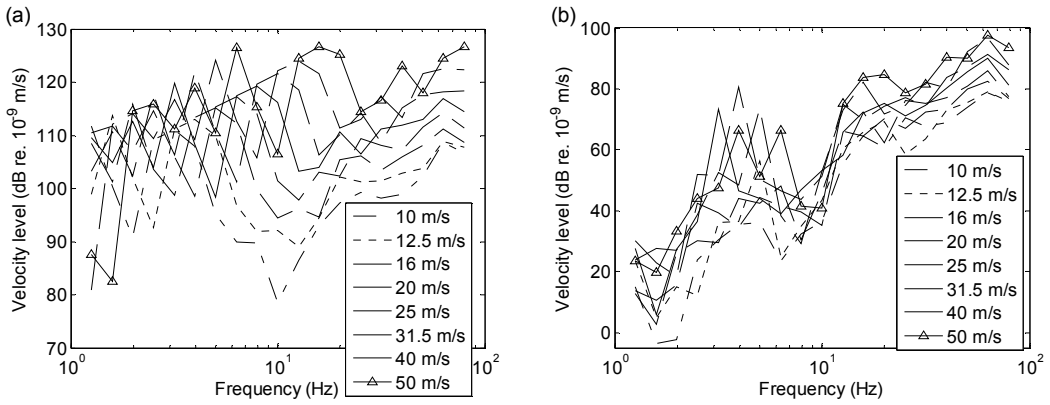

Figure 4.32. Ground vibration for variety of train speeds on clay soil (a) at 0 m and (b) 25 m.

As the speed of the train increases the effect of the quasi-static component dominates the vibration response at higher frequencies as shown in Figure 4.33. At distances further from the track the effect of the quasi-static component reduces. On the other hand the dynamic component dominates the vibration response at high frequencies above about 20 Hz for all distances as shown in Figure 4.33.

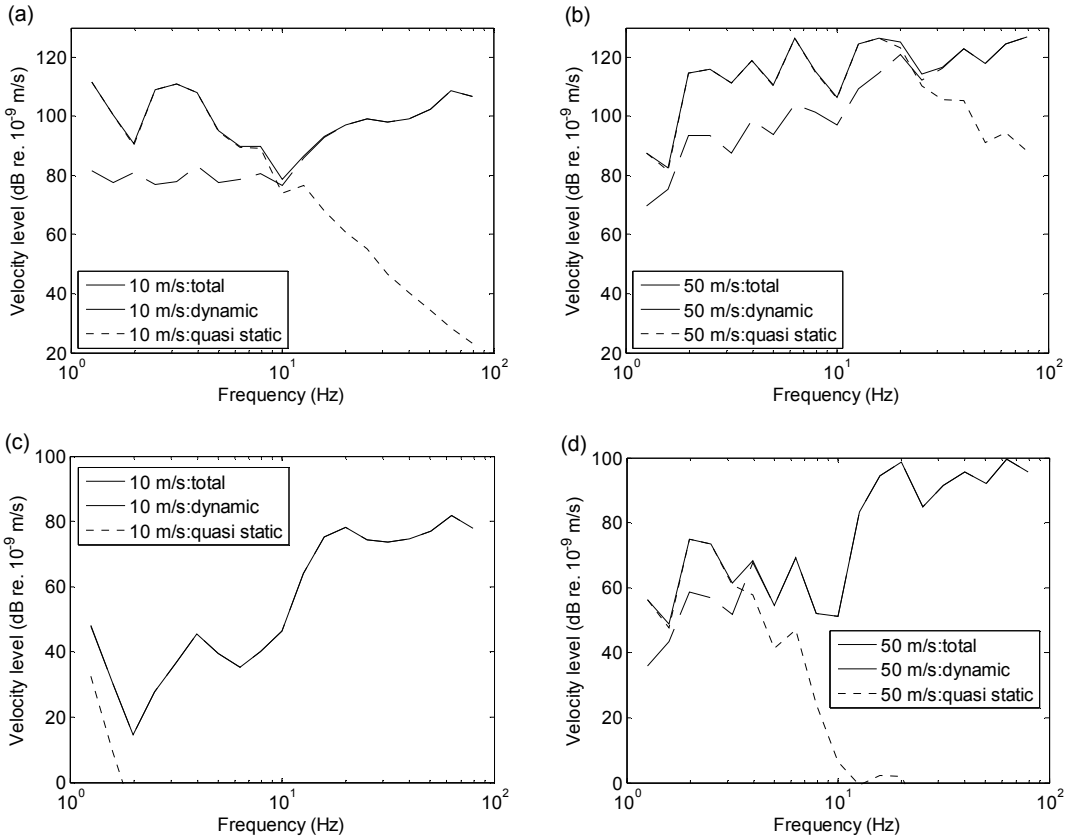

Figure 4.33. Ground vibration for variety of train speeds on clay soil (a) at 0 m with the train speed of 10 m/s, (b) at 0 m with the train speed of 50 m/s, (c) at 10 m with the train speed of 10 m/s and (d) at 10 m with the train speed of 50 m/s from the track; comparing total, quasi-static and dynamic loads.

4.5.6 The effect of axle spacing

The last parameter considered is the axle spacing. The effect of changing the axle spacing is investigated in terms of the response at different distances away from the track and for various ground stiffnesses. For the reference case a peak is found at 3.3 Hz which is caused by the third harmonic of the vehicle length, 23 m, at the train speed of 25 m/s, as shown in Figures 4.5 and 4.32.

The modified vehicle has the bogie centre distance and bogie wheelbase chosen to give four axles that are equally spaced along the vehicle (5.75 m between axles). Changing the axle spacing to a regular spacing of 5.75 m causes a strong peak at about 4 Hz (4^{th} harmonic of the vehicle length corresponding to the wheel spacing of 5.75 m) and also at 8 Hz, as shown in Figure 4.34. It can be seen from Figure 4.34 that at further distances the ground stiffness has less effect on the ground vibration as

also seen previously in Figure 4.5. Nevertheless at 10 m away from the track there are some differences in the response particularly between 10 and 25 Hz corresponding to the ground properties.

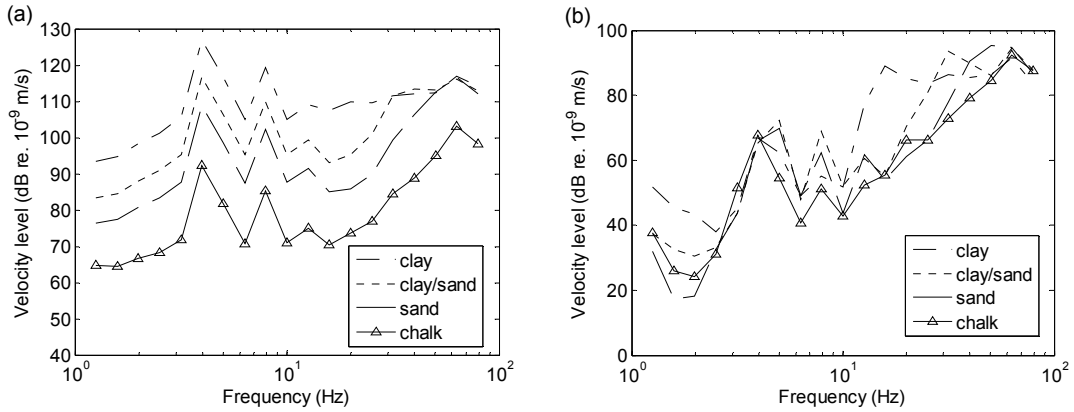

Figure 4.34. Ground vibration for the case of changing axle spacing on different soils (a) at 0 m and (b) 10 m from the track.

4.6 Conclusions

The effects of different parameters on the vibration have been investigated using a semi-analytical model of ground vibration (TGV) for a wide range of conditions at locations close to the track and further away. The predicted ground vibration is investigated on the soft clay soil due to quasi-static and dynamic load separately. It can be seen that the response beneath the track is dominated by the quasi-static loads up to 12.5 Hz whereas at 10 m away the dynamic loads are dominant above about 3 Hz. Similar conclusions have been found by Lombaert [2]. The insertion gain for the overall response follows that of the dynamic excitation for locations far from the track, but at 0 m it follows the quasi-static curve up to about 10 Hz, above which it tends towards the curve for dynamic excitation. It is clear from these results that an assessment of the insertion gain due to a change in rail pad stiffness should not be based on measurements too close to the track – in this case the distance should be at least 10 m to give representative results of the effect on the far field response.

The effects of variation in ground properties have been investigated on the track response, the dynamic and quasi-static components of the insertion gain due to changing support stiffness. It is found that ground stiffness has no effect on the track

response above 100 Hz (the resonance frequency of the track on support stiffness). At lower frequencies there are modest differences in track mobility due to the ground stiffness.

The effect of different ground properties on the vibration response has also been investigated. It is found that the responses at 0 m are significantly affected by the ground stiffness whereas the response at 10 m from the track is affected much less. A peak at 20 Hz found in the response at 10 m for clay soil shifts towards higher frequency as the ground becomes stiffer. This corresponds to the cut-on frequency of the ground layer.

The variations of ground properties have virtually no effect on the dynamic and quasi-static components of the insertion gain due to changing pad stiffness. It can be seen that both dynamic and quasi-static components are virtually unaffected by the ground stiffness. Introducing a typical soft baseplate with a more moderate change in stiffness ($1x10^8$ N/m^2) in the track support gives similar but reduced trends of insertion gains to the case for very soft baseplate ($3.5x10^7$ N/m^2).

Like softer rail pads, ballast mats and sleeper soffit pads lead to significant increases in ground vibration in the region 20-40 Hz at 10 m and beyond due to the lowered vehicle/track resonance. Reductions in vibration only occur above about 50 Hz. However, a measurement close to the track would suggest that the benefits extend to lower frequencies.

The train speed is also considered. The insertion gain corresponding to the quasi-static component shifts towards higher frequencies as the speed increases whereas that for the dynamic component is independent of train speed. Thus the overall results are slightly different for different speeds.

A number of vehicle design variants are considered. The effect of axle load has been investigated by doubling the body mass. It is found that the body mass affects the quasi-static component by a constant factor at all frequencies. Conversely the dynamic excitation is only affected at low frequencies, mainly below 5 Hz. It can

be seen that the overall insertion gain is dominated by the quasi-static excitation at 0 m. The effect is limited to lower and lower frequencies as the distance increases.

The effect of the vehicle unsprung mass has also been investigated. The wheelset mass is set to twice the reference value, corresponding to a typical powered axle. It is found that the dynamic component is affected by the unsprung mass above about 6 Hz whereas the quasi-static component is unaffected at all frequencies.

Comparisons between the responses at various speeds, from 10 to 50 m/s, are considered. As the speed of the train increases the effect of the quasi-static component dominates the vibration response at higher frequencies. At distances further from the track the effect of the quasi-static component reduces. On the other hand the dynamic component dominates the vibration response at high frequencies above about 20 Hz for all distances.

The effect of changing the axle spacing is investigated in terms of the response at different distances away from the track and for various ground stiffnesses. The modified vehicle has the bogie centre distance and bogie wheelbase chosen to give four axles that are equally spaced along the vehicle. This causes a strong peak at about 4 Hz (4^{th} harmonic of the vehicle length corresponding to the wheel spacing of 5.75 m) and also at 8 Hz. It is found that at further distances the ground stiffness has less effect on the ground vibration.

The TGV model, validated in Chapter 3, has been used to investigate the relative importance of quasi-static load and dynamic load in different situations at locations close to the track and further away. However the model is limited to excitation by stationary roughness profiles. Therefore a new model is developed, using a hybrid approach. In Chapter 5 the model will be introduced and described in detail.

5. Hybrid model

5.1 Introduction

In Chapter 4 the ground responses due to quasi-static and dynamic loads have been investigated using the TGV model. The track in TGV is represented as an infinite, layered beam resting on one or more elastic layers overlying a three-dimensional half-space of ground material. The applied force is determined from the moving axle loads and/or the vertical rail irregularities. The vehicles can be described as multiple rigid body systems which are coupled with the track/ground model. However, the model cannot be used to investigate other excitation mechanisms. Moreover the maximum frequency is limited to 80 Hz in one-third octave bands due to a numerical integration problem.

Therefore, in this chapter an alternative modelling approach is introduced. This will allow investigation of some other excitation mechanisms, such as parametric excitation due to sleeper-passing effects, dynamic excitation due to defects on the track at particular fixed locations and excitation due to variations in ballast or ground stiffness beneath each sleeper. It is easier to use the finite element method to study such effects. To achieve this, the wheel/track interaction model developed by Croft [109] is applied. This model is originally based on the work of Nielsen and Igeland [110] and Nielsen and Oscarsson [111]. It consists of a series of wheels running along a track supported by discrete sleepers on ballast spring over a rigid ground. Vibration is induced by the roughness between the rail and wheel as well as the moving axle loads. The model operates in the time and spatial domain and was originally developed to study wheel/track interaction and rail roughness growth [109,112]. As the ballast is modelled as a damped spring connected at each sleeper to the rigid ground underneath, this allows various excitation mechanisms to be modelled. It also allows the calculation of wheels moving along the track in the time domain.

However the ground in this model is represented as a rigid support. Therefore, this model is modified here to add the influence of the ground underneath the ballast instead of a rigid ground. The spring and damper beneath the sleeper are modified to represent the ballast and the ground beneath. The model is used to determine the force

time histories beneath each sleeper. The axisymmetric layered ground model developed by Kausel and Roesset (kandr model used in Chapter 3 and described in Appendix A) [33] is then applied to represent an elastic layered ground. This is used to obtain transfer mobilities from each sleeper position to a receiver position. These are combined with force spectra obtained from the wheel/track interaction model (including cross spectra between the various sleeper positions) to give the response at the receiver location. This can therefore be seen as a hybrid model which combines the time domain wheel-track interaction model and a simple layered ground model in the wavenumber-frequency domain.

5.2 Time domain vehicle-track interaction model

In this section the model of Croft [109] is described. This will later be modified. The finite element method is used to predict the vibration of the track system. This time domain vehicle-track interaction model, based on the work of Nielsen et al [110,111], consists of a series of wheels running along a track. The track is supported by discrete sleepers on springs/dampers representing ballast above a rigid ground, as shown in Figure 5.1. The vehicle is represented as unsprung masses with no coupling between the wheels. As shown in Chapter 4 the effect of the primary and secondary suspensions on the vibration response is limited to frequencies below about 7 Hz. For frequencies between this and about 200 Hz, the wheel mobility can be represented using a simple model based on its unsprung mass with no need to include bending modes of the wheel [3]. This is therefore sufficient for the frequency range of interest in this study.

The track is truncated to 60 sleeper bays. The rail is connected to discrete sleeper masses at an equal spacing of 0.6 m although this can also be varied. Rail pads and ballast are modelled as spring-damper elements, with a simple viscous damping model, located at the sleeper positions. Timoshenko or Euler-Bernoulli beam elements can be selected. For the present study, Euler-Bernoulli beam elements are chosen due to the frequency range of interest which is up to 250 Hz. The Euler beam model can be used reliably to predict the rail response due to vertical dynamic excitation for frequencies up to 500 Hz [3].

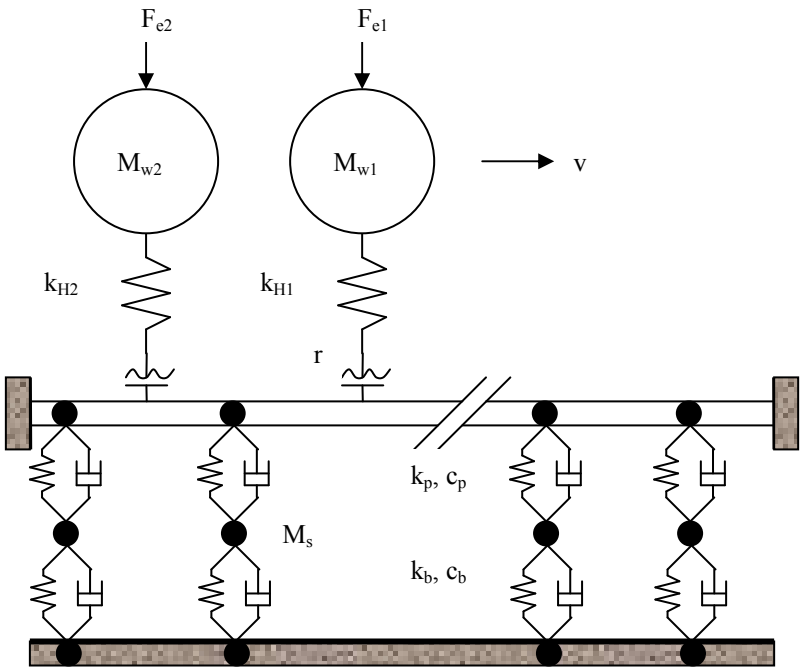

Figure 5.1. Time and spatial domain wheel track interaction model [109].

In the original model the track ends are constrained in displacement and rotation to represent clamped ends. At all other nodes only vertical displacement and rotation in the vertical plane are considered; lateral effects are not included. In order to reduce calculation times, a modal summation approach is used and only modes with natural frequency up to 800 Hz are included. Whereas Croft used 6 or more beam elements for the rail for each sleeper span, in the present study only 2 elements per span are used. This is sufficient as the wavelength in the rail at 250 Hz is 2.8 m (more than four sleeper spans) as shown in Figure 5.2. This gives more than nine elements per wavelength.

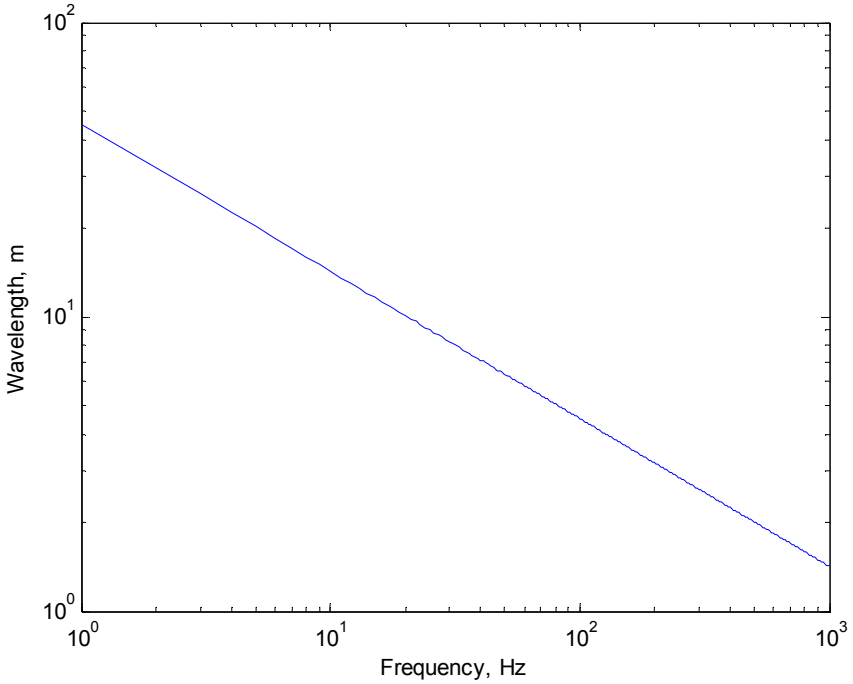

Figure 5.2. Calculation of wavelength for the rail using Euler-Bernoulli beam model.

Equations of motion for the track and vehicle including coupling of wheel and track models can be found in Appendix C. Although Croft and Nielsen et al used this model to represent a single rail, in the present study the track parameters are chosen to represent two rails and the vehicle unsprung masses represent the whole wheelset. This allows direct comparison with the models in Chapters 2 to 4.

As shown in Figure 5.1 axle loads are applied to each wheelset. The equations of motion of the system are solved using a state-space formulation with a time-stepping routine, including motion of the wheelsets along the track. A similar technique was used by Nielsen and Igeland [110]. Four wheelsets are used to represent two adjacent bogies (at the ends of adjacent coaches) as shown in Figure 5.3. Each is linked to the rail by a non-linear Hertzian contact spring. A roughness profile has been generated based on the one-third octave spectrum of roughness measured at the Steventon site (see Figure 3.45). This is used as the excitation. The response can also be calculated using a smooth track for calculation of the vibration response due to only quasi-static loads.

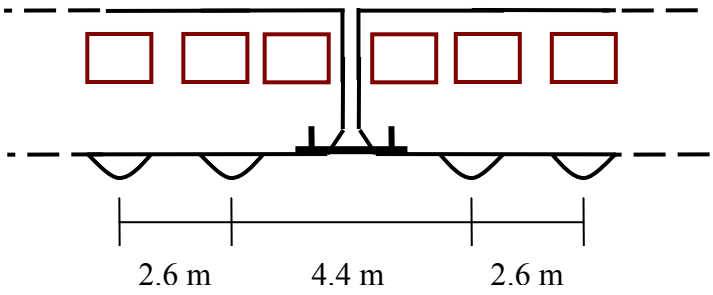

Figure 5.3. Spacing between wheels set used in the hybrid model.

Due to the use of a finite element model of the track its length has to be truncated; similar to Croft [109] 60 sleeper bays are used. However, in order to reduce the effect of the finite length, the track has been modified to make it 'circular'. The details of this will be described later in section 5.4.

5.3 Frequency-wavenumber ground model

A layered ground model based on equations presented by Kausel and Roesset [33] is an efficient method for predicting ground vibration due to point or line loads. It is based on a transfer matrix approach relating displacements and internal stresses at a given interface (between layers) to those at neighbouring interfaces. The model has already been used in Chapter 3 and is described in Appendix A.

The model is used to represent an elastic layered ground underneath the track. It is used to obtain transfer receptances from each sleeper position to a receiver position at a radial distance given by,

$$r = \sqrt{d^2 + x^2} \tag{5.1}$$

where d is the perpendicular distance from the receiver position to the track and x is the distance along the track, as shown in Figure 5.4.

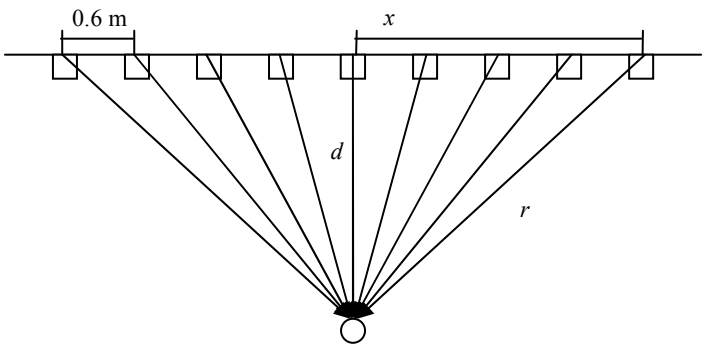

Figure 5.4. Positions of predicted receptances from the observation point to each sleeper.

The kandr model is used in this chapter to represent two different grounds, a soft clay soil and a stiffer ground typical of chalk. The clay soil has a 3 m soft layer over a stiffer half-space whereas the chalk ground has similar properties for the upper layer and the half-space. These two grounds are chosen as extremes of what is likely to occur in practice and are similar to ground properties considered in Chapter 4 although there the chalk ground had slightly different properties for the upper layer. The parameters used in the kandr model for ground properties are shown in Table 5.1.

The force in the kandr model is applied to a rigid circular indenter. The effect of indenter size on the point receptance is shown in Figure 5.5. The vibration response at the drive point becomes lower as the diameter of indenter size is increased, as the force is spread over a bigger area. However the indenter size has little influence on the response at a distance of 10 m away from the drive point as shown in Figure 5.5 (c) and (d) for chalk and clay soils respectively.

For the clay soil a broad peak occurs at about 20 Hz, corresponding to the cut on frequency of the layered ground. The results from kandr in Figure 5.5(d) at 10 m contain a dip at a frequency above 30 Hz, depending on the indenter width. At this frequency the wavelength in the top layer corresponds to the indenter size. Therefore, the transfer mobility is independent of indenter size only if the wavelength is greater than the indenter size.

Table 5.1. The parameters used in kandr for various types of ground.

Parameters of ground	Type		
	Clay	Chalk	Half-space
P-wave speed	1700 m/s	2100 m/s	2100 m/s
S-wave speed	120 m/s	1200 m/s	1200 m/s
density of layer material	2000 kg m^{-3}	2000 kg m^{-3}	2000 kg m^{-3}
Loss factor for layer material	[0.1 at 0 Hz] [0.3 at 300 Hz]	[0.1 at 0 Hz] [0.3 at 300 Hz]	[0.1 at 0 Hz] [0.3 at 300 Hz]
Layer depth	3.0 m	3.0 m	infinite

Note: The parameters for chalk in the present chapter are slightly different from those in Chapter 4.

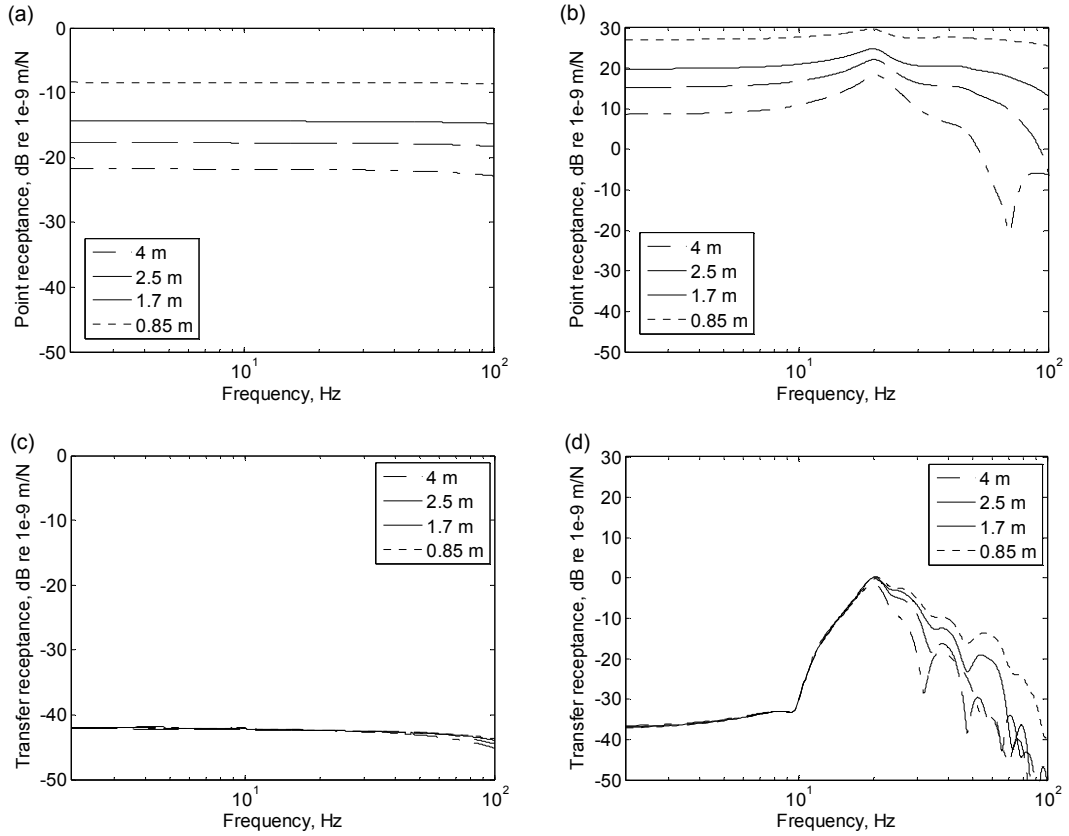

Figure 5.5. Point receptance for (a) chalk, (b) clay and Transfer receptance at 10 m away from the applied force for (c) chalk and (d) clay, with different indenter sizes in kandr model.

To consider possible interactions between adjacent sleepers, the predicted transfer receptances from the kandr model at various distances are shown in Figure 5.6 for an indenter size of 0.6 m. As the purpose is to investigate the effects of the adjacent sleepers in the direction along the track the indenter size is set to 0.6 m here to avoid the width exceeding the sleeper spacing. The predictions of ground response for clay are higher by about 35 dB than those for chalk. The difference between the response at 0 and 0.6 m for both properties of the soil is consistent except for clay at 20 Hz. The peak at 20 Hz is due to the cut-on frequency of the 3 m depth of clay on the stiff chalk half-space. Apart from this, the transfer receptance at the point 0.6 m away, is about 15 dB lower than the point receptance for both soil types considered. Therefore to include the ground beneath each sleeper in the hybrid model it is sufficient to consider only the point receptance. That is, coupling terms between the ground under adjacent sleepers can be ignored.

For use with the wheel/track interaction model the results from kandr are precalculated at a series of distances equally spaced from 0 to 160 m at a spacing of 0.6 m. The indenter size used here is 2.5 m which is the length of the sleeper in the direction perpendicular to the track. This indenter size is chosen in order to obtain the ground response as close as possible to those from TGV in which the width of the track-ground connection is 2 m. In order to calculate the response at various distances perpendicular to the track due to forces at all sleepers, an interpolation is applied to the predicted data to determine the transfer receptance at other points as required.

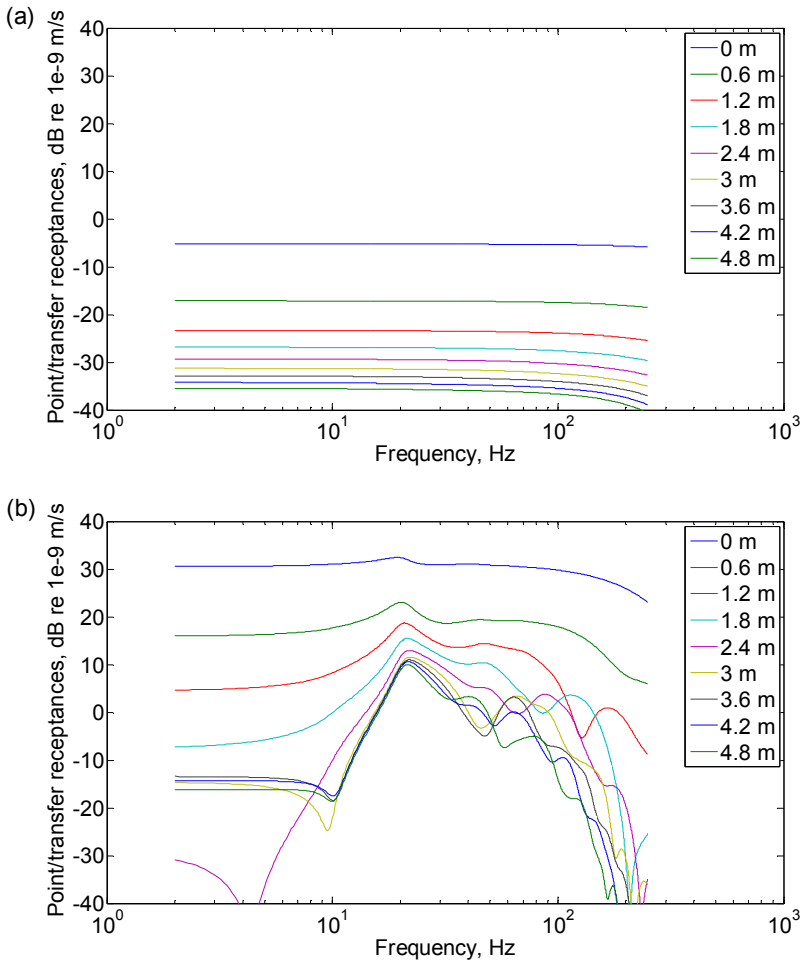

Figure 5.6. The point/transfer receptances predicted by kandr model at distances r varying from 0 to 4.8 m, for (a) chalk and (b) clay.

5.4 Hybrid model

The hybrid model combines the time and spatial domain wheel track interaction model with the transfer mobilities from kandr (obtained from the receptances by multiplying by $i\omega$). The parameters used to represent the vehicles are shown in Table 4.1 (except that suspension and sprung masses are not included). Track parameters are the same as those used in Chapter 4 (sleeper mass, rail mass and stiffness, rail pad stiffness and ballast stiffness including damping loss factors) as shown in Table 4.5 for the reference case. For the indenter size used here the diameter is 2.5 m.

5.4.1 Equivalent stiffness and damping loss factor

In the finite element model the "ballast" spring and damper should be chosen to represent the influence of the ground as well as the ballast. To add the influence of

the ground underneath the ballast instead of a rigid ground, this model is modified using the axisymmetric layered ground model [33]. Consider the system shown in Figure 5.7 (a). The ballast support consists of a stiffness, k_b, and damper, c_b. Beneath this is the layered ground represented by the mobility Y_g obtained from kandr. The objective is to find an equivalent spring and damper as shown in Figure 5.7(b) that represents this system as closely as possible for use in the time domain wheel/track interaction model. For harmonic motion the equations of motion can be written as follows

$$F = \left(k_b + c_b i\omega\right)\left(u_1 - u_2\right) \tag{5.2}$$

$$F = \frac{i\omega u_2}{Y_g} \tag{5.3}$$

where F is the applied force and u_1 and u_2 are the displacements above and below the spring/damper. Eliminating x_2 this gives

$$\frac{F}{u_1} = \frac{k_b i\omega - c_b\omega^2}{i\omega + k_b Y_g + c_b i\omega Y_g} = k_{eq} + i\omega c_{eq} \tag{5.4}$$

The real part of the equation gives the equivalent stiffness k_{eq} and the imaginary part gives the equivalent damping coefficient c_{eq}. Results are shown in Figure 5.8 for the two grounds considered here. Although there is some frequency dependence, especially for the softer soil, the average values are used in the model. These average values of equivalent stiffness and damping are used to represent ballast and ground support to replace k_b and c_b in the finite element model.

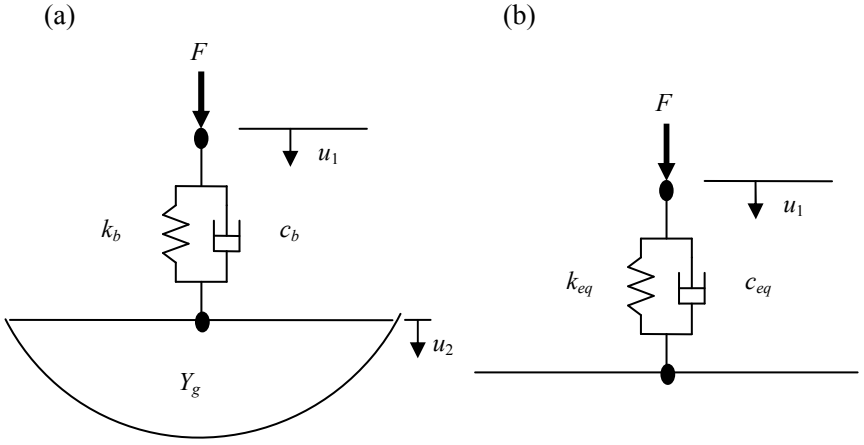

Figure 5.7. (a) The coupled system of ballast and layered ground (in hybrid model) and (b) equivalent spring-damper system.

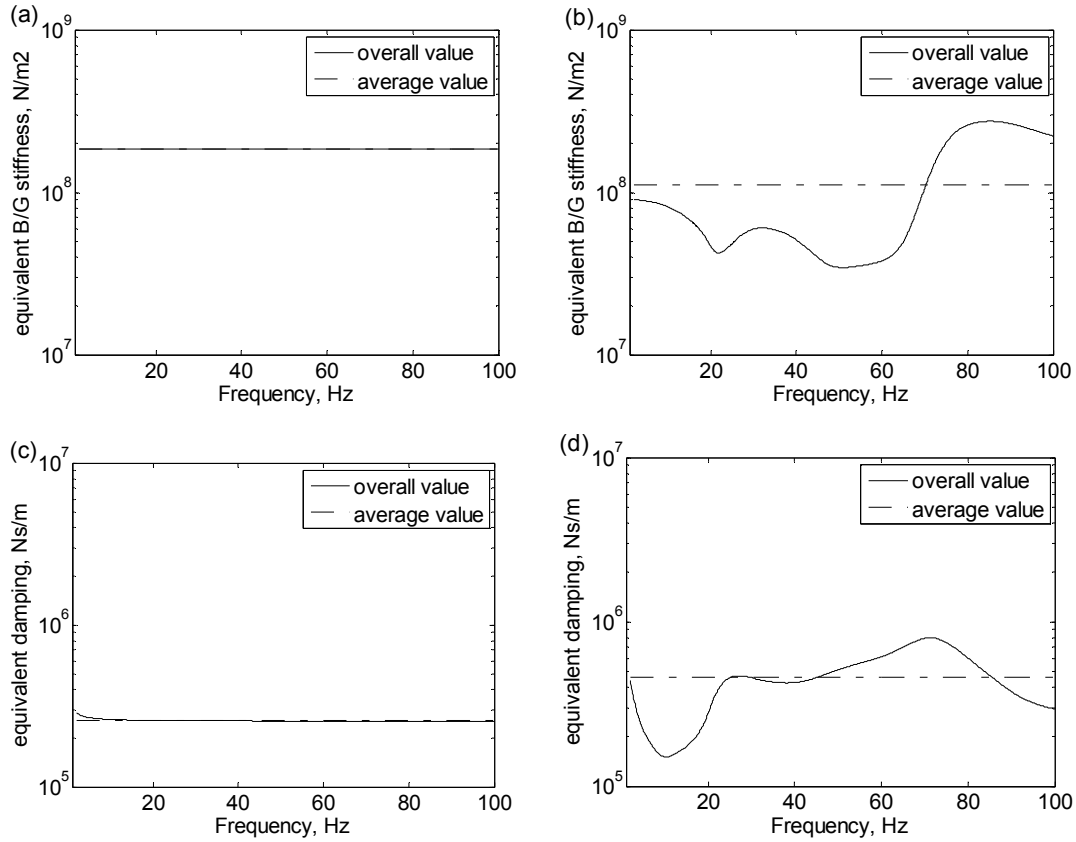

Figure 5.8.The equivalent ballast/ground stiffness for (a) chalk and (b) clay, the equivalent ballast/ground damping for (c) chalk and (d) clay.

5.4.2 Force acting on ground

The finite element model produces time histories of interaction forces, wheel displacements and velocities and track modal displacements and velocities. Using the modal summation method the latter can be used to find the displacements and velocities of each node point in the track model. In order to extract the forces, F_{ground}, acting at the ground interface beneath each sleeper, the displacements and velocities of each sleeper, u_s and $\dot{u}_s$, are multiplied by the ballast stiffness, k_b and damping c_b (the k_{eq} and c_{eq} determined in the previous section)

$$F_{ground} = k_b u_s + c_b \dot{u}_s \tag{5.5}$$

This yields a time history of the force acting on the ground below each sleeper. Examples are shown in Figure 5.9 for a case with no roughness. The force for each sleeper is offset vertically for clarity.

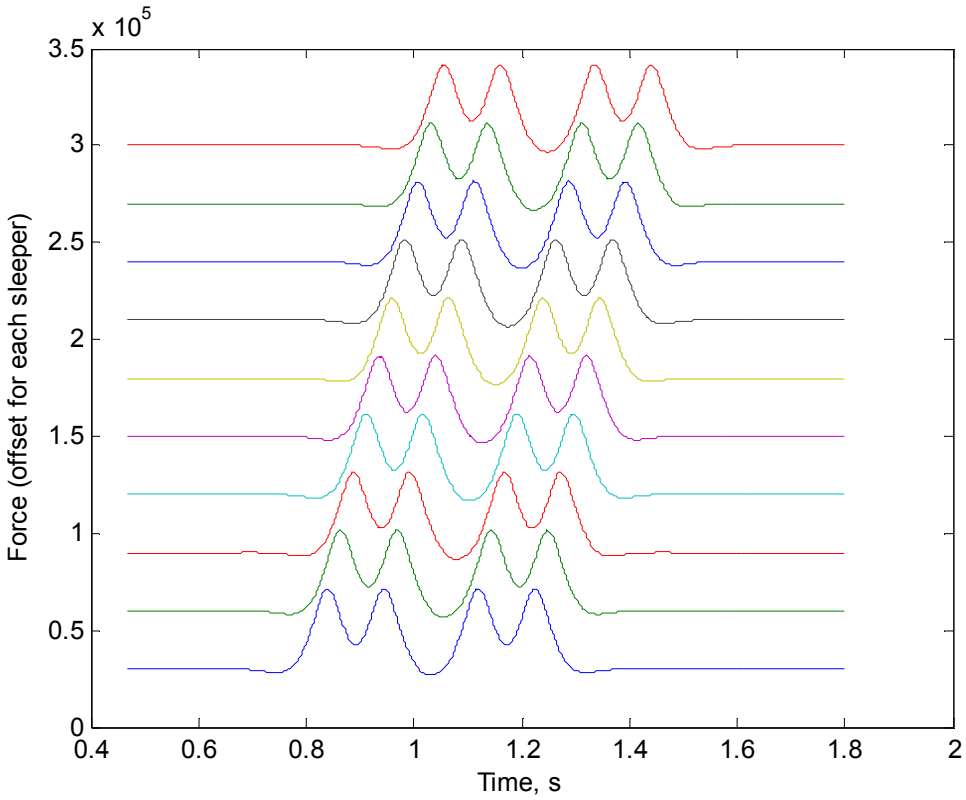

Figure 5.9. Examples of time history of applied forces for each sleeper.

5.4.3 Linking approach

Having obtained the force time histories these need to be converted to the frequency domain to allow them to be combined with the ground mobilities. The approach is to multiply force spectra from the wheel/track interaction model (including cross spectra) with the mobilities of the ground. The applied forces at the ground surface F_{ground} are converted to power spectral densities and cross power spectral densities, written as $\mathbf{S_{FF}}$. It is important to include all the cross spectral densities as these include information about the relative phase of each force and here account for movement of the wheels along the track. The spectral density of the ground response velocity at the receiver position is given by [113]

$$S_{vv} = \mathbf{Y}^{\mathbf{H}}\mathbf{S_{FF}}\mathbf{Y} \tag{5.6}$$

where S_{vv} is the power spectral density of the ground velocity,

$\mathbf{Y}$ is a matrix of ground mobilities,

$\mathbf{S_{FF}}$ is a matrix of power spectral densities and cross power spectral densities of the forces at the ground surface,

^{H} is the Hermitian transpose (complex conjugate transpose).

The power spectral densities and cross power spectral densities of the forces, the elements of $\mathbf{S_{FF}}$, can be found from $S_{F_iF_j}(f) = \frac{1}{T}\left[\tilde{F}_i^*(f)\tilde{F}_j(f)\right]$, [113], where

$\tilde{F}_i(f)$ is the discrete Fourier transform of the force $F_i(t)$

* is complex conjugate

T is the analysis length,

f is frequency.

The velocity response is finally converted to one-third octave bands and expressed as an average over the passage time of the "vehicle", in this case corresponding to a length of 9.6 m, to allow direct comparison with results from TGV.

5.4.4 Circular track

In order to reduce the effect of the finite length, the track has been modified to make it 'circular'. The modified model is shown in Figure 5.10. The advantage of the circular track compared with making the track longer is that the number of degrees of freedom is not increased. Both ends of the track are then connected together.

Figure 5.11 shows the point receptance of the track and the transfer receptances to two distances along the track. It can be seen that at only 5.4 m from the drive point, the vibration drops by over 40 dB at low frequency. This shows that the length of track (36 m) is sufficient to avoid interference from waves propagating around the circular track.

The length of the track for the normal case is 36 m. To allow the vehicle to travel further than this results are calculated for more than one lap. The results shown in this chapter and Chapters 6 and 7 are based on calculations over 4 laps unless otherwise stated.

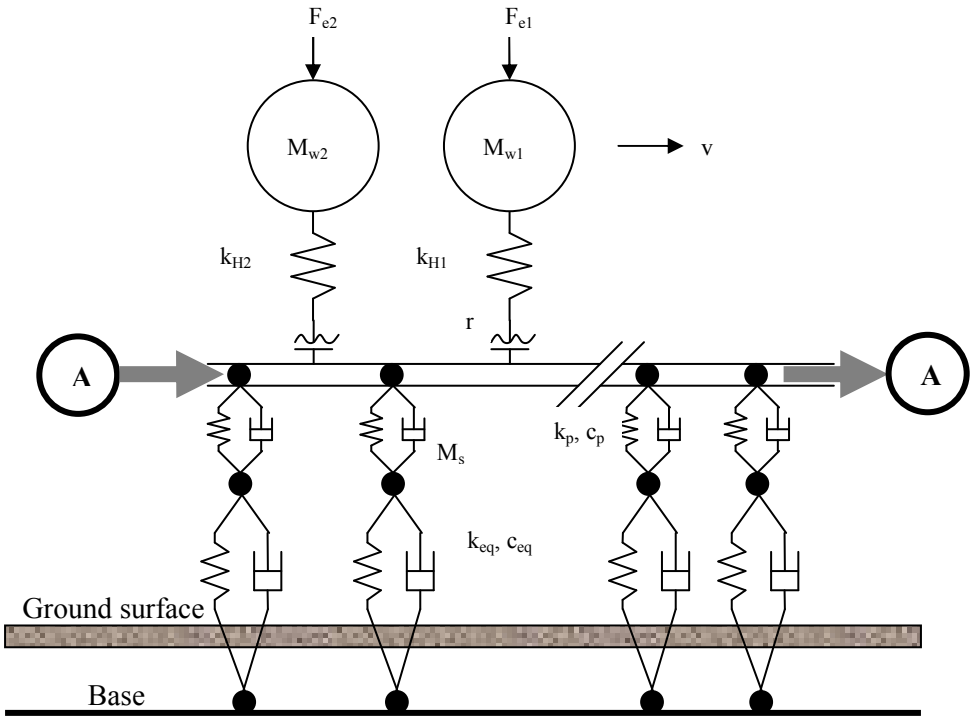

Figure 5.10. Modified model with circular track on a layered ground.

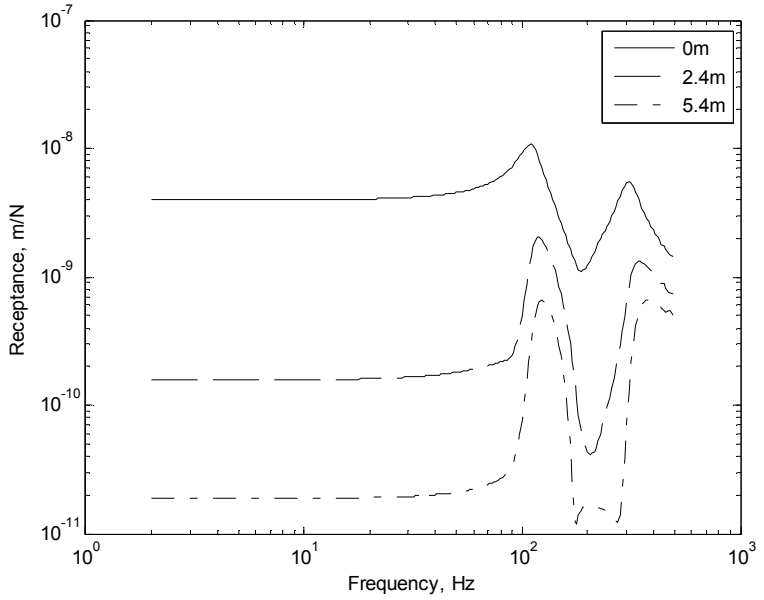

Figure 5.11. Point and transfer receptance on the circular track.

5.4.5 Unravel and zero padding

In order to extract the forces from the circular track, for instance for four laps, a specific 'unravel' process is applied. This method rearranges the forces applied at each sleeper to reconstruct a longer section of track. Consider the four wheels centred on a certain position B as shown in Figure 5.12(a). The sleepers in front and behind of

B can be associated with the points on the circle up to a point A located on the opposite side of the circle. Points beyond A will have a negligible force so these forces are set to zero in Figure 5.12(b). Figure 5.13 shows the force time histories before and after the unravel process has been applied.

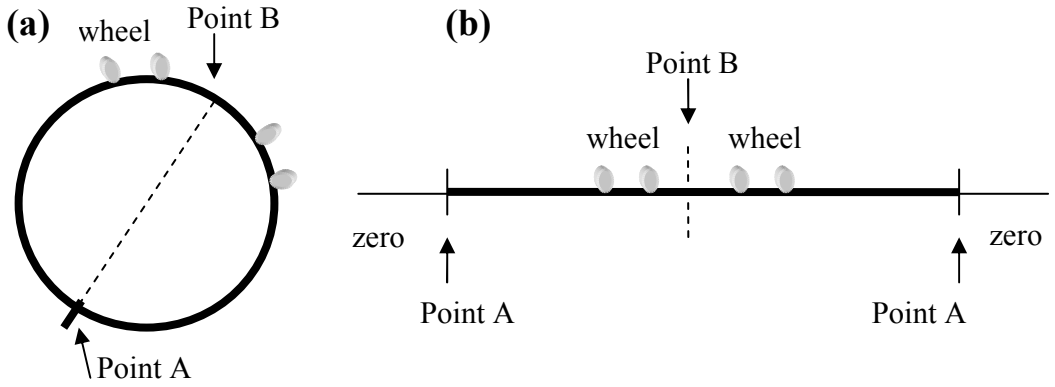

Figure 5.12. Start and end point in the circular track (a) before and (b) after unravel process.

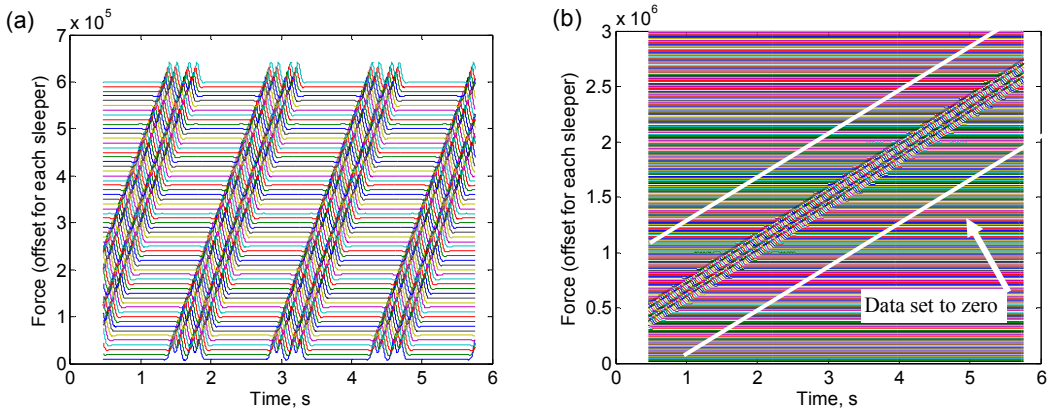

Figure 5.13. Applied force acting on each sleeper (a) before and (b) after unravel process.

In addition zero padding is applied to F_{ground} in order to make the frequency array obtained from the hybrid model match with those in the precalculated results from the kandr model. The frequency spacing used in the kandr model is 0.1 Hz whereas in the results from the time domain model it depends on the analysis time $df = 1/T$. T is selected such that df is a multiple of 0.1 Hz. Then the frequencies from kandr are selected corresponding to the frequencies obtained from the time domain

model in order to evaluate equation (5.6). Finally the narrow frequency band spectrum of velocity S_{vv} is converted to one third octave bands.

5.5 Comparison of hybrid model and TGV model

5.5.1 Parameters

In order to validate the hybrid model, the TGV model is used to compare the prediction of ground vibration at various distances. As mentioned in Chapter 3, the track is represented in TGV as an infinite, layered beam resting on one or more elastic layers overlying a three-dimensional half-space of ground material. The model operates in the frequency/wavenumber domain. It is coupled to a moving vehicle model.

The vertical dynamic behaviour of the train is modelled in TGV using a multi-body system with both primary and secondary suspensions. As in Chapter 4 the parameters used represent a typical EMU train with a speed of 25 m/s (see Table 5.2). The support system underneath the track is also included with no embankment. For simplicity, the ground is modelled as a half-space of chalk (see Table 5.1). The clay soil will also be considered in Chapters 6 and 7. Track parameters used in the hybrid model are also shown in Table 5.3.

Table 5.2. Properties used to represent the vehicles in TGV model.

	Mass (kg)		Stiffness (MN/m)	Damping (kNs/m)
Wheelset	1200	Contact stiffness	2420	-
Bogie	4700	Primary suspension	1.6	20
Vehicle body	30000	Secondary suspension	0.47	33.6

Table 5.3. Parameters used to represent track in hybrid model (for two rails).

Parameters			Reference
Rail	bending stiffness, N/m^2		1.26×10^7
	loss factor		0
	mass per unit length, kg/m		120
Rail pad	stiffness per sleeper, N/m		2.1×10^8
	damping factor, Ns/m		1.84×10^4
Sleeper	mass per sleeper, kg		294
Ballast	Connected with chalk ground	Equivalent stiffness, N/m	1.84×10^8
		Equivalent damping, Ns/m	2.56×10^5
	Connected with clay ground	Equivalent stiffness, N/m	1.11×10^8
		Equivalent damping, Ns/m	4.57×10^5

The vehicle and track parameters used in TGV are the same as in Chapter 4 except ballast damping is set to 1.0 in Chapters 5 to 7. Although a value of 0.2 was found in recent measurements of the dynamic ballast stiffness by Herron [106] and used in Chapter 3, the value of 1.0 is retained. Here, however, the train is set to one car (four wheelsets) representing the bogies at the ends of adjacent vehicles (as in the hybrid model, see Figure 5.3). This "vehicle" has a length of 9.6 m with a wheelset spacing of 2.6 m within a bogies and 7.0 m between bogies centres. The excitation due to the roughness is based on the measured spectrum from Steventon (see Chapter 3, Figure 3.45). The four wheelsets are allowed to run four times around the circular track to generate a long enough signal. The parameters used in the hybrid model are set as close as possible to those in TGV.

The contact width between the track and ground in TGV is chosen as 2 m. For the indenter size used in hybrid the diameter is chosen as 2.5 m in order to obtain the ground response as close as possible to those from TGV, as shown in Figure 5.20.

The effect of the contact width has been investigated in order to check sensitivity. Figure 5.14 shows results for the quasi-static load only for two different

contact widths. Figure 5.15 shows equivalent results including the dynamic excitation as well. These are both for the chalk soil. The results show that the contact width has a strong effect on the vibration response due to quasi-static load, immediately underneath the track. Also for the dynamic load, Figure 5.15(a) there is a consistent although smaller difference. Increasing its size by a factor of 2 gives about 5 dB less response at all frequencies. On the other hand at 10 m the contact width has no effect on the quasi-static ground response below 5 Hz. Above 5 Hz a difference of about 20 dB can be found due to the quasi-static load. However, the ground response here is dominated by the dynamic excitation as shown in Figure 5.15 (b) which is unaffected by the contact width. In other words the track width has no effect on the overall ground response at the distance further away.

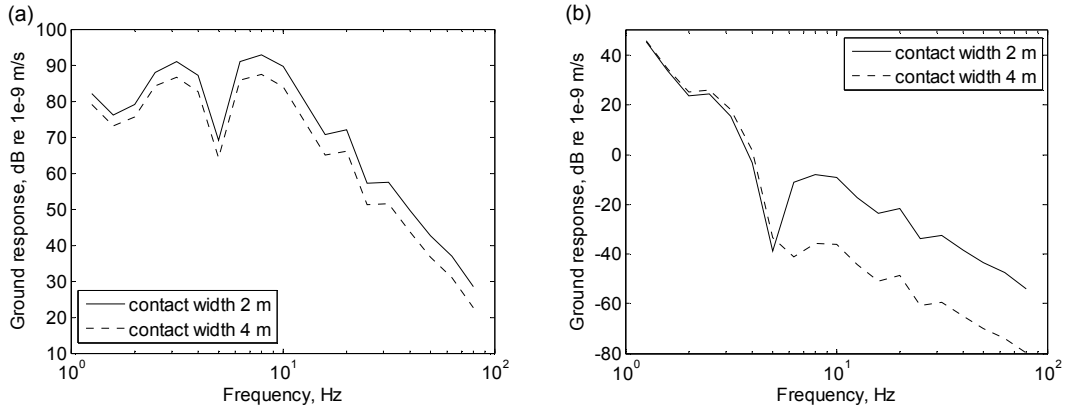

Figure 5.14. Comparison of the ground responses at (a) 0 m directly underneath the track and (b) 10 m away from the track for contact width of 2 m and 4 m, due to quasi-static load in TGV.

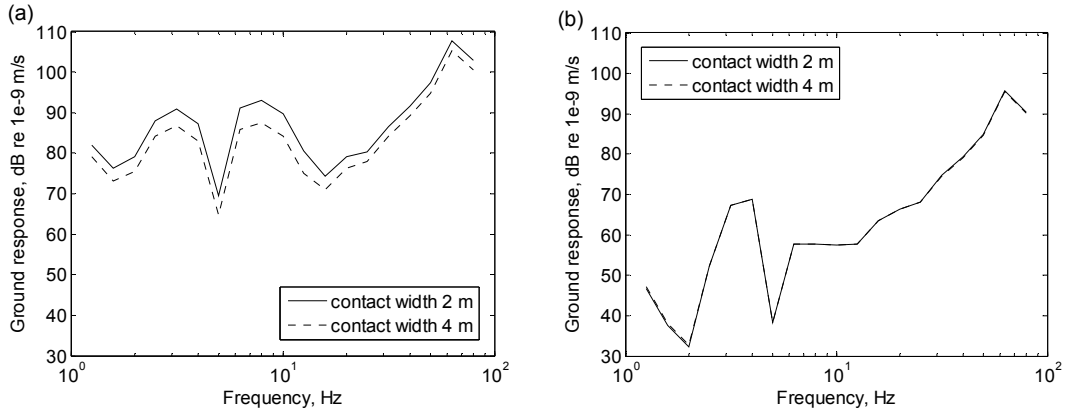

Figure 5.15. Comparison of the ground responses at (a) 0 m directly underneath the track and (b) 10 m away from the track for contact width of 2 m and 4 m, due to total excitation in TGV.

5.5.2 Comparison of rail vibration

5.5.2.1 Quasi-static component

Due to the different approaches used in the hybrid and TGV models, a comparison is made first of the rail responses predicted with the same parameters. The rail responses are also due to quasi-static and dynamic loads. In order to check the responses due to the quasi-static load, the rail deflection in the wheel/track interaction model is first compared with a calculation of estimated total track stiffness. Figure 5.16 shows the deflection under each wheelset at the middle of the track when the train passes. As each wheel passes along it produces a deflection on the rail.

To check the static deflections, the total track stiffness K_T [3] can be found as

$$K_T = 2\sqrt{2}\left(EI\right)^{1/4} s^{3/4} \tag{5.7}$$

where $s = \left(\frac{1}{K_P} + \frac{1}{K_b}\right)^{-1} / 0.6$ is the support stiffness per unit length

K_b is the stiffness of ballast per sleeper (176.6 MN/m)

K_P is the stiffness of rail pad per sleeper (210 MN/m)

EI is the bending stiffness of the rail (12.6 MNm^2)

Using these values, K_T is found to be 239.6 MN/m. For an axle load W of 108.3 kN this gives an expected deflection $W / K_T =$ 0.45 mm (downward). This agrees reasonably well with the results from the hybrid model shown in Figure 5.16.

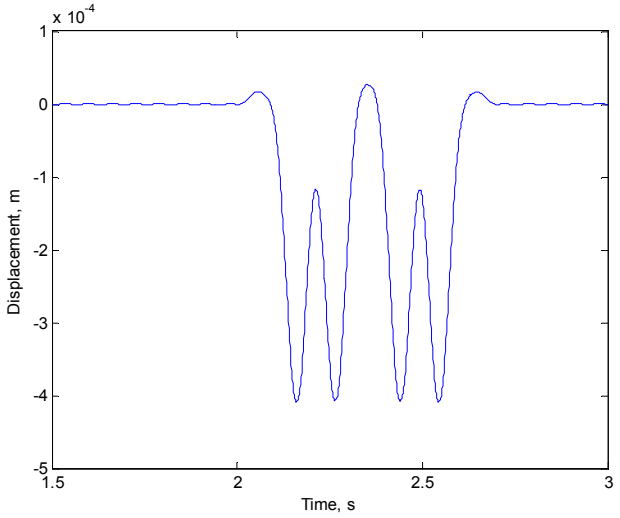

Figure 5.16. Deflection of the rail at a point in the centre during the passage of four wheelsets from time domain model.

5.5.2.2 Dynamic component

To provide an independent check of the two different approaches, TGV and hybrid model, a simple wheel/rail interaction model is used. The surface irregularities or roughness profiles are represented by their one-third octave spectra. The wheel is modelled as an unsprung mass connected to the rail by the Hertzian contact spring. In order to compare the three different models for the simplest condition, the rail responses are predicted, not the ground vibration response. The track is modelled using a beam on a continuous foundation of rail pads, sleeper and ballast in a model (called 'rodel') developed for rolling noise [3]. This track model is based originally on the work of Grassie et al [114]. This model is extended to calculate the average rail response during a pass-by. This combined model is newly called 'robin', which stands for 'response of beam interaction'.

The details for the wheel/rail interaction and excitation by roughness are described in Appendix D. The average vibration during the passage of a wheel is calculated allowing for the rate of decay of vibration with distance [3].

$$\overline{u_r^2} = \frac{1}{L}\int_{-L/2}^{L/2} \left(u_{r_0} e^{-\beta x}\right)^2 dx \tag{5.8}$$

where β = imaginary part of rail wavenumber (propagating wave)

x = distance

L = integration length

u_{r_0} = rail vibration at contact point

The vibration is also normalised by the time taken for the passage of the "train", i.e. the vehicle of length 9.6 m as for TGV. All parameters used in TGV, hybrid and robin are chosen as closely as possible among these three models. The results showing the comparison of rail responses between the three models are given in Figure 5.17. The quasi-static load dominates the response below about 12 Hz (as also found in Chapter 4). Therefore the static deflection in the hybrid model was checked independently as shown above[5].

[5] It was found that the results from TGV had to be increased by 3 dB to achieve this agreement. It was confirmed that this error was in the post processing of TGV and not the hybrid method by calculating the static deflection above. The results shown throughout this thesis include this correction. This correction should also be applied to calculations for ground vibrations in [115-117].

The rail response from robin is also compared as shown in Figure 5.17. The result from the robin model is due to only the dynamic load (no quasi-static load). Therefore the result below 25 Hz is much less than from the other models.

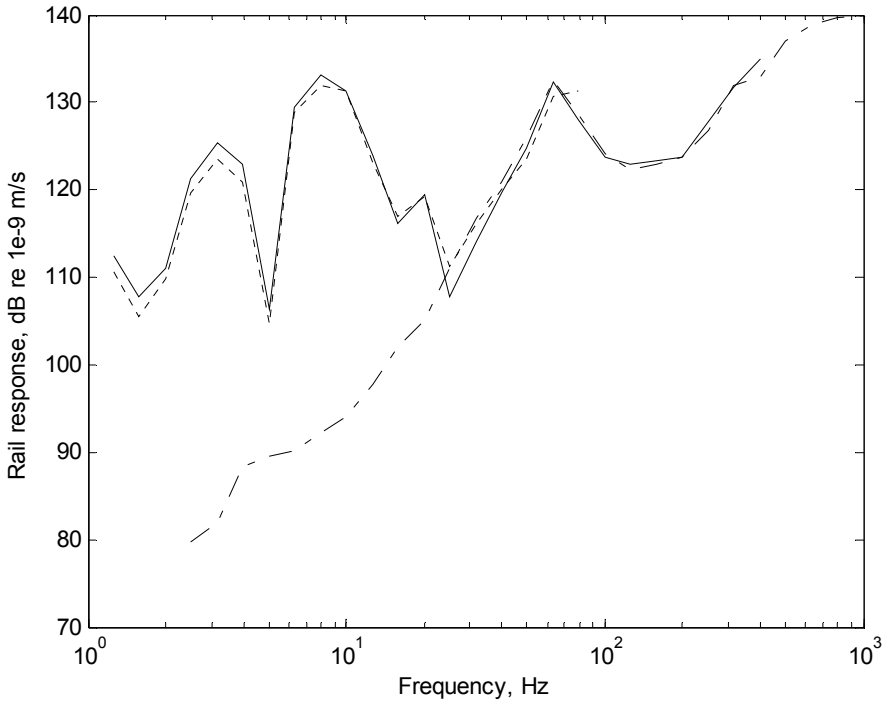

Figure 5.17. Comparison of rail responses due to total load between. — hybrid; ·····, TGV and; – · – robin models.

Comparison between the rail responses of the three models shows good agreement. Below 20 Hz the rail response is dominated by the moving quasi-static load and the results of the hybrid model and TGV match very well. Above 25 Hz, where the dynamic component dominates, all three models give similar results. This confirms the validity of the models

5.5.3 Results for ground vibration

Comparisons of the ground responses due to quasi-static and total excitation at 0 and 3 m away from the track between TGV and the hybrid model are shown in Figures 5.18 to 5.21. Figure 5.18 shows the ground responses due to the quasi-static load at 0 m (underneath the track). The peaks at about 40 and 80 Hz are due to the sleeper passing effect. For a train speed of v = 25 m/s, when a train passes over the sleepers at spacing λ = 0.6 m, a frequency $f = \frac{v}{\lambda} = \frac{25}{0.6} = 41.6$ Hz and its harmonic

are generated. The results from the TGV model contain no effect of the sleeper spacing due to the use of a continuous support whereas this effect can be seen in the results from hybrid model (which has discrete supports) as seen in Figures 5.18 and 5.19.

A reasonable agreement is found at low frequency. The peaks below 10 Hz are due to the axle spacings. The difference found is probably caused by the circular and rectangular shapes of the contact between ground and track in the two models. The ground response in TGV due to quasi-static load has a good agreement with that from hybrid. Although primary and secondary suspensions are included in TGV whereas only the unsprung mass is modelled in the hybrid model, it has been shown in Chapter 4 that the dynamic properties of the vehicle have no effect on the response at 0 m (i.e. the quasi-static response).

Figures 5.20 and 5.21 show the responses due to total excitation at 0 and 3 m away from the track respectively. It can be seen that the agreement is generally good especially above 10 Hz. The result from the hybrid model was lower than that from TGV for the rail response. However, the ground response from the hybrid model is slightly higher as shown in Figure 5.20. This might be due to the contact width used in the hybrid model being slightly larger than that in TGV.

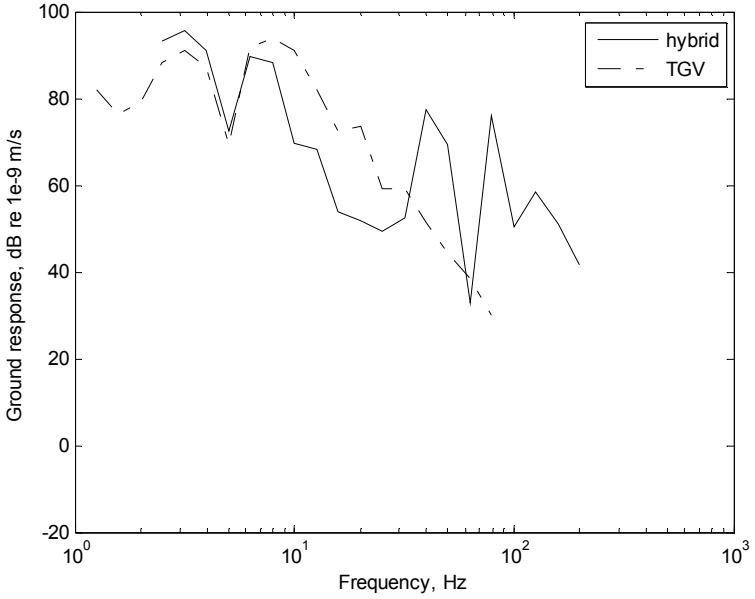

Figure 5.18. The ground responses due to quasi-static load at 0 m underneath the track from hybrid model comparing with the results from TGV model.

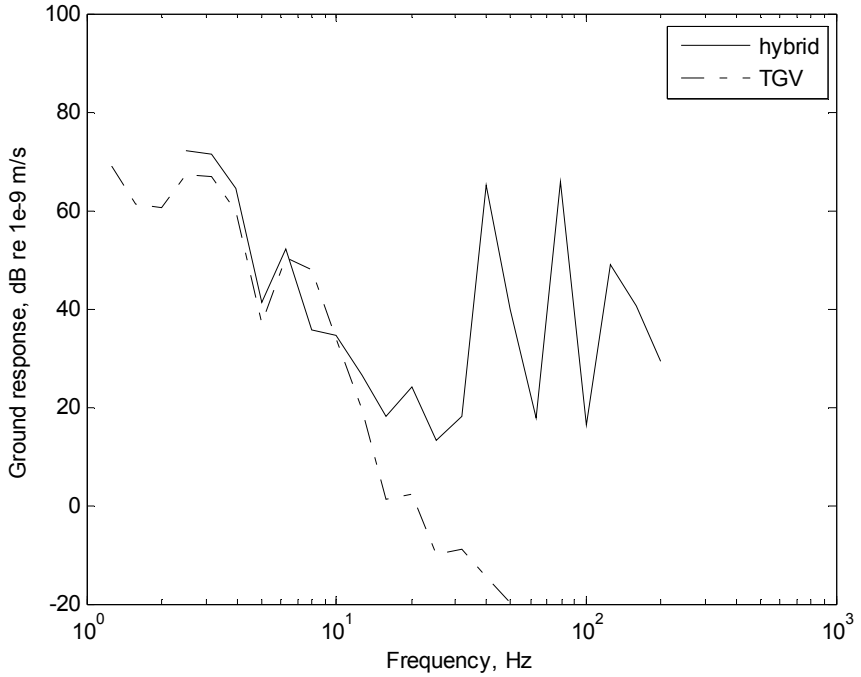

Figure 5.19. The ground responses due to quasi-static load at 3 m away from the track from hybrid model comparing with the results from TGV model.

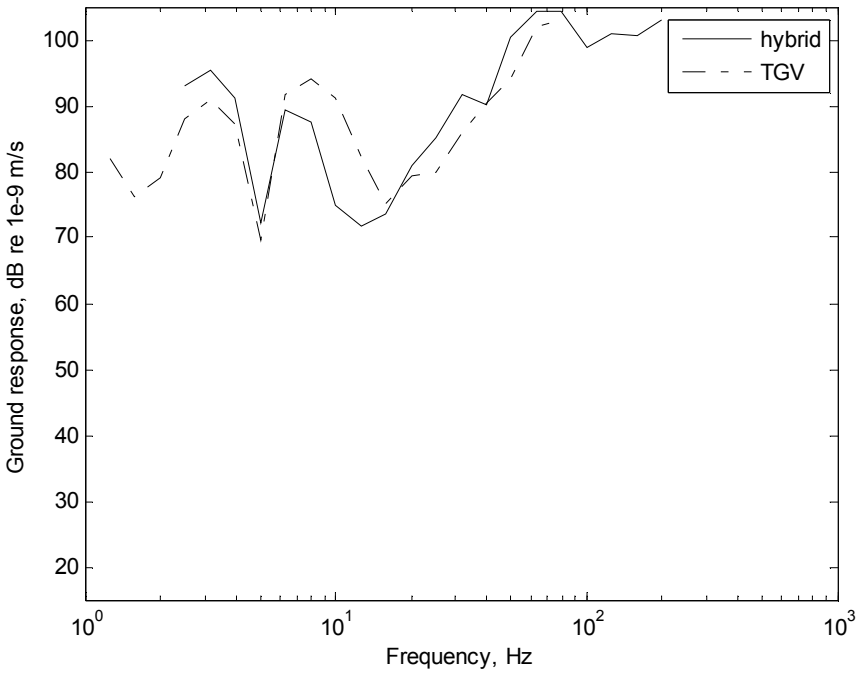

Figure 5.20. The ground responses due to total excitation at 0 m underneath the track from hybrid model comparing with the results from TGV model.

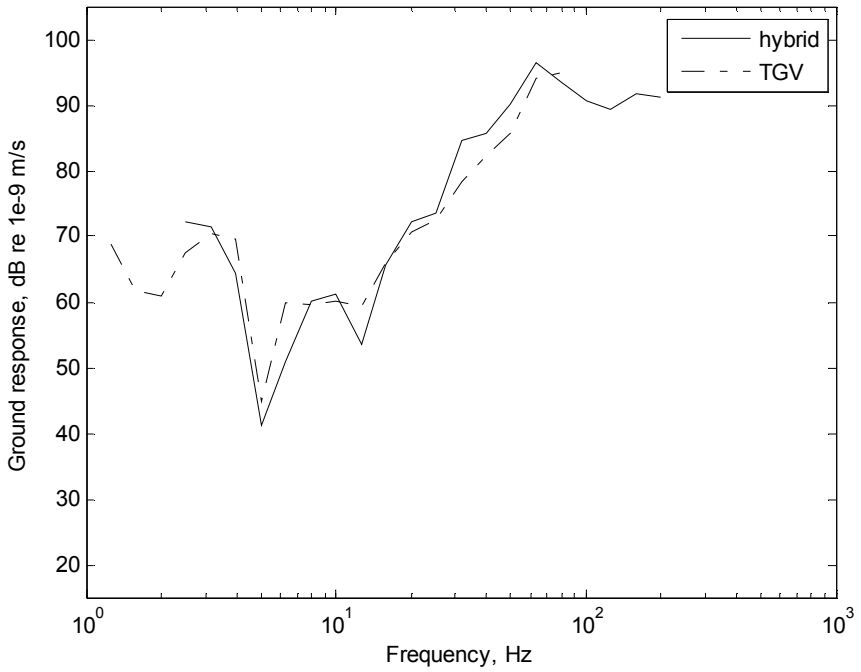

Figure 5.21. The ground responses due to total excitation at 3 m away from the track from hybrid model comparing with the results from TGV model.

5.5.4 Effect of number of laps

To investigate the effect of the track length on the ground response, Figure 5.22 shows results when the vehicle is allowed to travel 1, 2 and 4 laps. The lengths of the track are 36, 72 and 144 m for 1, 2 and 4 laps respectively. The longer track is needed due to the effect of truncation of the quasi-static load on the ground response at distances further away from the track.

At a position underneath the track (0 m) the length of the track has only a small effect on the ground response. At 3 m away the effect on the quasi-static response is quite significant. The response at 3 m away from the track for 4 laps is about 20 dB lower than that for 1 lap. The results in Figure 5.22(b) show that the ground response due to a shorter track length contains higher frequency content than that from a longer one.

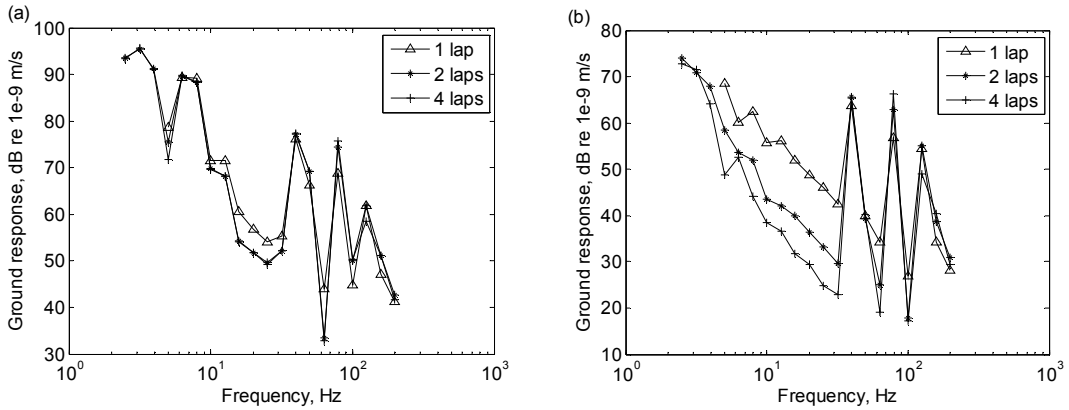

Figure 5.22. Ground responses due to quasi-static load at (a) 0 m and (b) 3 m away from the track with various track lengths.

This can be explained by the ground deflection as shown in Figure 5.23. This shows the ground deflection underneath the track and at 3 m away. The length of the track considered has little effect on the ground deflection at the position underneath the track as shown in Figure 5.23 (a) and (c). Here it can be seen that the deflection is close to the level before it deforms at both ends. On the other hand a gap is found at both ends for the track of 1 lap as shown in Figure 5.23 (d). This is due to the deflection spreading out over a wider area. Therefore, this might cause a discontinuity in the data when an FFT is calculated.

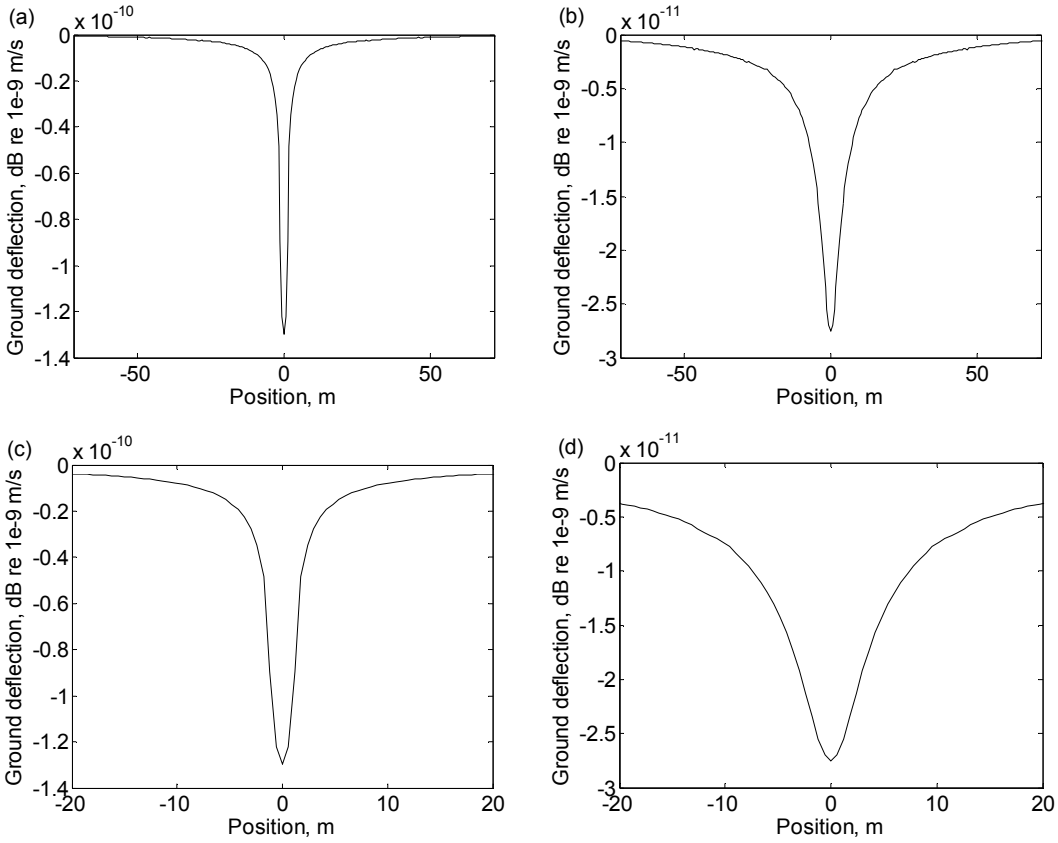

Figure 5.23. Ground deflection for the track length of 4 laps at (a) 0 m and (b) 3 m and those of 1 lap at (c) 0 m and (d) 3 m away.

5.5.5 The effect of windowing

The results from the hybrid model up to now have been derived using a Hanning window in order to reduce the effect of an artificial impulse force caused at the end of the analysis window. In order to investigate the effect of windowing, three cases of the windowing are applied: “full windowing”, “ends windowing” and “no windowing”. For the first case the Hanning window is applied to all of the data. In second case it is applied to the data at the end on both sides. In the last case ground responses are shown without applying a window. The ground responses, due to quasi-static load, at distances away from the track are shown in Figure 5.24 with various cases of applied windowing. Corresponding results due to total excitation are shown in Figure 5.25. It can be seen that applying a window affects the ground response mostly due to the quasi-static load especially for further distances from the track. The effect of windowing on the ground response at further distance due to the quasi-static load can be understand from Figure 5.26 for cases without and with the applied Hanning window. In this figure results are shown for a simple rectangular signal.

On the other hand applying the window has no effect on the response including the dynamic load except at 3 and 6 m away from the track below about 20 Hz.

The results show that the ground responses with full windowing are much closer to the results from TGV than the other cases. This can be seen in Figure 5.19 as there the hybrid model used full windowing.

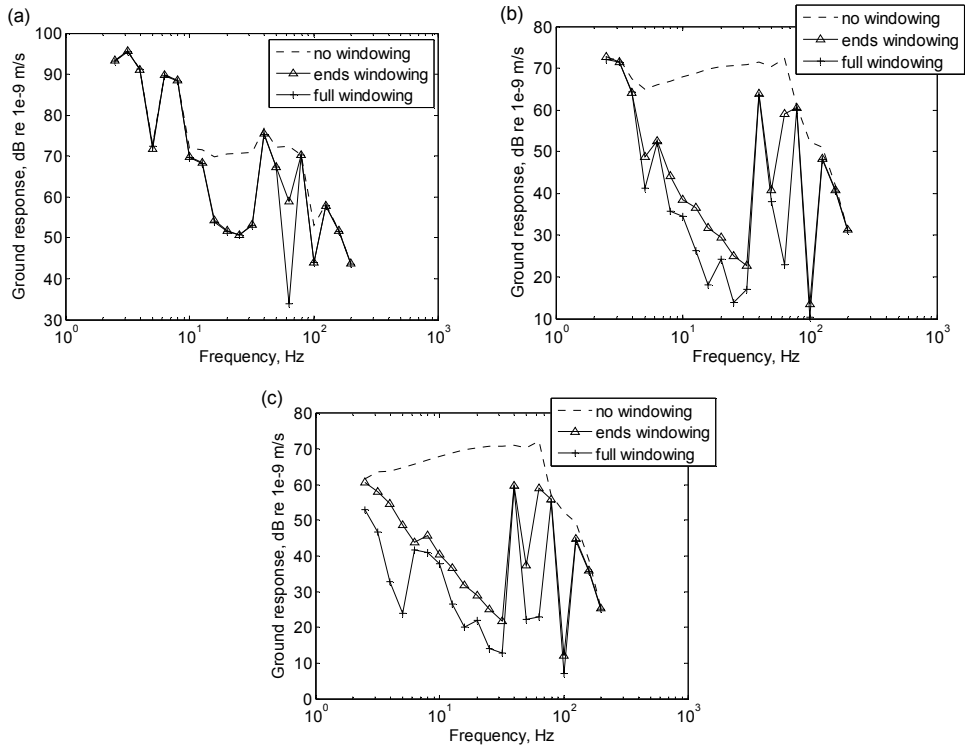

Figure 5.24. The effect of windowing applied to the ground responses in hybrid model at (a) 0 m underneath the track and (b) 3 m and (c) 6 m away from the track, due to quasi-static load.

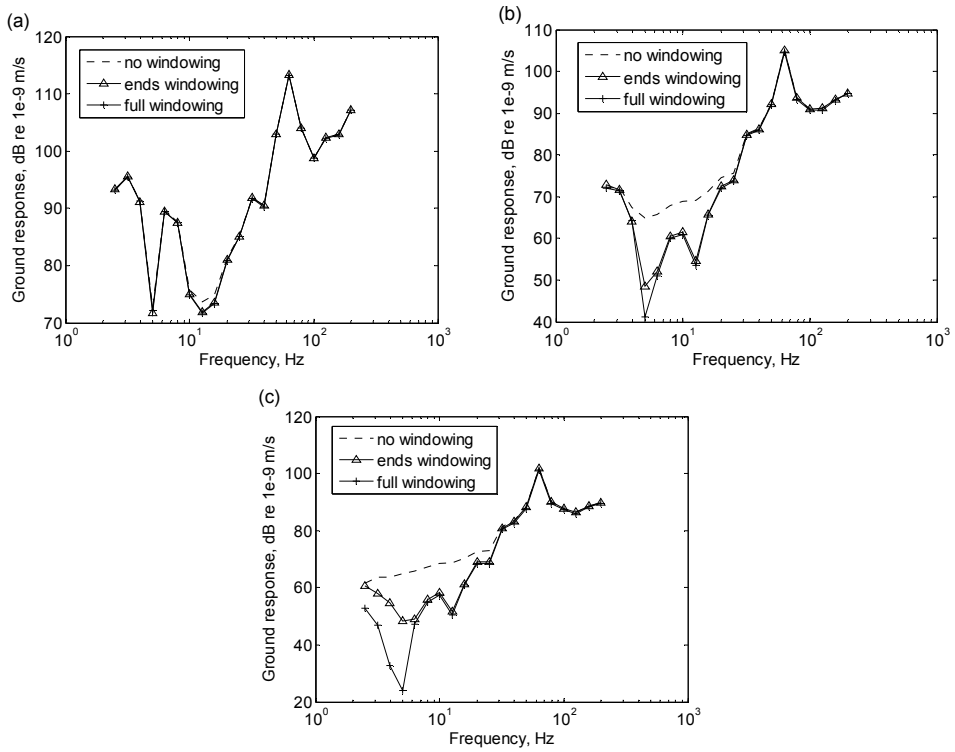

Figure 5.25. The effect of windowing applied to the ground responses in hybrid model at (a) 0 m underneath the track and (b) 3 m and (c) 6 m away from the track, due to total excitation using Steventon roughness profiles.

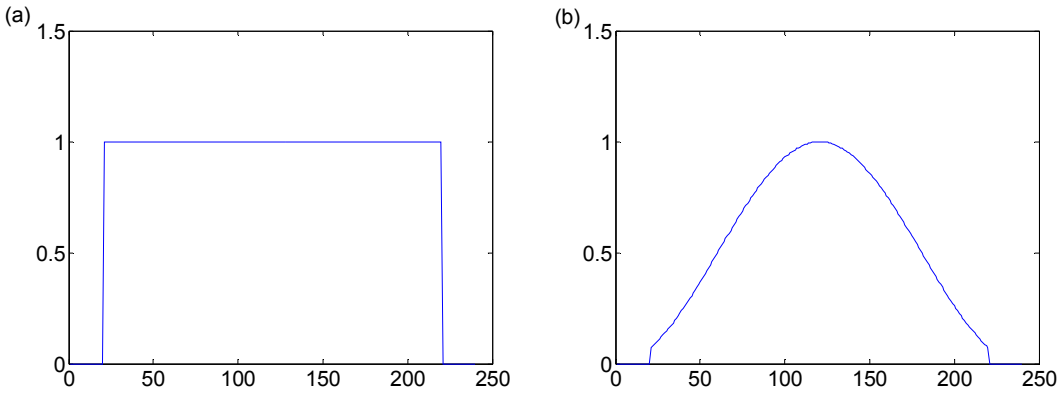

Figure 5.26. The effect of windowing applied to a unit rectangular signal (a) before and (b) after.

5.5.6 The effect of equivalent stiffness

In order to investigate the sensitivity of the results to the value of equivalent stiffness used to represent the ground and ballast, this stiffness is halved from 110 MN/m to 55 MN/m. The results in Figure 5.27 show the ground response using the equivalent stiffness of 110 and 55 MN/m due to quasi-static load and total excitation.

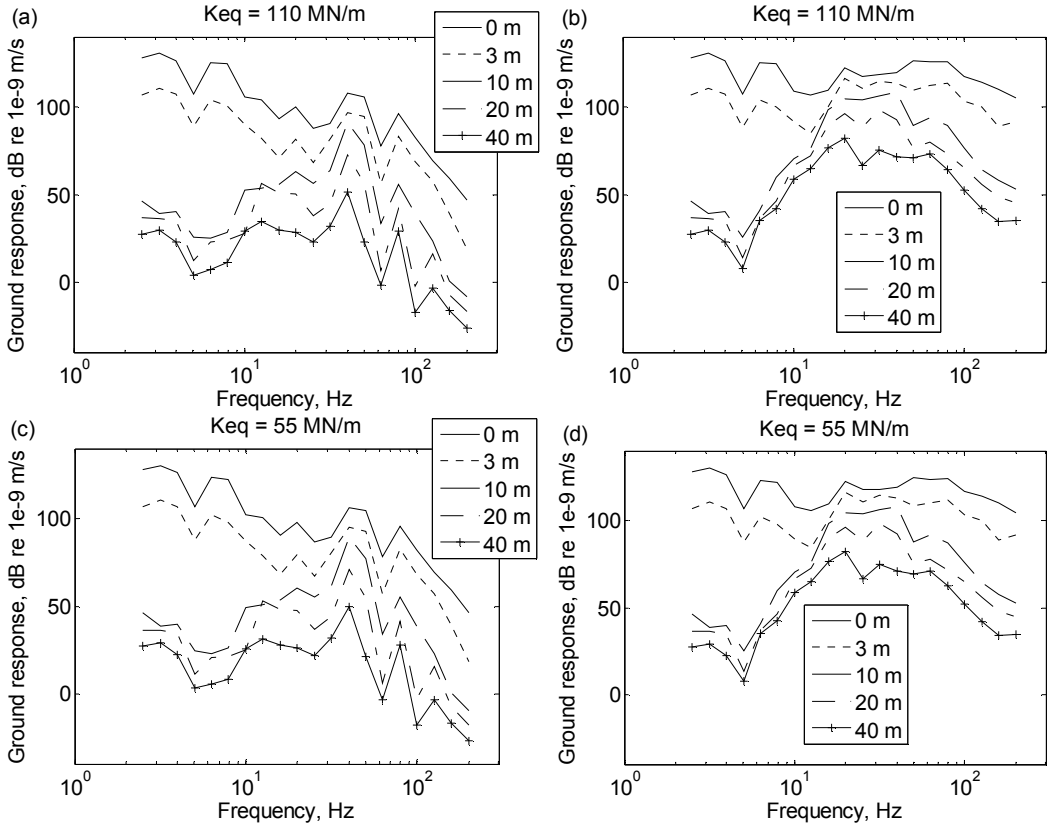

Figure 5.27. Ground response due to (a) quasi-static load and (b) total excitation using the equivalent stiffness of 110 MN/m at the contact force and due to (c) quasi-static load and (d) total excitation using the equivalent stiffness of 55 MN/m.

Figure 5.28 shows the ratio of these results. Although there are differences of up to 3 dB in quasi-static response at around 10 Hz and 2 dB in dynamic response around 50 Hz, on the whole the results are not particularly sensitive to the value of equivalent stiffness used.

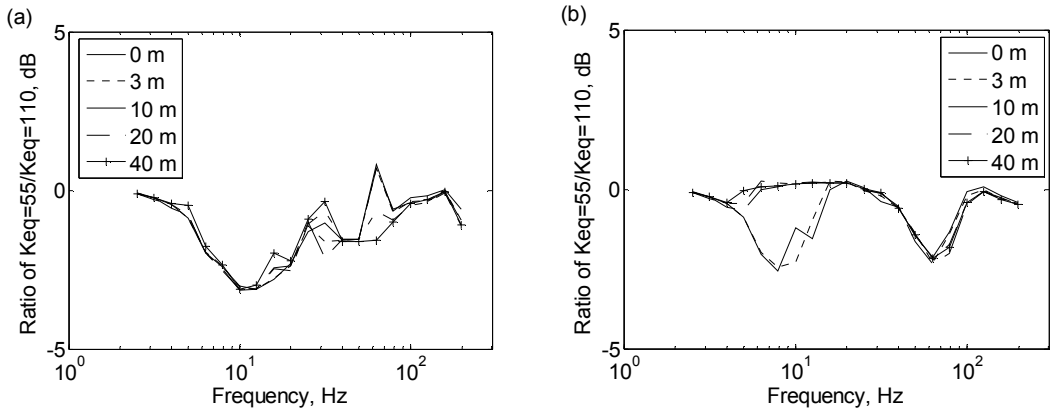

Figure 5.28. The ratio of the ground response using the equivalent stiffness of 55 MN/m to 110 MN/m at the contact force, due to (a) quasi-static load and (b) total excitation.

5.5.7 The effect of the four wheelsets

In both the TGV and hybrid models the excitation due to each wheelset is assumed to be coherent, that is their relative phase is taken into account.

To investigate the effect of coherence between wheels on the ground response, Figure 5.29 shows a comparison between results for four wheelsets (coherent) and for a single wheelset (increased by 6 dB to represent the incoherent sum for four wheelsets). These results are at 0 m, underneath the track. It can be seen that a large difference is found at 5 Hz. The incoherent sum does not include the peaks and dips at low frequency caused by interference between wheels. Nevertheless the overall response is quite similar above 10 Hz. At 3 m away from the track, a similar trend can be found as shown in Figure 5.30.

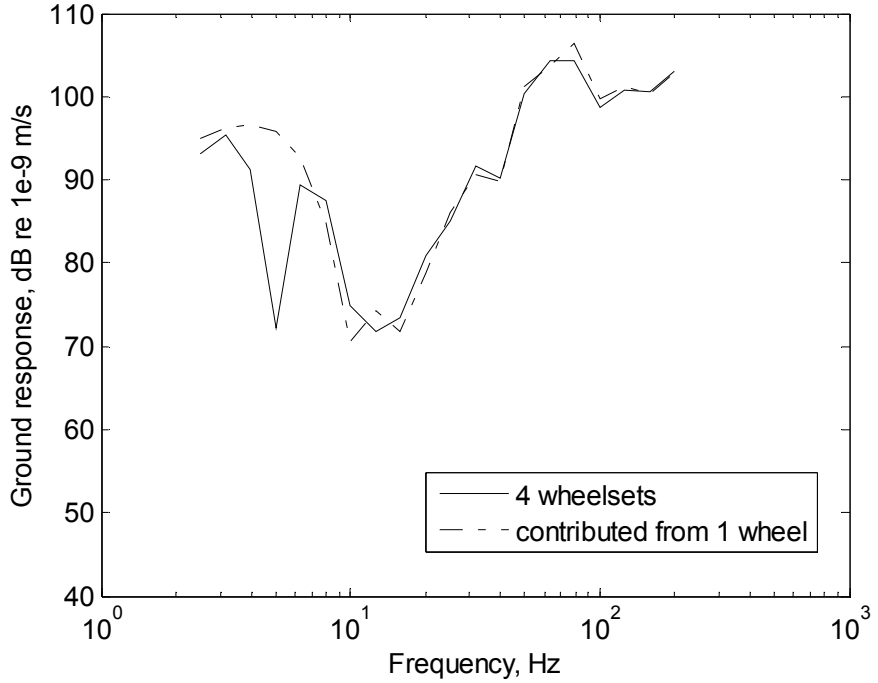

Figure 5.29. The ground responses due to total load comparing between the case of coherent- and incoherent- contributions from four wheelsets, at 0 m underneath the track.

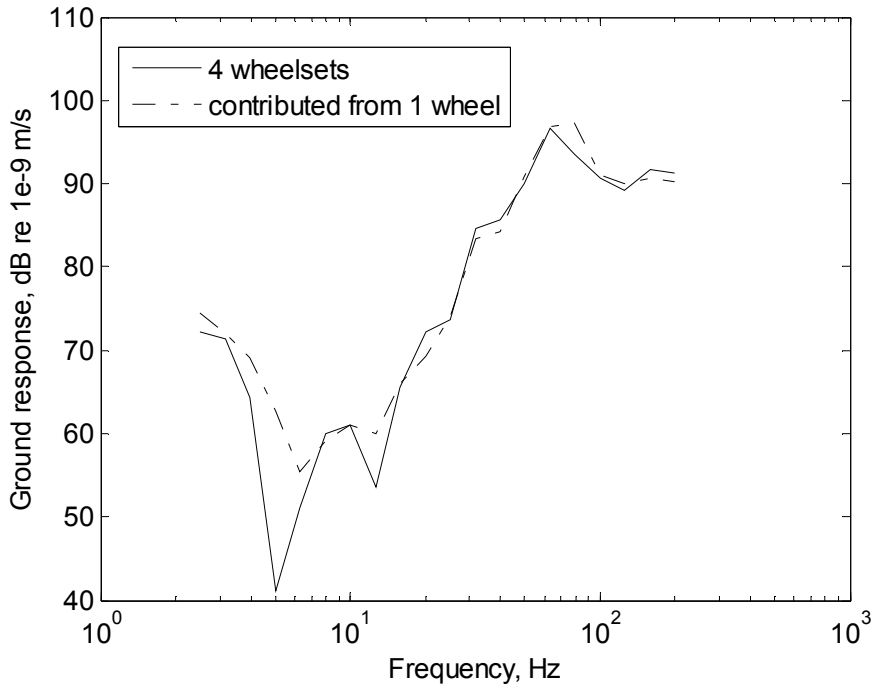

Figure 5.30. The ground responses due to total load comparing between the case of coherent- and incoherent- contributions from four wheelsets, at 3 m away from the track.

5.5.8 The effect of rail irregularities

A roughness profile has been generated based on the one-third octave spectrum of roughness measured at the Steventon site. This is used as the excitation. As this is effectively a random function, it is expected that different results of ground vibration will occur at different positions along the track direction. Figure 5.31 shows the ground response at various x distances for both y = 0 and 3 m perpendicular to the track. It can be seen that at 0 m the ground responses occur randomly above 10 Hz where the dynamic component dominates. It is also shown that at 3 m away from the track the variation is less.

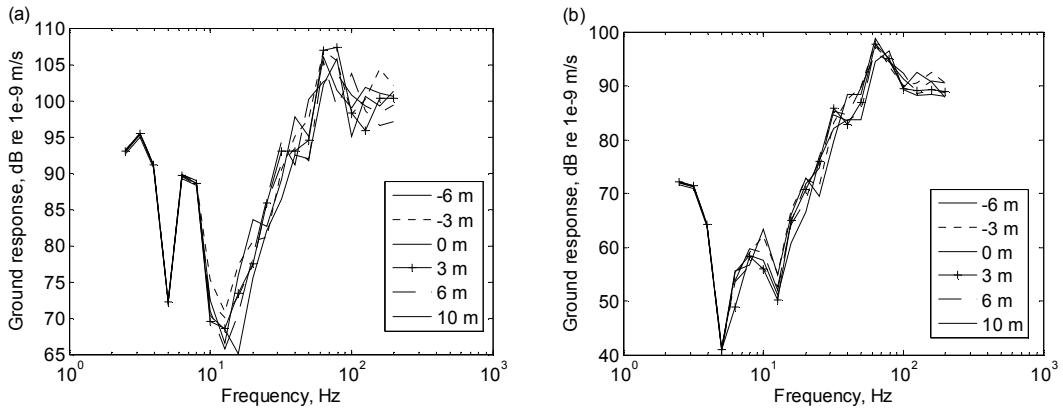

Figure 5.31. The ground response at various x distances along the track for (a) y = 0 and (b) y = 3 m perpendicular to the track.

5.6 Conclusions

To investigate the relevance of alternative excitation mechanisms of ground vibration, a new model has been developed. The time and spatial domain wheel/track interaction model from Croft [109] has been modified and connected to an axisymmetric layered ground model [33], to form a 'hybrid' model. A layered ground is added underneath the ballast instead of a rigid ground. Having extracted the force acting at the ground interface and then converted them to power spectral densities and cross power spectral densities, the ground response at the receiver position can be calculated. This is obtained by multiplying the force spectral matrix by the ground mobilities.

In order to reduce the effect of the finite length, the track has been modified to make it 'circular'. The advantage of the circular track compared with making the track

longer is that the number of degrees of freedom is not increased. A longer track response is obtained by allowing the vehicle to travel more than one lap.

The TGV model has been used to validate the hybrid model. A simple wheel/rail interaction model is also used as a third model to predict the rail response. The comparisons are made among these three models and a reasonable agreement is found.

It is found that the contact width in TGV has a strong effect on the ground response only immediately under the track. The effect of applying a window to the data is also investigated. It is found that applying a window mostly only affects the ground response due to quasi-static load especially for further distances. On the other hand applying a window has little effect on the response due to dynamic excitation.

This hybrid model will be used to investigate the relevance of alternative excitation mechanisms of ground vibration: the following chapter will consider parametric excitation due to sleeper-passing effects and other track properties and Chapter 7 will consider dynamic excitation due to defects on the track at particular fixed locations, excited by each wheel as it passes.

6. Excitation mechanisms associated with variations in track properties

6.1 Introduction

The hybrid model has been developed in Chapter 5 to predict ground vibration due to motion of a train along a track. The results have been compared with TGV in order to validate the model. The hybrid model is a time domain wheel/track interaction model coupled with a layered ground underneath. This allows changes in various parameters of the track support to be investigated. A number of parameters are considered in this chapter: sleeper passing effect, variable sleeper spacing and variable ballast stiffness.

For simplicity, the ground models used throughout this chapter and Chapter 7 are based on only two different soil types: a soft clay soil and a stiffer ground typical of chalk. The parameters used to represent the properties of the ground are shown in Table 6.1; these are the same as used in Chapter 5. The vehicle is modelled as 4 axles without primary and secondary suspensions. Track and vehicle parameters are also the same as used in Chapters 4 and 5, shown in Tables 5.2 and 5.3. Various modified vehicle/track parameters are also considered in this chapter, as listed in Table 6.2.

Table 6.1. The parameters used for various types of ground.

Parameters of ground	Type		
	Clay	Chalk	Half-space
P-wave speed	1700 m/s	2100 m/s	2100 m/s
S-wave speed	120 m/s	1200 m/s	1200 m/s
density of layer material	2000 kg m^{-3}	2000 kg m^{-3}	2000 kg m^{-3}
Layer depth	3.0 m	3.0 m	infinite

Throughout this chapter unless, otherwise stated, roughness excitation is neglected by considering the response to movement of the wheels along a perfectly smooth track. Where roughness is included it is based on the measurements from Steventon (see Figure 3.45) which represents a track with a relatively low level of roughness.

Table 6.2. Properties used to represent the modified vehicles/track.

Parameters of Vehicle			Reference	Modified parameters		
				1.Axle load (kN)	2. Vehicle speed (m/s)	3.rail pad stiffness (MNm)
Vehicle	Axle load (kN)		108.3	216.6	-	-
	Speed (m/s)		25	-	12.5, 16, 20, 32, 40, 50	
Track	Rail pad stiffness (MN/m)	moderate stiffness rail pad	210	-	-	630
		typical soft baseplates				210
		very soft baseplates				70

6.2 Sleeper passing effect

The purpose of this section is to investigate the sleeper passing effect on the surface ground vibration at various distances from the track. The effects on this of changes in axle load, vehicle speed, ground types and rail pad stiffness are also considered. The sleeper passing effect has already been noted in Section 5.5.3.

For the reference case, ground responses at various distances perpendicular to the track due to quasi-static load and total excitation are shown in Figure 6.1. It can be seen that sleeper passing effect dominates the response for all distances at the frequencies of about 40 and 80 Hz. The frequencies of these peaks can be estimated from the speed v = 25 m/s and the sleeper spacing λ = 0.6 m using $f = \frac{v}{\lambda} = \frac{25}{0.6} = 41.6\,\text{Hz}$ and its first harmonic. By comparing these results with the corresponding ones including roughness in Figure 6.1 (b) it can be seen that the sleeper passing excitation has less effect on the ground response than the excitation including the roughness. Similar to the results found in Chapter 4 using TGV, the quasi-static load dominates the ground response only immediately underneath the track. At a distance of only 3 m away from the track the response drops off approximately 30 dB below 12 Hz.

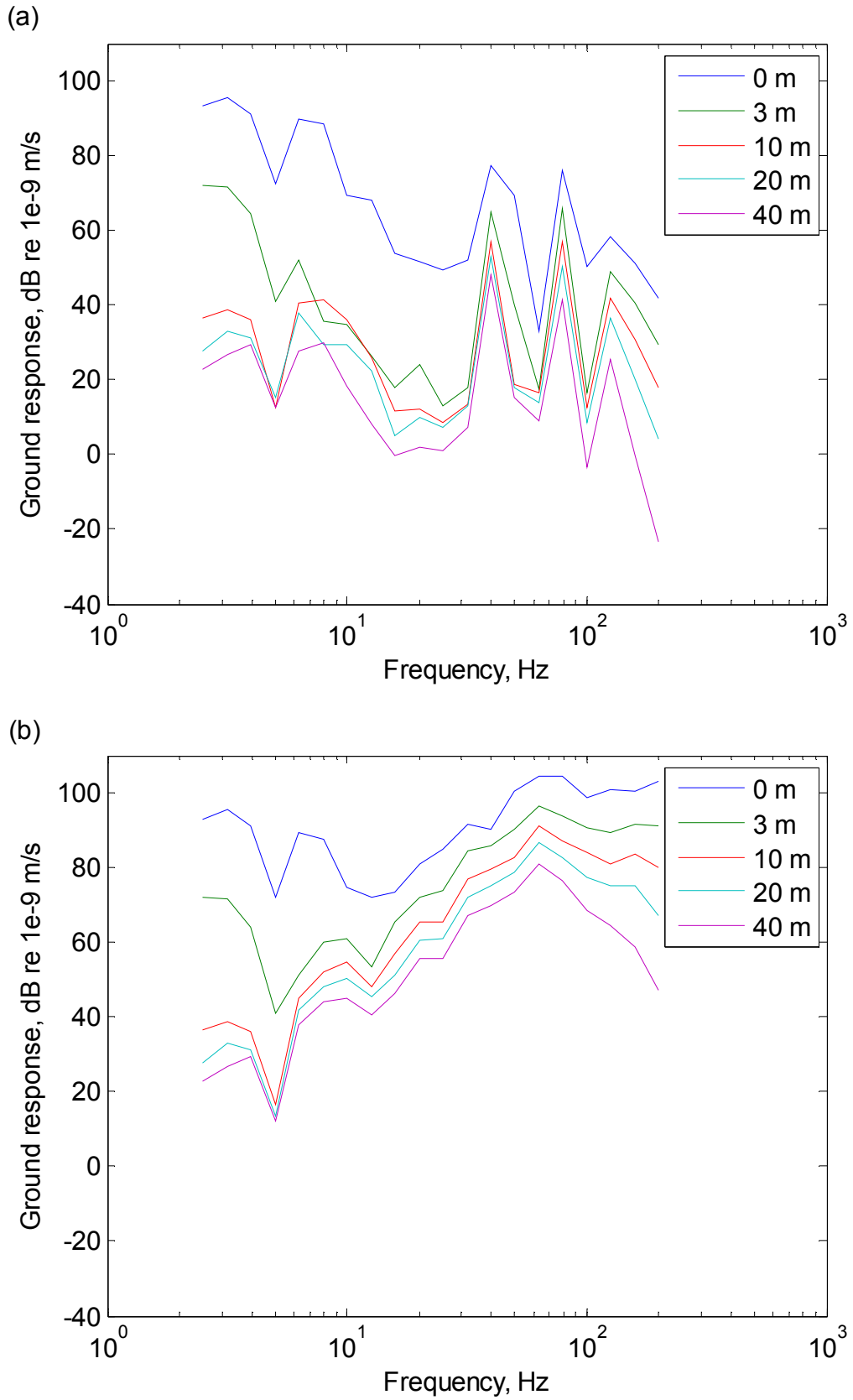

Figure 6.1. Ground responses on half-space of chalk due to (a) quasi-static load and (b) total excitation.

The ground responses due to quasi-static load and total excitation are also considered in terms of the relative level at different distances. These results are shown in Figures 6.2 and 6.3 for 40 and 80 Hz respectively.

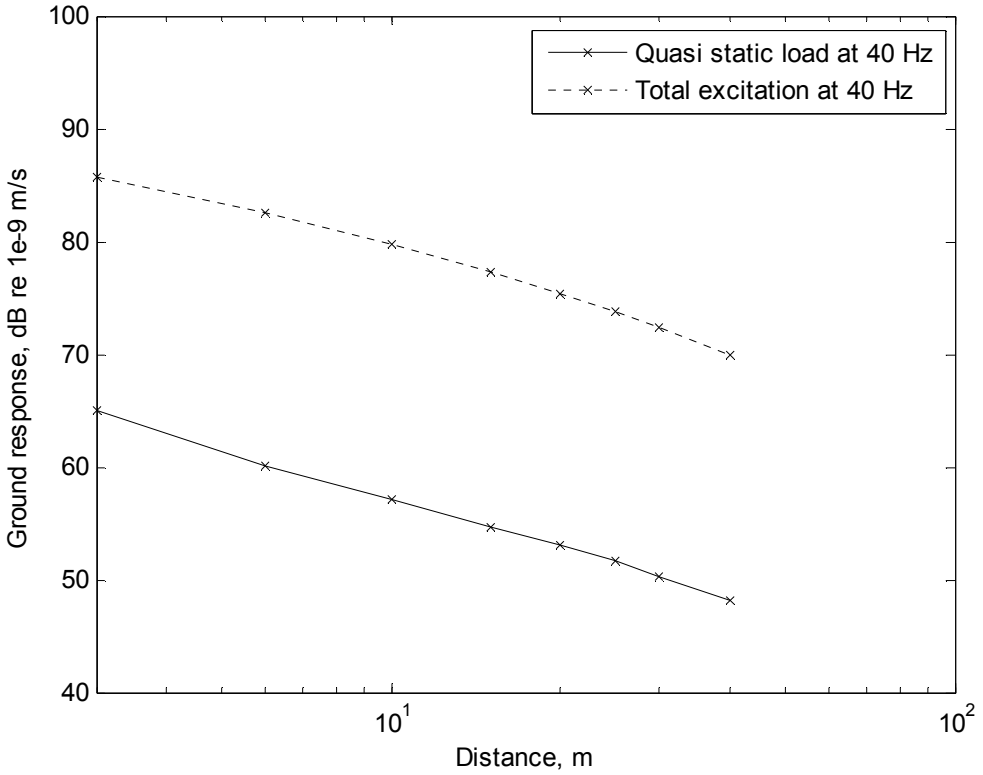

Figure 6.2. Propagation of vibration away from the track due to quasi-static load and total excitation in terms of level at different distances for 40 Hz.

From these figures it is clear that the results due to quasi-static load (including sleeper passing effect) are 20 dB lower than the response due to roughness at 40 Hz and 30 dB lower at 80 Hz. These differences are independent of distance from the track.

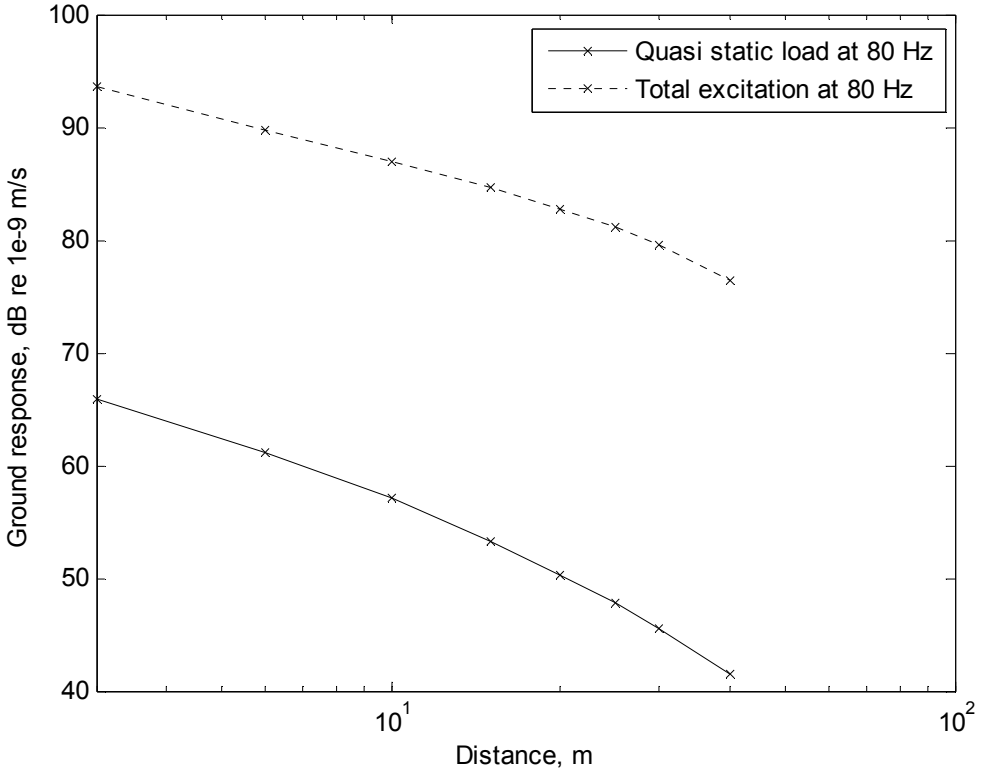

Figure 6.3. Propagation of vibration away from the track due to quasi-static load and total excitation in terms of level at different distances for 80 Hz.

6.2.1 Axle load effect

To investigate the effect of axle load, it is set to twice the original value. Comparisons between reference and modified values of axle load are shown in Figure 6.4 for the response due to quasi-static load. It can be seen that by doubling the axle load the vibration level increases by about 6 dB at both 0 and 10 m. This agrees with the results from Chapter 4 obtained by doubling the body mass, as shown in Figure 4.21(c). In the present results the response at the sleeper passing frequency also increases with the increase in axle load by the same amount.

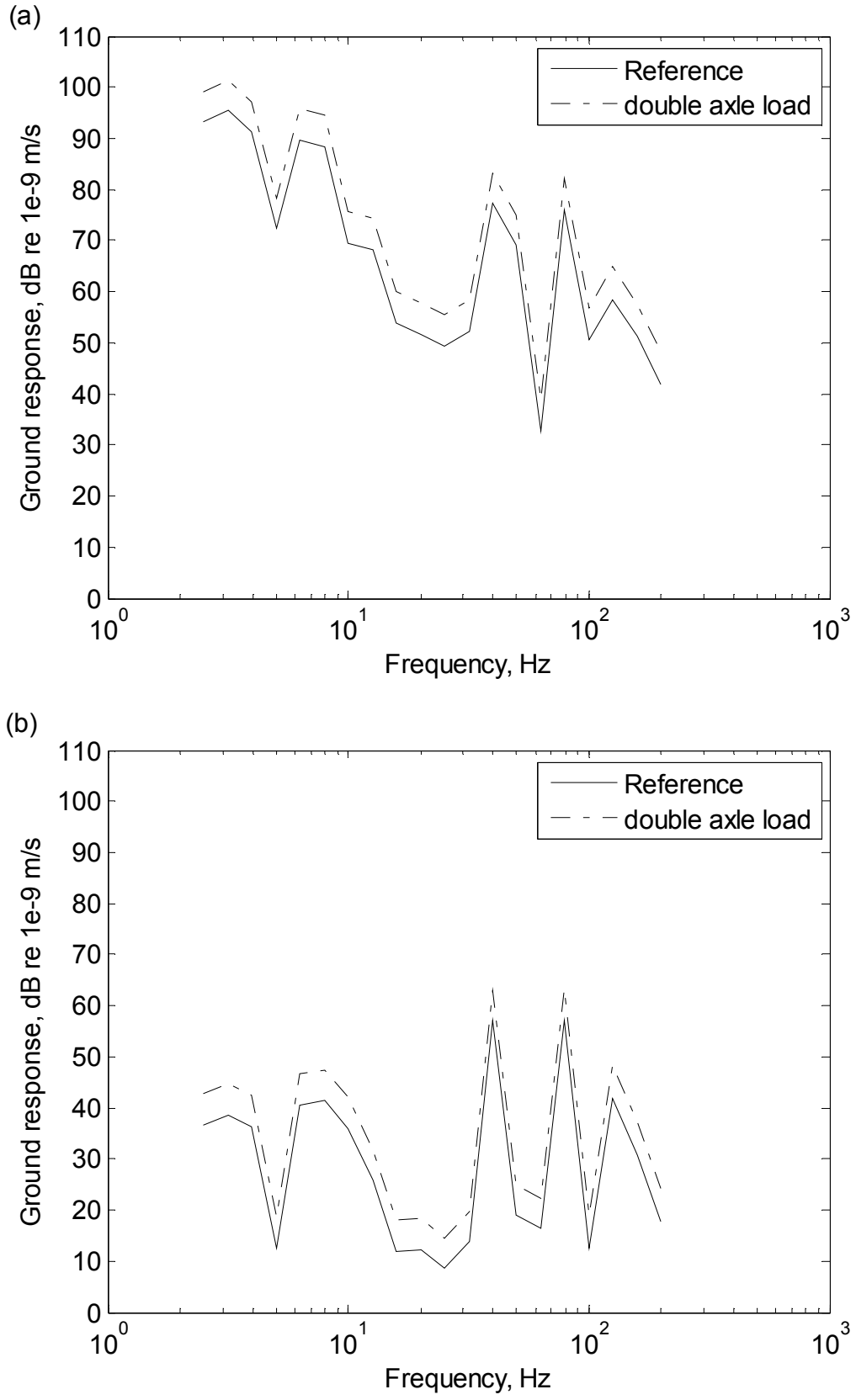

Figure 6.4. Comparisons of ground response due to quasi-static load for changing in axle load at (a) 0 m and (b) 10 m.

Similar comparisons for the responses due to total excitation are shown in Figure 6.5. The effects of axle load agree with the results from Chapter 4 for a doubling of the body mass, as shown in Figure 4.21(a). As the distance increases the axle load has less effect on the ground response for the case including roughness as the dynamic component of the response is unaffected. This shows that axle load affects the overall ground response only below about 10 Hz.

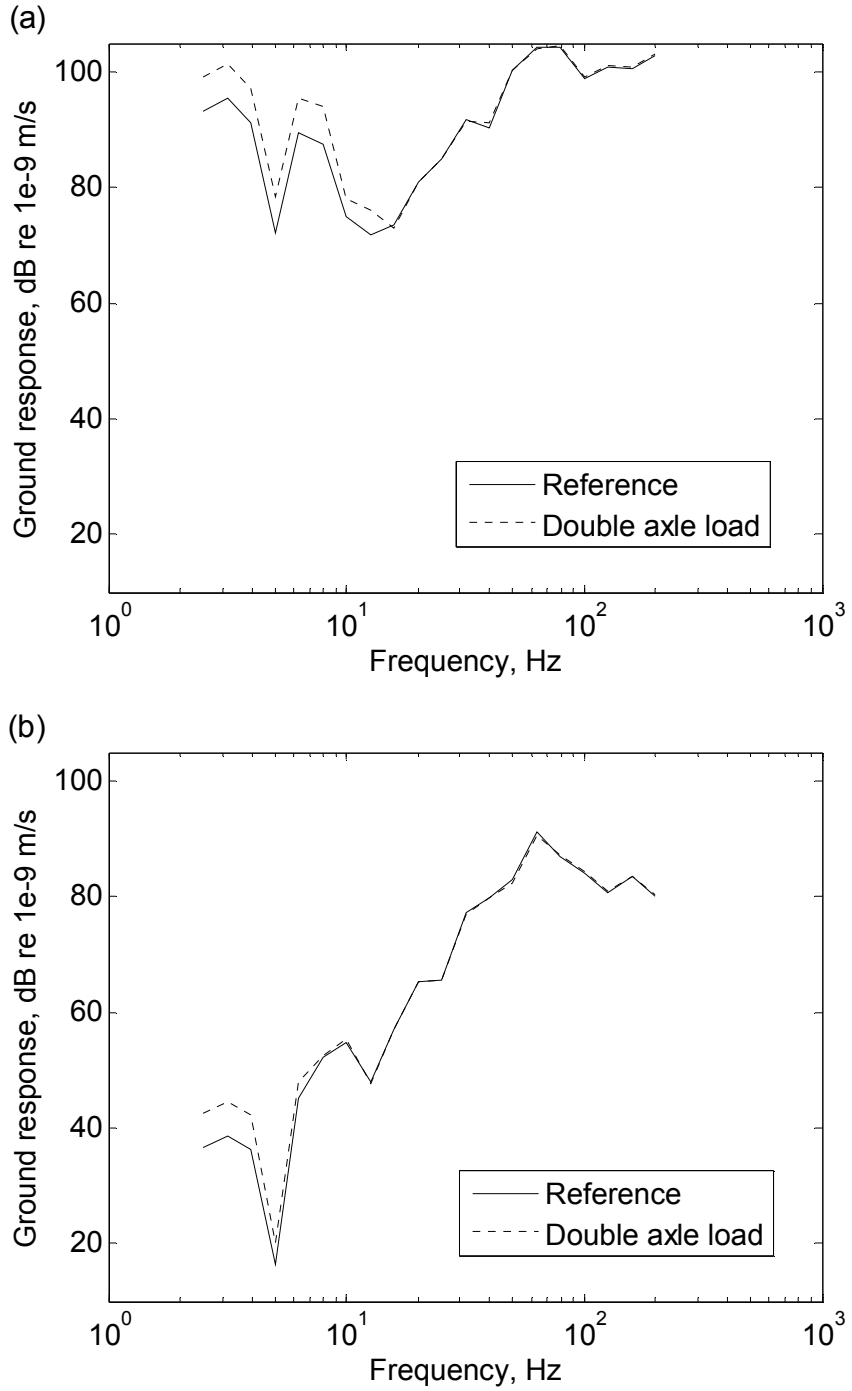

Figure 6.5. Comparisons of ground response due to total excitation for changing in axle load at (a) 0 m and (b) 10 m.

6.2.2 Vehicle speed effect

As the speed of the train increases the effect of the quasi-static component dominates the vibration response to higher frequencies. This was shown using the TGV model in Figure 4.33. Nevertheless at distances further from the track the effect of the quasi-static component reduces.

The ground response from the hybrid model due to the quasi-static load for various speeds of the train is shown in Figure 6.6. This shows a comparison of results for train speeds between 12.5 and 50 m/s at 0 and 10 m away from the track. The peaks at low frequencies correspond to the axle spacings. These differ from those in Figure 4.32 as the current results are for a single vehicle. The peaks clearly shift to higher frequencies as speed increases, as found in Figure 4.32. The sleeper passing frequency also increases with train speed. The results at 0 and 10 m show a consistent trend in the amplitude at high frequencies. When the speed of the train increases to 40 m/s the sleeper passing frequency occurs at 63 Hz which corresponds to the resonance of unsprung mass bouncing on the track. The ground response therefore has maximum amplitude at this frequency. Figure 6.7 shows the ground response due to the quasi-static load and total excitation for the train speed of 40 m/s. Even in this case the sleeper passing effect is about 20 dB less than the response due to roughness.

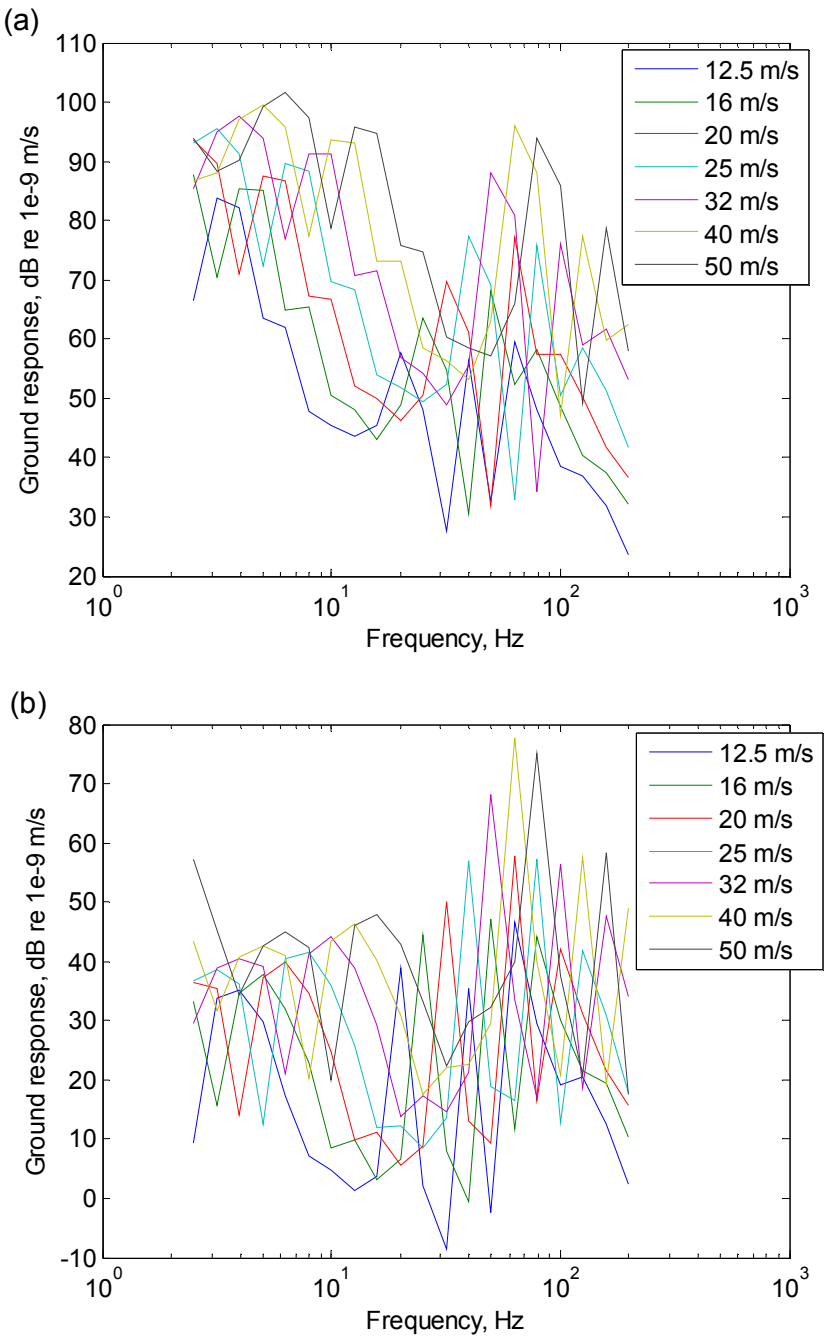

Figure 6.6. Ground responses due to quasi-static load for various speeds of the train at (a) 0 m and (b) 10 m away from the track.

From Figure 6.6(a), at 0 m the results show clear peaks in the response which correspond to the first few harmonics of the sleeper passing effect. Figure 6.8 shows the amplitude of these peaks for the first, second and third harmonics. These are plotted against frequency for each speed of the train. Each harmonic reaches a maximum when its frequency corresponds to the bouncing mode at 63 Hz.

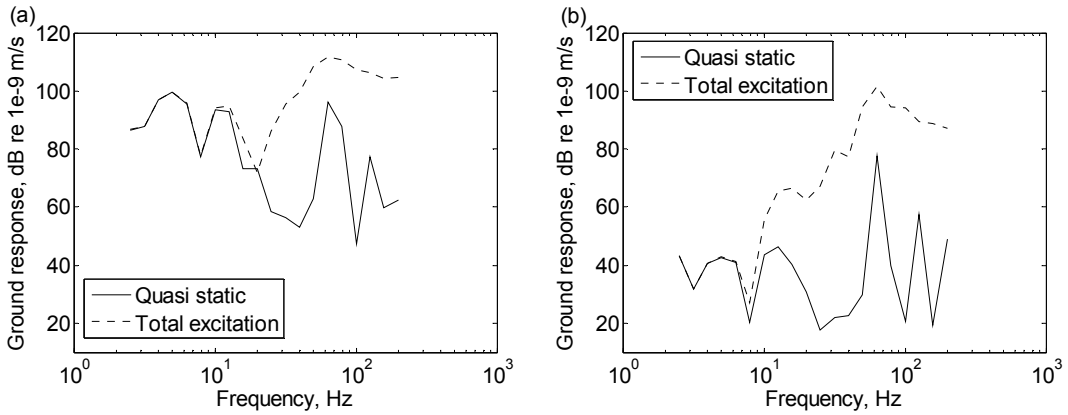

Figure 6.7. Ground responses due to quasi-static load and total excitation for the train speed of 40 m/s at (a) 0 m and (b) 10 m away from the track.

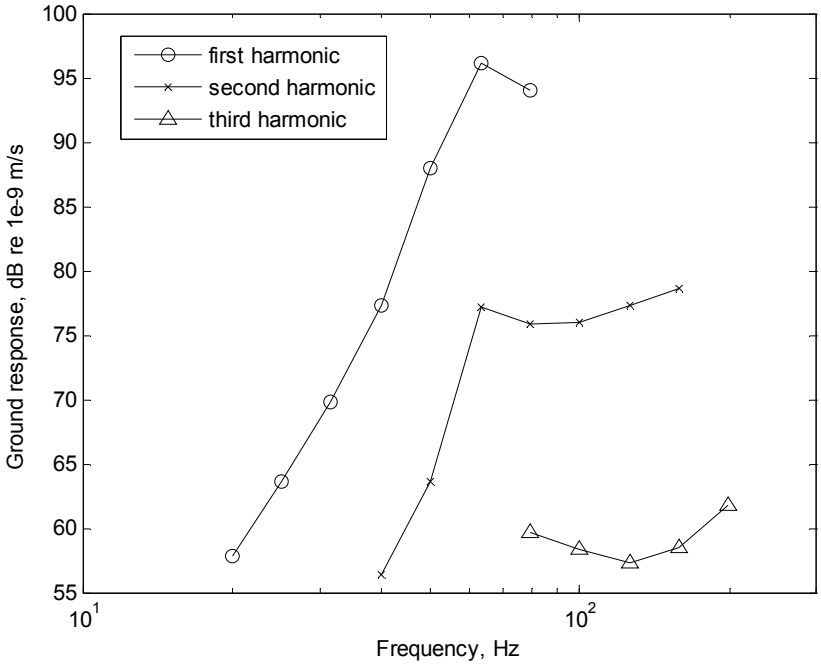

Figure 6.8. Peaks of first, second and third harmonics for each speed of the train.

6.2.3 Effect of different ground properties

In order to see the effect of different ground properties on the vibration response at the sleeper passing frequency, Figure 6.9 shows ground responses for clay soil at various distances perpendicular to the track due to the quasi-static load. This can be compared with Figure 6.1 (a). As the results show, the ground responses for clay soil are greater than those for the stiffer chalk soil especially below 50 Hz. Results at 10 m are compared in Figure 6.10 for the two soils.

A broad peak at about 10 to 20 Hz corresponds to the cut-on frequency for the upper layer of the ground (3 m of clay overlying half-space of chalk). This can be seen in Figure 5.6. The point/transfer receptances in the kandr model have a peak at 20 Hz. The peak at 40 Hz corresponding to the sleeper passing frequency occurs for both ground properties but it is 30 dB higher for the clay soil. Nevertheless the response due to roughness is also greater for this soil as will be seen.

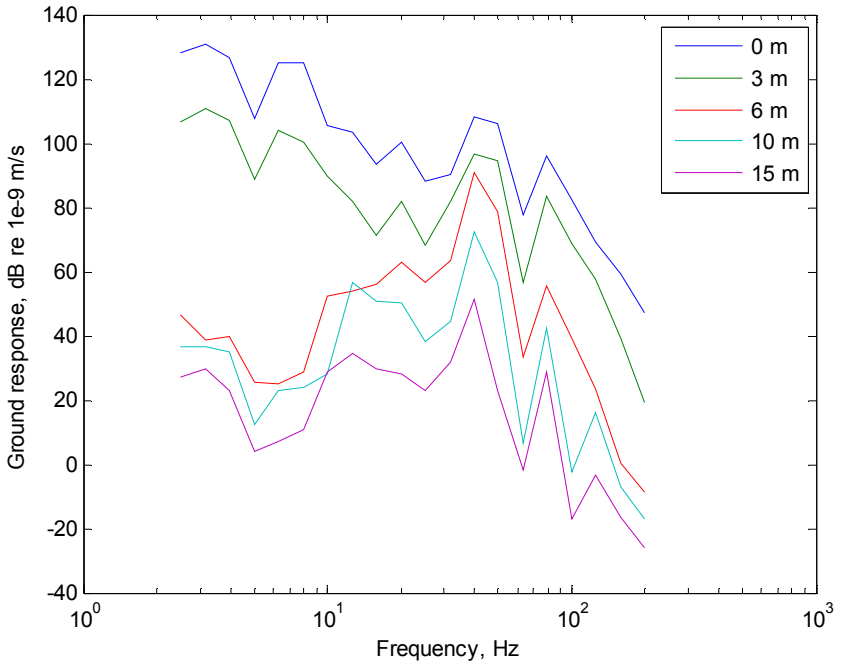

Figure 6.9. Ground responses due to quasi-static load on a layer of clay above half-space of chalk at various distances perpendicular to the track.

Figure 6.11 shows the response at 40 Hz due to quasi-static excitation and the total excitation. For all distances the sleeper passing component remains more than 15 dB below the dynamic component due to roughness. These results can be compared with the results for the stiffer soil in Figure 6.2 from which it can be seen that the relative importance of the sleeper passing effect is no greater on soft soil than on stiff soil. The results at the second harmonic (80 Hz) are shown in Figure 6.12 from which similar conclusions can be reached by comparison with Figure 6.3.

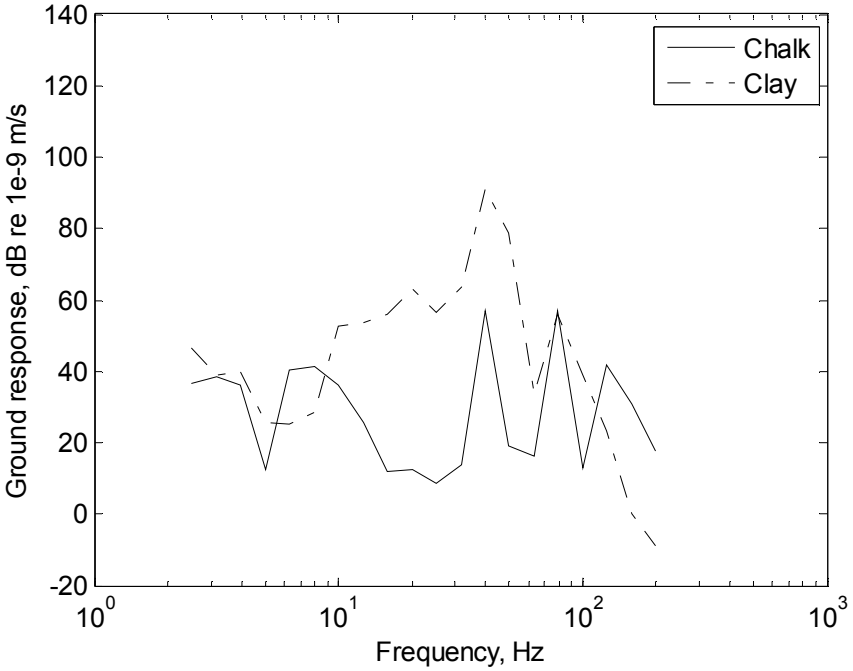

Figure 6.10. Ground responses due to quasi-static load comparing between chalk and clay soil at 10 m away from the track.

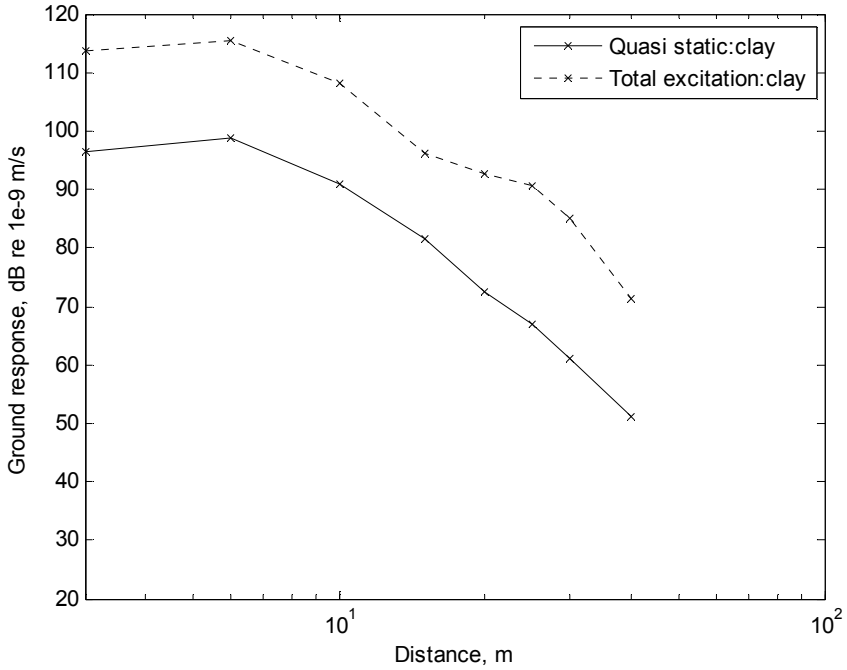

Figure 6.11. Propagation of vibration due to quasi-static load and total excitation on clay soil in terms of level at different distances for 40 Hz.

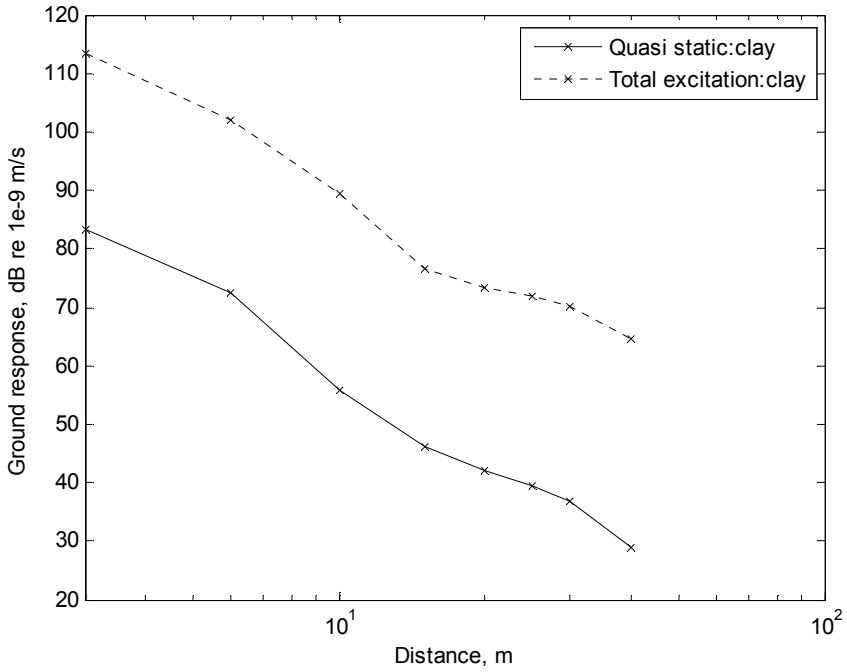

Figure 6.12. Propagation of vibration due to quasi-static load and total excitation on clay soil in terms of level at different distances for 80 Hz.

6.2.4 Rail pad stiffness

The effects of rail pad stiffnesses on the ground response have also been investigated. As in Chapter 4 the rail pad stiffnesses (for two rails) are chosen as 7.0×10^7, 2.1×10^8 and 6.3×10^8 N/m to represent 'very soft baseplates', 'typical soft baseplates' and 'moderate stiffness rail pad' respectively. According to this the rail pad stiffnesses are set as three times softer and stiffer than the reference. The results are shown in Figure 6.13 for quasi-static excitation. Introducing a softer spring in the track support affects the ground response between 6 and 30 Hz and above about 100 Hz by decreasing the ground response by about 3 and 5 dB respectively. A small change occurs at the sleeper passing frequencies where the soft pad leads to an increased response. The ground response below about 10 Hz is consistent, with no change.

Inserting a softer pad reduces the ground response by an average of 2.6 dB between about 6 and 30 Hz. This is due to the quasi-static load effect as seen in Figure 4.8(d). However it gives a higher amplitude by 2.5 dB at 40 Hz due to the sleeper passing effect. When the wheel passes over each sleeper, a softer pad allows

the rail to deflect more giving a greater vibration. Apart from sleeper passing effect, these results agree with the comparison in Figure 4.8(d) for different ground stiffnesses as shown in Figure 6.14. Figure 6.14 shows insertion gain of the ground vibration due to the quasi-static component for change in rail pad stiffness from typical soft baseplates to very soft baseplates at 0 and 10 m away from the track on two soil types.

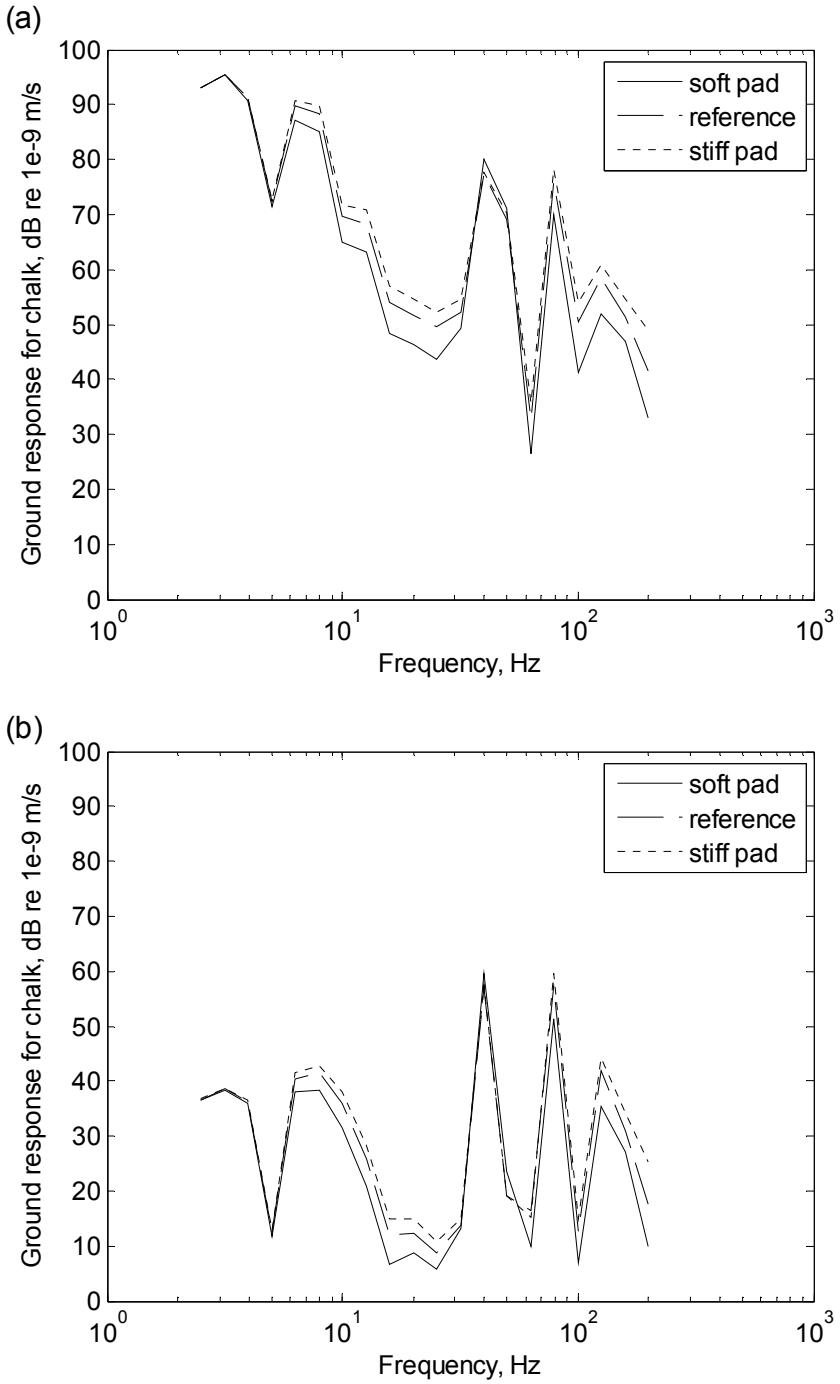

Figure 6.13. Comparisons of ground responses, on chalk half-space, due to quasi-static load for changes in rail pad stiffnesses at (a) 0 m and (b) 10 m.

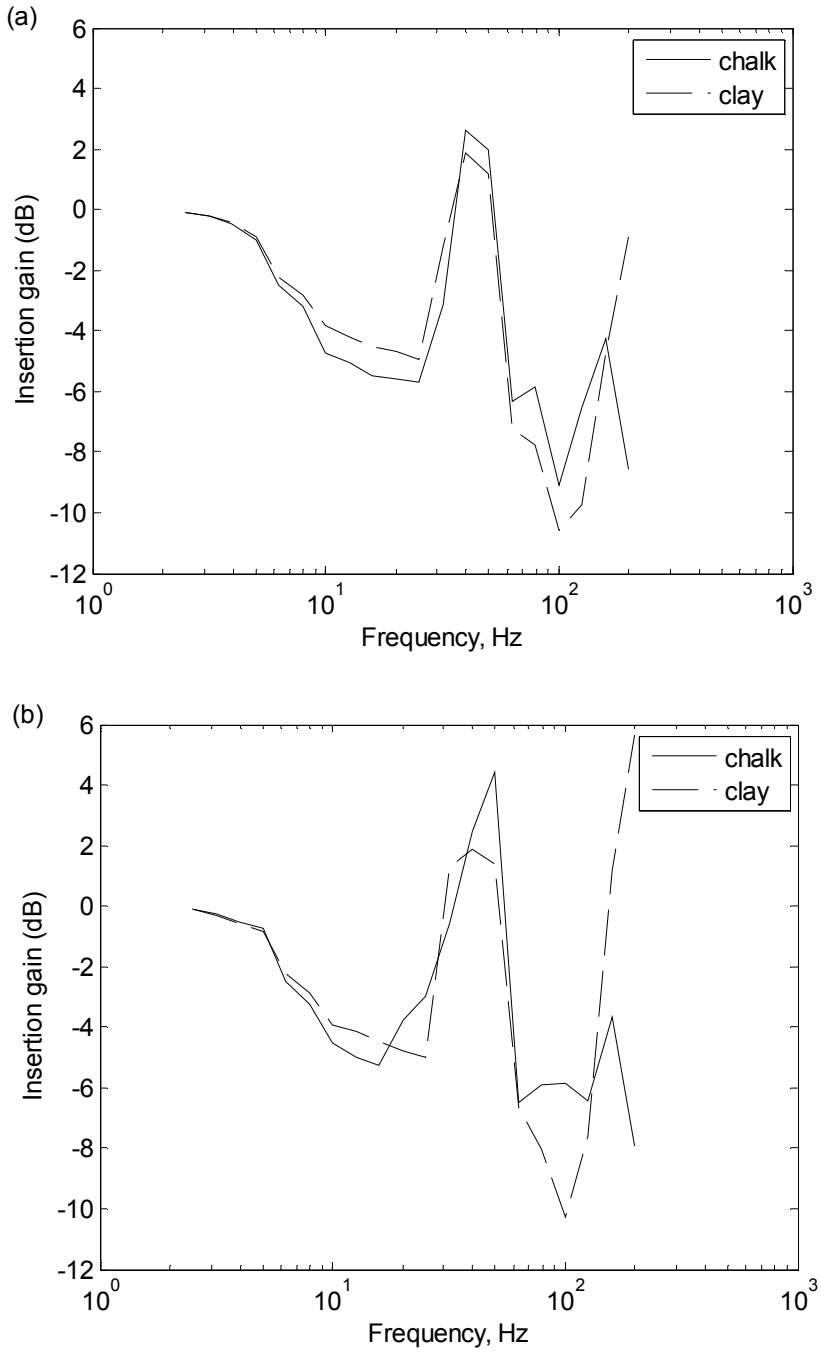

Figure 6.14. Insertion gain of the ground vibration due to quasi-static component for a change in rail pad stiffness from typical soft baseplates to very soft baseplates on two soil types at (a) 0 m and (b) 10 m away from the track.

For the case of clay soil, a similar trend is found on the ground response due to inserting a softer pad. At frequencies between 6 and 30 Hz the soft pad gives an amplitude reduction of 2.5 dB as shown in Figure 6.15, but it gives an increase in amplitude of 1.8 dB at 40 Hz.

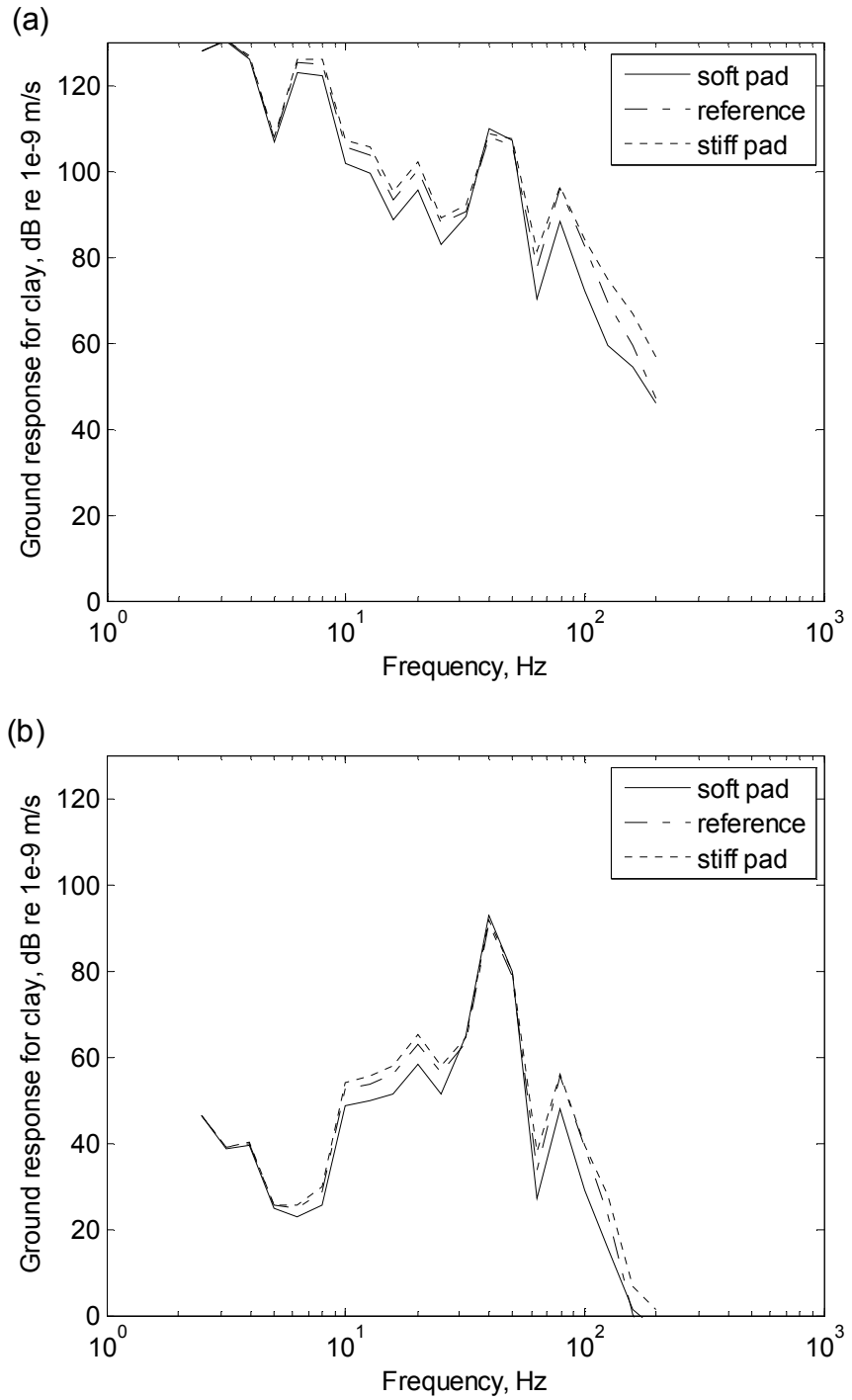

Figure 6.15. Comparisons of ground responses, on clay soil, due to quasi-static load for changes in rail pad stiffnesses at (a) 0 m and (b) 10 m.

6.3 Variable sleeper spacing

In practice the sleeper spacing will not be exactly regular. A standard deviation of 6% in variation of sleeper spacing has been found from measurements [3,118]. The effect of variable sleeper spacing is therefore investigated by introducing

a random spacing between each sleeper. A standard deviation of 6% is assumed around a mean value of 0.6 m. Each of the sleeper spacings along the track for one lap is generated randomly, as shown in Figure 6.16. The minimum and maximum spacing are 0.52 and 0.68 m.

The change in sleeper spacing affects the average ballast stiffness; therefore to avoid changing this at the same time the individual ballast stiffness and damping values are set to correspond to each of those spacings. This gives a constant stiffness per unit length. Comparisons of ground response due to the track with variable sleeper spacing and the reference case (sleeper passing case with constant sleeper spacing of 0.6 m) are considered.

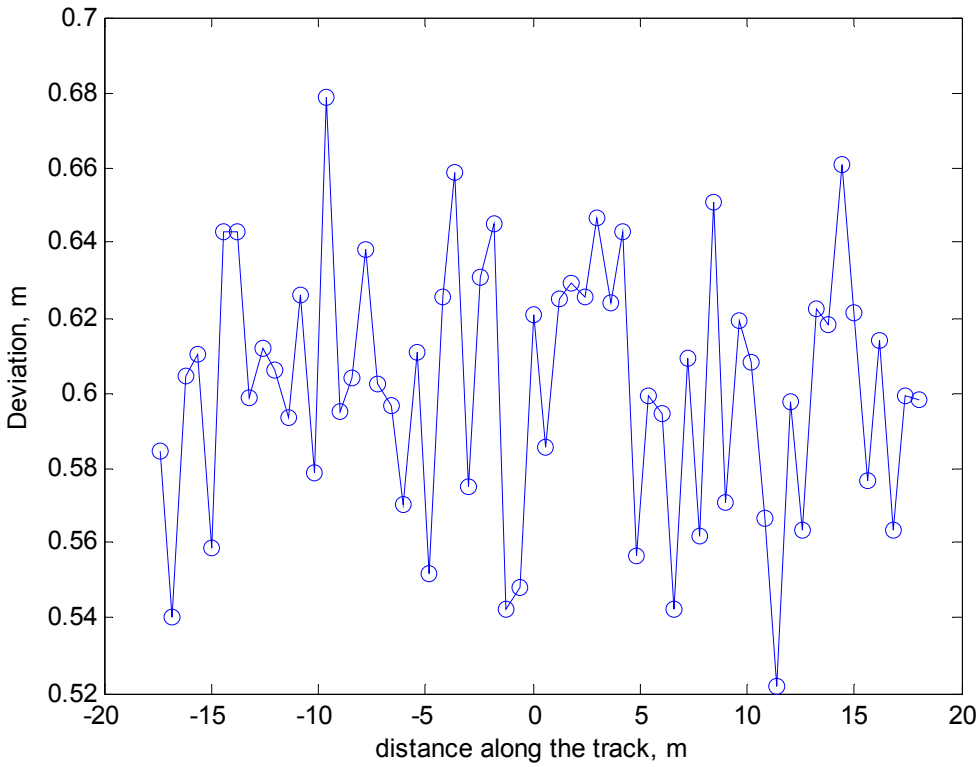

Figure 6.16. Variation of sleeper spacing along the track for 1 lap.

The results for the random sleeper spacing are shown in Figures 6.17 and 6.18. These results show the ground responses on a half-space of chalk due to the quasi-static load with random sleeper spacing, at the positions of 0 and 10 m in the direction perpendicular to track (y as shown in Figure 6.19). Results are shown for various

positions in the direction along the track (x) due to the fact that at the position closest to the response point the spacing could have any value deviating from 0.6 m.

The peaks at around 40 and 80 Hz correspond to the sleeper passing effect for a constant spacing, as mentioned in section 6.2. As the sleeper spacing has been changed randomly, those peaks randomly deviate from these frequencies. In other words, the peaks become blurred due to the unequal spacing, especially for $y = 0$. This can also be seen in Figure 6.20 which shows the average ground responses over various x positions due to the quasi-static load. This average response contains a broad peak around the sleeper passing frequencies for the case of random spacing. The peak in the average response is also slightly greater than for regular spacing by about 3 dB at y = 10 m while the response away from the peaks increases considerably.

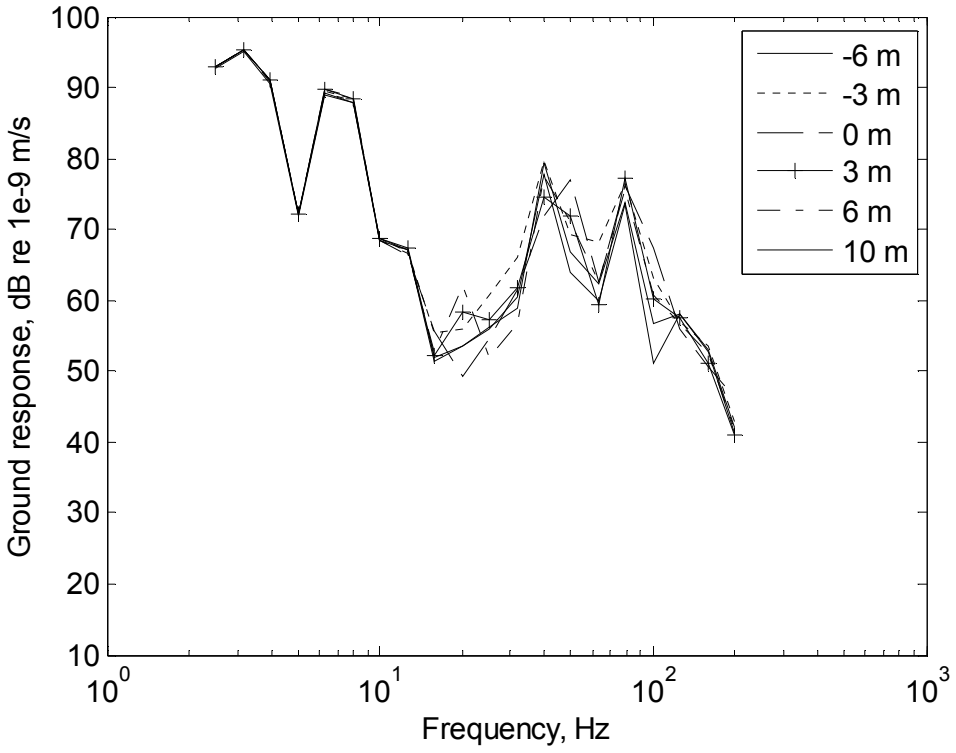

Figure 6.17. Ground responses due to quasi-static load with random sleeper spacing at $y = 0$ underneath the track, for various positions along the track (x direction).

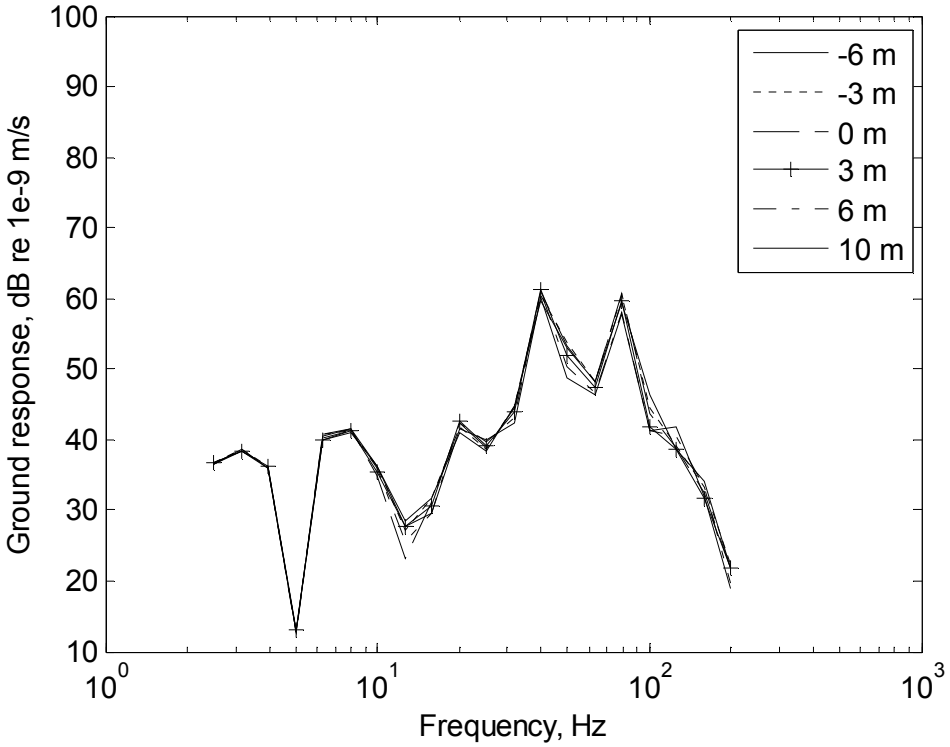

Figure 6.18. Ground responses due to quasi-static load with random sleeper spacing at y = 10 m perpendicular away from the track, for various positions along the track (x direction).

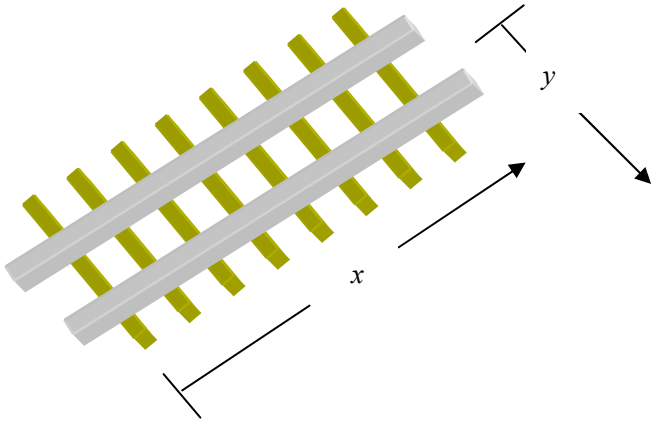

Figure 6.19. Direction, x along the track and y perpendicular away from the track.

Comparisons similar to those in Figure 6.20 are shown in Figure 6.21 for the clay soil. The overall responses increase as the ground properties become softer. Introducing the variation of sleeper spacing on the clay soil gives a slightly smaller

amplitude than the reference case at 0 m below 50 Hz. However the ground response at 10 m increases by 16 dB at 20 Hz compared with the reference case.

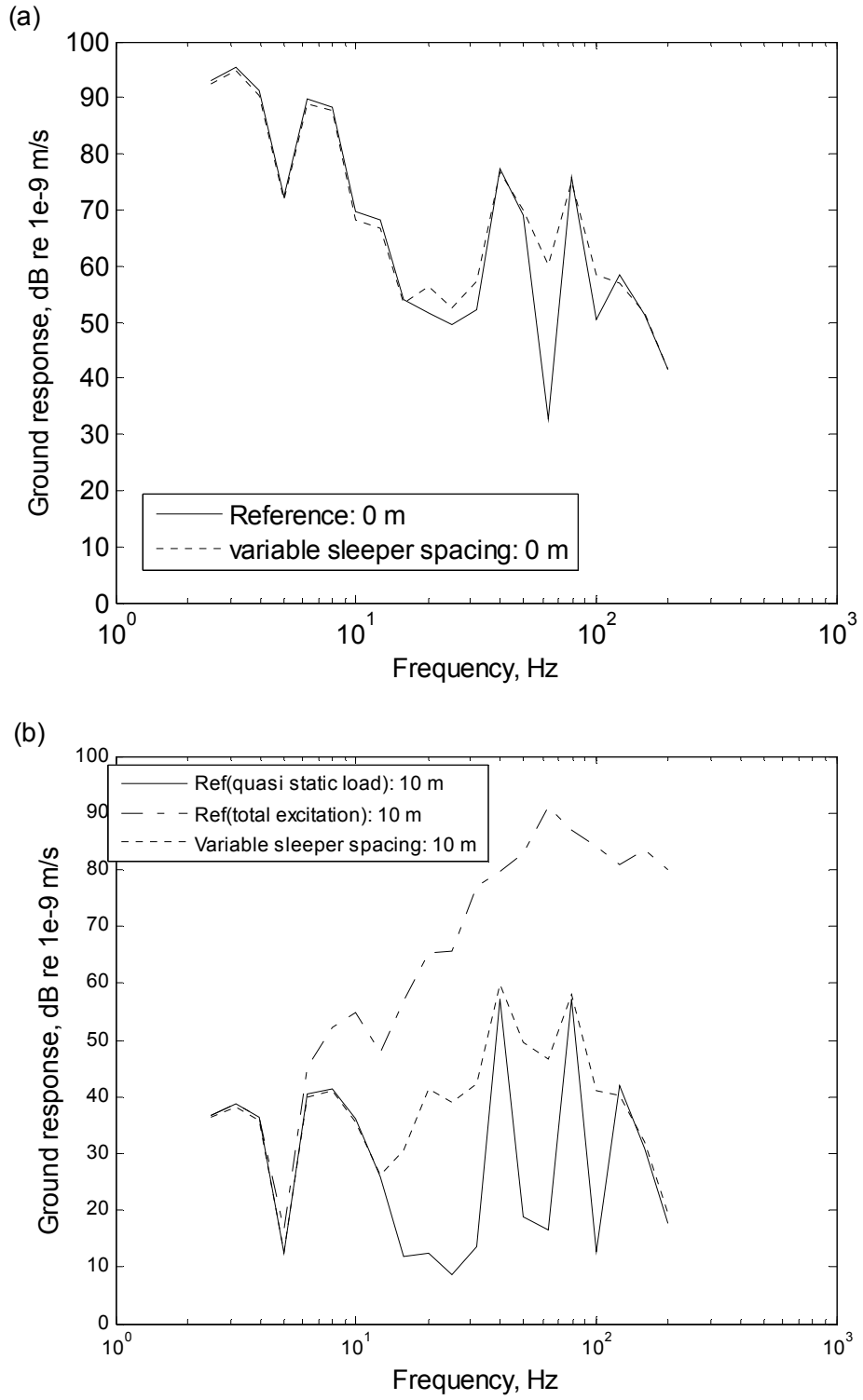

Figure 6.20. Comparisons of ground responses due to quasi-static load between reference case and the average for the case of random sleeper spacing at (a) y = 0 m and (b) y = 10 m on a half-space of chalk.

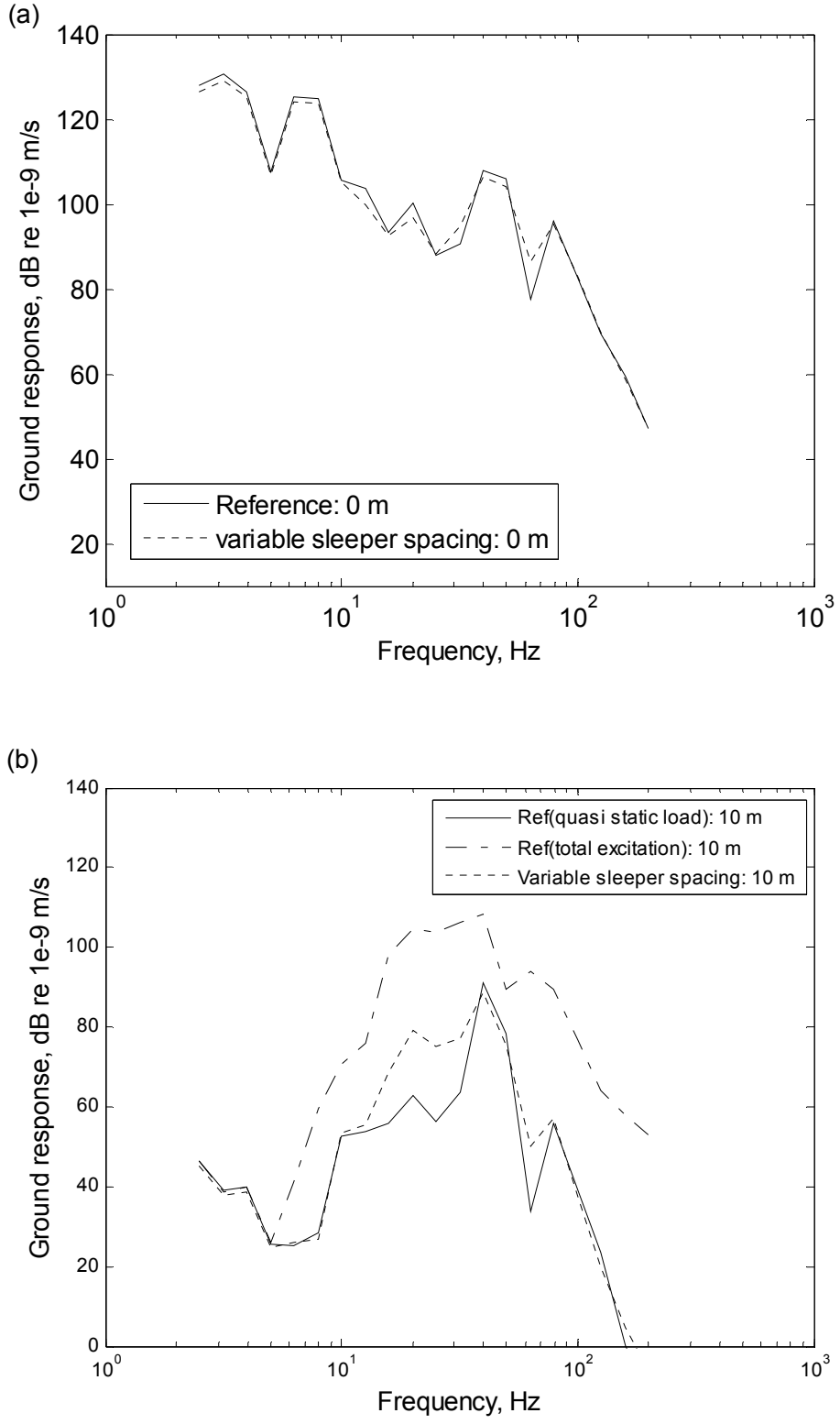

Figure 6.21. Comparisons of ground responses due to quasi-static load between reference case and the average for the case of random sleeper spacing at (a) y = 0 m and (b) y = 10 m on clay soil.

6.4 Variable ballast stiffness

The last parameter considered in this chapter is variable ballast stiffness. As a track is used over a period of time, its stiffness gradually changes as trains run past due to degradation of the ballast and subgrade. In order to investigate variations of ballast stiffness along the track, the stiffness has been assigned a random value, as shown in Figure 6.22. The standard deviation assumed of 12% of the mean value, for variation of ballast stiffness is based on measured values [3]. The support stiffness beneath each sleeper consists of the combination of ballast stiffness and the ground stiffness. It is this combined stiffness with a mean value of 1.84×10^8 N/m^2 which is varied with a standard deviation of 12% (for the clay soil the mean value is 1.1×10^8 N/m^2).

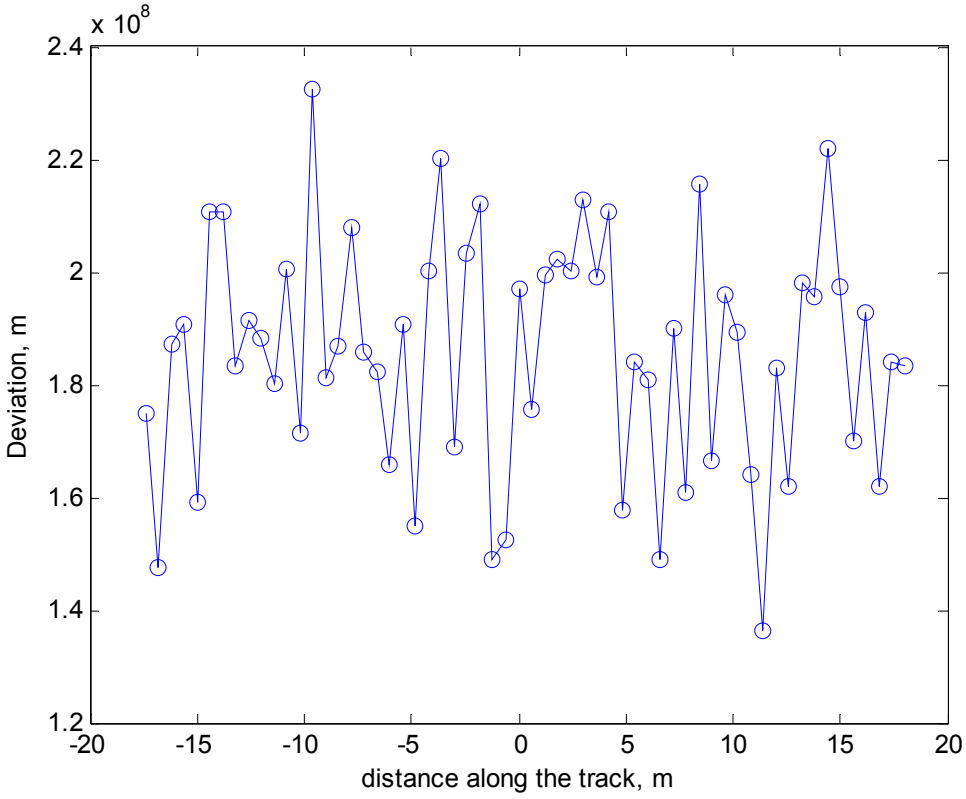

Figure 6.22. Variation of ballast stiffness along the track for 1 lap.

Figure 6.23 shows the ground responses on a half-space of chalk due to the quasi-static load with random ballast stiffness. The positions of the response are at 0 and 10 m in the *y* direction and various positions in the *x* direction. A small change at the sleeper passing frequency is found. As the sleeper spacing remained constant the

sleeper passing frequency itself is unaffected. The random change in ballast stiffness affects the ground response between 8 and 30 Hz compared with the case of constant stiffness. This can be seen in Figure 6.24 which shows the average ground responses over various x positions due to the quasi-static load at $y = 0$ and $y = 10$ m. Peaks still occur at 40 and 80 Hz and on average are unaffected in level.

By comparing the average ground response, similar effects are found in the results due to changes in sleeper spacing and ballast stiffness on the clay soil as shown in Figures 6.21 and 6.25. For both soils changes in sleeper spacing and ballast stiffness lead to changes in the response to quasi-static loads above 10 Hz, especially at 10 m from the track. However the response at these frequencies remains insignificant compared with that due to roughness excitation.

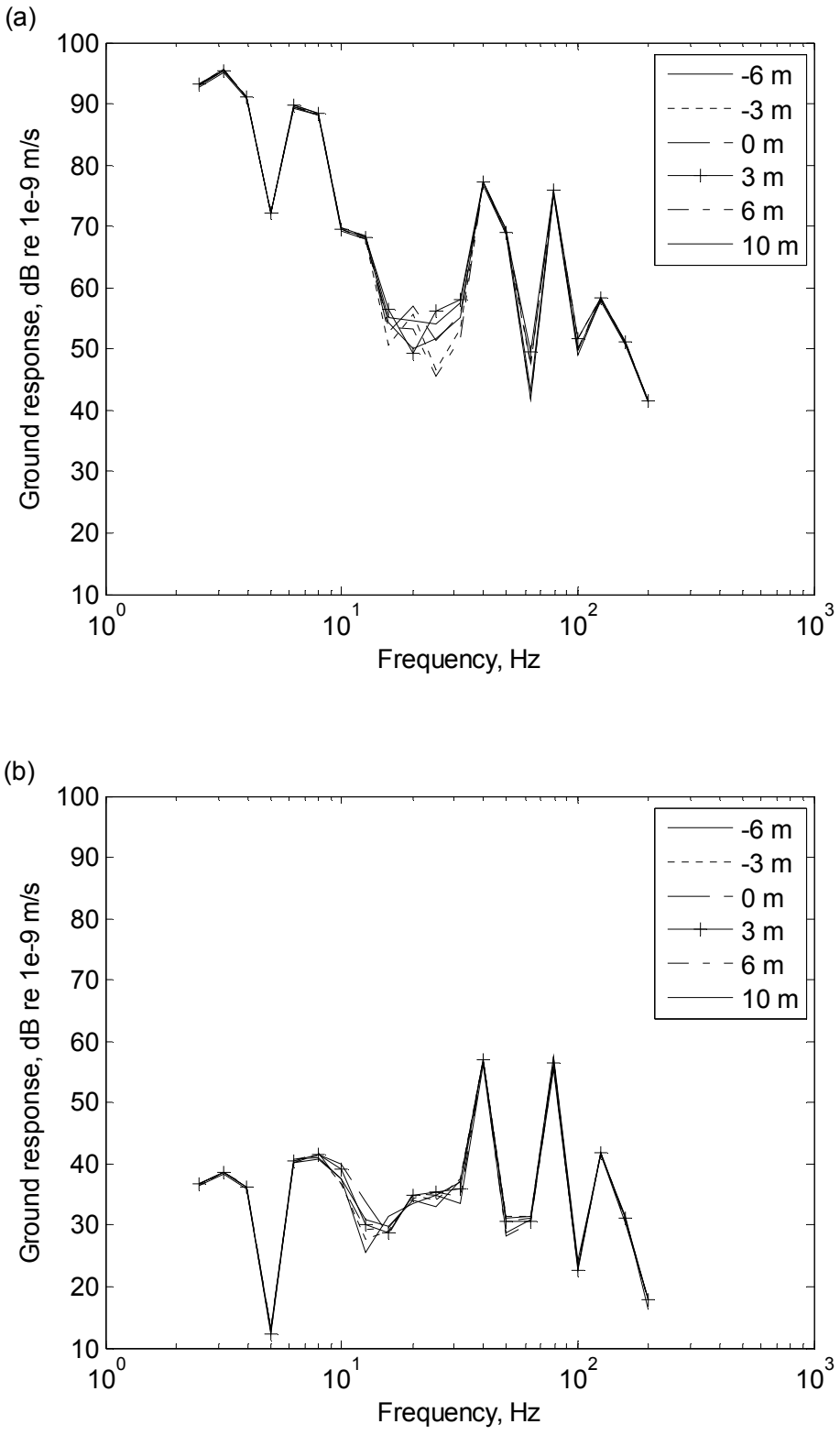

Figure 6.23. Ground responses due to quasi-static load with random ballast stiffness at (a) $y = 0$ and (b) $y = 10$ m perpendicular away from the track, for various positions along the track.

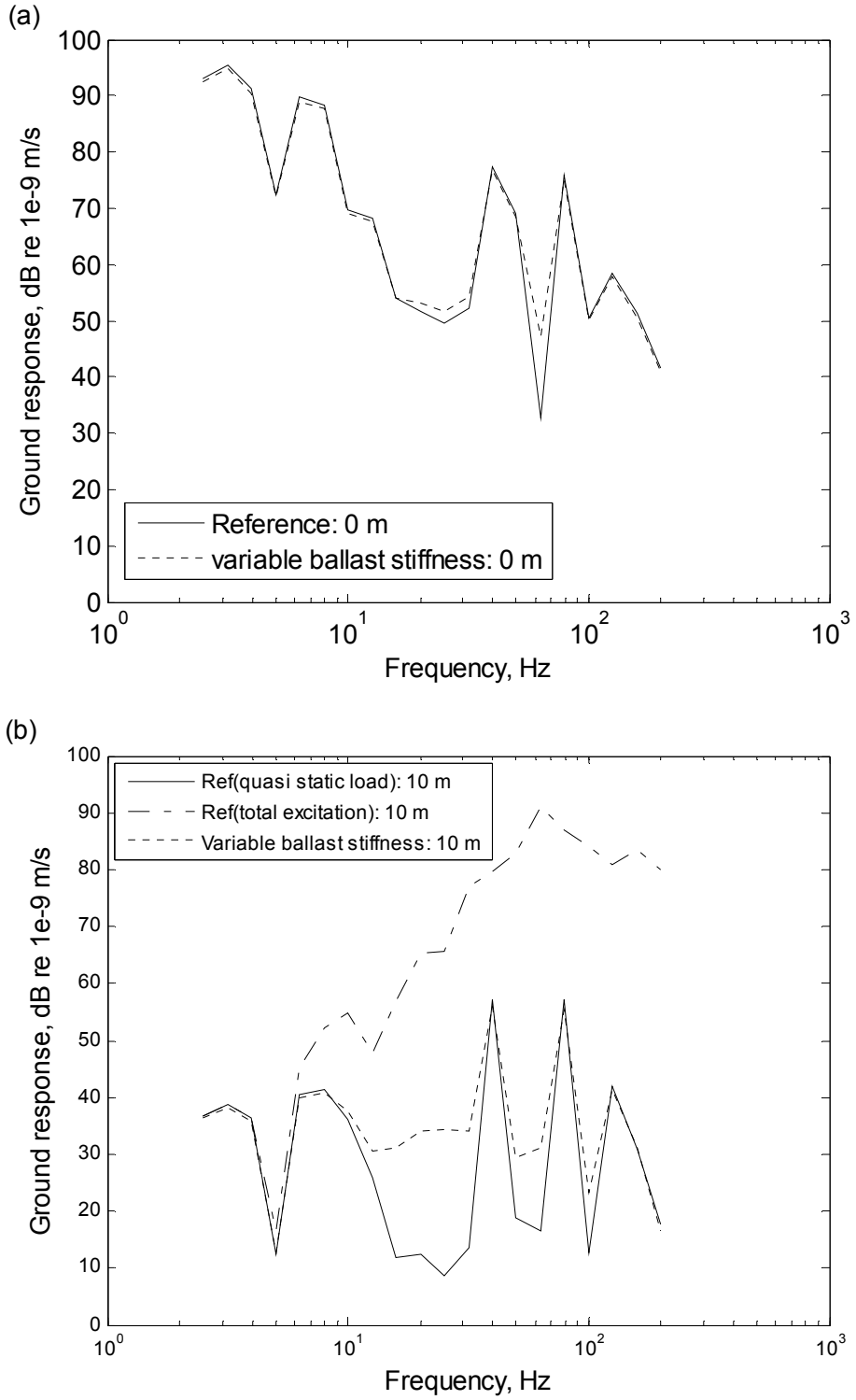

Figure 6.24. Comparisons of ground responses due to quasi-static load between reference case and the case for the average of ballast stiffness at (a) y = 0 m and (b) y = 10 m.

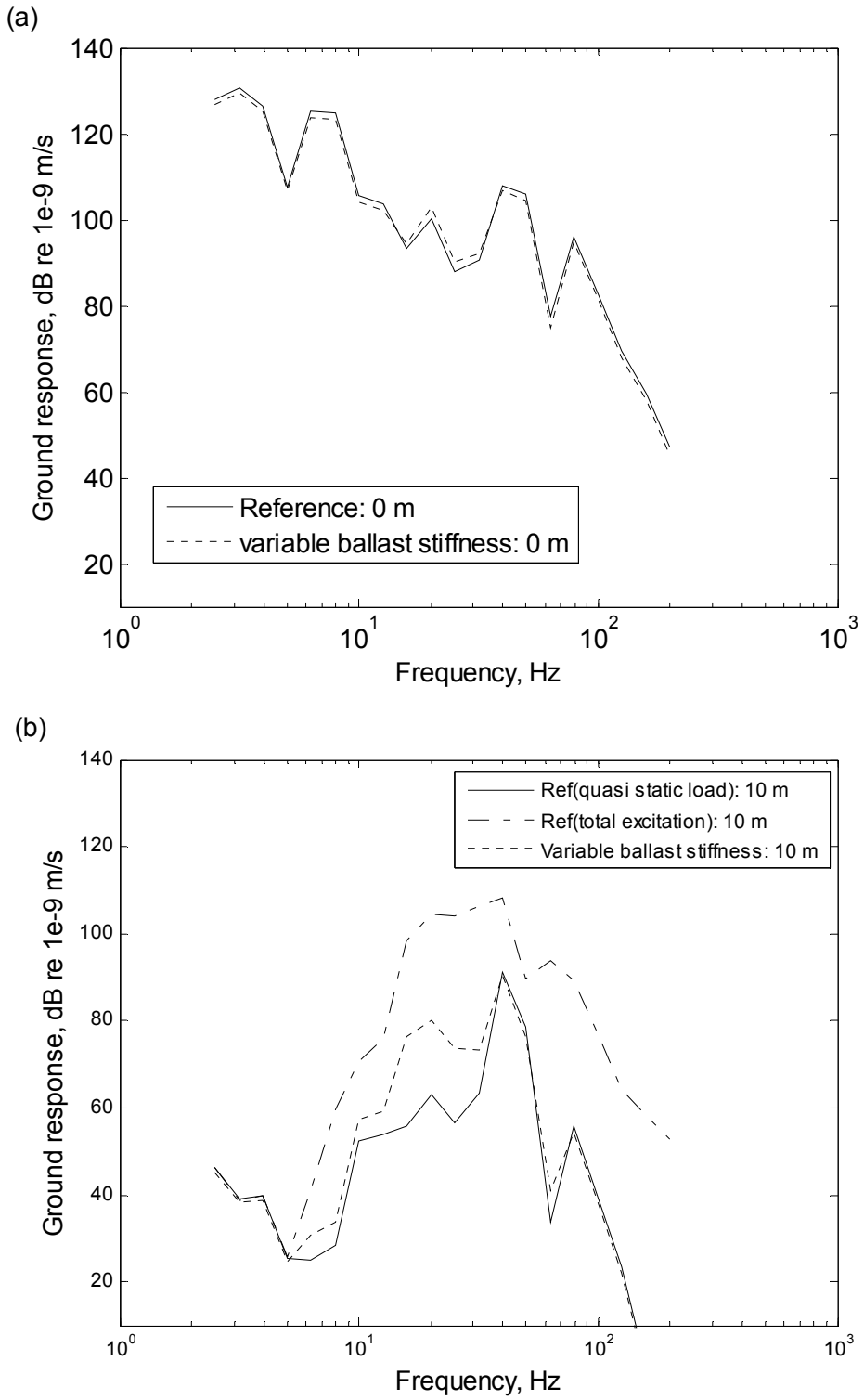

Figure 6.25. Comparisons of ground responses due to quasi-static load between reference case and the case for the average of ballast stiffness at (a) y = 0 m and (b) y = 10 m on clay soil.

6.5 Conclusions

The hybrid model combines a time and spatial domain wheel/track interaction model with the transfer mobilities from kandr. The model operates in the time and spatial domain. This allows investigation of various excitation mechanisms, for instance parametric excitation due to sleeper-passing effects and excitation due to variations in ballast or ground stiffness beneath each sleeper. These have been investigated in this chapter. The effects of changes in various track/train parameters have been estimated for locations close to the track and further away in order to see the effect of the sleeper passing frequency with and without roughness applied as an excitation.

As found in Chapter 5 the sleeper passing effect dominates the response due to quasi-static loads for all distances at the frequencies of about 40 and 80 Hz (for a train speed of 25 m/s). However it has much less effect on the ground response than the excitation due to roughness.

The effects of changes in axle load, vehicle speed, ground type and rail pad stiffness on the ground response have been considered. The ground models used in this Chapter are based on only two different soil types: a soft clay soil and a stiffer ground typical of chalk. The ground responses for the clay soil are greater than those for chalk by about 30 dB but the effect of the sleeper passing frequency remains a similar amount below the overall response due to roughness.

It is found that by doubling the axle load the vibration level due to the quasi-static load (including the sleeper passing effect) increases by about 6 dB at both 0 and 10 m.

The effect of the quasi-static component dominates the vibration response towards higher frequencies as the speed of the train increases. The sleeper passing frequency also increases with train speed. A peak at 60 Hz corresponds to the unsprung mass bouncing on the track. The ground response has maximum amplitude when the sleeper passing frequency coincident with this frequency.

Inserting a softer pad gives a lower ground response due to quasi-static load over much of the frequency range. But it gives a higher amplitude at the sleeper passing frequency.

Variation of sleeper spacing has been investigated to see the effect on the ground response by introducing a random spacing between each sleeper. As the sleeper spacing has been changed randomly, the peaks at the sleeper passing frequency become blurred due to the unequal spacing. The average ground responses over various positions along the track have a broad peak around the sleeper passing frequencies. The peak in the average response is also slightly greater than for regular spacing on the half-space of chalk. On the other hand, there is much less effect on the level on the clay soil.

Finally the effect of variable ballast stiffness on the vibration response has been investigated. As the sleeper spacing remained constant the sleeper passing frequency is unaffected. The random change in ballast stiffness affects the ground response between 8 and 30 Hz compared with the case of constant stiffness.

In summary all the parameters investigated in this chapter have a fairly small effect on the ground vibration as the dynamic load dominates the response at frequencies corresponding to the sleeper passing effects.

7. Modelling vibration from discrete track defects

7.1 Introduction

The conventional sources of roughness associated with ground vibration from trains are mainly random rail-surface roughness and wheel roughness [15]. However, at certain locations discrete irregularities of the rail can lead to local increase in vibration. Examples are rail joints and switches and crossings.

The purpose of this Chapter is to study the effects of discrete track defects on the ground vibration at locations close to the track and further away. Rail joints can lead to increased vibration in the vicinity of the joint. Due to the occurrence of large impact forces when each wheel runs past the effect of such impact forces on ground vibration is investigated using the hybrid model. This model allows the vehicle/track interaction to be calculated in the time domain before calculating the ground response in the frequency domain. Various dipped welds and step-up joints are investigated.

All parameters used to represent the vehicle, track system and ground properties are the same as used in Chapter 6.

Track defects are usually characterized in terms of the angle of the dip [73]. EN 15610 also presents a guideline to identify the rail defects in term of geometric features [119]. To represent a dipped weld the expression given by [120] and [73] is used:

$$z = -\left(\frac{2}{L}\right)^2 z_0 \left(x - \frac{L}{2}\right)^2 = -\left(\frac{2}{L}\right)^2 z_0 \left\{x^2 - \frac{2xL}{2} + \left(\frac{L}{2}\right)^2\right\} \tag{7.1}$$

The height z is a function of the overall depth z_0 and the width L as shown in Figure 7.1. Differentiation of z with respect to x yields an angle $\theta/2$ at $x = 0$ as shown below

$$\frac{\theta}{2} = \left(\frac{dz}{dx}\right)_{x=0} \tag{7.2}$$

Substituting $\left(\frac{dz}{dx}\right) = -z_0 \left(\frac{2}{L}\right)^2 \{2x - L\}$ at $x = 0$ into (7.2) gives

$$\frac{\theta}{2} = z_0 \frac{4}{L} \tag{7.3}$$

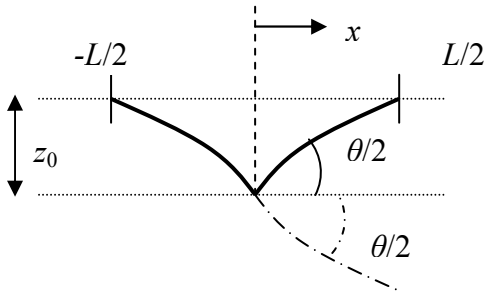

Figure 7.1. Geometry of the discrete track defect.

The discrete track defect is defined as a dipped weld with the above shape situated at the middle of the track length with zero amplitude on both sides beyond the length of $\pm L/2$, as shown in Figure 7.2. This is introduced as a 'roughness' which is input to the model in a similar way to the random roughness considered in the previous chapters.

A depth of 1 mm is chosen to represent a reference case for a dipped weld. Although in the regulations for new track such dips are typically limited to 0.2 mm [121], larger values are considered here to represent track that has been used. A number of cases are considered as listed in Table 7.1. For a step-up joint, a depth of 2.5 mm (with a step of 1.0 mm) is chosen to represent a reference case. The step-up joints are considered in Section 7.3 below.

Table 7.1. Parameters used to represent different sizes of track defect.

Parameters		Height (mm)	Width (m)	Angle (rad)	Step (mm)
Dipped welds	Small	0.2	1.0	0.0016	0
	Medium	1.0	1.0	0.008	0
	Large	2.5	1.0	0.02	0
Step-up joints	Small	1.0	1.0	0.008	1.0
	Medium	2.5	1.0	0.02	1.0
	Large	5.0	1.0	0.04	1.0

The shape of these features for dipped welds is shown in Figure 7.2, in this case for a depth of 2.5 mm.

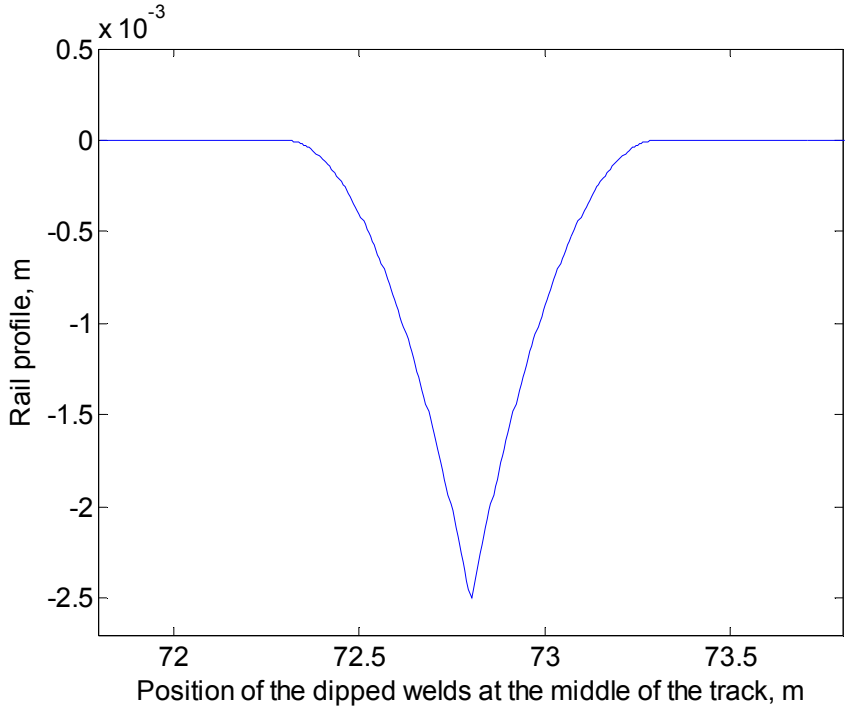

Figure 7.2. Shape of the dip for large dipped welds at the middle of the track.

As each wheel runs past, interaction forces are generated. For a case of a dipped weld Figure 7.3 shows the interaction forces between wheel and rail for each wheel separately, along with the input roughness at an expanded scale. At the time when the first wheel reaches the dipped weld this wheel shows a large interaction force. A small effect at the position of the second wheel can also be seen as the first wheel reaches the dipped weld, whereas there is no effect on the interaction force at the positions of third and fourth wheels. This is due to the attenuation of vibration along the rail. Although a small effect is found at the position of the second wheel, it is negligible compared with the interaction force due to the first wheel. The pattern of the interaction response occurs similarly as each of the four wheels runs past.

Figure 7.4 shows equivalent results as in Figure 7.3(b) for four different cases: medium dipped weld, large dipped weld, medium step-up joint and large step-up joint. In the results shown in Figure 7.4 (b), (c) and (d) loss of contact can be found for

large defects. The interaction forces for small rail defects are not shown here as only small effects are found.

Figure 7.5 shows in more detail the interaction force for the first wheel, the same as shown in Figure 7.3 (a). The interaction force drops a little just after it reaches the edge of the dip due to the inertia of the wheel which prevents it following the dip. The width of the dip is 1 m. At the deepest point of the dip, the maximum force can be seen due to impact. The coupled vehicle/track system starts to oscillate at about 60 Hz after the impact. This is the coupled vehicle/track-ground resonance as also shown in next section.

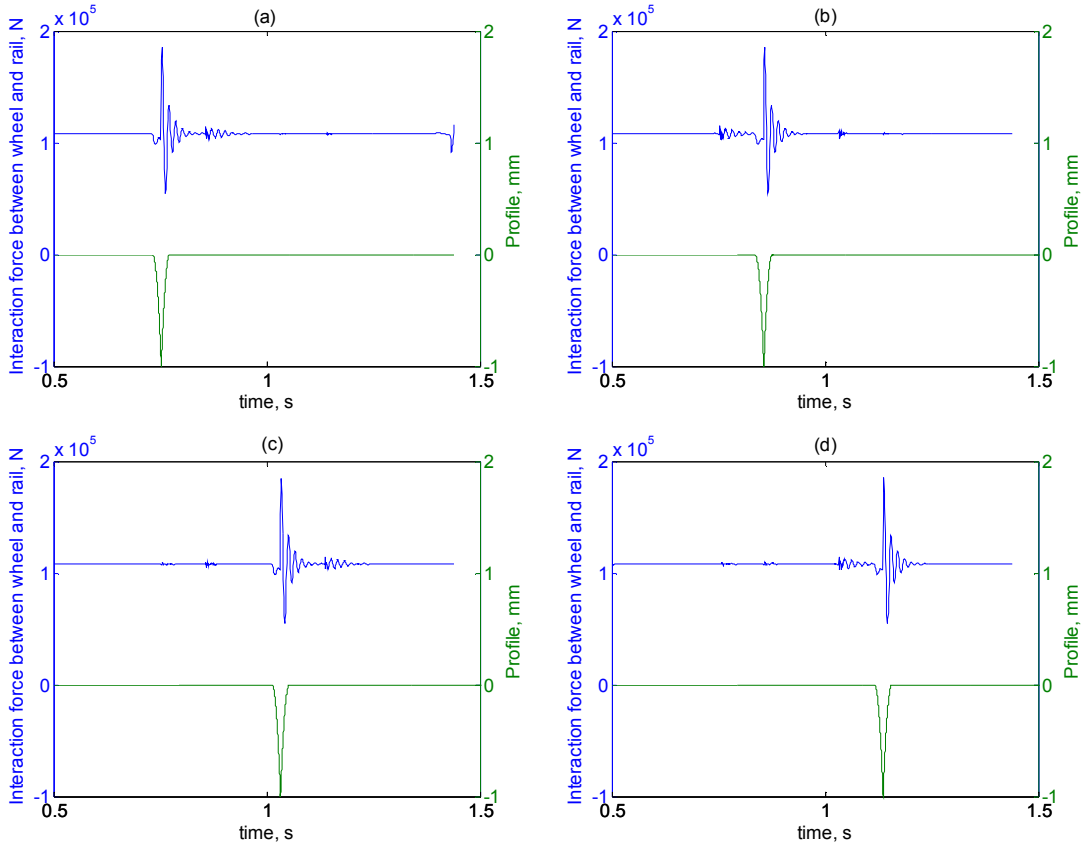

Figure 7.3. Interaction forces between wheel and rail with expanded scale of roughness for (a) first wheel, (b) second wheel, (c) third wheel and (d) fourth wheel.

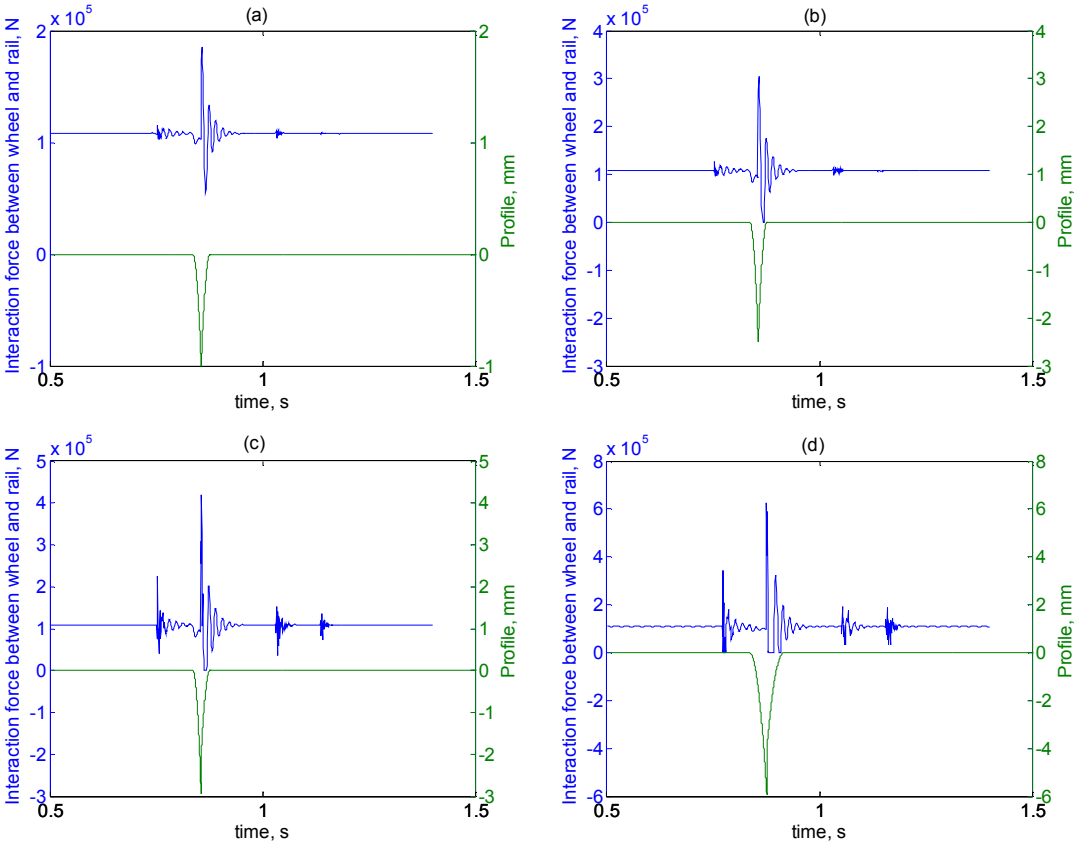

Figure 7.4. Interaction forces between second wheel and rail with expanded scale of roughness for (a) medium dipped welds, (b) large dipped welds, (c) medium step-up joint and (d) large step-up joint.

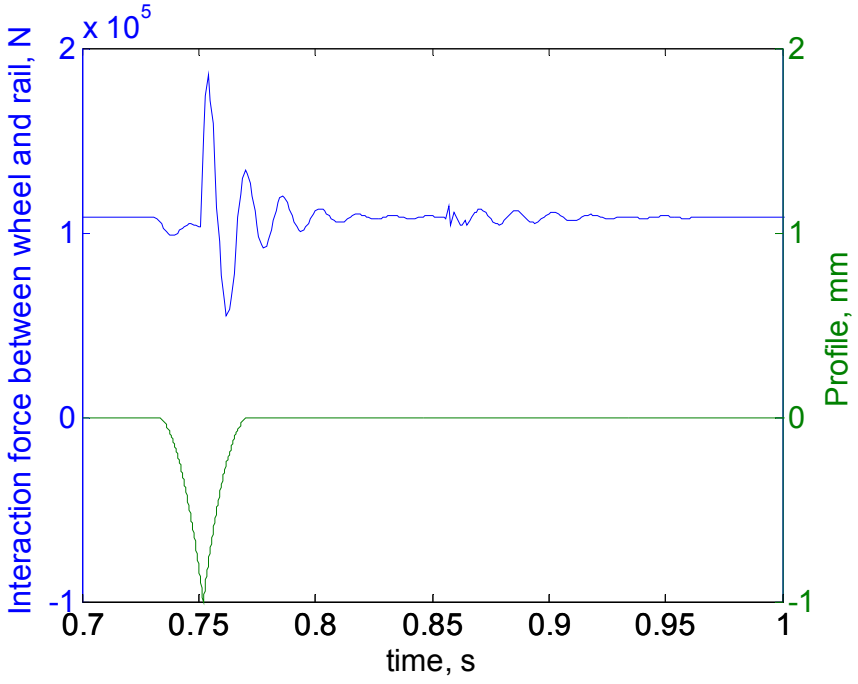

Figure 7.5. Interaction force between wheel and rail for first wheel with expanded scale of roughness.

7.2 Dipped welds

7.2.1 Spectra

To investigate the effect of dipped welds on the ground response due to the occurrence of impact forces when each wheel runs past, three heights of dipped weld, 0.2, 1 and 2.5 mm, are considered. The track/vehicle parameters and ground properties used in the model are the same as in Chapter 6.

Comparison of the ground response due to various excitations: smooth roughness (only moving quasi-static load), Steventon roughness from Chapter 3, small dipped welds, medium dipped welds and large dipped welds are shown in Figures 7.6 to 7.8. This shows a comparison between the ground response due to these excitations at 0, 10 and 25 m away from the track. In each case the 1/3 octave spectra are calculated from the complete passage of the four wheelsets over 144 m of track (4 laps) using the same analysis procedure as in Chapter 5. The results are expressed as equivalent levels over the 'train' pass-by length of 9.6 m.

The results show that all cases of dipped weld excitation give higher ground response than the case of smooth roughness (quasi-static load) at distances close to and further from the track above about 8 Hz. The deeper the dipped weld the greater the ground response becomes. It can clearly be seen that the medium and large dipped welds dominate the response at all distances considered. However, the Steventon roughness still dominates the ground response compared with a case of small dipped welds (limit of rail defect size for new track). An increase of about 8 dB is found above 10 Hz as the height of the dipped welds increases from 1 to 2.5 mm at all distances. Similarly an increase of 14 dB is found between depths of 0.2 and 1 mm. The sleeper passing effect cannot be seen in the ground response when the roughness is included.

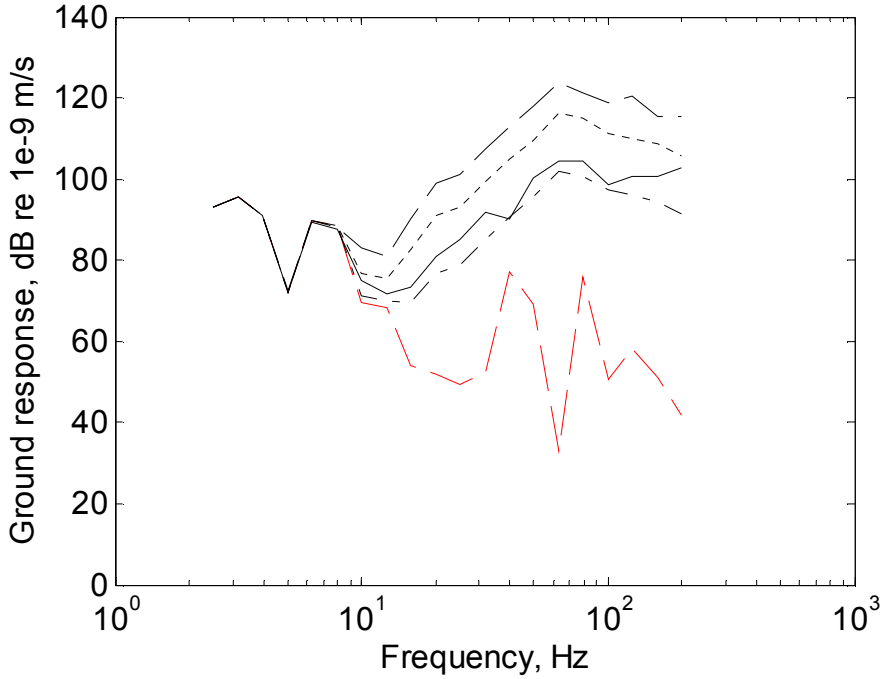

Figure 7.6. Comparison of ground response due to – –, reference: smooth; —, reference: Steventon roughness; – · – , dipped welds: 0.2 mm; ·····, dipped welds: 1 mm; – –, dipped welds: 2.5 mm at 0 m underneath the track.

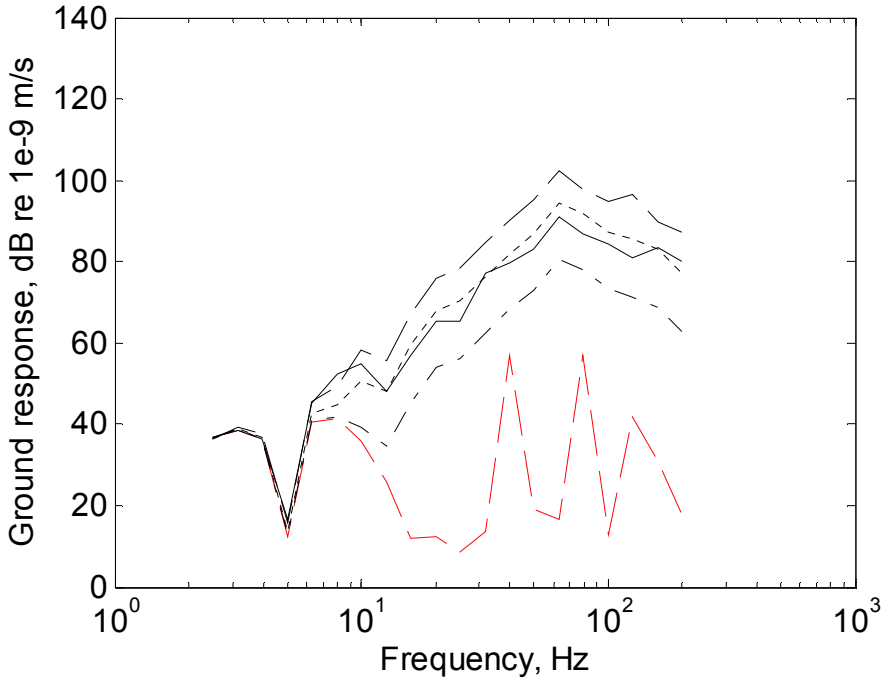

Figure 7.7. Comparison of ground response due to – –, reference: smooth; —, reference: Steventon roughness; – · – , dipped welds: 0.2 mm; ·····, dipped welds: 1 mm; – –, dipped welds: 2.5 mm at 10 m away from the track.

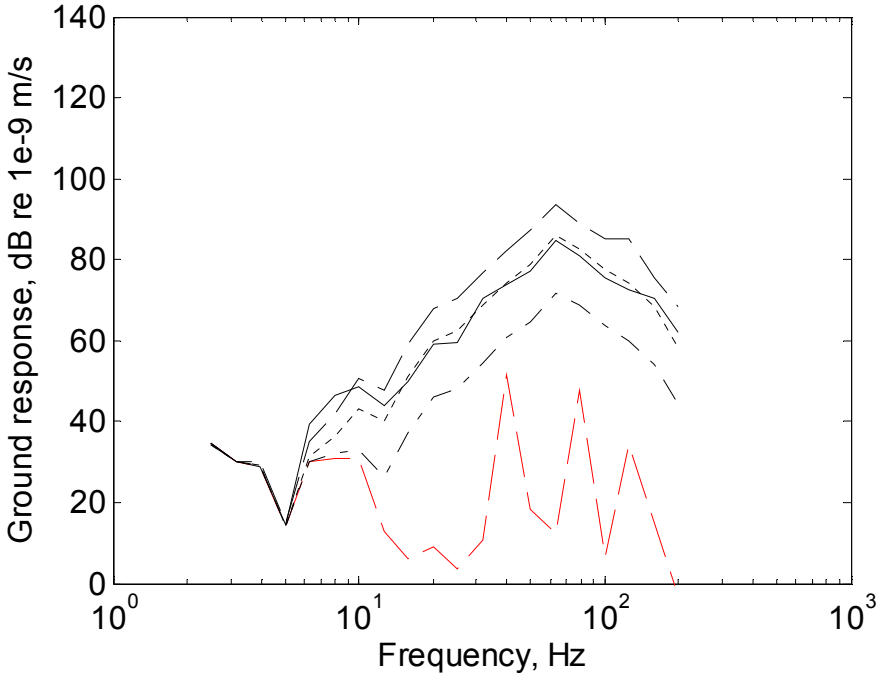

Figure 7.8. Comparison of ground response due to – –, reference: smooth; —, reference: Steventon roughness; – · – , dipped welds: 0.2 mm; ·····, dipped welds: 1 mm; – –, dipped welds: 2.5 mm at 25 m away from the track.

The vibration level drops off as the distance increases as shown in Figure 7.9 which shows the ratio of the response at 10 m to that at 0 m. The differences are found to be -15 dB for roughness excitation and -25 dB for dipped welds. The dipped weld excitation has a form more like a point source whereas roughness excitation is more like a line source. The response due to a point source drops more rapidly than that due to a line source. The ratio of the response due to roughness excitation is not constant. This is due to random variations in the roughness along the track (see Section 5.5.8). For the results below 10 Hz the difference is much larger due to the quasi-static component which dominates the response.

Similarly considering the ratio of the responses at 20 m and 10 m, as shown in Figure 7.10 a drop of 6 dB is found due to the dipped welds and 4 dB due to roughness excitation. For a point source a drop of $20\log_{10}\left(\frac{20}{10}\right)$ = 6 dB would be expected. The response at low frequencies, due to quasi-static excitation does not drop

consistently and may be affected by limited length of track (see Chapter 5). At high frequencies damping in the ground causes the decay with distance to increase.

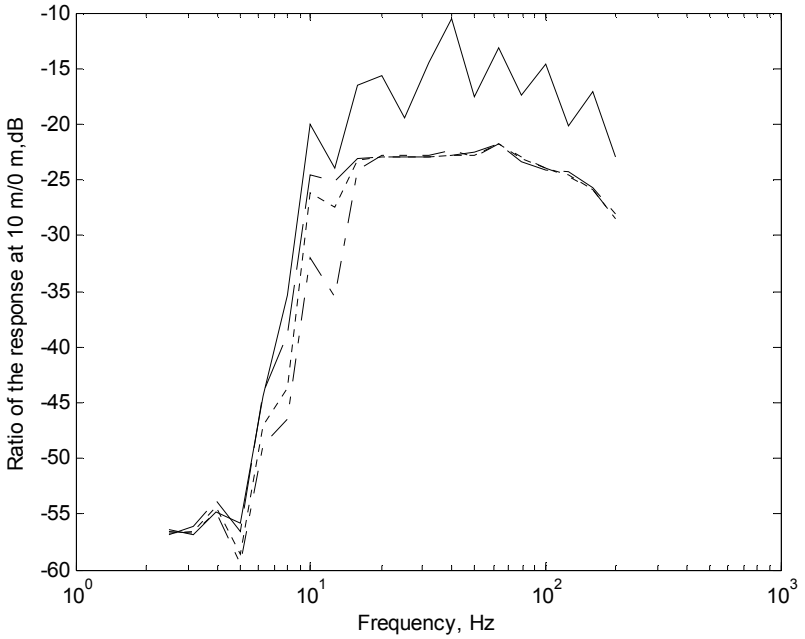

Figure 7.9. The ratio of ground response comparing the position 10 m and underneath the track for the case of —, reference: Steventon roughness; – · – , dipped welds: 0.2 mm; ·····, dipped welds: 1 mm; – –, dipped welds: 2.5 mm.

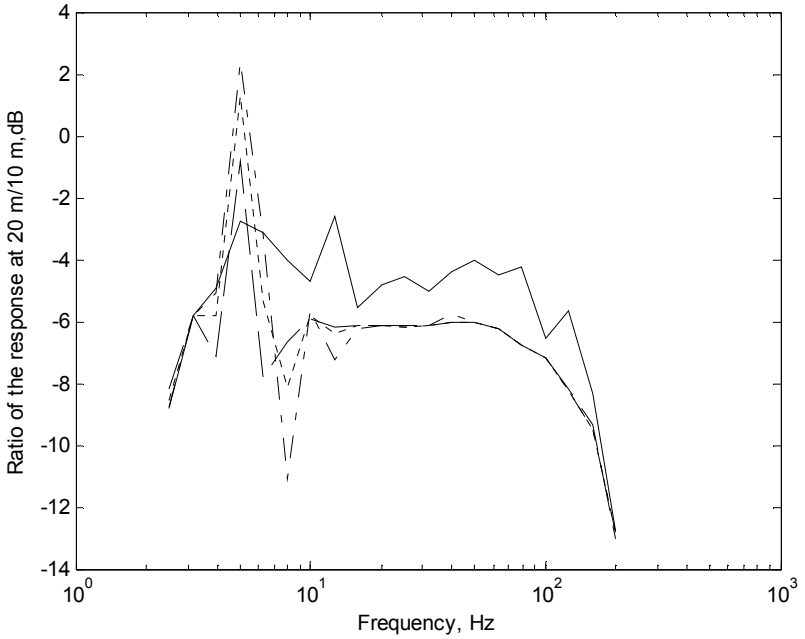

Figure 7.10. The ratio of ground response comparing at the position 20 and 10 m away from the track for the case of —, reference: Steventon roughness; – · – , dipped welds: 0.2 mm; ·····, dipped welds: 1 mm; – –, dipped welds: 2.5 mm.

To demonstrate that the vibration due to dipped welds spreads out as a circular wave, Figure 7.11 shows the ratio of the ground response for various locations due to the medium dipped welds. The solid line compares results at the location x = 10 m, y = 0 m and x = 0 m, y = 10 m. These points are equi-distant from the location of the dipped welds and as expected they give the same response above 20 Hz. The ratio of the ground response of 0 dB is expected. The difference of about 56 dB below 10 Hz is due to the quasi-static component which dominates the response at y = 0.

The dashed line shows the ratio of two points at a radius of 20 m from the dipped welds; these are at x = 0, y = 20 and x = 10, y = 17.3. Again these give similar results above 10 Hz.

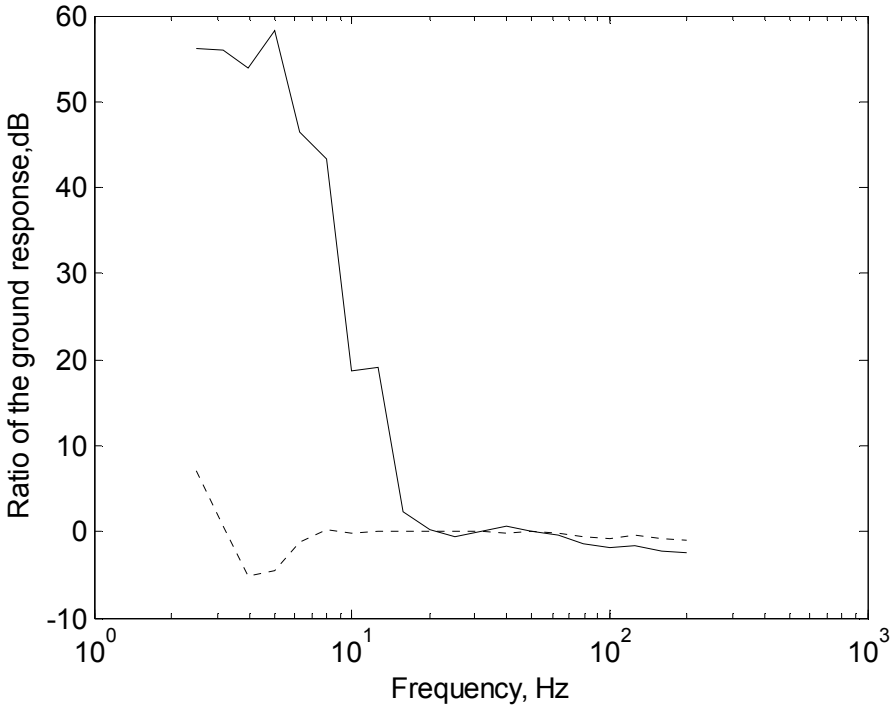

Figure 7.11. The ratio of ground response comparing at the position. —, x = 10 m at y = 0 m and x = 0 m at y = 10 m; ····· , radius (r) = 20 m and x = 0 m at y = 20 m for the medium dipped welds.

The effect of changes in the depth of dipped welds is shown in Figure 7.12. This shows the ratio of ground response between two depths, 1 and 2.5 mm, at 0, 10 and 25 m away from the track. The depth of dipped welds has no effect on the ground response below about 10 Hz whereas it gives about 8 dB difference above

approximately 16 Hz for all distances. This corresponds to $20\log_{10} 2.5$ which suggests an approximately linear relation to dip size despite the occurrence of loss of contact for the longer dipped weld (see Figure 7.4).

A similar effect of change in the depth of dipped welds is shown in Figure 7.13 for smaller dips. It shows the ratio of ground response between depths of 0.2 and 1 mm at 0, 10 and 25 m away from the track. The difference of 14 dB corresponds to $20\log_{10}\left(\frac{1}{0.2}\right)$ apart from the effect of the quasi-static component below about 20 Hz where the differences are smaller.

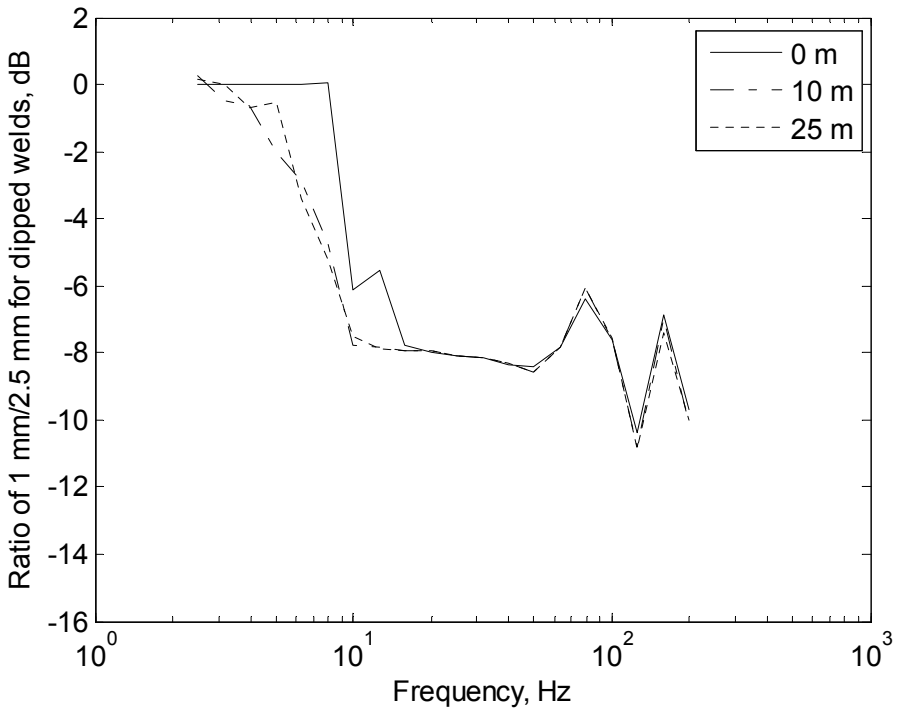

Figure 7.12. The ratio of ground response comparing between two depths of 1 and 2.5 mm for the dipped welds.

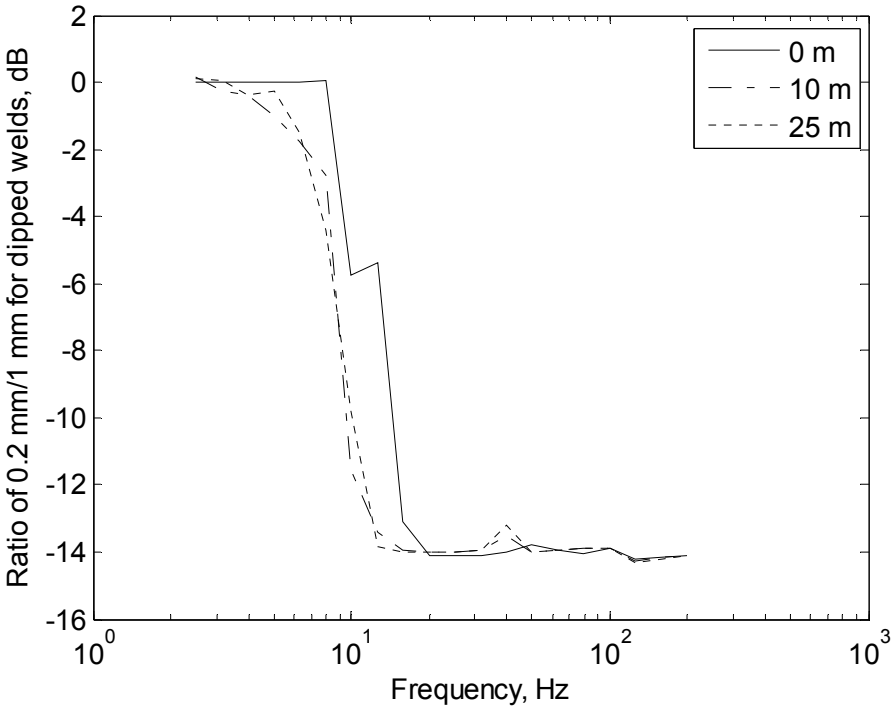

Figure 7.13. The ratio of ground response comparing between two depths of 0.2 and 1 mm for the dipped welds.

7.2.2 Decay with distance

The attenuation with distance of vibration level due to discrete track defects (point source) is expected to be greater than that due to roughness (line source). For example in [122] it is shown that the attenuation of line-source transfer mobility with distance is less than that for a point source.

As mentioned in Chapter 2, surface waves involve coupled components of compressive and shear deformation [19]. Richart et al. [16] presented the wave field generated by a circular footing transmitting away by a combination of P, S and Rayleigh waves. With increasing distance the waves decrease in energy density or displacement amplitude, due to geometrical damping. The value of the exponent α corresponding to the reduction in the amplitude of the Rayleigh wave is stated in [16] to be 0.5.

Figures 7.14 and 7.15 show the ground response in various frequency bands in terms of the level at different distances normalized to the level at 0 m. Results are shown for the response on a half-space of chalk due to the 'small' dipped welds and

Steventon roughness using the hybrid model in Figure 7.14 and due to Steventon roughness using the TGV model in Figure 7.15. The investigation of geometrical spreading for waves propagating through the ground due to various excitations is considered. Comparisons of the ground response for medium and large dipped welds are also shown in Figure 7.16 on a half-space of chalk. These results are almost identical to the results for the small dipped weld. It is found that the factor α for all depths of dipped welds is 1.0 at frequencies 20, 40 and 80 Hz, corresponding to 6 dB/doubling of distance. For the Steventon roughness a value of α of 0.7 is found for the hybrid model. The results from TGV show a shallower decay corresponding to a value of α of 0.4. Despite differences, there is a clear trend that α is greater for a point source than for a line source.

For 160 Hz, it can be seen that the damping of the ground affects the amplitude much more than at low frequency. Note that frequencies above 100 Hz are not available from the TGV results due to numerical problems.

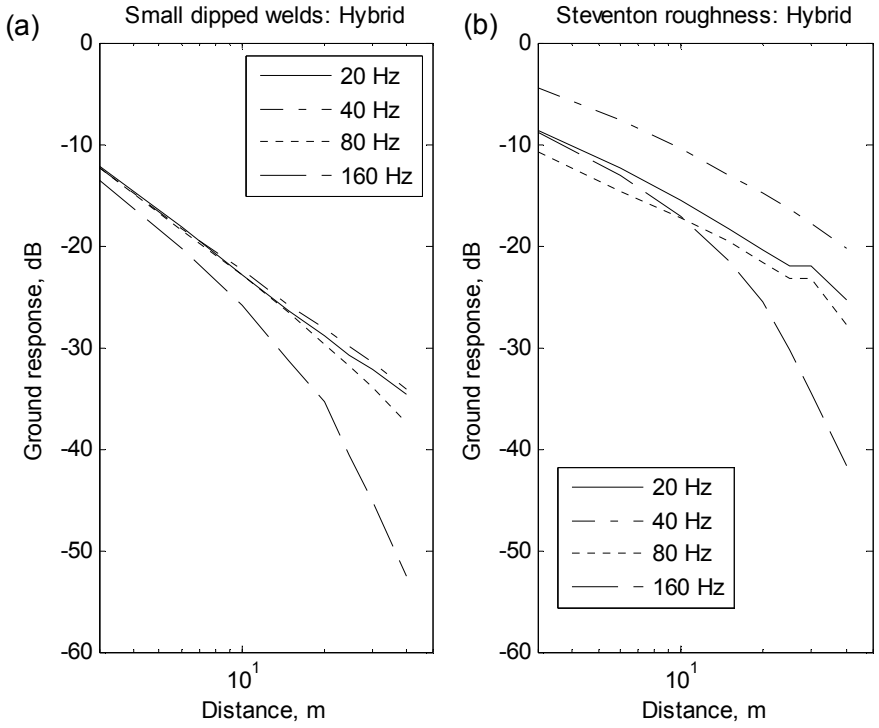

Figure 7.14. The ground response in terms of the relative level at different distances, due to (a) small dipped welds and (b) Steventon roughness using hybrid model, on half-space of chalk.

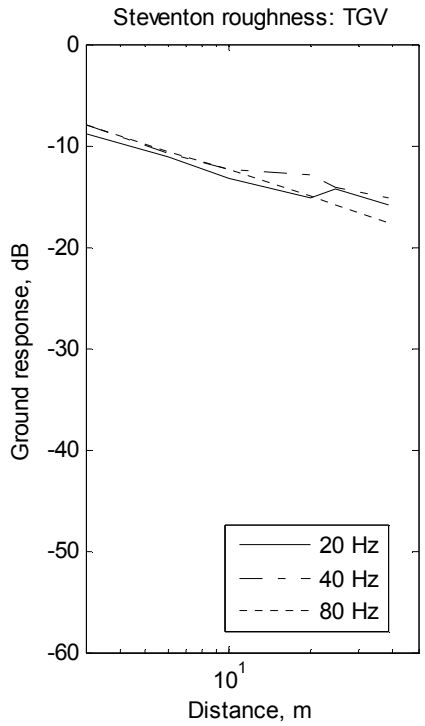

Figure 7.15. The ground response in terms of the relative level at different distances, due to Steventon roughness using TGV model, on half-space of chalk.

For comparison, the results for each of these cases on clay soil are shown in Figures 7.17 and 7.18. The amplitude changes, for the case of small dipped welds, by about 40 dB from 3 to 40 m at 20 and 40 Hz. The factor α can be found as 1.8 by taking 20 log of both sides of equation (2.13). Using a similar procedure to investigate the decay of wave amplitude, factors α of 1.5 and 1.4 are found for the hybrid and TGV results respectively. Only small differences are found between the three cases of dipped welds. The factor α found for all cases is also shown in Table 7.2, including the case of step-up joints, details of which are described in the next section.

The results in Table 7.2 differ from the values usually quoted in the literature. One reason is that the clay soil investigated here corresponds to a 3 m layer of clay overlying a stiffer half-space, whereas the usual result quoted in literature, that α is ½ for a Rayleigh wave, only applies to a half-space. The results found for the case of clay soil are clearly different. Besides, the factor α found in this chapter is associated with the combination of wave types on the ground surface (not a pure Rayleigh as described in the literature).

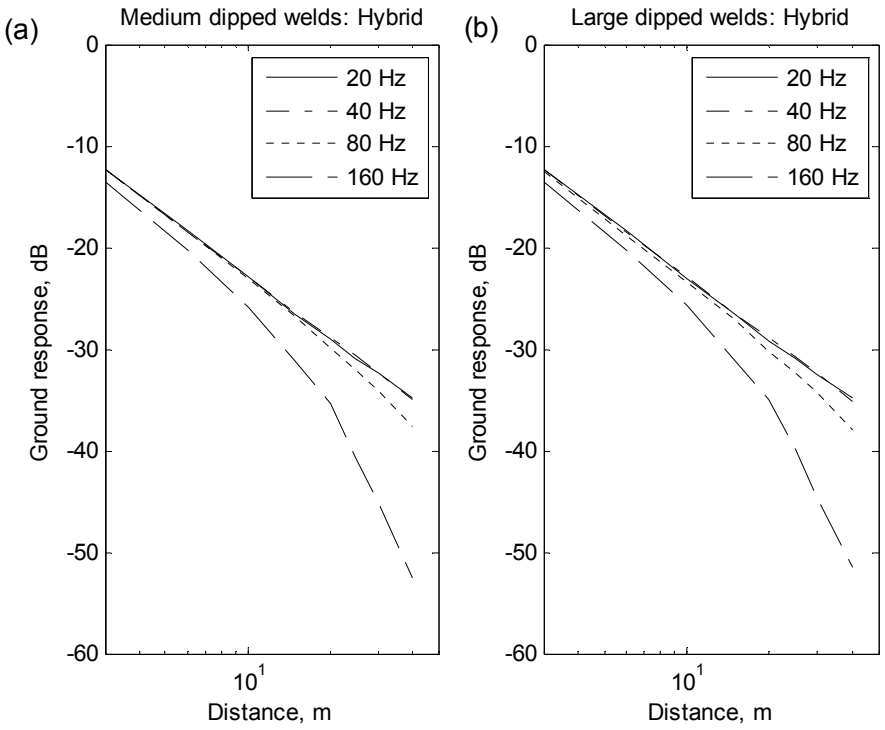

Figure 7.16. The ground response in terms of the relative level at different distances, due to (a) medium and (b) large dipped welds, on half-space of chalk.

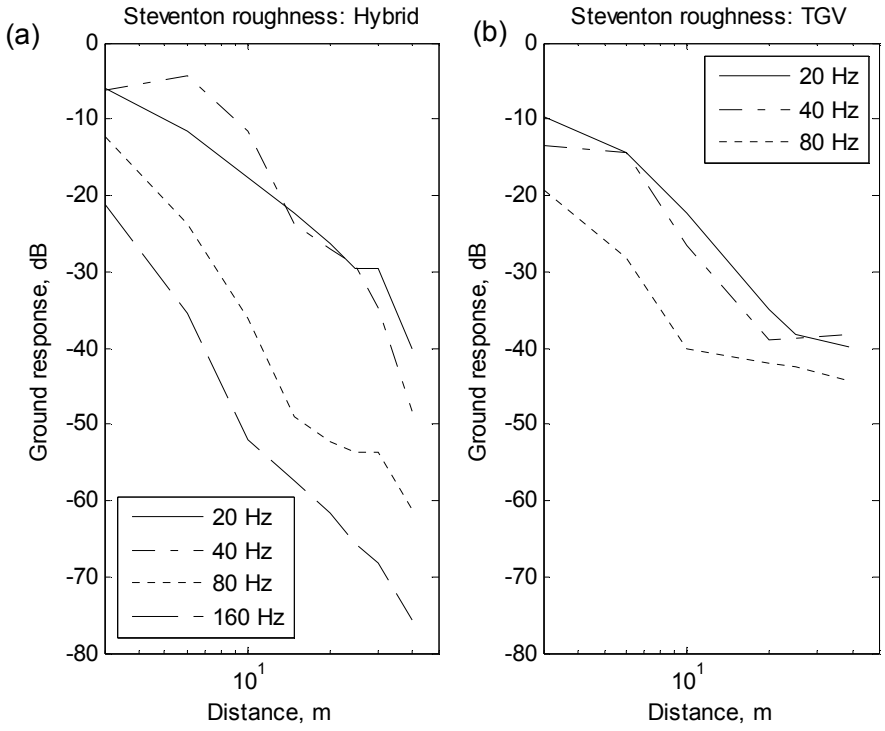

Figure 7.17. The ground response in terms of the relative level at different distances, due to Steventon roughness using (a) hybrid model and (b) TGV model, on clay soil.

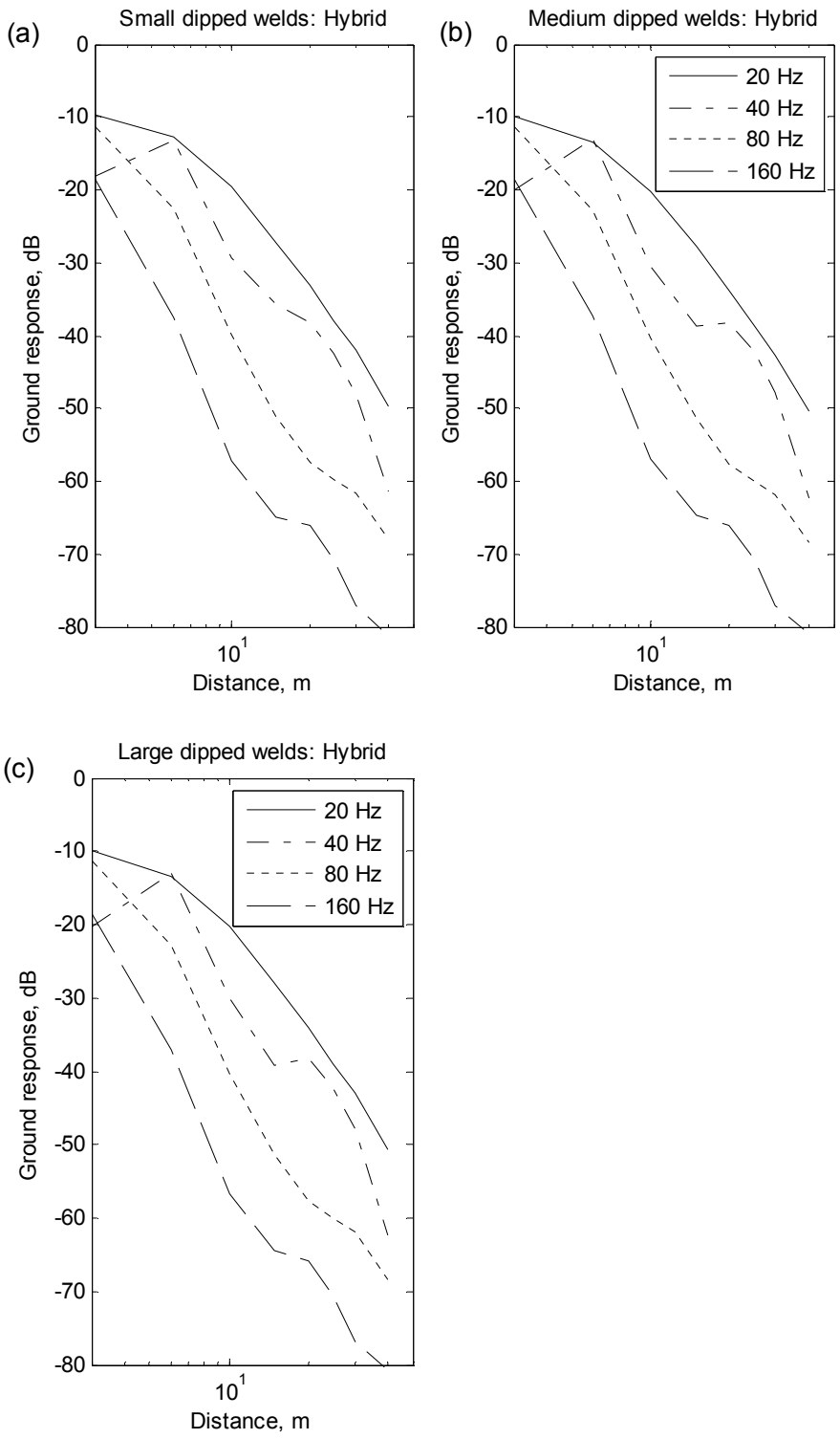

Figure 7.18. The ground response in terms of the relative level at different distances, due to (a) small and (b) medium dipped welds and (c) large dipped welds, on clay soil.

Table 7.2. The exponent α corresponding to the vibration on the surface ground found using the hybrid model.

Excitation Parameters	Exponent α corresponding to propagation on the ground surface	
	chalk	clay
Dipped welds: 0.2 mm	1.0	1.8
Dipped welds: 1 mm	1.0	1.8
Dipped welds: 2.5 mm	1.0	1.8
Step-up joint: 1 mm	1.0	1.8
Step-up joint: 2.5 mm	1.0	1.8
Step-up joint: 5 mm	1.0	1.8
Steventon roughness using hybrid model	0.7	1.5
Steventon roughness using TGV model	0.4	1.4

7.3 Step-up joints

Another track defect that can cause large impact forces is a step-up joint. This might also produce large effects on the ground vibration. Therefore step-up joints are investigated here. The shape of the step-up joint is modified from the above geometry by introducing a step height as shown in Figure 7.19. In practice the wheel cannot follow such a shape due to its large radius of curvature. Therefore a geometric filtering procedure is adopted as described in [119]. This involves matching the roughness profile to the wheel curvature at each longitudinal position and determining the height of the wheel centre, ignoring any dynamic effects. The filtered profile is also shown in Figure 7.19. Note that the profile is adjusted so that it starts and finishes at 0. For the dipped weld the effect of this filtering is negligible as shown in Figure 7.20. Therefore the filter was not applied for the dipped welds.

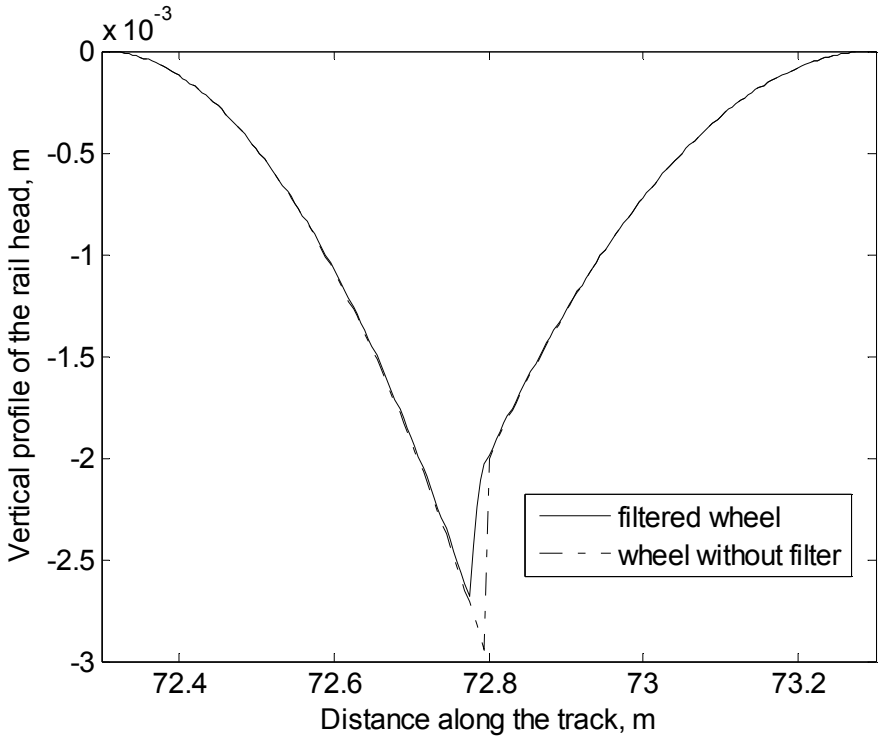

Figure 7.19. Shape of the dip for medium step-up joints.

The depths of the step-up joint are chosen to correspond to values, used in Thompson [3], which are greater than normally permitted in new track [121]. The step-up joint is situated at the middle of the track length. Three sizes of the step-up joint, shown in Table 7.1, have been used to investigate the effect of the sudden jump on the interaction between wheel and rail and then the vibration propagating away through the ground. In each case the step size is 1 mm while the dip is 1 mm, 2.5 mm or 5 mm. However, the case of the large step-up joint (5 mm dip with 1 mm step) might not occur in reality.

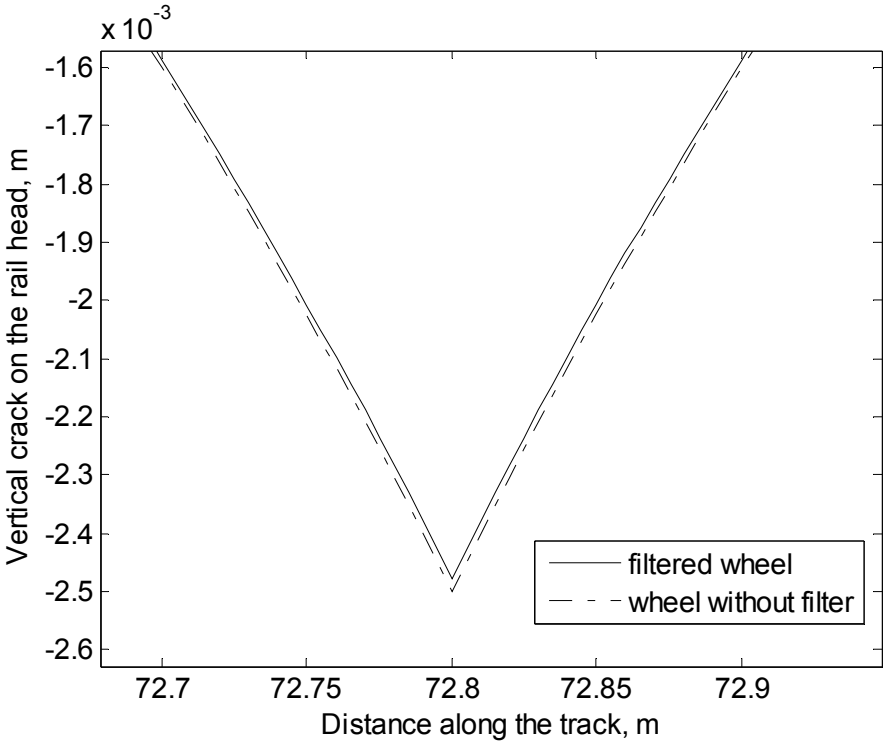

Figure 7.20. Shape of the dip for large dipped welds.

The ground response due to various depths of step-up joints: small, medium and large are investigated. The results are shown in Figures 7.21 to 7.23 along with the ground response due to a smooth rail and the Steventon roughness. The figures show the comparison between the ground response due to these step-up joints at 0, 10 and 25 m away from the track. The step-up joints dominate the response above about 8 Hz. Even at 25 m away from the track, the step-up joints still dominate the response above about 8 Hz. As before, a difference of about 8 dB is found at all distances above 20 Hz as the size of the step-up joints increases from 1 to 2.5 mm. However, if the depth is increased from 2.5 to 5.0 mm, only about a 4 dB increase is found for the further distance which is less than the 6 dB what might be expected. This is due to loss of contact between wheel and rail as shown in Figure 7.4. Therefore, the increase in amplitude of the response behaves non-linearly.

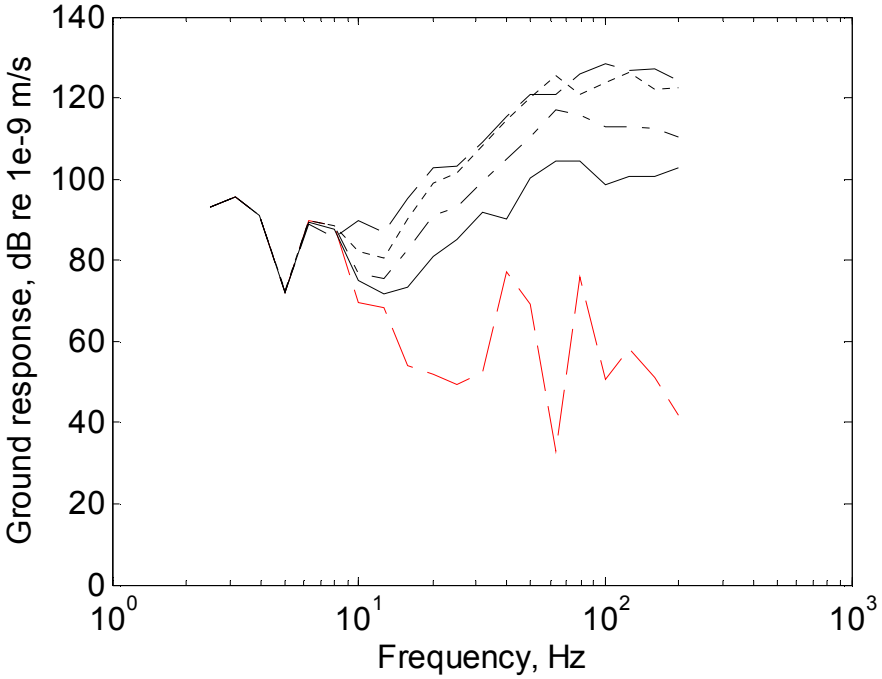

Figure 7.21. Comparison of ground response due to – –, reference: smooth; —, reference: Steventon roughness; – · – , step-up joints: 1 mm; ····· step-up joints: 2.5 mm; – –, step-up joints: 5 mm at 0 m underneath the track.

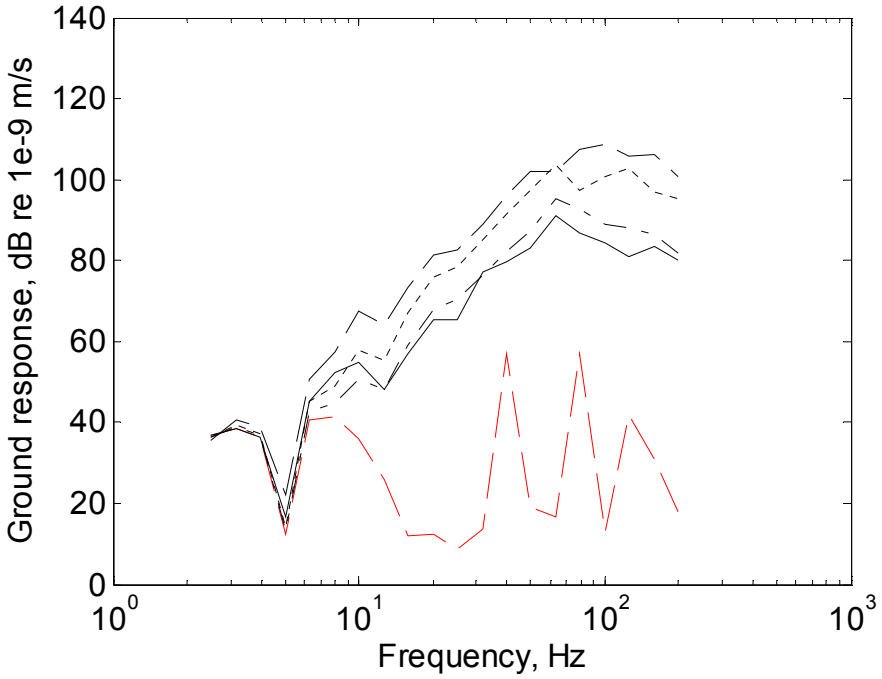

Figure 7.22. Comparison of ground response due to – –, reference: smooth; —, reference: Steventon roughness; – · – , step-up joints: 1 mm; ····· step-up joints: 2.5 mm; – –, step-up joints: 5 mm at 10 m away from the track.

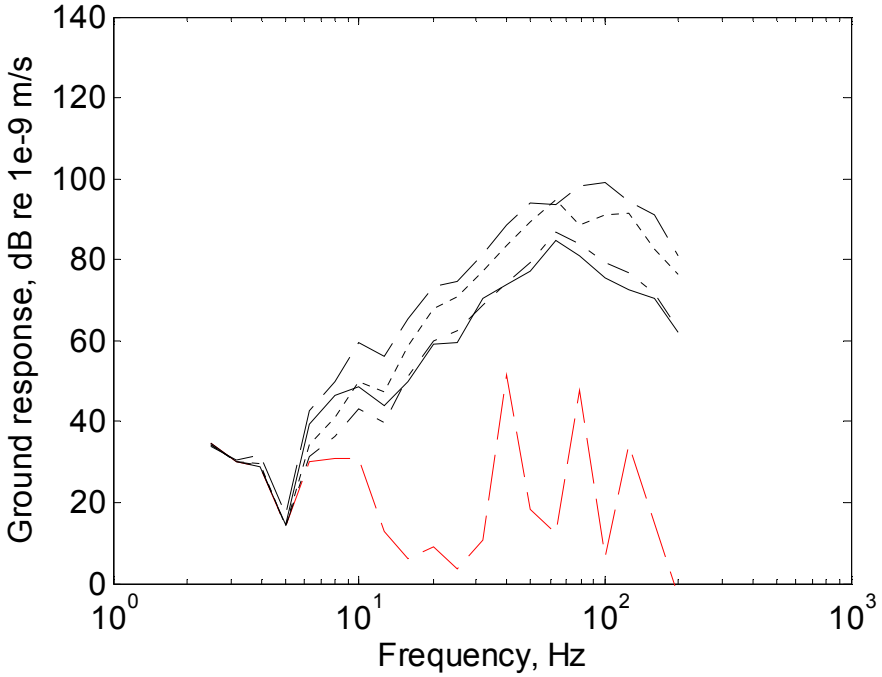

Figure 7.23. Comparison of ground response due to – –, reference: smooth; —, reference: Steventon roughness; – · – , step-up joints: 1 mm; ····· step-up joints: 2.5 mm; – –, step-up joints: 5 mm at 25 m away from the track.

The effect of change in the depth of step-up joint is also shown in Figure 7.24. This shows the ratio of ground response between two depths of 1 and 2.5 mm at 0, 10 and 25 m away from the track. A slight difference is found between these ratios of ground response for the case of step-up joints and the earlier results for dipped welds (Figure 7.12). This is due to the occurrence of loss of contact as shown in Figure 7.4.

As loss of contact occurred for the interaction force corresponding to both medium and large step-up joints, stronger non-linear behaviour can be found as shown in Figure 7.25. The expected ratio would be 6 dB but the presence of non-linearities means that the ratio varies considerably with frequency.

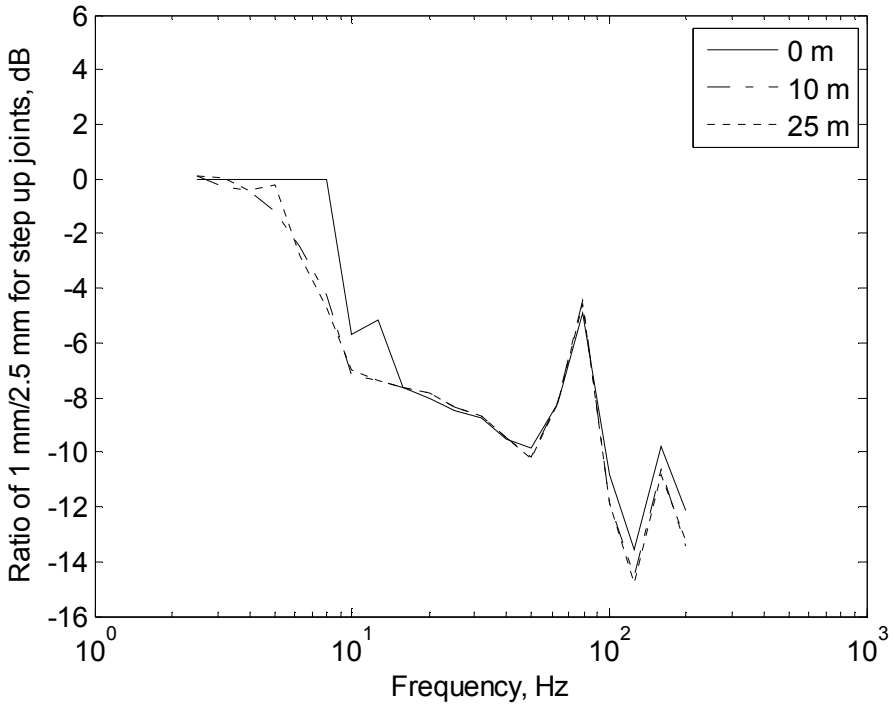

Figure 7.24. The ratio of ground response comparing between two depths of 1 and 2.5 mm for the step-up joints.

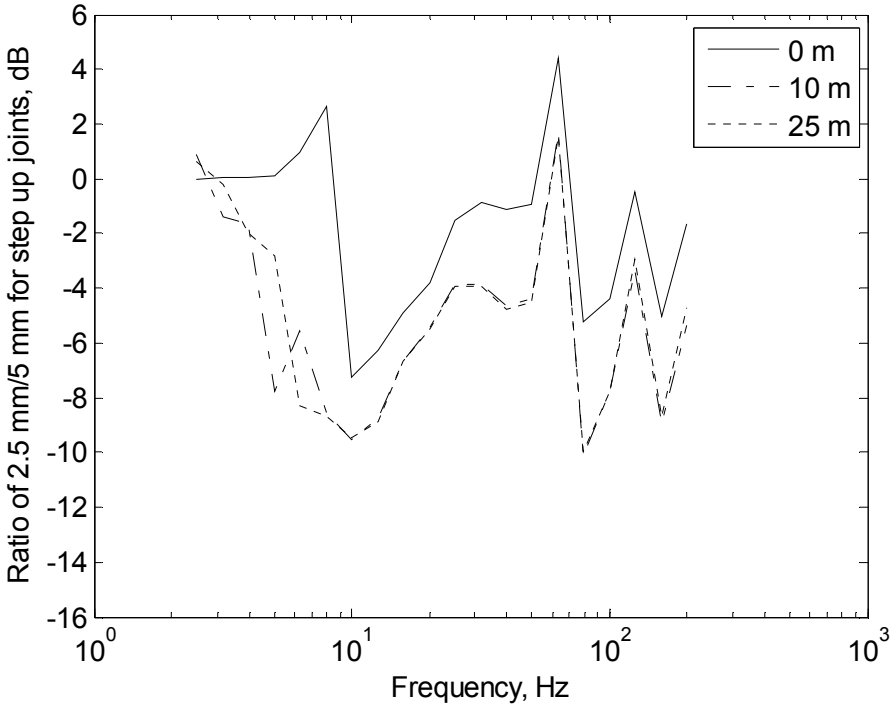

Figure 7.25. The ratio of ground response comparing between two depths of 2.5 and 5 mm for the step-up joints.

The effect of 1 mm step is also investigated. Figure 7.26 shows the ratio of ground response between step-up joints and dipped welds for two heights of 1 and 2.5 mm at 0 m underneath the track. It can be seen that the step of 1 mm affects the ground response at high frequencies especially above 80 Hz. This might due to a sudden impact which contains more amplitude at high frequencies.

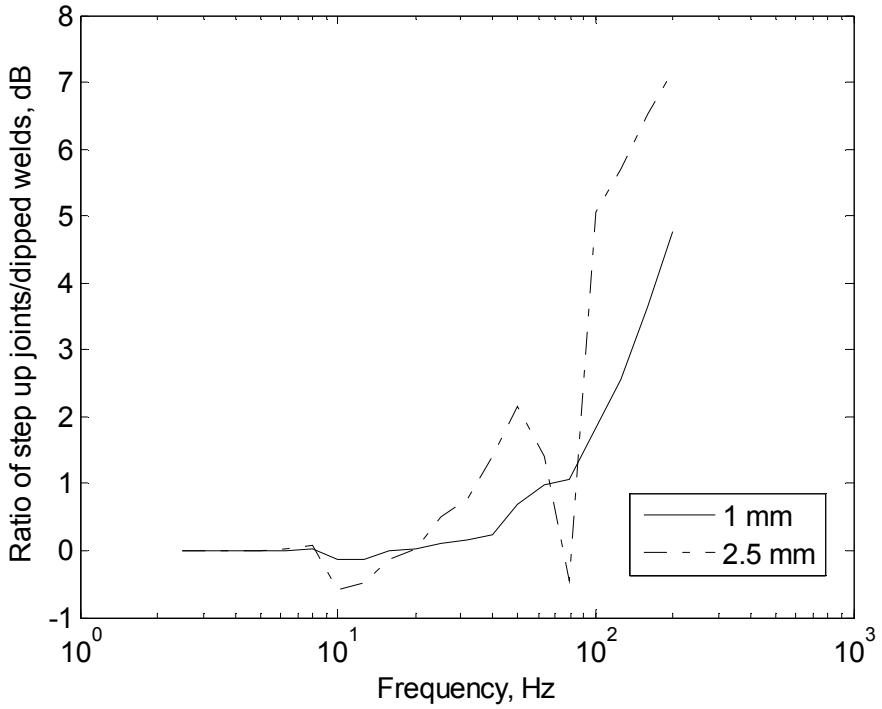

Figure 7.26. The ratio of ground response comparing step-up joint with dipped weld for two depths of 1 and 2.5 mm.

7.4 Conclusion

In this chapter excitation due to discrete track defects has been investigated, by using the hybrid model. The ground response has been determined due to defects on the rail head at particular fixed locations: dipped welds and step-up joints. It is expected in practice that these can be important features producing vibration in the ground at particular locations.

Various depths of dipped welds and step-up joints on the rail head have been investigated to see the effect on the ground response near to and further away from the track. It is found that the deeper the dipped welds the greater the ground response would be above about 10 Hz for all distances. A similar trend is found for the step-up

joints. It can clearly be seen that the medium and large dipped welds dominate the response at all distances considered.

A difference of about 8 dB is found above 10 Hz at all distances as the height of the dipped welds increases from 1 to 2.5 mm. However, for step-up joints when the depth is increased from 2.5 to 5.0 mm, only about a 4 dB increase is found for the further distances. This is due to loss of contact between wheel and rail. Therefore, the increase in amplitude the response behave like non linear.

The vibration due to dipped welds and step-up joints spreads out as a circular wave, with behaviour similar to a point source.

The investigation of geometrical spreading for waves propagating through the ground due to various excitations is considered in this chapter. It is found that the exponent α corresponding to the reduction in the amplitude due to dipped welds and step-up joints is 1.0 at frequencies 20, 40 and 80 Hz, on a half-space of chalk. This is larger than the factor α given in [16]. Richart et al. [16] give the value of α corresponding to the reduction in the amplitude of a Rayleigh wave as 0.5. For the roughness excitation values of α of 0.7 and 0.4 are found using the hybrid and TGV models respectively. The attenuation of vibration corresponding to geometrical spreading for waves propagating through the ground found in this thesis is due to a combination of wave types on the ground surface (not a pure Rayleigh wave).

Step-up joints and dipped welds are significant factors. These defects produce up to about 20 dB more ground vibration at 0 m than the response due to roughness. The effect of such impact forces at dipped welds on the ground response show similar trends to those due to dynamic loads.

8 Conclusions and recommendations

8.1 Conclusions

The aim of this thesis was to improve the understanding of the relative importance of the quasi-static load and dynamic load along with the occurrence of other excitation mechanisms such as impact forces. A new model, combined two existing different approaches, has been developed to investigate these excitation mechanisms. The model has been validated by comparison with the TGV model, which has been validated by measurements in a previous step. The measurements were carried out at two sites in Southern England as part of RRUK project work. The effect of different track/vehicle components on the ground response at various distances has been examined.

To gain confidence in the models used in this work, firstly measurements have been carried out to validate the TGV model. Measurements using hammer excitation have been performed at two sites in order to determine ground parameters for use in the model. The ground at both sites can be modelled using three layers overlying a stiffer half-space of material. Various methods were investigated to extract soil parameters from the measurements. The properties of the upper layer could be identified by comparison with predictions from a layered ground model expressed in the frequency-wavenumber domain. The properties of the third layer and the half-space affect the response only at low frequencies, below 10 Hz, which could only be identified using the train measurements. Good agreement is found between predictions using the TGV model and measurements of vibration from passing trains.

Later the hybrid model has been validated by comparison with results from the TGV model.

The main purpose of this work is to study relative importance of the moving quasi-static load and dynamic load as well as the occurrence of impact forces. Therefore the effects of different parameters on the ground vibration have been investigated for a wide range of conditions at locations close to the track and further away. It was found that the response beneath the track is dominated by the quasi-static

loads up to 12.5 Hz, whereas at 10 m away the dynamic loads are dominant above about 3 Hz.

The effects of changes in various track/train parameters are estimated for locations close to the track and further away in terms of an insertion gain in order to see the effect of the quasi-static and dynamic loads on the ground vibration. It can be found that the insertion gain for the overall response follows that of the dynamic excitation for locations far from the track, but at 0 m it follows the quasi-static curve up to about 10 Hz, above which it tends towards the curve for dynamic excitation. It is clear from these results that an assessment of the insertion gain due to a change in track support stiffness should not be based on measurements too close to the track – in this case the distance should be at least 10 m to give representative results of the effect on the far field response.

It is clear from these various results that softer rail pads, ballast mats and soffit pads lead to significant increases in ground vibration in the region 20-40 Hz at 10 m and beyond due to the lowered vehicle/track resonance. Reductions in vibration only occur above about 50 Hz. However, a measurement close to the track would suggest that the benefits extend to lower frequencies.

To allow variations in track support properties, a time and spatial domain wheel/track interaction model has been developed. It is connected to an axisymmetric layered ground model in order to investigate the effect of changes in parameters on the ground response. In order to reduce the effect of the finite length, the track has been modified to make it 'circular'. The advantage of the circular track compared with making the track longer is that the number of degrees of freedom is not increased. The important development is to link these two different approaches. The ground response can be obtained by extracting the forces acting at the ground interface from the wheel/track interaction model. These are then converted to a matrix of power and cross spectral densities and multiplied by the ground mobilities from the axisymmetric layered ground model.

As found in Chapter 5 the sleeper passing effect dominates the response due to quasi-static load for all distances at the frequencies of about 40 and 80 Hz (for a train

speed of 25 m/s). However it has less effect on the ground response than the excitation due to roughness. Variations of sleeper spacing and ballast stiffness have also been investigated. It is found that all such parameters, investigated in Chapter 6, have a fairly small effect on the ground vibration as the dynamic load dominates the response.

In Chapter 7 step-up joints and dipped welds are shown to be significant factors. These defects can produce up to 20 dB more ground vibration than the response due to roughness above 10 Hz.

The investigation of geometrical spreading for waves propagating through the ground due to various excitations is considered. It is found that the exponent α corresponding to the reduction in the amplitude due to dipped welds and step-up joints is 1.0 at frequencies 20, 40 and 80 Hz, on a half-space of chalk. This is larger than the factor α given in [16] which, for a Rayleigh wave, is given as 0.5.

For the roughness excitation values of α of 0.7 and 0.4 are found using the hybrid and TGV models respectively. The attenuation of vibration corresponding to geometrical spreading for waves propagating through the ground found here is due to a combination of wave types on the ground surface (not a pure Rayleigh wave).

8.2 Recommendations for future work

The hybrid model has been shown to be a reliable tool to investigate the effects of change in parameters on the ground response. Future work on the hybrid model should consider including a vehicle model with primary and secondary suspensions and investigating whether this leads to a change in the ground vibration.

The wheel roughness should be included in the hybrid model as up to now it was assumed to be included in the rail roughness.

It has been found that step-up joints and dipped welds are significant factors. This should be extended to include the effect of switches where a large gap width is present.

The contact between the track and the ground in the hybrid model is based on a rigid circular indenter. A better approximation is required for a proper spreading of the loads.

As people experience the vibration at locations along a railway line, it is important to determine how much these vibrations can produce annoyance to people who live or work close to the line. It is therefore important to investigate if the buildings are included in the model, whether any changes are found in the vibration field.

Appendix A
Stiffness matrices for layered soils

The axisymetric layered ground model used in this thesis to calculate the ground response on the surface is based on [33].

The layer stiffness matrices method developed by Kausel and Roesset [33] has several advantages over the transfer matrix method: the matrices are symmetrical, require fewer operations, allow easier treatment of multiple loadings, are applicable for substructuring techniques and asymptotic expressions follow naturally from the expressions (for very thick layers or high frequencies) [33]. This method is derived from the Haskell [36] - Thomson [37] transfer matrix method.

The propagation of waves in layered media presented by Haskell [36] and Thomson [37] is based on the use of transfer matrices in the frequency-wavenumber domain. The solution is obtained in terms of temporal and spatial Fourier transforms. The harmonic displacements at the layer interfaces can be calculated due to harmonic loads. In the transfer matrix approach, the displacements and internal stresses at a given interface define the state vector. This is related by the transfer matrix to the state vector at neighbouring interfaces.

The state vector can be defined by the presence of external loads at a given elevation for Cartesian or cylindrical coordinates. This method involves the radial direction by the use of Bessel, Neumann, or Hankel functions. It corresponds to the decomposition of the displacements and stresses in a Fourier series. Hankel functions are commonly used in wave propagation problems as they are asymptotically like complex exponentials.

The equations are briefly shown here.

For a layered soil system as shown in Figure A1, the interfaces between its layers can be represented by discontinuities in material properties in the vertical direction. The state vectors can then be defined for Cartesian coordinates as

$$\mathbf{Z} = \left\{ \bar{u}_x,\ \bar{u}_y,\ i\bar{u}_z,\ \bar{\tau}_{xz},\ \bar{\tau}_{yz},\ i\bar{\sigma}_z \right\}^T = \begin{bmatrix} \bar{\mathbf{U}} \\ \bar{\mathbf{S}} \end{bmatrix} \tag{A.1}$$

or for cylindrical coordinates as

$$\mathbf{Z} = \left\{ \bar{u}_\rho,\ \bar{u}_\theta,\ \bar{u}_z,\ \bar{\tau}_{\rho z},\ \bar{\tau}_{\theta z},\ \bar{\sigma}_z \right\}^T = \begin{bmatrix} \bar{\mathbf{U}} \\ \bar{\mathbf{S}} \end{bmatrix} \tag{A.2}$$

where $\bar{u}$, $\bar{\tau}$ and $\bar{\rho}$ are the displacement, shear and normal stress components at a given elevation. The displacement vector $\bar{\mathbf{U}}$ and stress vector $\bar{\mathbf{S}}$ are functions of the vertical coordinate z only. In Cartesian coordinates the actual displacements and stresses at a point are given by,

$$\begin{bmatrix} \mathbf{U} \\ \mathbf{S} \end{bmatrix} = \begin{bmatrix} \bar{\mathbf{U}} \\ \bar{\mathbf{S}} \end{bmatrix} \exp i(\omega t - kx - ly) \tag{A.3}$$

where k and l are the wavenumbers in x and y direction.

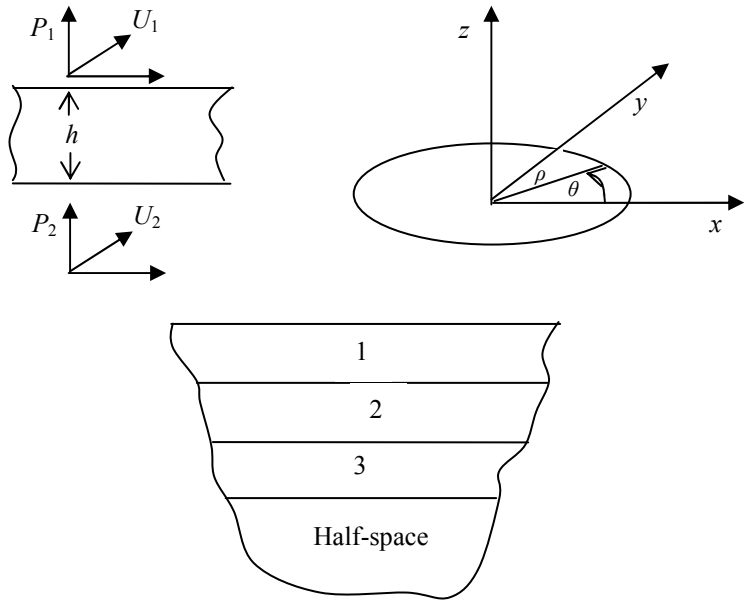

Figure A1. A layered soil system.

Considering only a plane strain condition, $l = 0$, the factor becomes exp $i(\omega t - kx)$.

For cylindrical coordinates, the variation in the radial direction is obtained multiplying $\bar{\mathbf{U}}$, $\bar{\mathbf{S}}$ by the matrix $\mathbf{C}$ as below

$$\begin{bmatrix} \mathbf{U} \\ \mathbf{S} \end{bmatrix} = \begin{bmatrix} \mathbf{C}\bar{\mathbf{U}} \\ \mathbf{C}\mathbf{S} \end{bmatrix} = \begin{bmatrix} \mathbf{C} & \\ & \mathbf{C} \end{bmatrix} \begin{bmatrix} \bar{\mathbf{U}} \\ \bar{\mathbf{S}} \end{bmatrix} \tag{A.4}$$

with

$$\mathbf{C} = \begin{bmatrix} \dfrac{d}{d(k\rho)}C_\mu & \dfrac{\mu}{k\rho}C_\mu & \\ \dfrac{\mu}{k\rho}C_\mu & \dfrac{d}{d(k\rho)}C_\mu & \\ & & -C_\mu \end{bmatrix} \tag{A.5}$$

where $C_\mu = C_\mu(k\rho)$ are cylindrical functions of μth order of the first, second, or third kind (Bessel, Neumann, or Hankel functions, respectively). k is the assumed wavenumber, and ρ is the radial coordinate.

Using the transfer matrix method, the state vector corresponding to other layers can be obtained as

$$\mathbf{Z}_{j+1} = \mathbf{H}_j \mathbf{Z}_j \tag{A.6}$$

where $\mathbf{H}_j$ is the transfer matrix of the jth layer. The transfer matrix is a function of the frequency of excitation ω, the wavenumbers k, l, the soil properties and the thickness of the layer. The transfer matrix has a structure in which its motions in a vertical plane (P-SV waves) uncouple from motions in a horizontal plane (SH waves).

The stiffness matrix approach, starts from the relation between external loads at the upper and lower interface and displacement at the upper and lower interface

$$\begin{bmatrix} \overline{\mathbf{U}}_2 \\ -\overline{\mathbf{P}}_2 \end{bmatrix} = \begin{bmatrix} \mathbf{H}_{11} & \mathbf{H}_{12} \\ \mathbf{H}_{21} & \mathbf{H}_{22} \end{bmatrix} \begin{bmatrix} \overline{\mathbf{U}}_1 \\ \overline{\mathbf{P}}_1 \end{bmatrix} \tag{A.7}$$

where $\mathbf{H}_{ij}$ are submatrices of the transfer matrix $\mathbf{H}_j$. This can be rearranged as

$$\begin{bmatrix} \overline{\mathbf{P}}_1 \\ \overline{\mathbf{P}}_2 \end{bmatrix} = \begin{bmatrix} -\mathbf{H}_{12}^{-1}\mathbf{H}_{11} & \mathbf{H}_{12}^{-1} \\ \mathbf{H}_{22}\mathbf{H}_{12}^{-1}\mathbf{H}_{11} - \mathbf{H}_{21} & -\mathbf{H}_{22}\mathbf{H}_{12}^{-1} \end{bmatrix} \begin{bmatrix} \overline{\mathbf{U}}_1 \\ \overline{\mathbf{U}}_2 \end{bmatrix} \tag{A.8}$$

or

$$\overline{\mathbf{P}} = \mathbf{K}\overline{\mathbf{U}} \tag{A.9}$$

where $\mathbf{K}$, $\overline{\mathbf{P}}$ and $\overline{\mathbf{U}}$ are the stiffness matrix of the layer, external load vector and displacement vector respectively. The global stiffness matrix is constructed by assembling the contribution of the layer matrices. The global load vector corresponds to the external stresses at the interfaces.

For the global stiffness matrix, only the final results are shown here. Also only the cases of plane (l = 0) and cylindrical waves are considered. For the exact solution, the 6 x 6 layer stiffness matrices are shown in Tables A1 to A5. The wave equations are solved in Cartesian and cylindrical coordinates. The matrices for P-SV waves are given in rows/columns 1, 3, 4, 6 in Table A1 to A4. The matrices for SH waves are given in rows/columns 2, 5 in Table A5. The coupling terms are zero. The following notation is used for Tables A1 to A5.

ω = frequency of excitation

k =wavenumber

h =layer thickness

G =shear modulus

$\alpha = \dfrac{C_s}{C_p}$ =shear wave velocity/dilatational wave velocity

$$r = \sqrt{1 - \left(\frac{\omega}{kC_P}\right)^2} \tag{A.10}$$

$$s = \sqrt{1 - \left(\frac{\omega}{kC_S}\right)^2} \tag{A.11}$$

For a discrete solution, this technique is used when the layer thickness is small compared to the wavelength of interest.

The layer stiffness matrices in the discrete case may be obtained as

$$\mathbf{K} = \mathbf{A}k^2 + \mathbf{B}k + \mathbf{G} - \omega^2\mathbf{M}$$

where k and ω are wavenumber and frequency of excitation respectively. The terms **A**, **B**, **G**, **M** are the matrices shown in Table A6.

As an example of application, the case of a layered soil over elastic rock is considered. The relation of external loads and the stiffness matrix is

$$\begin{bmatrix} \mathbf{K}_{11}^1 & \mathbf{K}_{12}^1 & & \\ \mathbf{K}_{21}^1 & \mathbf{K}_{22}^1 + \mathbf{K}_{11}^2 & \mathbf{K}_{12}^2 & \\ & \mathbf{K}_{21}^2 & \mathbf{K}_{22}^2 + \mathbf{K}_{11}^3 & \mathbf{K}_{12}^3 \\ & & \mathbf{K}_{21}^3 & \mathbf{K}_{22}^3 + \mathbf{K}^4 \end{bmatrix} \begin{bmatrix} \bar{\mathbf{U}}_1 \\ \bar{\mathbf{U}}_2 \\ \bar{\mathbf{U}}_3 \\ \bar{\mathbf{U}}_4 \end{bmatrix} = \begin{bmatrix} \bar{\mathbf{P}}_1 \\ \bar{\mathbf{P}}_2 \\ \bar{\mathbf{P}}_3 \\ \bar{\mathbf{P}}_4 \end{bmatrix} \tag{A.12}$$

where k_{ij}^{n} refer to n^{th} layer and terms k_{ij} are found in Tables A1 and A2.

For problems formulated in cylindrical coordinates, the procedure is shown in [33].

Table A1

P-SV waves: stiffness matrix for nonzero frequency, nonzero wavenumber

$$\omega > 0 \quad k > 0$$

$$C^r = \cosh krh \quad S^r = \sinh krh$$

$$C^s = \cosh ksh \quad S^s = \sinh ksh$$

$$D = 2\left(1 - C^r C^s\right) + \left(\frac{1}{rs} + rs\right) S^r S^s$$

$$\mathbf{K} = 2kG \begin{bmatrix} \mathbf{K_{11}} & \mathbf{K_{12}} \\ \mathbf{K_{21}} & \mathbf{K_{22}} \end{bmatrix}$$

$$\mathbf{K_{11}} = \frac{1-s^2}{2D} \begin{bmatrix} \frac{1}{s}\left(C^r S^s - rsC^s S^r\right) & -\left(1 - C^r C^s + rsS^r S^s\right) \\ -\left(1 - C^r C^s + rsS^r S^s\right) & \frac{1}{r}\left(C^s S^r - rsC^r S^s\right) \end{bmatrix} - \frac{1+s^2}{2} \begin{bmatrix} 0 & 1 \\ 1 & 0 \end{bmatrix}$$

$\mathbf{K_{22}}$ is the same as $\mathbf{K_{11}}$, with off-diagonal signs changed

$$\mathbf{K_{12}} = \frac{1-s^2}{2D} \begin{bmatrix} \frac{1}{s}\left(rsS^r - S^s\right) & -\left(C^r - C^s\right) \\ C^r - C^s & \frac{1}{r}\left(rsS^s - S^r\right) \end{bmatrix}$$

$$\mathbf{K_{21}} = \mathbf{K_{12}^T}$$

Half-space (opening downward)

$$\mathbf{K} = 2kG \left[\frac{1-s^2}{2\left(1-rs\right)} \begin{bmatrix} r & 1 \\ 1 & s \end{bmatrix} - \begin{bmatrix} 0 & 1 \\ 1 & 0 \end{bmatrix} \right]$$

(for half-space opening upward, reverse off-diagonal terms)

Table A2

P-SV waves: stiffness matrix for zero frequency, nonzero wavenumber

$$\omega = 0 \quad k > 0 \quad \kappa = kh$$

$$C = \cosh \kappa \quad S = \sinh \kappa$$

$$D = \left(1+\alpha^2\right)^2 S^2 - \kappa^2 \left(1-\alpha^2\right)^2$$

$$\mathbf{K} = 2kG \begin{bmatrix} \mathbf{K_{11}} & \mathbf{K_{12}} \\ \mathbf{K_{21}} & \mathbf{K_{22}} \end{bmatrix}$$

$$\mathbf{K_{11}} = \frac{1}{D} \begin{bmatrix} \left(1+\alpha^2\right) SC - \kappa\left(1-\alpha^2\right) & \left(1+\alpha^2\right) S^2 \\ \left(1+\alpha^2\right) S^2 & \left(1+\alpha^2\right) SC + \kappa\left(1-\alpha^2\right) \end{bmatrix} - \begin{bmatrix} 0 & 1 \\ 1 & 0 \end{bmatrix}$$

$\mathbf{K_{22}}$ is the same as $\mathbf{K_{11}}$, with off-diagonal signs changed

$$\mathbf{K_{12}} = \frac{1}{D} \begin{bmatrix} \kappa\left(1-\alpha^2\right) C - \left(1+\alpha^2\right) S & -\kappa\left(1-\alpha^2\right) S \\ \kappa\left(1-\alpha^2\right) S & -\left(\kappa\left(1-\alpha^2\right) C + \left(1+\alpha^2\right) S\right) \end{bmatrix}$$

$$\mathbf{K_{21}} = \mathbf{K_{12}^T}$$

Half-space (opening downward)

$$\mathbf{K} = \frac{2kG}{1+\alpha^2} \begin{bmatrix} 1 & -\alpha^2 \\ -\alpha^2 & 1 \end{bmatrix}$$

(for $k < 0$, reverse diagonal terms)

(for half-space opening upward, reverse off-diagonal terms)

Table A3

P-SV waves: stiffness matrix for nonzero frequency and zero wavenumber

$$\omega > 0 \qquad k = 0$$

$$\eta = \frac{\omega h}{C_s} \qquad \alpha\eta = \frac{\omega h}{C_p}$$

$$\mathbf{K} = \rho C_s \omega \begin{bmatrix} \cot\eta & & -\dfrac{1}{\sin\eta} & \\ & \dfrac{1}{\alpha}\cot\alpha\eta & & -\dfrac{1}{\alpha}\dfrac{1}{\sin\alpha\eta} \\ -\dfrac{1}{\sin\eta} & & \cot\eta & \\ & -\dfrac{1}{\alpha}\dfrac{1}{\sin\alpha\eta} & & \dfrac{1}{\alpha}\cot\alpha\eta \end{bmatrix}$$

Half-space

$$\mathbf{K} = i\omega\rho C_s \begin{bmatrix} 1 & \\ & \dfrac{1}{\alpha} \end{bmatrix}$$

Table A4

P-SV waves: stiffness matrix for zero frequency and zero wavenumber

$$\omega = 0 \qquad k = 0$$

$$\mathbf{K} = \frac{G}{h} \begin{bmatrix} 1 & & -1 & \\ & \dfrac{1}{\alpha^2} & & -\dfrac{1}{\alpha^2} \\ -1 & & 1 & \\ & -\dfrac{1}{\alpha^2} & & \dfrac{1}{\alpha^2} \end{bmatrix}$$

Half-space

$\mathbf{K} = \mathbf{0}$ (the null matrix)

Table A5

SH waves

(a) Nonzero wavenumber, nonzero frequency

$$k > 0\,, \quad \omega > 0$$

$$\mathbf{K} = \frac{ksG}{\sinh ksh}\begin{bmatrix} \cosh ksh & -1 \\ -1 & \cosh ksh \end{bmatrix}$$

Half-space

$$\mathbf{K} = ksG$$

(b) Nonzero wavenumber, zero frequency

$$k > 0\,, \quad \omega = 0$$

Same as (a), with $s = 1$. $\left(s = -1 \text{ if } k < 0\right)$

(c) Zero wavenumber, nonzero frequency

$$k = 0, \quad \omega > 0$$

$$\mathbf{K} = \frac{\rho C_s \omega}{\sin \eta}\begin{bmatrix} \cos \eta & -1 \\ -1 & \cos \eta \end{bmatrix}, \quad \eta = \frac{\omega h}{C_s}$$

Half-space

$$\mathbf{K} = i\omega\rho C_s$$

(c) Zero wavenumber, nonzero frequency

$$k = 0, \quad \omega = 0$$

$\mathbf{K} = \mathbf{0}$ (the null matrix)

Half-space

$$\mathbf{K} = \mathbf{0}$$

Table A6

Layer stiffness matrices

$$\mathbf{A}=\frac{h}{6}\begin{bmatrix} 2(\lambda+2G) & & & \lambda+2G & & \\ & 2G & & & G & \\ & & 2G & & & G \\ \lambda+2G & & & 2(\lambda+2G) & & \\ & G & & & 2G & \\ & & G & & & 2G \end{bmatrix}$$

$$\mathbf{B}=\frac{1}{2}\begin{bmatrix} & \lambda-G & & -(\lambda+G) \\ \lambda-G & & \lambda+G & \\ & \lambda+G & & -(\lambda-G) \\ -(\lambda+G) & & -(\lambda-G) & \end{bmatrix}$$

$$\mathbf{G}=\frac{1}{h}\begin{bmatrix} G & & -G & & & \\ & G & & -G & & \\ & & \lambda+2G & & & -(\lambda+2G) \\ -G & & & G & & \\ & -G & & & G & \\ & & -(\lambda+2G) & & & \lambda+2G \end{bmatrix}$$

$$\mathbf{M}=\frac{\rho h}{6}\begin{bmatrix} 2 & & & 1 & & \\ & 2 & & & 1 & \\ & & 2 & & & 1 \\ 1 & & & 2 & & \\ & 1 & & & 2 & \\ & & 1 & & & 2 \end{bmatrix}$$

λ = Lame constant, G = shear modulus } for soil with damping, use complex values.

ρ = mass density $\qquad \mathbf{K}=\mathbf{A}k^2+\mathbf{B}k+\mathbf{G}-\omega^2\mathbf{M}$

h = layer thickness

Appendix B

A semi-analytical model, Train-induced Ground Vibration (TGV)

The semi-analytical Train-induced Ground Vibration model is based on [12].

The track is represented as an infinite, layered beam resting on one or more elastic layers overlying a three-dimensional half-space of ground material. The rails are modelled as Euler beams which is acceptable in the ground-borne vibration frequency range of interest. The mass of the rail beam and its bending stiffness are defined. The sleeper is modelled as a mass with no bending stiffness. The railpads are modelled as a continuously distributed complex spring stiffness. The ballast and embankment are modelled as elastic bars with continuously distributed stiffness and mass. The bending stiffness of the embankment is ignored.

The ground is represented by horizontal layers on a half-space. It consists of a number of parallel layers of different materials. Instead of using the exact or discretized dynamic stiffness matrix techniques developed by Kausel and Roesset [33], it can be achieved by using the dynamic flexibility matrix approach to improve computational efficiency. This was a similar method to the Haskell [36]-Thomson [37] technique. The equations are given as

$$\left.\begin{aligned}
\left(\lambda_j+\mu_j\right)i\beta\overline{\Delta}_j+\mu_j\left(\frac{d^2\overline{u}_j}{dz^2}-\beta^2\overline{u}_j-\gamma^2\overline{u}_j\right)&=\rho_j\frac{\partial^2\overline{u}_j}{\partial t^2}\\
\left(\lambda_j+\mu_j\right)i\gamma\overline{\Delta}_j+\mu_j\left(\frac{d^2\overline{v}_j}{dz^2}-\beta^2\overline{v}_j-\gamma^2\overline{v}_j\right)&=\rho_j\frac{\partial^2\overline{v}_j}{\partial t^2}\\
\left(\lambda_j+\mu_j\right)\frac{\partial\overline{\Delta}_j}{\partial z}+\mu_j\left(\frac{d^2\overline{w}_j}{dz^2}-\beta^2\overline{w}_j-\gamma^2\overline{w}_j\right)&=\rho_j\frac{\partial^2\overline{w}_j}{\partial t^2}
\end{aligned}\right\}\left(j=1,2,\ldots,n+1\right) \qquad \text{(B.1)}$$

$$\lambda_j=\frac{v_jE_j\left(1+i\eta_j\ \mathrm{sgn}\left(\omega\right)\right)}{\left(1+v_j\right)\left(1-2v_j\right)},\ \mu_j=\frac{E_j\left(1+i\eta_j\ \mathrm{sgn}\left(\omega\right)\right)}{2\left(1+v_j\right)}\quad\left(j=1,2,\ldots,n+1\right) \qquad \text{(B.2)}$$

where λ_j and μ_j are Lamé constants of the *j*th layer. The displacement amplitudes in *x*, *y*, *z* directions are denoted by $\overline{u}_j$, $\overline{v}_j$ and $\overline{w}_j$. For the *j*th layer the material constants

are: elastic modulus, E_j, Poisson ratio, $v_{j,\text{ density,}}$ ρ_j and loss factor, η_j. The direction β and γ denote the Fourier transform of x and y.

For the model of track and ground shown in Figure B1, the differential equation of motion of the railway track and the ground are presented as

$$EI\beta^4\overline{w}_R(\beta,t)+m_R\frac{\partial^2\overline{w}_R(\beta,t)}{\partial t^2}+k_P\left[\overline{w}_R(\beta,t)-\overline{w}_S(\beta,t)\right]=e^{-i\beta ct}\sum_{l=1}^{M}P_l(t)e^{-i\beta a_l} \quad \text{(B.3)}$$

$$\frac{m_B}{6}\begin{bmatrix}2 & 1\\ 1 & 2\end{bmatrix}\begin{Bmatrix}\dfrac{\partial^2\overline{w}_S(\beta,t)}{\partial t^2}\\ \dfrac{\partial^2\overline{w}_C(\beta,t)}{\partial t^2}\end{Bmatrix}+k_B\begin{bmatrix}1 & -1\\ -1 & 1\end{bmatrix}\begin{Bmatrix}\overline{w}_S(\beta,t)\\ \overline{w}_C(\beta,t)\end{Bmatrix}=\begin{Bmatrix}\overline{F}_2(\beta,t)\\ -\overline{F}_3(\beta,t)\end{Bmatrix} \quad \text{(B.4)}$$

where $w_R(x,t)$ and $w_S(x,t)$ are the vertical displacements of the rail beam and the sleeper beam respectively and the vertical displacements of the track centre-line in the plane of contact with the ground is $w_C(x,t)$. The railpad complex stiffness is denoted by $k_P=k'_P\left(1+i\eta_P\,\mathrm{sgn}(\omega)\right)$, where k'_P is the stiffness of rail pad for a unit length of track. The mass per unit length of track of the rail beam and its bending stiffness are denoted by m_R and EI respectively while the mass of the sleeper beam per unit length track is denoted by m_s without any bending stiffness. The vertical wheel-rail interaction forces are denoted by $P_l(t)$.

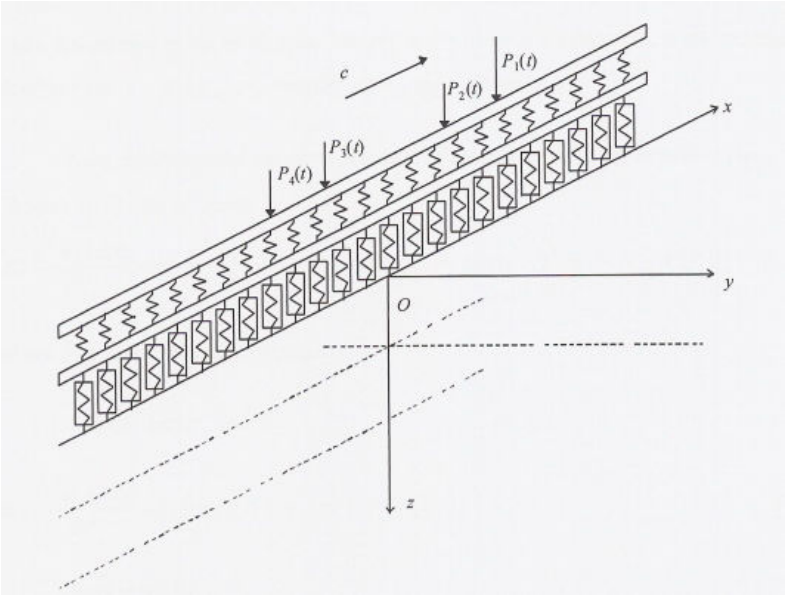

Figure B1. Model for track/ground system.

The model allows the moving axle loads and the vertical rail roughness as its input introducing a relative displacement to the vehicle/track system. Trains run at speeds of $c = f\lambda$ corresponding to a wavelength λ at a frequency of excitation, f.

The vehicle is modelled as a multiple rigid body system. Only the vertical dynamics is considered. The mass and pitch inertia of the car body are denoted by M_C and J_C, and for the mass of each wheelset is denoted by M_W. The dynamic stiffness of the primary and secondary suspensions are denoted by k_1 and k_2. Hysteretic damping may also be incorporated into the suspension by introducing a complex spring stiffness.

In this thesis, vehicle type I has been used for the comparison with the measurements in Chapter 3, as shown in Figure B2. The displacement vector of the coach is defined as

$$\mathbf{z}_{\mathrm{V}}(t) = \left\{ z_C(t), \varphi_C(t), z_{B1}(t), \varphi_{B1}(t), z_{B2}(t), \varphi_{B2}(t), z_{W1}(t), z_{W2}(t), z_{W3}(t), z_{W4}(t) \right\}^T \quad \text{(B.5)}$$

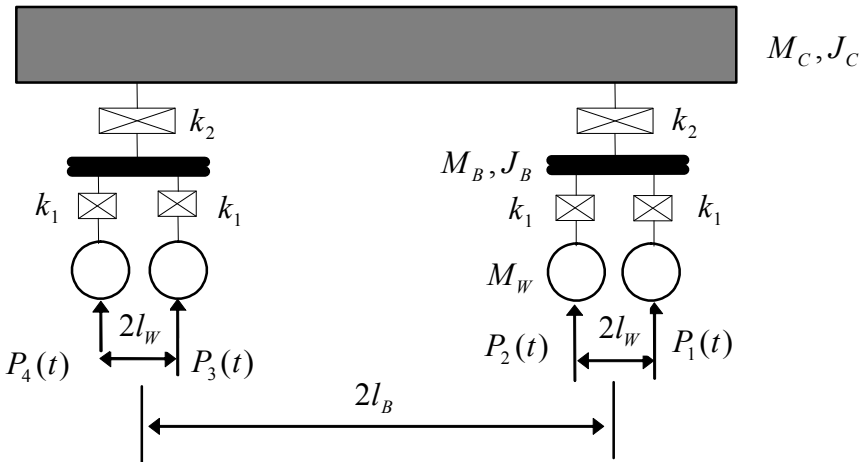

Figure B2. Type I: A vehicle system with primary and secondary suspensions.

Appendix C

A finite element track and wheel/track interaction model

The dynamic interaction between the vehicle and the track used in Chapter 5 to 7 of this thesis is based on [109,110,112].

A finite element track model and wheel/track interaction model used in this thesis, are described below. The length of the track is truncated to 36 m with a sleeper spacing of 0.6 m. In each sleeper bay the rail is divided into two elements. The support at each sleeper consists of two spring-damper elements in order to represent the rail pad and ballast along with the sleeper mass.

C1. Equation of motion for track

The track is modelled as an Euler Bernoulli beam on discrete supports. Only vertical motion and rotation in the vertical plane are allowed. The displacement vector $\mathbf{u}_{ij}$ for the model of one element is given by

$$\mathbf{u}_{ij} = \begin{Bmatrix} u_i \\ \theta_i \\ u_j \\ \theta_j \end{Bmatrix} \tag{C.1}$$

The mass and stiffness matrices of the beam element are represented as the equivalent Euler beam. The mass matrix is then

$$\mathbf{m}_r = \frac{\rho A a}{210}\begin{bmatrix} m_1 & m_2 & m_3 & m_4 \\ m_2 & m_5 & -m_4 & m_6 \\ m_3 & -m_4 & m_1 & -m_2 \\ m_4 & m_6 & -m_2 & m_5 \end{bmatrix} + \frac{\rho I}{30a}\begin{bmatrix} m_7 & m_8 & -m_7 & m_8 \\ m_8 & m_9 & -m_8 & m_{10} \\ -m_7 & -m_8 & m_7 & -m_8 \\ m_8 & m_{10} & -m_8 & m_9 \end{bmatrix} \tag{C.2}$$

where

$$\begin{aligned} m_1 &= 156 \\ m_2 &= 44a \\ m_3 &= 54 \\ m_4 &= -26a \\ m_5 &= 16a^2 \end{aligned} \tag{C.3}$$

$$m_6 = -12a^2$$

$$m_7 = 18$$

$$m_8 = 3a$$

$$m_9 = 8a^2$$

$$m_{10} = -2a^2$$

The stiffness matrix is given by

$$\mathbf{k_r} = \frac{EI}{2a^3}\begin{bmatrix} 3 & 3a & -3 & 3a \\ 3a & 4a^2 & -3a & 2a^2 \\ -3 & -3a & 3 & -3a \\ 3a & 2a^2 & -3a & 4a^2 \end{bmatrix} \tag{C.4}$$

And the damping matrix for a rail element is given by

$$\mathbf{c_r} = a_2\mathbf{k_r} \text{ where } a_2 = \frac{2\zeta}{\omega} \tag{C.5}$$

For a rail pad, the mass, stiffness and damping matrices, including the sleeper mass, are shown below

$$\mathbf{m_p} = \begin{bmatrix} 0 & 0 & 0 & 0 \\ 0 & 0 & 0 & 0 \\ 0 & 0 & m_s & 0 \\ 0 & 0 & 0 & 0 \end{bmatrix} \tag{C.7}$$

$$\mathbf{k_p} = \begin{bmatrix} k_p & 0 & -k_p & 0 \\ 0 & \frac{k_p L_P^2}{12} & 0 & -\frac{k_p L_P^2}{12} \\ -k_p & 0 & k_p & 0 \\ 0 & -\frac{k_p L_P^2}{12} & 0 & \frac{k_p L_P^2}{12} \end{bmatrix} \tag{C.8}$$

$$\mathbf{c_p} = \begin{bmatrix} c_p & 0 & -c_p & 0 \\ 0 & \frac{c_p L_P^2}{12} & 0 & -\frac{c_p L_P^2}{12} \\ -c_p & 0 & c_p & 0 \\ 0 & -\frac{c_p L_P^2}{12} & 0 & \frac{c_p L_P^2}{12} \end{bmatrix} \tag{C.9}$$

while for the ballast elements

$$\mathbf{m_b}=\begin{bmatrix}0&0&0&0\\0&0&0&0\\0&0&0&0\\0&0&0&0\end{bmatrix};\ \mathbf{k_b}=\begin{bmatrix}k_b&0&-k_b&0\\0&0&0&0\\-k_b&0&k_b&0\\0&0&0&0\end{bmatrix};\ \mathbf{c_b}=\begin{bmatrix}c_b&0&-c_b&0\\0&0&0&0\\-c_b&0&-c_b&0\\0&0&0&0\end{bmatrix} \tag{C.10}$$

Therefore, the equation of motion for the track model can be described as

$$\mathbf{M\ddot{u}+C\dot{u}+Ku=f} \tag{C.11}$$

where **M**, **C** and **K** are the global mass, damping and stiffness matrices. **u** is the vector of displacements and **f** is a vector of forces and moments acting on the nodes. This can be rearranged as a first order system shown below

$$\mathbf{A}^{\mathbf{track}}\dot{\mathbf{y}}+\mathbf{B}^{\mathbf{track}}\mathbf{y}=\begin{Bmatrix}\mathbf{f}\\\mathbf{0}\end{Bmatrix} \tag{C.12}$$

where $\mathbf{A}^{\text{track}}$ and $\mathbf{B}^{\text{track}}$ are assembled from the global mass, stiffness and damping matrices. And y is a vector of the displacements and velocities.

$$\mathbf{A}^{track}=\begin{bmatrix}\mathbf{C}&\mathbf{M}\\\mathbf{M}&\mathbf{0}\end{bmatrix};\ \mathbf{B}^{track}=\begin{bmatrix}\mathbf{K}&\mathbf{0}\\\mathbf{0}&\mathbf{-M}\end{bmatrix};\ \mathbf{y}=\begin{Bmatrix}\mathbf{u}\\\dot{\mathbf{u}}\end{Bmatrix};\ \dot{\mathbf{y}}=i\omega\mathbf{y} \tag{C.13}$$

This is shown the eigenvalue problem where ω_n and φ^n are the eigenvalues and the eigenvectors respectively.

A complex modal matrix **P** consists of the eigenvalues and eigenvectors as columns

$$\mathbf{P}=\begin{bmatrix}\varphi^{(1)}&&\varphi^{(2N)}\\i\omega_1\varphi^{(1)}&\dots&i\omega_{2N}\varphi^{(2N)}\end{bmatrix} \tag{C.14}$$

In order to transform the equation of motion of the track into modal coordinates, the modal matrix **P** is used. The transformation can be written as follow

$$\mathbf{y=Pq},\qquad \mathbf{Q=P}^{\mathrm{T}}\begin{Bmatrix}\mathbf{f}\\\mathbf{0}\end{Bmatrix} \tag{C.15}$$

where **q** is the modal displacement vector and **Q** is the modal load vector. The uncoupled equations of motion of the track are [110]

$$\mathbf{diag(a)\dot{q}+diag(b)q=Q} \tag{C.16}$$

where

$$\mathbf{diag(a)}=\mathbf{P}^T\mathbf{A}^{track}\mathbf{P};\quad \mathbf{diag(b)}=\mathbf{P}^T\mathbf{B}^{track}\mathbf{P}; \tag{C.17}$$

The equation of motion of the track (C.16), the equation of the vehicle (C.26) and the governing of the wheel/track interaction (C.42) are solved using state-space formulation and a time-stepping routine as shown later.

Additionally the track receptance can be calculated as

$$\alpha_{jk}(\omega) = \sum_{r=1}^{n} \frac{\mathrm{P}_{j,r}\mathrm{P}_{k,r}}{(\mathrm{a})_{r,r}(i\omega - i\omega_r)} \tag{C.18}$$

The receptance is the response in degree of freedom *j* due to a harmonic force of unit magnitude and frequency ω applied to degree of freedom *k*.

C2. Model of vehicle

The vehicle is modelled in this thesis by up to four uncoupled wheel masses linked to the rail by a non-linear Hertzian contact spring. An external static force, F_{ei}, is applied to this system as shown in Figure C.1.

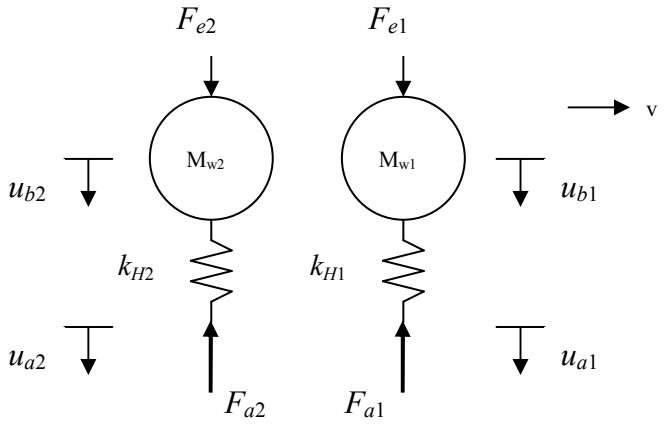

Figure C.1. Wheels and contact springs including applied force [110].

The contact force at the interface with the rail is F_{ai}. The contact stiffnesses are then determined by

$$k_{Hi} = \begin{cases} C_H\sqrt{u_{bi} - u_{ai}}\ \mathrm{N/m} & \text{for} \quad u_{bi} - u_{ai} > 0 \\ 0 & \text{else} \end{cases} \tag{C.19}$$

where C_H is a constant for an elliptical point contact. The relation between the contact force and the approach of distant points δ is given by

$$\delta = \left(\frac{9}{16}\frac{F_{ai}^2}{RE^{*2}}\right)^{1/3} \tag{C.20}$$

where *R* is defined from the radius of the wheel R_w and the radius of the rail R_r as

$$R = \sqrt{R_w R_r} \tag{C.21}$$

E^* is given by the Young's modulus and Poisson's ratio of the wheel and rail

$$E^* = \left(\frac{1-\nu_w^2}{E_w} + \frac{1-\nu_r^2}{E_r} \right)^{-1} \tag{C.22}$$

Then equation (C.20) can be rearranged as

$$F_{ai} = C_H \delta^{3/2} \tag{C.23}$$

where C_H is given by

$$C_H = \frac{4}{3}\sqrt{RE^{*2}} \tag{C.24}$$

Therefore, the equations of motion for a single wheel vehicle model and a two wheel model are given by

$$\begin{bmatrix} 0 & 0 \\ 0 & M_w \end{bmatrix} \begin{Bmatrix} \ddot{u}_a \\ \ddot{u}_b \end{Bmatrix} + \begin{bmatrix} k_H & -k_H \\ -k_H & k_H \end{bmatrix} \begin{Bmatrix} u_a \\ u_b \end{Bmatrix} + \begin{Bmatrix} F_a \\ 0 \end{Bmatrix} = \begin{Bmatrix} 0 \\ F_e \end{Bmatrix} \tag{C.25}$$

and

$$\begin{bmatrix} 0 & 0 & 0 & 0 \\ 0 & 0 & 0 & 0 \\ 0 & 0 & M_{w1} & 0 \\ 0 & 0 & 0 & M_{w2} \end{bmatrix} \begin{Bmatrix} \ddot{u}_{a1} \\ \ddot{u}_{a2} \\ \ddot{u}_{b1} \\ \ddot{u}_{b2} \end{Bmatrix} + \begin{bmatrix} k_{H1} & 0 & -k_{H1} & 0 \\ 0 & k_{H2} & 0 & -k_{H2} \\ -k_{H1} & 0 & k_{H1} & 0 \\ 0 & -k_{H2} & 0 & k_{H2} \end{bmatrix} \begin{Bmatrix} u_{a1} \\ u_{a2} \\ u_{b1} \\ u_{b2} \end{Bmatrix} + \begin{Bmatrix} F_{a1} \\ F_{a2} \\ 0 \\ 0 \end{Bmatrix} = \begin{Bmatrix} 0 \\ 0 \\ F_{e1} \\ F_{e2} \end{Bmatrix} \tag{C.26}$$

A four wheel model is written similarly as an extension of this. The force at the contact point F_a between each wheel and the rail is distributed between the nodes of the track model on either side of the actual wheel location in order to couple the physical model of the wheel with the modal track model. Figure C.2 shows geometry of the finite element between two track nodes.

Displacement $u_{t,2j-1}$ Displacement $u_{t,2j+1}$

Rotation $\theta_{t,2j}$ Rotation $\theta_{t,2j+2}$

Figure C.2. Geometry of finite element between two track nodes [109].

The distribution of load from the wheel at position $\xi_j(t)$ on the adjacent nodes is obtained by using Hermite interpolating polynomials, cited in [109]:

$$H_{1,j} = 1 - \frac{3\xi_j^2}{L_j^2} + \frac{2\xi_j^3}{L_j^3} \tag{C.27}$$

$$H_{2,j} = \xi_j - \frac{2\xi_j^2}{L_j} + \frac{\xi_j^3}{L_j^2} \tag{C.28}$$

$$H_{3,j} = \frac{3\xi_j^2}{L_j^2} - \frac{2\xi_j^3}{L_j^3} \tag{C.29}$$

$$H_{4,j} = -\frac{\xi_j^2}{L_j} + \frac{\xi_j^3}{L_j^2} \tag{C.30}$$

A matrix **H** is formed as an assembly of the interpolating polynomials in the order of a vertical and a rotational term for each node. The cubic polynomials are chosen to represent Euler beam bending [123].

$$\mathbf{H} = \begin{bmatrix} H_1 & H_2 & H_3 & H_4 \end{bmatrix} \tag{C.31}$$

The displacement of the wheel at a point between two nodes of the track is given by the displacement of the rail and the relative displacement between the track and wheel,

$$u_{ai}(t) = \mathbf{H} \begin{Bmatrix} u_{t,2j-1} \\ \theta_{t,2j} \\ u_{t,2j+1} \\ \theta_{t,2j+2} \end{Bmatrix} + r(\xi_j) \tag{C.32}$$

At the interface the displacement of the wheel and track can be described in modal coordinates as

$$u_{ai}(t) = \mathbf{H}\mathbf{P}^{\mathbf{int}}\mathbf{q}(t) + r(\xi_j) \tag{C.33}$$

where $\mathbf{P}^{\text{int}}$ is the modal matrix. The velocity and acceleration of the interfacial degree of freedom are given by

$$\dot{u}_{ai}(t) = \mathbf{T}(t)\dot{\mathbf{q}}(t) + \mathbf{U}(t)\mathbf{q}(t) + \dot{r} \tag{C.34}$$

$$\ddot{u}_{ai}(t) = \mathbf{R}(t)\dot{\mathbf{q}}(t) + \mathbf{S}(t)\mathbf{q}(t) + \ddot{r} \tag{C.35}$$

where **T**, **U**, **R** and **S** are defined by

$$\mathbf{T}(t) = \mathbf{H}\mathbf{P}^{\text{int}} \tag{C.36}$$

$$\mathbf{U}(t) = \frac{d\mathbf{H}}{d\xi} v\mathbf{P}^{\text{int}} \tag{C.37}$$

$$\mathbf{R}(t) = 2\frac{d\mathbf{H}}{d\xi} v\mathbf{P}^{\text{int}} + \mathbf{H}\mathbf{P}^{\text{int}} diag(i\omega_n) \tag{C.38}$$

$$\mathbf{S}(t) = \frac{d^2\mathbf{H}}{d\xi^2} v^2\mathbf{P}^{\text{int}} \tag{C.39}$$

The derivatives with respect to time of the initial roughness function, cited in [109], are expressed by:

$$\dot{r} = \frac{dr}{d\xi} v(t) \tag{C.40}$$

$$\ddot{r} = \frac{d^2 r}{d\xi^2} v^2(t) + \frac{dr}{d\xi} \dot{v}(t) \tag{C.41}$$

The distribution of the loads between the nodes either side of the contact point are written in terms of modal coordinates as

$$\mathbf{Q} = \mathbf{P}^{\mathrm{int}T} \mathbf{H}^T \mathbf{F}_a(t) \tag{C.42}$$

C3. State-space solution to equations of motion of system

The equations of motion for the track, vehicle and the interaction between these components including roughness and contact force, are solved in term of modal coordinates. The equations (C16), (C26) and (C42) are rearranged in a standard matrix form as [110]

$$\mathbf{A}(\mathbf{g},t)\dot{\mathbf{g}} + \mathbf{B}(\mathbf{g},t)\mathbf{g} = \mathbf{F}(\mathbf{g},t) \tag{C.43}$$

where $\mathbf{A}(\mathbf{g},t)$ and $\mathbf{B}(\mathbf{g},t)$ are defined [110] as

$$\mathbf{A}(\mathbf{g},t) = \begin{bmatrix} \mathbf{diag(a)} & \mathbf{0} & \mathbf{0} & \mathbf{0} & \mathbf{0} & \mathbf{-P^{intT}H^T} \\ \mathbf{0} & \mathbf{0} & \mathbf{0} & \mathbf{0} & \mathbf{0} & \mathbf{I} \\ \mathbf{0} & \mathbf{0} & \mathbf{C_w} & \mathbf{0} & \mathbf{M_w} & \mathbf{0} \\ \mathbf{0} & \mathbf{0} & \mathbf{I} & \mathbf{0} & \mathbf{0} & \mathbf{0} \\ \mathbf{R} & \mathbf{0} & \mathbf{0} & \mathbf{-I} & \mathbf{0} & \mathbf{0} \\ \mathbf{T} & \mathbf{-I} & \mathbf{0} & \mathbf{0} & \mathbf{0} & \mathbf{0} \end{bmatrix} \tag{C.44}$$

$$\mathbf{B}(\mathbf{g},t) = \begin{bmatrix} \mathbf{diag(b)} & \mathbf{0} & \mathbf{0} & \mathbf{0} & \mathbf{0} & \mathbf{0} \\ \mathbf{0} & \mathbf{K_H} & \mathbf{-K_H} & \mathbf{0} & \mathbf{0} & \mathbf{0} \\ \mathbf{0} & \mathbf{-K_H} & \mathbf{K_H} & \mathbf{0} & \mathbf{0} & \mathbf{0} \\ \mathbf{0} & \mathbf{0} & \mathbf{0} & \mathbf{0} & \mathbf{-I} & \mathbf{0} \\ \mathbf{S} & \mathbf{0} & \mathbf{0} & \mathbf{0} & \mathbf{0} & \mathbf{0} \\ \mathbf{U} & \mathbf{0} & \mathbf{0} & \mathbf{0} & \mathbf{0} & \mathbf{0} \end{bmatrix} \tag{C.45}$$

where $\boldsymbol{g}(t)$ is a vector constructed from the modal coordinates $\mathbf{q}$ with the interaction force in the form of the impulse $\hat{\mathbf{F}}_a$ and the displacement and velocity of the wheel centre and the contact point.

$$\mathbf{g}(t) = \left\{ \mathbf{q} \quad \mathbf{u_a} \quad \mathbf{u_b} \quad \dot{\mathbf{u}}_\mathbf{a} \quad \dot{\mathbf{u}}_\mathbf{b} \quad \hat{\mathbf{F}}_\mathbf{a} \right\} \tag{C.46}$$

The forcing term $\mathbf{F}(\mathbf{g},t)$ is given by

$$\mathbf{F}(\mathbf{g},t) = \left\{ \mathbf{0}^{\mathbf{T}} \quad \mathbf{0}^{\mathbf{T}} \quad \mathbf{F_b}^{\mathbf{ext^T}} \quad \mathbf{0}^{\mathbf{T}} \quad \mathbf{-\ddot{r}}^{\mathbf{T}} \quad \mathbf{-\dot{r}}^{\mathbf{T}} \right\}^{T} \tag{C.47}$$

An ordinary differential equation for equation (C43) can be written as

$$\dot{\mathbf{g}} = \mathbf{A}^{-1}(\mathbf{F} - \mathbf{B}\mathbf{g}), \quad \mathbf{g}(t=0) = g_0 \tag{C.48}$$

To save time of calculation, the matrix $\mathbf{A}(\mathbf{g},t)$ is divided into submatrices:

$$\mathbf{A}(\mathbf{g},t) = \begin{bmatrix} \mathbf{A_{11}} & \mathbf{A_{12}} \\ \mathbf{A_{21}} & \mathbf{A_{22}} \end{bmatrix} \tag{C.49}$$

The inverse of $\mathbf{A}(\mathbf{g},t)$ can be calculated [124] by

$$\begin{bmatrix} \mathbf{A_{11}} & \mathbf{A_{12}} \\ \mathbf{A_{21}} & \mathbf{A_{22}} \end{bmatrix}^{-1} = \begin{bmatrix} \mathbf{A_{11}}^{-1} + \mathbf{A_{11}}^{-1}\mathbf{A_{12}}\mathbf{G}^{-1}\mathbf{A_{21}}\mathbf{A_{11}}^{-1} & \mathbf{-A_{11}}^{-1}\mathbf{A_{12}}\mathbf{G}^{-1} \\ \mathbf{-G}^{-1}\mathbf{A_{21}}\mathbf{A_{11}}^{-1} & \mathbf{G}^{-1} \end{bmatrix} \tag{C.50}$$

where

$$\mathbf{G} = \left(\mathbf{A_{22}} - \mathbf{A_{21}}\mathbf{A_{11}}^{-1}\mathbf{A_{12}} \right) \tag{C.51}$$

The Matlab routine ODE113, as used in [109], has been used for the calculation.

Appendix D

A simple wheel/rail interaction and excitation by roughness

A model for wheel/rail interaction and excitation by roughness is given in this appendix based on [3].

The wheel/rail interaction and excitation by roughness can be represented by two dynamic systems connected at a point as shown in Figure D.1. A 'moving excitation' represents the roughness as a strip which is pulled along between the surface of wheel and rail. Only vertical vibration is considered here.

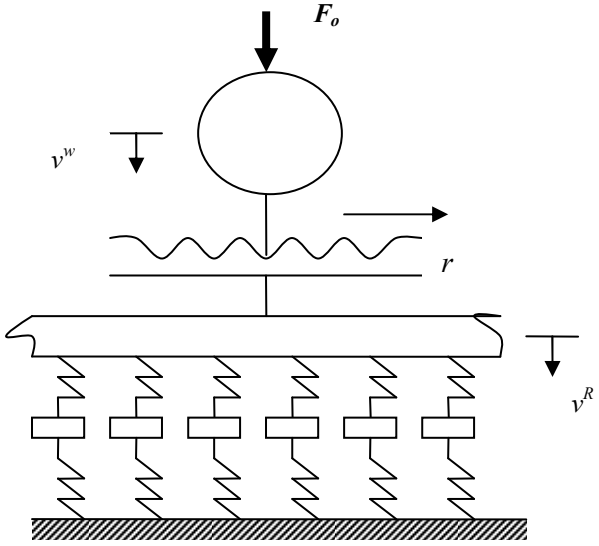

Figure D.1. The wheel/rail interaction and excitation by roughness.

The rail is excited by a vertical harmonic force $Fe^{i\omega t}$ of circular frequency ω and complex amplitude F. Then the velocity amplitude v^R with moving direction positive downwards is given by

$$v^R = Y^R F \tag{D.1}$$

where Y^R is the rail mobility. An equal reaction force acts upwards on the wheel so the downwards wheel velocity v^W is given by

$$v^W = -Y^W F \tag{D.2}$$

where Y^W is the wheel mobility. The roughness amplitude r at circular frequency ω, and the various velocities are related by

$$v^R = i\omega r + v^W \tag{D.3}$$

where $i\omega r$ is the roughness velocity amplitude. The frequency $\omega = 2\pi f$ is determined from $f = \frac{v}{\lambda}$, where v is the train speed and λ is the wavelength of irregularity of the wheel or rail surface. Combining equations (D.1- D.3) gives the force amplitude,

$$F = \frac{i\omega r}{Y^R + Y^W} \tag{D.4}$$

Then the velocity amplitudes can be obtained as

$$v^R = \frac{i\omega r Y^R}{Y^R + Y^W} \tag{D.5}$$

$$v^W = \frac{-i\omega r Y^W}{Y^R + Y^W} \tag{D.6}$$

The force amplitude is derived from the combined dynamic properties of the wheel and rail. The wheel can be represented by its unsprung mass for frequencies up to 200 Hz (the range which is relevant to ground vibration and ground-borne noise).

$$Y^W = \frac{-i}{\omega M_W} \tag{D.7}$$

The track mobility can be found from the model in [3]. Below the resonance frequency of the track mass on the ballast stiffness the mobility of the track can be approximated as

$$Y^R = \frac{i\omega}{\widetilde{K}_T} \tag{D.8}$$

where $\widetilde{K}_T$ is a complex stiffness; $\widetilde{K}_T = K_T(1 + i\eta_T)$, and η_T is the damping loss factor. K_T is determined by the rail bending stiffness as well as the support stiffness.

From equation (D.7) at low frequencies the wheel mobility dominates as it is mass-controlled whereas the rail is stiffness-controlled as in equation (D.8). According to this for the frequencies up to about 60 Hz the wheel has a larger mobility. Then equations (D.5) and (D.6) can be approximated to

$$v^R \approx i\omega r \frac{Y^R}{Y^W} \approx -i\omega r \frac{\omega^2 M_W}{\widetilde{K}_T} \tag{D.9}$$

$$v^W \approx -i\omega r \tag{D.10}$$

Thus the wheel moves in the same direction as the track but its amplitude is larger as it moves with the roughness amplitude.

At the frequency about 60 Hz the mobilities of the wheel mass and track are equal and opposite, as shown in Figure 4.3

$$\mathrm{Im}\left(Y^W + Y^R\right) = 0 \tag{D.11}$$

giving a coupled resonance of the wheel-track system,

$$\omega = \sqrt{\frac{K_T}{M_W}} \tag{D.12}$$

At this frequency the system response has a maximum and the denominator in equations (D.5) and (D.6) is given by

$$Y^W + Y^R = \frac{-i\omega}{K_T} + \frac{i\omega}{K_T(1+i\eta_T)} = \frac{\omega\eta_T}{K_T(1+i\eta_T)} \tag{D.13}$$

Then the vibration amplitudes are

$$v^R \approx i\omega r \frac{K_T(1+i\eta_T)}{\omega\eta_T} \frac{i\omega}{K_T(1+i\eta_T)} = \frac{-\omega r}{\eta_T}, \tag{D.14}$$

$$v^W \approx -i\omega r \frac{K_T(1+i\eta_T)}{\omega\eta_T}\left(\frac{-i\omega}{K_T}\right) = -\frac{\omega r}{\eta_T}(1+i\eta_T) \tag{D.15}$$

For low damping these are approximately equal in magnitude and are in phase with each other. This might occur in the case of a slab track system which has low damping whereas the ballast track system has a higher damping loss factor which gives a peak with a smaller magnitude.

For the higher frequencies above the coupled resonance, the track mobility dominates the response and equations (D.5) and (D.6) can be approximated to

$$v^R \approx i\omega r \tag{D.16}$$

$$v^W \approx -i\omega r \frac{Y^W}{Y^R} \approx i\omega r \frac{K_T}{\omega^2 M_W} \tag{D.17}$$

Thus the rail moves with the larger amplitude which is equal to the roughness amplitude; it still moves in the same direction as the wheel, whereas the wheel has less motion due to its inertia.

REFERENCES

1. D.J. Thompson and C.J.C. Jones, “Low noise track meets environmental concerns”, Railway Gazette International July 2002.
2. G. Lombaert and G. Degrande, “Ground-borne vibration due to static and dynamic axle loads of InterCity and high-speed trains,” Journal of Sound and Vibration 319 (2009), pp.1036-1066.
3. D.J. Thompson, “Railway noise and vibration: mechanisms, modelling and means of control,” 1st edition, Elsevier, UK, 2008.
4. P. Galvin, A. Romero and J. Dominguez, “Fully three-dimensional analysis of high-speed train-track-soil-structure dynamic interaction,” Journal of Sound and Vibration 329 (2010), pp.5147-5163.
5. C.J.C. Jones, “Groundborne noise from new railway tunnels,” Inter noise 96, 25th Anniversary Congress-Liverpool, INCE: 13.4.2.
6. M.F.M. Hussein and H.E.M. Hunt, “A numerical model for calculating vibration from a railway tunnel embedded in a full-space,” Journal of Sound and Vibration 305 (2007), pp.401-431.
7. C.J.C. Jones, X. Sheng and D.J. Thompson, “Ground vibration from dynamic and quasi-static loads moving along a railway track on layered ground,” Wave 2000, Chouw & Schmid (eds), 2000 Balkema, Rotterdam, pp.83-97.
8. V.V. Krylov and C. Ferguson, “Calculation of low-frequency ground vibrations from railway trains”, Applied Acoustics No.42 (1994), pp.199-213.
9. V.V. Krylov, “Vibrational impact of high-speed trains. I. Effect of track dynamics”, Journal of Acoustical Society of America No.100(5) (1996), pp.3121-3134.
10. V.V. Krylov, “Comments on Chapter 12 of “Railway Noise and Vibration: Mechanisms, Modelling and Means of Control”, by D. Thompson (with contributions from C. Jones and P.-E. Gautier), Elsevier, 2009”, Applied Acoustics No.72 (2011), pp.785-786.
11. X. Sheng, C.J.C. Jones and D.J. Thompson, “A comparison of a theoretical model for quasi-statically and dynamically induced environmental vibration from trains with measurements”, Journal of Sound and Vibration 267 (2003), pp.621-635.

12. X. Sheng, “Ground vibrations generated from trains,” PhD Thesis University of Southampton, 2001.
13. X. Sheng, C.J.C. Jones and M. Petyt, “Ground vibration generated by a load moving along a railway track,” Journal of Sound and Vibration 228(1) (1999), pp.129-156.
14. C.J.C. Jones, X. Sheng and M. Petyt, “Simulations of ground vibration from a moving harmonic load on a railway track,” Journal of Sound and Vibration 231(3) (2000), pp.739-751.
15. H.E.M. Hunt, “Types of rail roughness and the selection of vibration isolation measures,” 9th IWRN, International Workshop on Railway Noise, Munich 2007, pp.341-347.
16. F.E. Richart, J.R. Hall and R.D. Woods, “Vibrations of soils and foundations,” 1st edition, Prentice-Hall, USA, 1970.
17. L. Fryba, “Vibration of solids and structures under moving loads,” 3rd edition, Thomas Telford, 1999, pp. 269-270.
18. J. Houbrechts, M. Schevenels, G. Lombaert, G. Degrande, W. Rucker, V. Cuellar and A. Smekal, “Test procedures for the determination of the dynamic soil characteristics,” Railway Induced Vibration Abatement Solutions RIVAS WP 1.3 Deliverable 1.1, Draft.
19. L. Cremer, M. Heckl and E.E. Ungar, “Structure-borne sound,” 2nd edition, Springer-Verlag, Germany, 1988.
20. O.A.B. Hassan, “Train-induced groundborne vibration and noise in buildings,” 1st edition, Multi-Science Publishing, 2006.
21. J. T. Nelson, “Prediction of ground vibration from trains using seismic reflectivity methods for a porous soil,” Journal of Sound and Vibration 231(3) (2000), pp. 727-737.
22. P. Coulier, G. Degrande, A. Dijckmans, J. Houbrechts, G. Lombaert, W. Rucker, L. Auersch, M. R. Plaza, V. Cuellar, D.J. Thompson, A. Ekblad and A. Smekal, “Scope of the parametric study on mitigation measures on the transmission path,” Railway Induced Vibration Abatement Solutions RIVAS WP 4.1 Deliverable 4.1, Draft.
23. M. Heckl, G. Hauck, R. Wettschureck, “Structure-borne sound and vibration from rail traffic,” Journal of Sound and Vibration 193(1) (1996), pp.175-184.

24. J.T. Nelson and H.J. Saurenman, “A prediction procedure for rail transportation groundborne noise and vibration,” Transportation Research Record 1143, pp.26-35.
25. C. Madshus, B. Bessason and L. Harvik, “Prediction model for low frequency vibration from high speed railways on soft ground,” Journal of Sound and Vibration 193(1) (1996), pp.195-203.
26. C.E. Hanson, D.A. Towers and L.D. Meister, “Transit noise and vibration impact assessment”, Federal Transit Administration, Department of Transportation United States of America, FTA-VA-90-1003-06, 2006.
27. H. Verbraken, G. Lombaert and G Degrande, “Verification of an empirical prediction method for railway induced vibrations by means of numerical simulations,” Journal of Sound and Vibration 330 (2011), pp.1692-1703.
28. H. Verbraken, H. Eysermans, E. Dechief, S. Francois, G. Lombaert and G. Degrande, “Verification of an empirical prediction method for railway induced vibration,” 10th International Workshop on Railway Noise, Nagahama, Japan, October 2010, pp.229-236.
29. G. Degrande, D. Clouteau, R. Othman, M. Arnst, H. Chebli, R. Klein, P. Chatterjee and B. Janssens, “A numerical model for ground-borne vibrations from underground railway traffic based on a periodic finite element-boundary element formulation,” Journal of Sound and Vibration 293(3-5) (2006), pp.645-666.
30. G. Degrande, M. Schevenels, P. Chatterjee, W. Van de Velde, P. Holscher, V. Hopman, A. Wang and N. Dadkah, “Vibrations due to a test train at variable speeds in a deep bored tunnel embedded in London clay,” Journal of Sound and Vibration 293 (2006), pp.626-644.
31. R.J. Greer, “AEL methodology for the prediction of re-radiated noise in residential buildings from trains travelling in tunnels,” Internoise Leuven, Belgium 1993.
32. R.A. Hood, R.J. Greer, M. Breslin and P.R. Williams, “The calculation and assessment of ground-borne noise and perceptible vibration from trains in tunnels,” Journal of Sound and Vibration 193(1) (1996), pp.215-225.
33. E. Kausel and J.M. Roesset, “Stiffness matrices for layered soils,” Bulletin of the Seismological Society of America, December 1981, Vol.71, No.6, pp.1743-1761.

34. X. Sheng, C.J.C. Jones and M. Petyt, “Ground vibration generated by a harmonic load acting on a railway track,” Journal of Sound and Vibration 225(1) (1999), pp.3-28.
35. H. Lamb, “On the propagation of tremors over the surface of an elastic solid,” Philosophical Transactions of the Royal Society of London, Series A, Vol. 203 (1904), pp.1-42.
36. N. Haskell, “The dispersion of surface waves on multilayered medium,” Bulletin of the Seismological Society of America Vol.43 (1953), pp.17-34.
37. W.T. Thomson, “Transmission of elastic waves through a stratified soil medium,” Journal of Applied Physics 21, 1950, pp.81-93.
38. S. Nazarian and M. R. Desai, “Automated surface wave method: field testing,” Journal of Geotechnical Engineering, Vol. 119 (1993), pp. 1094-1111.
39. D. Yuan and S. Nazarian, “Automated surface wave method: inversion technique,” Journal of Geotechnical Engineering, Vol. 119 (1993), pp. 1112-1126.
40. H. Grundmann, M. Lieb and E. Trommer, “The response of a layered half-space to traffic loads moving along its surface,” Applied Mechanics 69 (1999), pp.55-67.
41. L. Auersch, “Wave propagation in layered soils: theoretical solution in wavenumber domain and experimental results of hammer and railway traffic excitation,” Journal of Sound and Vibration 173(2) (1994), pp.233-264.
42. X. Sheng, C.J.C. Jones and D.J. Thompson, “A theoretical model for ground vibration from trains generated by vertical track irregularities,” Journal of Sound and Vibration, 272 (3-5) (2004), pp.937-965.
43. C. Madshus and A.M. Kaynia, “High-speed railway lines on soft ground: dynamic behaviour at critical train speed,” Journal of Sound and Vibration 231(3) (2000), pp.689-701.
44. A. Karlstrom and A. Bostrom, “An analytical model for train-induced ground vibrations from railways,” Journal of Sound and Vibration 292 (2006), pp.221-241.
45. C.J.C. Jones and J.R. Block, “Prediction of ground vibration from freight trains,” Journal of Sound and Vibration 193(1) (1996), pp. 205-213.

46. G. Degrande, “Free field vibrations during the passage of a Thalys high-speed train at variable speed,” Journal of Sound and Vibration 247(1) (2001), pp.131-144.
47. X. Sheng, C.J.C. Jones and D.J. Thompson, “Ground vibration generated by a harmonic load moving in a circular tunnel in a layered ground,” Journal of Low Frequency Noise, Vibration and Active Control volume 22 (2003), pp.83-96.
48. J.A. Forrest, H.E.M. Hunt, “A three-dimensional tunnel model for calculation of train-induced ground vibration,” Journal of Sound and Vibration 294 (2006), pp.678-705.
49. J.A. Forrest, H.E.M. Hunt, “Ground vibration generated by trains in underground tunnels,” Journal of Sound and Vibration 294 (2006), pp.706-736.
50. M.F.M. Hussein and H.E.M. Hunt, “Modelling of floating-slab tracks with continuous slabs under oscillating moving loads,” Journal of Sound and Vibration 297 (2006), pp.37-54.
51. M.F.M. Hussein and H.E.M. Hunt, “Modelling of floating-slab tracks with discontinuous slab Part2: response to moving trains,” Journal of Low Frequency Noise, Vibration and Active Control, Vol.25 No.2, 2006, pp.111-118.
52. M.F.M. Hussein and H.E.M. Hunt, “Using the PiP model for fast calculation of vibration from a ralway tunnel in a multi-layered half-space,” 9th IWRN, International Workshop on Railway Noise, Munich 2007.
53. K. Kuo and H.E.M. Hunt, “The role of structural foundations in transmission of vibration from underground railways,” The sixteenth International Congress on Sound and Vibration, Krakow, 2009.
54. S. Jones and H.E.M. Hunt, “The effect of voids around underground railway tunnels on ground vibration,” The sixteenth International Congress on Sound and Vibration, Krakow, 2009.
55. S. Jones and H.E.M. Hunt, “Voids at the tunnel-soil interface for calculation of ground vibration from underground railways,” Journal of Sound and Vibration, 330 (2011), pp.245-270.

56. X. Sheng, C.J.C. Jones and D.J. Thompson, “Prediction of ground vibration from trains using the wavenumber finite and boundary element methods,” Journal of Sound and Vibration 293 (2006), pp.575-586.
57. S. Gupta, M.F.M. Hussein, G Degrande, H.E.M. Hunt and D. Clouteau, “A comparison of two numerical models for the prediction of vibrations from underground railway traffic,” Soil Dynamics and Earthquake Engineering 27(7) (2007), pp.608-624.
58. M. Katou, T. Matsuoka, et al, “Numerical simulation study of ground vibrations using forces from wheels of a running high-speed train,” Journal of Sound and Vibration 318 (2008), pp.830-849.
59. C.J.C. Jones, D.J. Thompson and M. Petyt, “A model for ground vibration from railway tunnels,” ICE Transport Journal 153 Issue 2, 2002, pp.121-129.
60. L. Andersen and C.J.C. Jones, “Coupled boundary and finite element analysis of vibration from railway tunnels-a comparison of two- and three-dimensional models,” Journal of Sound and Vibration 293 (2006), pp.611-625.
61. L. Andersen and C.J.C. Jones, “Vibration from a railway tunnel predicted by coupled finite element and boundary element analysis in two and three dimensions,” 2002 Swets & Zeitlinger, Lisse, pp.1131-1136.
62. X. Sheng, C.J.C. Jones and D.J. Thompson, “Modelling ground vibration from railways using wavenumber finite- and boundary-element methods,” Proc. R. Soc. A (2005) 461, pp.2043-2070.
63. P. Jean, C. Guigou and M. Villot, “A 2.5D BEM model for ground-structure interaction,” Journal of Building Acoustics, Vol.11 No.3 (2004), pp.157-173.
64. G. Lombaert, G. Degrande, J. Kogut and S. Francois, “The experimental validation of a numerical model for the prediction of railway induced vibrations,” Journal of Sound and Vibration 297 (2006), pp.512-535.
65. G. Lombaert, G. Degrande, B. Vanhauwere, B. Vandeborght and S. Francois, “The control of ground borne vibrations from railway traffic by means of continuous floatings slabs,” Journal of Sound and Vibration 297 (2006), pp.946-961.
66. G. Lombaert, G. Degrande, P. Galvin, E. Bongini and F. Poisson, “A comparison of predicted and measured ground vibrations due to high speed, passenger, and freight trains,” 10th International Workshop on Railway Noise, Nagahama, Japan, October 2010, pp.221-228.

67. S. Francois, M. Schevenels, G. Lombaert, P. Galvin and G. Degrande, "A 2.5D coupled FE-BE methodology for the dynamic interaction between longitudinally invariant structures and a layered halfspace," Computer Methods in Applied Mechanics and Engineering, 199(23-24) (2010), pp.1536-1548.
68. S. Gupta, G Degrande and G. Lombaert, "Experimental validation of a numerical model for subway induced vibrations", Journal of Sound and Vibration 321 (2009), pp.786-812.
69. S. Gupta, H. Van den Berghe, G. Lombaert and G Degrande, "Numerical modelling of vibrations from a Thalys high speed train in the Groene Hart tunnel," Soil Dynamics and Earthquake Engineering 30 (2010), pp.82-97.
70. S. Gupta, Y. Stanus, G. Lombaert and G Degrande, "Influence of tunnel and soil parameters on vibrations from underground railways," Journal of Sound and Vibration 327 (2009), pp.70-91.
71. P. Galvin, S. Francois, M. Schevenels, E. Bongini, G Degrande and G. Lombaert, "A 2.5D coupled FE-BE model for the prediction of railway induced vibrations," Soil Dynamics and Earthquake Engineering 30 (2010), pp.1500-1512.
72. E.A. Forchap and G. Schmid, "Determination of sub-soil properties using a frequency-wavenumber analysis of Rayleigh surface waves", Structural Dynamics, EURODYN Vol.2 (1999), Rotterdam, pp.983-988.
73. BS ISO14837-1:2005, "Mechanical vibration – ground-borne noise and vibration arising from rail systems – Part 1: General guidance".
74. A. Karlstrom and A. Bostrom, "Efficiency of trenches along railways for trains moving at sub-or supersonic speeds," Soil Dynamics and Earthquake Engineering (2007), Vol.27, pp.625-641.
75. L.Anderson and S.R.K. Nielsen, "Reduction of ground vibration by means of barriers or soil improvement along a railway track," Soil Dynamics and Earthquake Engineering (2005), Vol. 25, pp.701-716.
76. A. Garcia-Bennett, "The effectiveness of trenches in reducing train-induced ground vibrations," MSc. Dissertation, University of Southampton, 2008.
77. A. Garcia-Bennett, C.J.C. Jones and D.J. Thompson, "A numerical investigation of railway ground vibration mitigation using a trench in a layered

soil," 10th International Workshop on Railway Noise, Nagahama, Japan, October 2010, pp.315-322.

78. C.J.C. Jones, D.J. Thompson and JI Andreu-Medina, "Initial theoretical study of reducing surface-propagating vibration from trains using earthworks close to the track," waiting to ask Eurodyn2011-paper-528.
79. A.T. Peplow, C.J.C. Jones and M. Petyt, "Surface vibration propagation over a layered elastic half-space with an inclusion," Applied Acoustics 56(1999), pp.283-296.
80. H. Lane, S. Berg and M. Larsson, "Finite element calculations of rail vibration countermeasures," Vehicle System Dynamics, Vol.45(6) (2007), pp.565-581.
81. J.F. Lu, B. Xu and J.H Wang, "Numerical analysis of isolation of the vibration due to moving loads using pile rows," Journal of Sound and Vibration 319 (2009), pp.940-962.
82. J.E. Phillips and J.T. Nelson, "Analysis and design of new floating slab track for special trackwork using finite element analysis (FEA)," 10th International Workshop on Railway Noise, Nagahama, Japan, October 2010, pp.263-269.
83. A. Wang and S.J. Cox, "Ground vibration control using pandrol vanguard in a tunnel on Guangzhou Metro Line 1," 2nd International Symposium on Environmental vibrations (ISEV2005).
84. N. Triepaischajonsak, "The effect of sleeper soffit pads on railway noise," MSc. Dissertation, University of Southampton, 2008.
85. D.J. Thompson, B. Hemsworth and N. Vincent, "Experimental validation of the TWINS prediction program for rolling noise, Part 1: description of the model and method," Journal of Sound and Vibration, Vol.193(1) (1996), pp.123-135.
86. D.J. Thompson, P. Fodiman, and H. Mahe, "Experimental Validation of the TWINS Prediction program for rolling noise, Part 2: Results," Journal of Sound and Vibration, Vol.193(1) (1996), pp.137-147.
87. D.J. Thompson, "Wheel-rail noise generation, part II: Wheel Vibration," Journal of Sound and Vibration, Vol.161(3) (1993), pp.401-419.
88. R. Garburg, "Under sleeper pads WP 3: noise and vibrations," presentation to project meeting, Munich, February 2007.
89. J.P. Talbot and H.E.M. Hunt, "On the performance of base-isolated buildings," Building Acoustics, Vol.7 No.3, 2000, pp.163-178.

90. J.P. Talbot and H.E.M. Hunt, “Isolation of buildings from rail-tunnel vibration: a review,” Building Acoustics, Vol.10 No.3, 2003, pp.177-192.
91. D.E. Newland and H.E.M. Hunt, “Isolation of buildings from ground vibration: a review of recent progress,” Proceedings of Institution of Mechanical Engineers, Part F, volume 205 (1991), pp.39-52.
92. H.E.M. Hunt, “Modelling of rail vehicles and track for calculation of ground-vibration transmission into buildings,” Journal of Sound and Vibration 193(1) (1996), pp.185-194.
93. L. Pyl, G. Degrande, G. Lombaert and W. Haegeman, “Validation of a source-receiver model for road traffic-induced vibrations in buildings. I: source model,” Journal of Engineering Mechanics Vol.130(12) (2004), pp.1377-1393.
94. L. Pyl, G. Degrande and D. Clouteau, “Validation of a source-receiver model for road traffic-induced vibrations in buildings. II: receiver model,” Journal of Engineering Mechanics Vol.130(12) (2004), pp.1394-1406.
95. J.A. Zapfe, H. Saurenman and S. Fidell, “Ground-borne noise and vibration in buildings caused by rail transit,” TCRP 2009.
96. J.W. Edwards, “Survey of environmental noise and vibration from London underground trains,” Internoise 96, Liverpool, INCE: 56, pp.2029-2032.
97. V.V. Krylov, “Generation of ground vibrations by superfast trains”, Applied Acoustics No.44 (1995), pp.149-164.
98. P. Kearey, M. Brooks and I. Hill, “An introduction to geophysical exploration,” 3rd edition, Blackwell Science Ltd, 2002, pp.100-102.
99. D. V. Jones, “The Surface Propagation of Ground Vibration,” PhD Thesis University of Southampton, 1987.
100. M.J. Griffin, “Handbook of human vibration,” 1st edition, Academic Press, 1990.
101. M. Brennan, “Mobility and impedance methods,” Vibration Control lecture notes, ISVR, University of Southampton 2007.
102. G.V. Frisk, “Ocean and seabed acoustic: A theory of wave propagation,” 1st edition, Prentice-Hall, Inc., 1994, pp.89.
103. BS EN ISO 3095:2005, “Railway applications acoustics measurement of noise emitted by railbound vehicles,” British Standard, 2005.

104. X. Sheng, C.J.C. Jones and D.J. Thompson, "TGV – a computer program for train-induced ground vibration," ISVR Technical Memorandum No:878, ISVR, Southampton University, 2001.

105. S.L. Grassie, M.J. Saxon and J.D. Smith, "Measurement of longitudinal rail irregularities and criteria for acceptable grinding," Journal of Sound and Vibration 227(5) (1999), pp.949-964.

106. D. Herron, "Vibration of railway bridges in the audible frequency range," EngD Thesis University of Southampton, 2009, pp.105-118.

107. S. Gupta, W. F. Liu, G. Degrande, G. Lombaert and W.N. Liu, "Prediction of vibrations induced by underground railway traffic in Beijing," Journal of Sound and Vibration 310 (2008), pp.608-630.

108. A.A. Mirza, A. Frid, J.C.O. Nielsen and C.J.C. Jones, "Ground vibration induced by railway traffic – the influence of vehicle parameters," 10th International Workshop on Railway Noise, Nagahama, Japan, October 2010, pp.245-252.

109. B.E. Croft, "The Development of Rail-head Acoustic Roughness," PhD Thesis University of Southampton, 2009.

110. J.C.O. Nielsen and A. Igeland, "Vertical dynamic interaction between train and track-influence of wheel and rail imperfections," Journal of Sound and Vibration 187(5) (1995), pp.825-839.

111. J.C.O. Nielsen and J. Oscarsson, "Simulation of dynamic train-track interaction with state-dependent track properties," Journal of Sound and Vibration 275(3-5) (2004), pp.515-532.

112. B.E. Croft, C.J.C. Jones and D.J. Thompson, "Reducing wheel-rail interaction forces and roughness growth by application of rail dampers," 9th IWRN, International Workshop on Railway Noise, Munich 2007.

113. K. Shin and J.K. Hammond, "Fundamentals of signal processing for sound and vibration engineers," 1st edition, Wiley, UK, 2008.

114. S.L. Grassie, R.W. Gregory, D. Harrison and K.L. Johnson, "Dyanmic response of railway track to high frequency vertical excitation," Journal of Mechanical Engineering Science 24(1982), pp. 77-90.

115. N. Triepaischajonsak, D.J. Thompson and C.J.C. Jones, "The experimental validation of a semi-analytical track/ground model for vibration

induced by trains," X International Conference on Recent Advances in Structural Dynamics, Southampton, UK, July 2010, No.139.

116. N. Triepaischajonsak, D.J. Thompson, C.J.C. Jones and J. Ryue, "Track-based control measures for ground vibration – the influence of quasi-static loads and dynamic excitation," 10th International Workshop on Railway Noise, Nagahama, Japan, October 2010, pp.237-244.

117. N. Triepaischajonsak, D.J. Thompson, C.J.C. Jones, J. Ryue and J.A. Priest, "Ground vibration from trains: experimental parameter characterization and validation of a numerical model, Proc. IMechE, Part F, Journal of Rail and Rapid Transit Vol. 225 (2011), pp 140-153.

118. G. de France, "Railway track: effect of rail support stiffness on vibration and noise," MSc Dissertation, ISVR. University of Southampton, 1998.

119. British Standard, BS EN 15610:2009, Railway applications – Noise emission – Rail roughness, measurement related to rolling noise generation.

120. T.X. Wu and D.J. Thompson, "On the impact noise generation due to a wheel passing over rail joints," Journal of Sound and Vibration 267 (2003), pp.485-496.

121. Standard NR/L2/TRK/3011, Issue 6 Continuous Welds Rail (CWR)

122. P.J. Remington, L.G. Kurzweil and D.A. Towers, "Low-frequency noise and vibration from trains," Chapter 16 in Transportation Noise Reference Book edited by P.M. Nelson, 1987.

123. M. Petyt, "Introduction to finite element vibration analysis," Cambridge University Press, Cambridge.

124. S. Barnett, "Matrix Methods for Engineers and Scientists," McGraw-Hill, London, 1979.